


5-2009

Evaluation of low-temperature fluoride routes to synthesize actinide nitrides and oxide solid solutions

Gunanda Waduge Chinthaka Silva
University of Nevada, Las Vegas

Follow this and additional works at: <https://digitalscholarship.unlv.edu/thesesdissertations>

 Part of the [Materials Chemistry Commons](#), [Nuclear Commons](#), [Nuclear Engineering Commons](#), and the [Radiochemistry Commons](#)

Repository Citation

Silva, Gunanda Waduge Chinthaka, "Evaluation of low-temperature fluoride routes to synthesize actinide nitrides and oxide solid solutions" (2009). *UNLV Theses, Dissertations, Professional Papers, and Capstones*. 1127.

<https://digitalscholarship.unlv.edu/thesesdissertations/1127>

This Dissertation is protected by copyright and/or related rights. It has been brought to you by Digital Scholarship@UNLV with permission from the rights-holder(s). You are free to use this Dissertation in any way that is permitted by the copyright and related rights legislation that applies to your use. For other uses you need to obtain permission from the rights-holder(s) directly, unless additional rights are indicated by a Creative Commons license in the record and/or on the work itself.

This Dissertation has been accepted for inclusion in UNLV Theses, Dissertations, Professional Papers, and Capstones by an authorized administrator of Digital Scholarship@UNLV. For more information, please contact digitalscholarship@unlv.edu.

EVALUATION OF LOW-TEMPERATURE FLUORIDE ROUTES TO SYNTHESIZE
ACTINIDE NITRIDES AND OXIDE SOLID SOLUTIONS

by

Gunanda Waduge Chinthaka Silva

Bachelor of Science
University of Colombo, Sri Lanka
2000

Master of Science in Chemistry
University of Nevada, Las Vegas
2005

A dissertation submitted in partial fulfillment
of the requirements for the

Doctor of Philosophy Degree in Radiochemistry
Department of Chemistry
College of Sciences

Graduate College
University of Nevada, Las Vegas
May 2009

UMI Number: 3383994

Copyright 2009 by
Silva, Gunanda Waduge Chinthaka

INFORMATION TO USERS

The quality of this reproduction is dependent upon the quality of the copy submitted. Broken or indistinct print, colored or poor quality illustrations and photographs, print bleed-through, substandard margins, and improper alignment can adversely affect reproduction.

In the unlikely event that the author did not send a complete manuscript and there are missing pages, these will be noted. Also, if unauthorized copyright material had to be removed, a note will indicate the deletion.

UMI[®]

UMI Microform 3383994
Copyright 2009 by ProQuest LLC
All rights reserved. This microform edition is protected against
unauthorized copying under Title 17, United States Code.

ProQuest LLC
789 East Eisenhower Parkway
P.O. Box 1346
Ann Arbor, MI 48106-1346

Copyright by Gunanda Waduge Chinthaka Silva 2009
All Rights Reserved



Dissertation Approval
The Graduate College
University of Nevada, Las Vegas

April 1st, 20 **09**

The Dissertation prepared by

Gunanda Waduge Chinthaka Silva

Entitled

Evaluation of Low-Temperature Fluoride Routes to Synthesize Actinide

Nitrides and Oxide Solid Solutions

is approved in partial fulfillment of the requirements for the degree of

Doctor of Philosophy in Radiochemistry

Examination Committee Chair

Dean of the Graduate College

Examination Committee Member

Examination Committee Member

Graduate College Faculty Representative

ABSTRACT

Evaluation of Low-Temperature Fluoride Routes to Synthesize Actinide Nitrides and Oxide Solid Solutions

by

Gunanda Waduge Chinthaka Silva

Dr. Kenneth R. Czerwinski, Examination Committee Chair
Professor of Chemistry
Head of the Department of Radiochemistry
University of Nevada, Las Vegas

Actinide mononitrides have been considered as a possible nuclear fuel for the Generation-IV nuclear reactor systems. In the process of evaluating these actinide mononitrides as nuclear fuel, it is important to study different chemical and physical characteristics of these compounds. Synthesis of the materials is thus important. Carbothermic reduction is one of the techniques that have been used to synthesize actinide mononitrides. In this method, a mixture of actinide oxide such as UO_2 and excess carbon is heat treated at temperatures greater than $1700\text{ }^\circ\text{C}$ under a nitrogen atmosphere. The technique is however not promising in synthesizing the actinide mononitrides due to a number of disadvantages the technique presents. Lack of phase purity due to secondary chemical phases with carbon and oxygen, need of high temperatures such as $2200\text{ }^\circ\text{C}$, and the low density of the final product compared to theoretical density are some of the drawbacks that the researches have been encountered. Most of all this method is tiresome and difficult to handle in ordinary laboratories where the experimental setups and

conditions are inadequate to synthesize actinide mononitrides up to an acceptable quality for chemical characterizations. Therefore, it is important to explore different routes that can be used to synthesize such actinide nitrides and characterize them properly.

A recent development of a low-temperature fluoride route in synthesizing UN_2 at $800\text{ }^\circ\text{C}$ and UN at $1100\text{ }^\circ\text{C}$, proposed a further investigation of this particular chemical route in synthesizing other nitrides of the actinide series. Thus, the possibility of making nitrides of thorium, neptunium, and mixed uranium-thorium by the above mentioned method was suggested. Mechanisms and kinetics involved in separate reactions were studied. Chemical characterizations of the as-synthesized materials were also completed using different techniques reported in Chapter 2.

Optimization of this low-temperature process to minimize the formation of secondary phases such as UO_2 was also examined in a typical experimental setup by exploring the uranium system. With the thorium, however, only ThNF could be synthesized up to a temperature of $1100\text{ }^\circ\text{C}$. Addition of lithium amide (LiNH_2) into the reactants in synthesizing ThN_x produced Th_2N_3 with some ThO_2 impurities. This finding is controversial and will discuss the relevant issues in the corresponding chapter. Characterization of $\text{Th}_2\text{N}_3/\text{ThO}_2$ samples revealed an interchangeable formation of ThO_2 in Th_2N_3 and vice versa suggesting a possible reason for the high susceptibility of ThN_x toward oxygen as general.

Evaluation of the neptunium system revealed 6 new compounds with isomorphous crystal structures to that of uranium with similar chemical compositions. XRD powder refinements could be used in solving these crystal structures. NpN was synthesized at $900\text{ }^\circ\text{C}$ and further experiments are required to check the lower temperatures for making

the mononitride. However, further experiments will be necessary to optimize the heating time. Microscopic characterization of NpN_x compounds was also conducted with SEM and TEM. Nanostructural studies conducted on these samples displayed high crystallographic order in their structures.

Uranium and thorium mixed system was also examined with an eye towards synthesizing uranium-thorium mixed nitrides. Less than 1 wt% thorium solubility was identified in the UN_2 with XRD and microscopic studies. Further application of the technique on oxides was explored and a novel route in synthesizing $(\text{U}, \text{Th})\text{O}_2$ solid solutions at temperatures of 1100 °C or less, depending on the chemical composition of the oxide solid solution, was established. Moreover, this novel route itself proposes a new and easy to use low-temperature path to fabricate actinide oxide solid solutions from initial, separate oxide starting phases.

TABLE OF CONTENTS

ABSTRACT.....	iii
LIST OF TABLES	vii
LIST OF FIGURES	viii
ACKNOWLEDGEMENTS.....	x
CHAPTER 1 INTRODUCTION	1
1.1 Actinide Nitrides as a Nuclear Fuel	1
1.2 Crystallography of Actinide Nitrides	4
1.3 Carbothermic Reduction	8
1.4 Low-Temperature Fluoride Route	10
CHAPTER 2 METHODOLOGY AND INSTRUMENTATION	18
2.1 Introduction	18
2.2 Reagents	18
2.3 Experimental Procedures	19
2.4 X-ray Powder Diffraction (XRD)	20
2.5 Transmission Electron Microscopy (TEM)	24
2.6 Scanning Electron Microscopy (SEM)	32
2.7 Electron Microprobe Analysis	34
CHAPTER 3 SYNTHESIS AND CHARACTERIZATION OF URANIUM NITRIDES	38
3.1 Introduction.....	38
3.2 Experimental details	40
3.3 Mechanism and Kinetics of UN ₂ Decomposition	41
3.4 Microscopic Evaluation of UN _x	54
3.5 Discussion	65
3.6 Conclusions	70
CHAPTER 4 EVALUATION OF THORIUM SYSTEM	73
4.1 Introduction.....	73
4.2 Experimental Details and Characterization Methods	76
4.3 Synthesis and Characterization of (NH ₄) ₄ ThF ₈	78
4.4 Synthesis and Characterization of ThNF	84
4.5 Ammonolysis of ThF ₄ and the Thermal Behavior of ThNF	91
4.6 Synthesis and Characterization of Th ₂ N ₃	95

4.7 Discussion	105
4.8 Conclusions.....	111
CHAPTER 5 SYNTHESIS AND CHARACTERIZATION OF NEPTUNIUM NITRIDES	
5.1 Introduction.....	115
5.2 Experimental Details and Characterization Methods	117
5.3 Results and Discussion	119
5.4 Conclusions	155
CHAPTER 6 EVALUATION OF URANIUM-THORIUM MIXED SYSTEM ...	
6.1 Introduction	160
6.2 Experimental Methods	162
6.3 Characterization methods	164
6.4 Results and Discussion	165
6.5 Conclusions	192
CHAPTER 7 CONCLUSIONS AND RECOMMENDATIONS	
7.1 Uranium System	195
7.2 Thorium System	196
7.3 Neptunium System	198
7.4 Uranium and Thorium Mixed System	200
VITA	203

LIST OF TABLES

Table 1.1	Comparison on actinide oxide, carbide, and nitride properties	2
Table 1.2	Crystallography of uranium nitrides	4
Table 1.3	Crystallography of thorium nitrides	6
Table 2.1	Cover gases used for the experiments	18
Table 2.2	Chemicals used in the research work	19
Table 2.3	Chemical composition of hard Spurr resin	32
Table 3.1	Lattice parameters and X-ray phase densities of the uranium nitrides calculated from experimental patterns using Rietveld analysis	42
Table 3.2	Elemental compositions determined by electron microprobe studies	45
Table 3.3	Products observed after heating UN ₂ at different temperatures and time intervals under argon atmosphere	48
Table 3.4	Rate constants of the UN _x decomposition reaction at 1000, 1050, and 1100 °C temperatures	53
Table 4.1	Temperature effect on the ammonolysis of (NH ₄) ₄ ThF ₈	84
Table 4.2	Elemental analysis of the as-synthesized ThNF by EDS	86
Table 4.3	Ammonolysis of ThF ₄	93
Table 4.4	Thermal behavior of ThNF under different atmospheric conditions	95
Table 4.5	Results obtained after heating different thorium fluorides with LiNH ₂ under ammonia	96
Table 4.6	Results obtained after heating Th ₂ N ₃ /ThO ₂ sample at different temperatures under high-purity argon for 30 min	96
Table 4.7	Interatomic distances for Th ₂ N ₃ with La ₂ O ₃ -type hexagonal $P\bar{3}m1$ crystal structure	98
Table 4.8	Elemental distribution of the as-synthesized Th ₂ N ₃ sample	99
Table 5.1	Refined lattice parameters of (NH ₄) ₂ NpF ₆ and (NH ₄) ₄ NpF ₈ structures	119
Table 5.2	Structure parameters of (NH ₄) ₂ NpF ₆	120
Table 5.3	Structure parameters of (NH ₄) ₄ NpF ₈	121
Table 5.4	Chemical analyses of (NH ₄) ₂ NpF ₆ and (NH ₄) ₄ NpF ₈ samples. Standard deviations (S.D.) of each experimental value are also given	127
Table 5.5	Heat treatment of ammonium neptunium fluorides under NH ₃ (g)	132
Table 5.6	Quantitative analysis of NpN ₂ sample with respect to the particle shape. Approximate error percentage is 1%	145
Table 5.7	Chemical analysis of NpN sample	148
Table 5.8	Reactions and products identify in the neptunium system	157
Table 5.9	Microscopic observations of neptunium compounds	158
Table 6.1	Sample compositions and the products formed after reacting with ammonium bifluoride (NH ₄ HF ₂)	163
Table 6.2	Products observed for the heat treatment of the (NH ₄) ₄ U _{0.9} Th _{0.1} F ₈ under NH ₃ gas	169

Table 6.3	Observed reaction products for the heating of $(\text{NH}_4)_4(\text{U}, \text{Th})\text{F}_8$ for 1 through 4 wt% of thorium under NH_3 . There is up to a 1% error in the wt% values ..	175
Table 6.4	Results obtained for the heating of the $(\text{NH}_4)_4\text{U}_{0.9}\text{Th}_{0.1}\text{F}_8$ under air	176
Table 6.5	Heat treatment of the samples at 1100 °C for 30 minutes under air	177
Table 6.6	Two-Stage Conversion of UT4 under static air / flowing argon	180
Table 6.7	Elemental analysis of oxide solid solutions of 60 and 90 wt% Th	183
Table 7.1	New compounds identified in the ammonolysis of $(\text{NH}_4)_x\text{NpF}_y$	199

LIST OF FIGURES

Figure 1.1	Figure 1.1 Fuel cross sections of UC (a) and UN (b) type K fuel after 0.5 at% burnup irradiated at 75 kW/m and 76 kW, respectively	3
Figure 1.2	Unit cell models of (a) UN ₂ , (b) U ₂ N ₃ , and (c) UN	5
Figure 1.3	Unit cells of (a) Th ₂ N ₃ , (b) Th ₃ N ₄ , and (c) ThN compounds	7
Figure 1.4	Cubic unit cell of NpN	8
Figure 1.5	NpO ₂ /NH ₄ HF ₂ solid mixture in the polyvinyl vial	12
Figure 2.1	Experimental setup used to heat the samples	20
Figure 2.2	Bragg's Law reflection	21
Figure 2.3	Example of an electron density map obtained from UCSF Chimera website	24
Figure 2.4	Diagrams displaying the two basic operations of the TEM: (A) viewing diffraction pattern and (B) viewing image	26
Figure 2.5	Calculated HRTEM image of UO ₂ correspond to (10-1) planes along [111] zone axis	27
Figure 2.6	Tilting effect on SAED patterns (NpF ₃): (a) strong diffraction spots for a single crystalline chemical phase and (b) after tilting the sample 20°	28
Figure 2.7	Comparison of XEDS and EELS mapping of UF ₄	29
Figure 2.8	A picture of the TEM instrument used in this study	30
Figure 2.9	Various reactions occur in electron interactions with specimen	33
Figure 2.10	Comparison of SE and BE SEM images of (U ₄ Th ₂ Zr ₉)H _{1.5} sample	34
Figure 2.11	(a) SEM and (b) EMPA instruments	35
Figure 3.1	XRD powder pattern of UN ₂ together with the calculated patterns	41
Figure 3.2	Rietveld refinement of U ₂ N ₃ sample. The displayed patterns are as of UN ₂ in Figure 3.1. Calculated pattern of U ₂ N ₃ is highlighted. UO ₂ impurity phase content of 2.1 (1) wt.% was identified and the R _{wp} = 9.6%	43
Figure 3.3	Observed patterns of UN ₂ samples showing the impurity peaks in the low 2theta angles: (a) synthesized by heating UF ₄ at 800 °C for 1 hour; (b) synthesized by heating at 800 °C for 6 and half hours. Calculated pattern or UO ₂ is highlighted	44
Figure 3.4	Rietveld analysis of the as-synthesized UN sample. Highlighted is the calculated pattern of UN. R _{wp} = 8.6%	44
Figure 3.5	Decomposition of UN ₂ under Ar(g) at 1100 °C as a function of time	46
Figure 3.6	Observed XRD powder pattern of UF ₄ after heating 30 min at 1000 °C and 1100 °C under NH ₃ (g) and Ar(g), respectively. Only the calculated pattern for UNF is highlighted for clarity (R _{wp} = 11.1%)	49
Figure 3.7	Lattice parameters of UN ₂ and α-U ₂ N ₃ as a function of the temperature used for decomposition	50
Figure 3.8	Change in the lattice parameter of the UN ₂ /α-U ₂ N ₃ system with respect to the N/U molar ratio	51

Figure 3.9	Lattice parameter of UN as a function of the temperature used for UN _x decomposition	52
Figure 3.10	Pseudo-first-order kinetics of UN _x decomposition at 1050 °C (a) and the Arrhenius plot for the reaction (b)	53
Figure 3.11	SE-SEM micrographs of UF ₄ {(a) commercial; (b) as-synthesized} and (c) as-synthesized UN ₂	55
Figure 3.12	HRTEM image of UN ₂ in [111] beam direction. Two insets are the FFT of the image and the BF image of the particle used to obtain the HRTEM image	56
Figure 3.13	HRTEM images of two UN ₂ particles (insets) prepared using solution-drop method	56
Figure 3.14	SE-SEM micrograph (left) and the line scan across A – B (right) of U ₂ N ₃	57
Figure 3.15	TEM images of U ₂ N ₃ : (a) TEM BF image; (b) SAD pattern in [111] zone axis; (c) HRTEM image	58
Figure 3.16	(a), (b) SE-SEM images of UN, and the line scan across the image in (b)	60
Figure 3.17	(a) TEM BF image of UN particles embedded on a C-Cu grid using solution-drop method. (b) and (c) are the magnified particle images corresponding to areas B and C in Figure (a), respectively. Highlighted areas in Figure (b) and (c) are used in obtaining the HRTEM images in Figure 3.18 and 3.19, respectively	61
Figure 3.18	HRTEM image of the highlighted area of the particle in Figure 8b	62
Figure 3.19	(a) HRTEM image of the particle shown in Figure 3.14c in [111] direction and (b) FFT micrograph. Figures (c), (d), and (e) indicate the intensity profiles of three different regions shown in (a) denoted by the lines AB, CD, and EF, respectively	63
Figure 3.20	HRTEM images of two thin areas of a 25 nm thick UN nano particle (cross-sectional TEM BF image is shown) prepared using the microtome cutting method. In HRTEM image, the area indicated by A shows both sets of reflections due to (200) UN planes. Lattice fringe spacing (0.335 nm) due to UO ₂ phase was found at one edge of the particle as indicated	65
Figure 4.1	XRD patterns indicating the reaction progress of ThO ₂ mixed with excess NH ₄ HF ₂ . Only a part of the XRD patterns are shown for clarity of the comparison	79
Figure 4.2	XRD powder refinements of (a) (NH ₄) ₄ ThF ₈ and (b) (NH ₄) ₃ ThF ₇ samples. Calculated patterns of both (NH ₄) ₄ ThF ₈ and (NH ₄) ₄ ThF ₈ are highlighted in the corresponding figure. X-axes are in 10 ⁻¹ nm units	80
Figure 4.3	Secondary-electron SEM image (a) and the corresponding EDS spectrum (b) of the synthesized (NH ₄) ₄ ThF ₈ and the SEM image of ThO ₂ (c)	81
Figure 4.4	(a) TEM BF image, (b) [111] electron diffraction pattern, and (c) HRTEM image of (NH ₄) ₄ ThF ₈ ground particle	82
Figure 4.5	(a) TEM BF image of another ground (NH ₄) ₄ ThF ₈ particle. (b) The HRTEM image of the circled area of (a) and (c) the corresponding FFT	83
Figure 4.6	XRD powder refinement of ThNF synthesized by heating (NH ₄) ₄ ThF ₈ at 1100°C for 15 min under NH ₃	85

Figure 4.7	Secondary electron SEM images of the ThNF sample, (a) showing the morphology at x5,000 magnification and (b) at x15,000 magnification, (c) the corresponding EDS spectrum of ThNF, (d) the SEM image of ThF ₄ ...	86
Figure 4.8	(a) TEM BF of a microtome cut ThNF sample, (b) HRTEM image, (c) FFT of HRTEM, (d) experimental intensity profile along A–B in HRTEM	88
Figure 4.9	(a) HRTEM of another area of the particle in Figure 4.8a. (b) Enlarged image of area denoted by letter A with a rectangle. The area B denoted by a rounded rectangle is used in Figure 4.10. Onsets of each image are the corresponding FFT micrographs	89
Figure 4.10	HRTEM of the particle area denoted by letter B in Figure 4.9. Inset to the upper right side is the electron density map calculated by ThNF XRD pattern using charge flipping. A model of the molecule in (111) direction is also inserted	90
Figure 4.11	XRD refinement of the sample synthesized heating (NH ₄) ₄ ThF ₈ at 800 °C for 60 min under NH ₃	92
Figure 4.12	XRD powder refinement of the ThF ₄ sample after the ammonolysis at 800 °C for 1 hour	92
Figure 4.13	XRD powder refinement of the ThF ₄ after the ammonolysis at 800 °C 300 min	94
Figure 4.14	XRD powder refinements of ThF ₄ after the ammonolysis at 800 °C for 600 min (a) and at 1000 °C for 75 min (b). Square root of counts was used as the scale of Y-axis for proper display of the calculated patterns	94
Figure 4.15	Crystal unit cell of Th ₂ N ₃ with La ₂ O ₃ -type hexagonal $P\bar{3}m1$ structure	97
Figure 4.16	(a) XRD powder refinement using Rietveld method and (b) the corresponding Fourier map of Th ₂ N ₃ . The sample contains 56 wt% ThO ₂ as a second chemical phase	98
Figure 4.17	SEM micrographs of the (a) synthesized Th ₂ N ₃ sample and (b) ThO ₂	99
Figure 4.18	(a) EDS spectrum and (b), (c) SEM micrographs of the Th ₂ N ₃ sample at different area of the sample. C and Au are from the tape used to mount the sample and gold coating, respectively	100
Figure 4.19	EELS elemental maps of Th ₂ N ₃ sample. (a) Zero energy-loss image, (b) Th map, (c) N map, (d) O map, and (e) F map	101
Figure 4.20	(a) HRTEM image of Th ₂ N ₃ sample, (b) magnified image of the square area in (a), (c) FFT of (b), (d) and (e) are the experimental intensity profiles of the HRTEM image in (b) along AB	102
Figure 4.21	(a) HRTEM and (b), (c) the corresponding FFT micrographs of the synthesized Th ₂ N ₃ sample. FFT in (a) and (b) are corresponding to the areas A and B, respectively	103
Figure 4.22	HRTEM image of another particle area of Th ₂ N ₃ sample	104
Figure 4.23	XRD powder refinements of the sample synthesized by heating a mixture of ThNF and LiNH ₂ at 800° 30min under NH ₃ . (a) Using only Th ₂ N ₂ O and (b) using only Th ₂ N ₃ crystal data. ThO ₂ (peaks highlighted with arrows) was not used in the refinement for clarit	109
Figure 5.1	Profile fit to the (NH ₄) ₂ NpF ₆ XRD powder pattern using jana2000. Observed intensities are in dots, the overlapping continuous line is the calculated profile, and the continuous line at the bottom is the difference.	

	Inset of the figure is a graphical interpretation of the unit cell of the compound	120
Figure 5.2	Profile fit to the $(\text{NH}_4)_4\text{NpF}_8$ XRD pattern using TOPAS. Inset of the figure is a graphical interpretation of a Fourier map of the compound	121
Figure 5.3	A structure fitting of $(\text{NH}_4)_2\text{NpF}_6$ using the electron density map calculated using charge flipping of the powder diffraction and a model of the crystal structure in [001] direction. Insets in left and right are the electron density map and a structural model, respectively	122
Figure 5.4	Structure fitting of $(\text{NH}_4)_4\text{NpF}_8$ using an electron density map (inset to left) and a model (inset to right) of the crystal structure in [010] direction	123
Figure 5.5	Profile fits of the XRD powder patterns of the NpO_2 and NH_4HF_2 mixture after 2 days at room temperature (a) and before completion of the conversion of $(\text{NH}_4)_4\text{NpF}_8$ into $(\text{NH}_4)_2\text{NpF}_6$ at 80 °C (b)	124
Figure 5.6	SEM images of (a) $(\text{NH}_4)_4\text{NpF}_8$ and (b) $(\text{NH}_4)_2\text{NpF}_6$. Insets of (a) and (b) are a sharp edged particle of $(\text{NH}_4)_4\text{NpF}_8$ and a magnified image of $(\text{NH}_4)_2\text{NpF}_6$	126
Figure 5.7	HRTEM image of $(\text{NH}_4)_4\text{NpF}_8$. (a) HRTEM showing polycrystalline character of the particle, (b) FFT of image (a), and (c) HRTEM of another area of two grains of single crystal	128
Figure 5.8	HRTEM of $(\text{NH}_4)_2\text{NpF}_6$. (a) HRTEM of a particle showing polycrystalline characteristics, (b) FFT of HRTEM in (a), (c) HRTEM of another particle area with three layers of single crystal, and (d) FFT of image in (c)	129
Figure 5.9	HRTEM of the mixed $(\text{NH}_4)_x\text{NpF}_y$ sample displaying a phase boundary of two chemical phases	130
Figure 5.10	HRTEM images of (a) $(\text{NH}_4)_4\text{NpF}_8$ and (b) $(\text{NH}_4)_2\text{NpF}_6$. Lattice fringes of both compounds are found to be due to (111) lattice planes	131
Figure 5.11	XRD patterns of the products obtained after heating $(\text{NH}_4)_4\text{NpF}_8$ at 250 °C (a) and 400 °C (b) for 60 min under $\text{NH}_3(\text{g})$	133
Figure 5.12	XRD patterns of the products formed after heating $(\text{NH}_4)_2\text{NpF}_6$ at 500°C for 30min (a) and 800 °C for 60 min (b) under NH_3 . The highlighted patterns are the calculated patterns for NpF_3 and NpN_xF_y in (a) and (b), respectively. Some peaks for NpF_4 identified are also displayed together with an inset of a database (ICSD) powder pattern of the NpF_4 crystal structure in (a)	135
Figure 5.13	Unit cell of NpN_xF_y determined in this study	136
Figure 5.14	XRD patterns of the products formed after heating $\text{NH}_4\text{-Np-F}$ at 800°C for 90min using a closed Pt sheet (a) and an open Pt sheet (b)	137
Figure 5.15	Unit cell of the newly discovered NpN_2	138
Figure 5.16	Unit cell of Np_2N_3	139
Figure 5.17	Observed and the calculated XRD patterns of the NpN sample synthesized by heating $(\text{NH}_4)_x\text{NpF}_y$ for 90 min at 800 °C under NH_3 and a continuous heating at 1100 °C for 30 min under high-purity argon. Peaks at 46° and 67.5° 2Theta values are due to the sample holder because of the kapton tape used to contain sample	140
Figure 5.18	Observed and the calculated XRD patterns of the NpN sample synthesized by heating $(\text{NH}_4)_x\text{NpF}_y$ for 30 min under NH_3 and a continuous heating for	

	another 30 min under high-purity argon at 900 °C. XRD pattern of the sample on the same day (a) and after three days (b)	142
Figure 5.19	Decay kinetics of NpN at ambient conditions as a function of time due to NpN transformation into NpO ₂	143
Figure 5.20	SEM images of NpN ₂ . Inset is the SEM of another area containing a cluster of particles	144
Figure 5.21	HRTEM images of two NpN ₂ nanoparticle areas	145
Figure 5.22	SEM micrographs of Np ₂ N ₃ showing a cluster of particles (a) and a flat area containing some separated particles (b)	146
Figure 5.23	HRTEM image of Np ₂ N ₃	146
Figure 5.24	SEM micrographs of NpN samples. (a) NpN sample with a 15.03(1) wt% mononitride (Figure 5.17) and (b) the sample containing 62.70(1) wt% NpN (Figure 5.18)	147
Figure 5.25	TEM BF and STEM images of few particles of NpN sample with a 15.03(1) wt% mononitride. XEDS profiles of two points rich with nitrogen and oxygen are also displayed	149
Figure 5.26	STEM and TEM BF images of the NpN sample containing 62.70(1) wt% NpN. XEDS spectrum of the particle highlighted in the STEM image is also displayed	150
Figure 5.27	HRTEM images of NpN samples. (a) Particles from 15.03(1) and (b) 62.70(1) wt% NpN samples. Both images contain lattice fringes from (111) planes of NpN	151
Figure 5.28	HTEM of the N rich a particle as shown in Figure 5.25	152
Figure 5.29	HRTEM of 15.03(1) wt% NpN sample. (a) Nitrogen rich and (b) oxygen rich areas. Area focused in (a) is about 40 nm into the particle from the edge of it.....	152
Figure 5.30	HRTEM of the area A displayed in Figure 5.26 TEM BF image	154
Figure 6.1	Drying effect on the sample phase purity: (a) XRD powder refinement of UT6 as-synthesized, (b) UT6 sample after dried at 80 °C for 7 days, and (c) enlarged powder pattern of as-synthesized UT6	166
Figure 6.2	Lattice parameter variation of the monoclinic (space group of <i>C2/c</i>) (NH ₄) ₄ UF ₈ as a function of ThO ₂ wt.% in the first six samples: (a) variation in <i>a</i> ; (b) variation in <i>b</i> ; (c) variation in <i>c</i>	167
Figure 6.3	Secondary electron SEM micrographs of three as-synthesized samples: (a) UT1; (b) UT6; (c) UT8	167
Figure 6.4	A comparison of the Th and U N-edge areas in EDS spectra of UT1, UT6, and UT8. Inset is the full spectra	168
Figure 6.5	XRD powder pattern refinement of sample synthesized by heating UT1 at 725°C for 14min in NH ₃ (g)	170
Figure 6.6	SEM micrographs of (a) UN ₂ and (b) (U, Th)N ₂ /ThO ₂ samples	170
Figure 6.7	XEDS of the as-synthesized sample by heating (NH ₄) ₄ U _{0.9} Th _{0.1} F ₈ under NH ₃ gas at 725 °C for 10 min. Inset is the STEM image. TEM BF and the EELS maps of U and Th re also displayed	171
Figure 6.8	(a) TEM BF image, (b) U map, and (c) Th map of (U, Th)N ₂ /U-ThO ₂ ...	172
Figure 6.9	A HRTEM image of the circled particle area in Figure 6.8	173
Figure 6.10	HRTEM images of two areas of the single particle shown in Figure 6.9	174

Figure 6.11	XRD powder pattern refinement and the Fourier map (inset) of $U_{0.9}Th_{0.1}O_2$ solid solution synthesized at 1100 °C	176
Figure 6.12	Refined XRD powder patterns of $U_{0.2}Th_{0.8}F_8$ synthesized by heating $(NH_4)_4(U_{0.2}Th_{0.8})F_8$ at 1100 °C for 30 min: (a) first; (b) second time	178
Figure 6.13	XRD pattern refinement of $(U, Th)O_2/U_3O_8$ after reduced in NH_3 at 650 °C for 1 hr	179
Figure 6.14	Lattice parameter variation of the $(U, Th)O_2$ solid-solutions as a function of the Th wt % used	181
Figure 6.15	SE SEM micrographs of $(U, Th)O_2$ solid solutions as a function of Th amounts: (a) 10 wt %; (b) 30 wt %; (c) 50 wt %; (d) 70 wt %	182
Figure 6.16	(a) HRTEM image of a well-crystallized particle area of $U_{0.9}Th_{0.1}O_2$ solid solution and (b) Bloch simulation of the oxide correspond to (220) reflection along [001]	184
Figure 6.17	HRTEM of another $U_{0.9}Th_{0.1}O_2$ particle area. (a) Grain boundaries, (b) magnified image of area B, and (c) magnified image of area A	185
Figure 6.18	(a) HRTEM image and experimental intensity profiles along (b) AB and (c) CD. Magnified image of the area in between AB and CD lines (d) and the Bloch simulation of UO_2 due to (111) planes along [101] zone axis	186
Figure 6.19	HRTEM of $U_{0.4}Th_{0.6}O_2$ oxide solid solution. Intensity profiles along A through D are also presented	188
Figure 6.20	HRTEM of two particle areas of $U_{0.2}Th_{0.8}O_2$ solid solution sample	189
Figure 6.21	Single crystal area of $U_{0.2}Th_{0.8}O_2$ solid solution with minor defects	190
Figure 6.22	HRTEM images of the as-synthesized $U_{0.2}Th_{0.8}O_2$ sample	191
Figure 6.23	HRTEM image showing a twin boundary of the as-synthesized $U_{0.2}Th_{0.8}O_2$ sample. Insets are the calculated Bloch images and the FFT	191

ACKNOWLEDGEMENTS

Great teachers that have ever been born in this world appreciate a good friendship because of many advantages. A help of a friend is always beneficial in achieving many good aims. Obtaining a high degree is such a goal of person's life that the helps of friends are most needed. Coming out here alone and pursuing my goal would have been difficult without the help of my friends and teachers.

I take this opportunity to make my first and utmost thanks to my advisor Professor Ken Czerwinski for his expert guidance and for the help he offered me throughout my studies. Secondly, I am grateful to Dr. Gary Cerefice and Dr. Alfred Sattelberger for their continuous guidance throughout my research works. I also thank Dr. Ralf Sudowe for his support as a committee member. I cannot forget to mention Dr. Thomas Hartmann and Dr. Longzhou Ma for their assistance on success of my research works.

I also take this moment to thank all my friends, especially Charles Yeaman, Fredric Poineau, Kiel Holiday, Nick Smith, Rich and Julie Gostic, Narek Gharibyan, and Chris Klug. I thank Tom O'Dou and Trevor Low for helping me to complete my work in the laboratory.

I am grateful for my parents for giving me birth to this world and taking care of me. Last but not least, I thank my wife Tharanga for her kind support in many ways.

CHAPTER 1

INTRODUCTION

1.1 Actinide Nitrides as a Nuclear Fuel

The need of alternate sources for electricity is growing as the use of fossil fuel such as coal and oil are being consumed in a rapid speed and most of all the risk of global warming caused by greenhouse gasses are of major concerns [1]. The alternate power sources therefore have to be clean like in the case of wind, hydro, and solar energy. However, all these sources have their own limitations with respect to the amount of energy they can produce. Nuclear power on the other hand can meet the energy needs at global scale. Moreover, it has been used for decades and research that has been conducted to improve the quality of using nuclear power significantly. At present, many new research projects are ongoing to find novel and sustainable energy while minimizing the waste produced by the nuclear power plants. Determination of the usage of nitride fuels is one such field of experiments scientists all over the world are developing. The current study also focused on the nitride fuels fabrication and characterization to support such efforts by providing valuable information on the chemistry of actinide nitrides.

At present, a wide variety of nuclear fuel concepts are under consideration for the advanced fuel cycle. The fundamental compositions include metals, oxides and nitrides. These can be in form of solid solutions or composite material. The materials comprise CERCER (ceramic-ceramic), CERMET (ceramic-metal) or METMET (metal-metal). On

the other hand, nitride fuels are the proposed fuel matrix for a number of advanced reactor designs and are an attractive option for the transmutation of Pu and other minor actinides [2] due to their advantageous neutronic and thermal properties together with many other unique chemical characteristics such as high solid phase solubilities for the early actinides.

Table 1.1 Comparison on actinide oxide, carbide, and nitride properties.

Property	$(U_{0.8}Pu_{0.2})O_{1.98}$	$(U_{0.8}Pu_{0.2})C$	$(U_{0.8}Pu_{0.2})N$
Theoretical density (g/cm^3)	11.06	13.62	14.30
Metal density (g/cm^3)	9.8	12.96	13.50
Metal fraction (%)	88.10	95.20	94.45
Melting point ($^{\circ}C$)	2700	2475	2800
Thermal conductivity (W/cm. $^{\circ}C$)			
700 $^{\circ}C$	0.035	0.188	0.158
1200 $^{\circ}C$	0.027	0.206	0.180
1700 $^{\circ}C$	0.019	0.212	0.201

Uranium mononitride (UN) has many favorable nuclear fuel properties such as high fissile atom density, high melting point comparable to that of the oxide fuel, and high thermal conductivity similar to that of metal fuel [3]. A comparison of properties for the oxide, carbide, and nitride of a mixed uranium and plutonium composition are provided in Table 1.1 [4]. Of the ceramic fuel matrices, the nitride fuels have the highest theoretical density, metal density, and melting point. The metal fraction of the nitride is

only slightly lower than that of the carbide. The thermal conductivity is slightly lower than the carbide but significantly higher than the oxide.

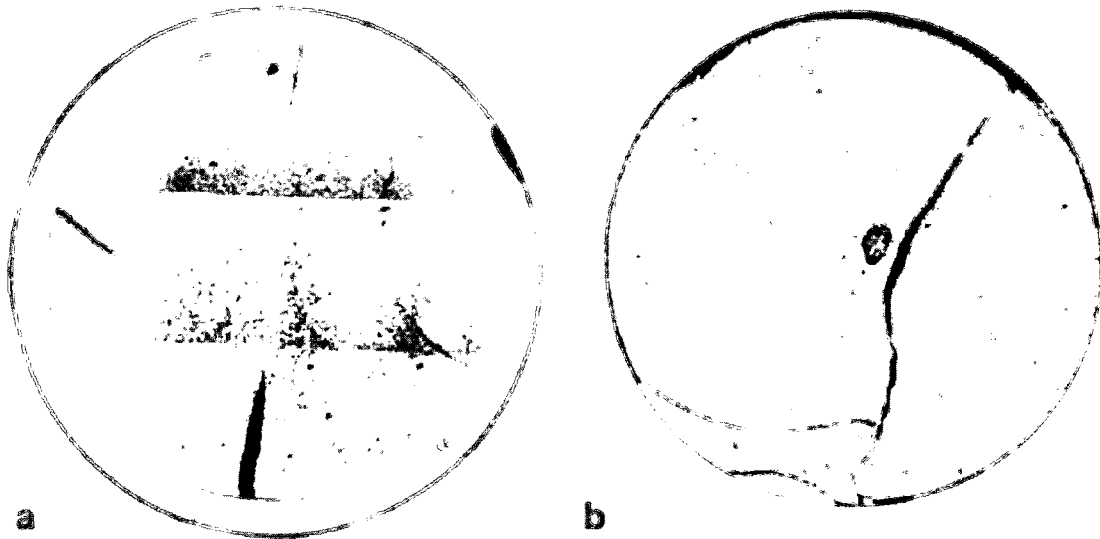


Figure 1.1 Fuel cross sections of UC (a) and UN (b) type K fuel after 0.5 at% burnup irradiated at 75 kW/m and 76 kW, respectively.

A comparative study on radiation damage shows that swelling of UC fuels at their burnup is faster than UN (UC ~ 0.5 atom%; UN ~ 2 to 3 at%) [5]. Figure 1.1 shows fuel cross sections of UC and UN reported in this study by H. Blank and his coworkers. Radiation damage studies on UN single crystals showed that U diffuses in it to counteract the damage and recover. In this process, U atom mobility is lower than any other advanced ceramic fuel and therefore UN is known as the “cold” fuel. These data indicate the suitability of nitrides as fuels over a number of other fuels being used or considered for advanced fuels.

1.2 Crystallography of Actinide Nitrides

1.2.1 Uranium Nitride System

There is a number of uranium nitrides of the general composition U_xN_y have been identified in the literature. Among them, UN_2 , U_2N_3 , and UN are common (Figure 1.2) [6]. Table 1.2 summarizes the crystal structure information of these three uranium nitrides. The UN_2 has a CaF_2 -type face-centered cubic lattice with a range of compositions described as UN_x where $2.0 \geq x \geq 1.75$ [7]. A theoretical value of 0.521 nm as the cubic lattice parameter of UN_2 with a $Fm\bar{3}m$ space group was given [8] where as an experimental lattice parameter of 0.530(1) could be found for a composition of $UN_{1.9}$ [9]. Rundle et al. [10], also gives a value of 0.531(1) nm for the composition of UN_2 based on their experiments conducted on a number of different compounds.

Table 1.2 Crystallography of uranium nitrides.

Compound	Crystal system	Space group	Lattice parameter (nm)
UN_2	Face-centered cubic	$Fm\bar{3}m$	0.531(1)
U_2N_3	Body-centered cubic	$Ia\bar{3}$	1.0678(5)
UN	Face-centered cubic	$Fm\bar{3}m$	0.48880(1)

U_2N_3 owns a body-centered cubic Mn_2O_3 -type structure with a $Ia\bar{3}$ space group and a lattice parameter of 1.0678(5) nm [10]. A range of stoichiometries for the U_2N_3 compound was also reported. This range varies as $1.5 \leq x \leq 1.75$ for a general composition of UN_x [11, 12]. In fact, UN_2 and U_2N_3 forms solid solutions [13] at chemical compositions UN_x where $1.5 \leq x < 2.0$ and are therefore difficult to differentiate

with X-ray diffraction studies when U_2N_3 chemical phase quantities are low. The mononitride, UN, is a NaCl-type face-centered cubic lattice of $Fm\bar{3}m$ space group with a 0.48880(1) nm lattice parameter when pure [14].

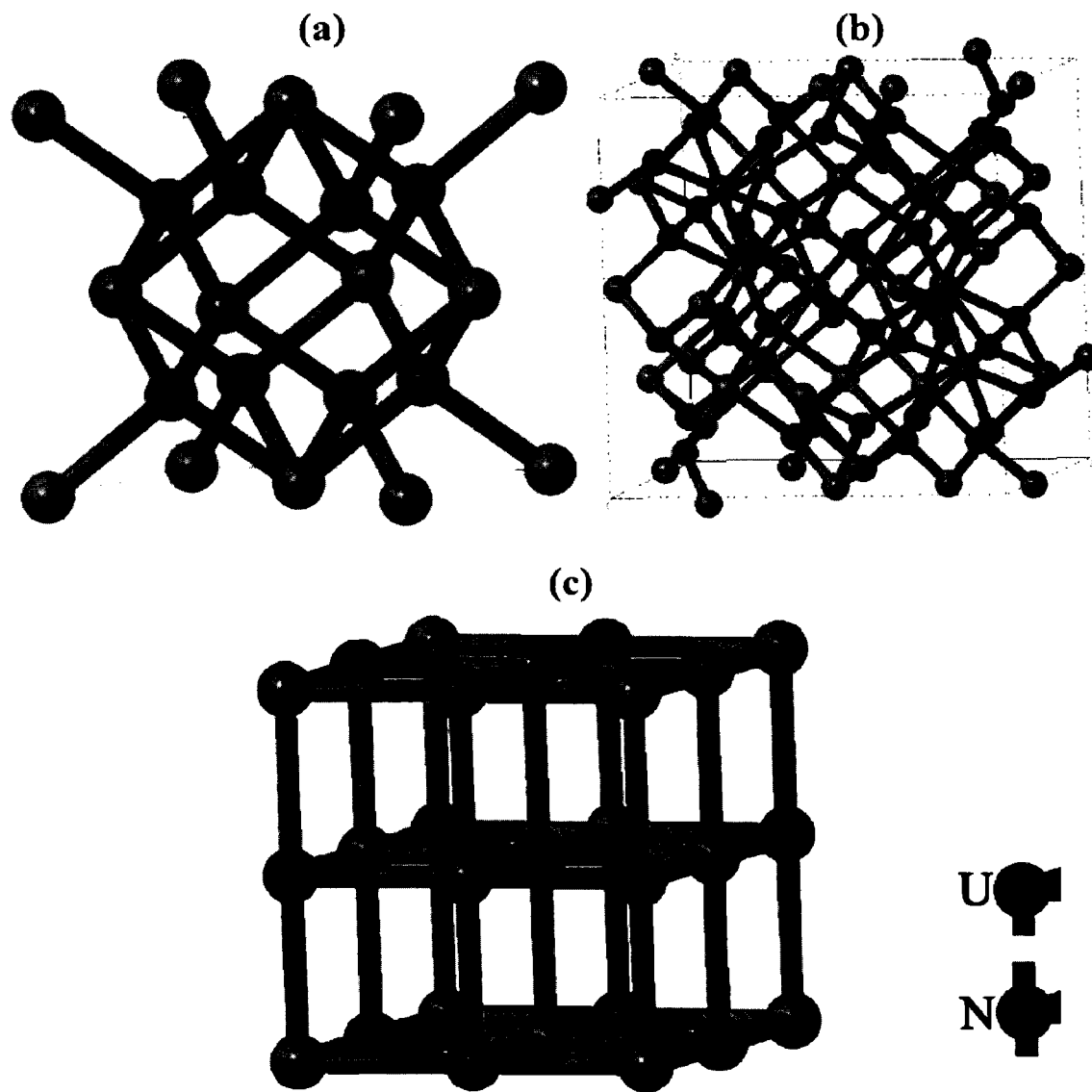


Figure 1.2 Unit cell models of (a) UN_2 , (b) U_2N_3 , and (c) UN.

1.2.2 Thorium Nitride System

Th_3N_4 and ThN are the most common thorium nitrides compared to a third chemical composition of Th_2N_3 according to the literature (Figure 1.3 and Table 1.3). Benz, et al. [15] reported a rhombohedral lattice with $a = 0.9398$ (2) nm and $\alpha = 23.78$ (1)° for Th_3N_4 crystal structure using XRD powder pattern. The space group of the compound is $R\bar{3}mR$. Thorium nitride of the chemical composition Th_2N_3 (thorium sesquinitride) is a controversial because of the expected oxidation state in Th is 4.5+ and it cannot have a value more than 4+ due to noble gas electronic configuration. The compound has a La_2O_3 type structure with a space group of $P\bar{3}m1$ and hexagonal unit cell dimensions of $a = 0.3875$ (2) nm and $c = 0.6175$ (4) nm [16]. Chiotti also reported a chemical composition close to Th_2N_3 with lattice parameters of $a = 0.387$ nm and $c = 0.616$ nm [17]. The current work also reports the Th_2N_3 compound in § 4.6. There are a number of reports discussing the crystallography and physical/chemical properties of ThN . This compound has the rock-salt structure as in the case of UN. Space group and the cubic unit cell parameters of ThN are $Fm\bar{3}m$ and $a = 0.51666$ (4) nm [18], respectively.

Table 1.3 Crystallography of thorium nitrides.

Compound	Crystal system	Space group	Lattice parameters (nm)
Th_2N_3	Hexagonal	$P\bar{3}m1$	$a = 0.3875$ (2) and $c = 0.6175$ (4)
Th_3N_4	Rhombohedral	$R\bar{3}mR$	0.9398(2)
ThN	Face-centered cubic	$Fm\bar{3}m$	0.48880(1)

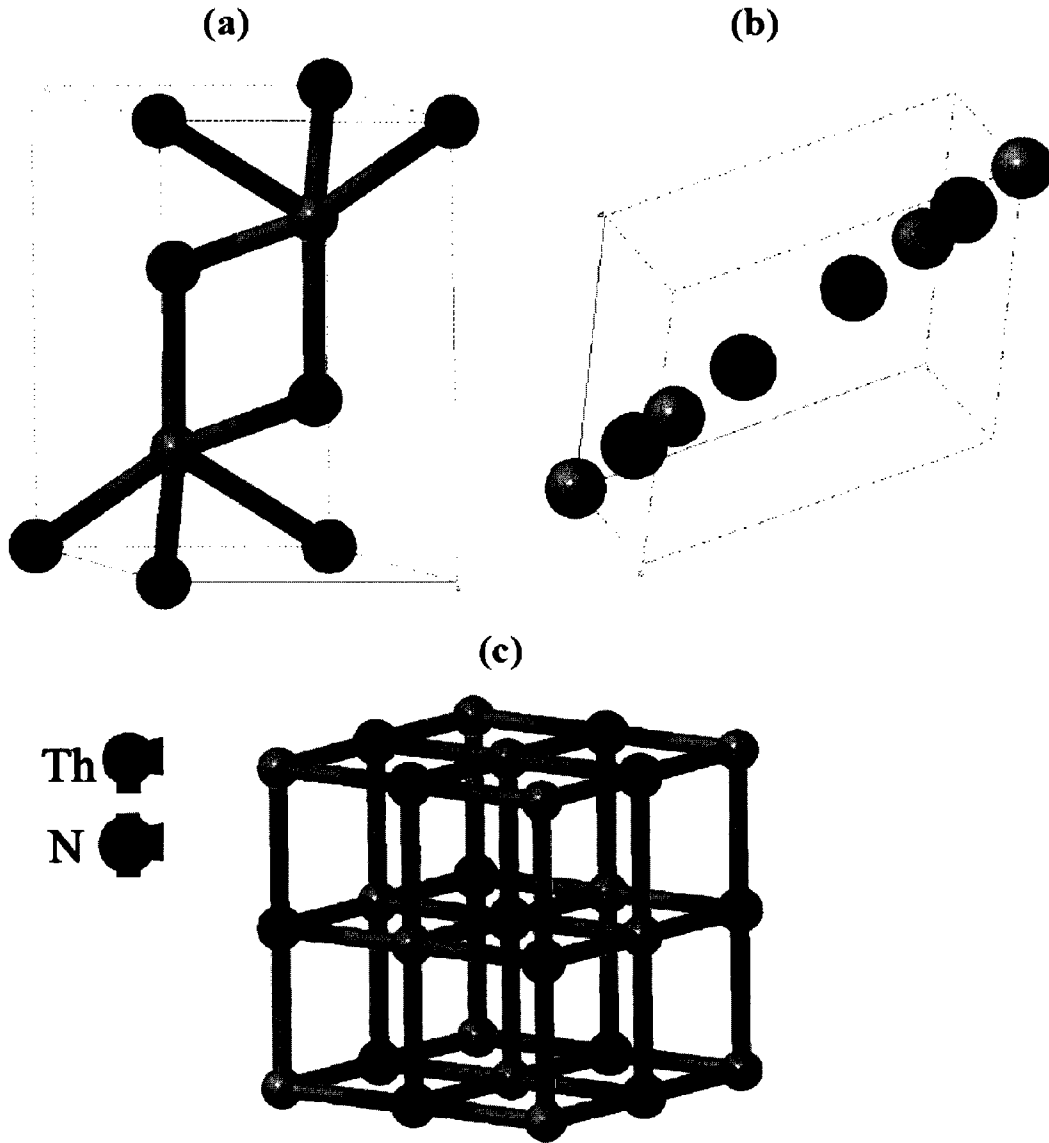


Figure 1.3 Unit cells of (a) Th_2N_3 , (b) Th_3N_4 , and (c) ThN compounds.

1.2.3 Neptunium Nitride System

NpN (Figure 1.4) is the only stoichiometric nitride of neptunium that has ever been reported to date. It has an isomorphous crystallography to that of UN [19]. Lattice parameter of the cubic unit cell of NpN is 0.48987 (5) nm with a $Fm\bar{3}m$ space group [20]. This same article reports that neptunium forms only NpN , similar to the plutonium

system, but our research work has identified two other neptunium nitrides, NpN_2 and Np_2N_3 , which are reported in § 5.3.4 of this report.

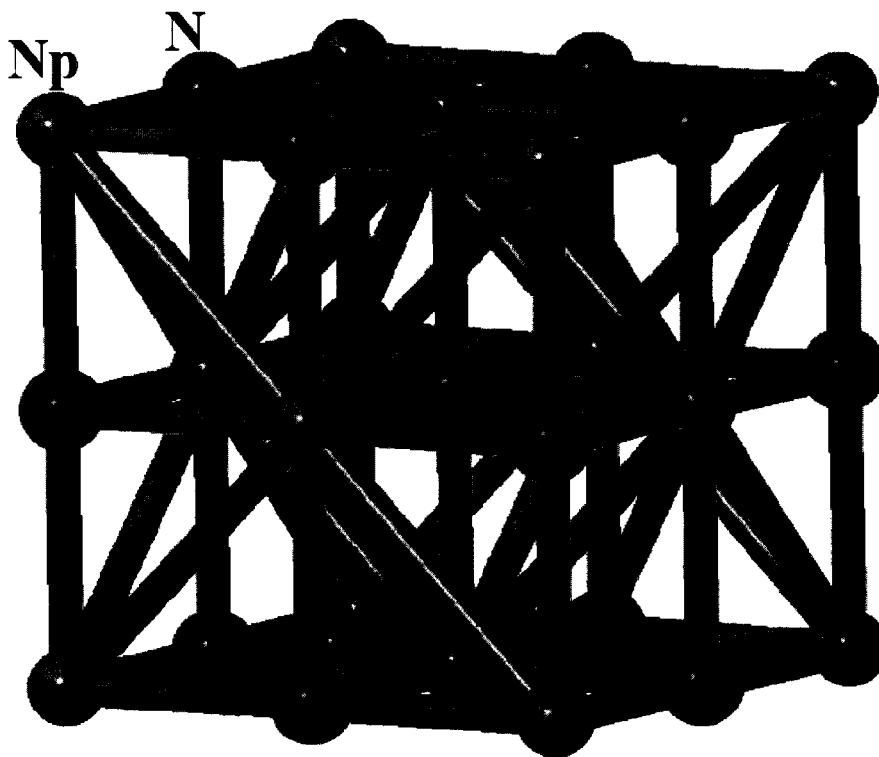
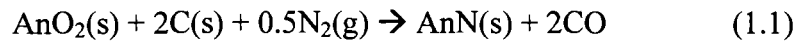


Figure 1.4 Cubic unit cell of NpN .

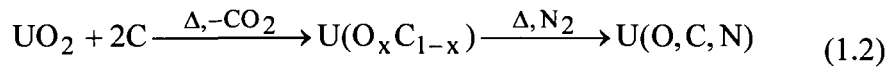
1.3 Carbothermic Reduction

Uranium oxides are generally the starting point for UN as well as UC synthesis. Oxides are fabricated using a precipitation method. An example of a precipitation process consists of dissolving and mixing the chloride or nitrate salts in purified water and then creating a precipitate with NH_4OH or oxalic acid. The precipitate is washed with acetone and purified water, milled, and dried at $90\text{ }^\circ\text{C}$. The dried precipitate is milled again and redried at $150\text{ }^\circ\text{C}$ for 2-3 hours. It is milled again and then calcined at $750\text{ }^\circ\text{C}$ for 1 hour.

The calcined powder is milled and then cold pressed into 13 or 7 mm diameter pellets for 2 minutes before being sintered under a mixture of argon and 4% hydrogen for four hours at 1500 °C. Nitride ceramics are produced using the carbothermic reduction process [21]. In this process, carbon is added in excess to actinide oxides. Heating under an inert gas such as Ar will form carbides. If the carbon/AnO₂ mixtures are heated in the range of 1500 – 1800 °C under a stream of N₂ gas, N₂-H₂ or NH₃-Ar then carbon monoxide is liberated and the intermediate actinide carbide is converted to the nitride as follows [22]:



The carbon monoxide concentration in the outgas is used to monitor the extent of the reaction. Unfortunately, this current synthesis route can carry significant levels of impurities into the final products as shown in the reaction below:



The presence of these impurities limits the utility of nitride fuels in advanced fuel cycles because they can affect the chemical and physical properties of the mononitrides. The presence of oxygen and other impurities in nitride fuels can lead to the formation of phases with different properties from the bulk material including the formation of secondary phases [23]. Oxygen present in the nitride can form oxides with fission products, altering the expected behavior of them. This limits the ability to fully develop nitride fuels for advanced reactors. Even small amount of oxygen in the nitride fuel can reduce thermal conductivity by 10 % [24]. Because the carbothermic reduction [25, 26] relies on the conversion of the uranium oxide and graphite to carbon monoxide and

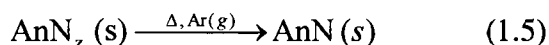
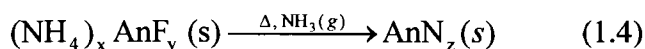
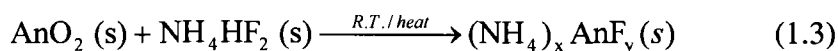
uranium nitride at elevated temperatures such as 1800 °C, unfortunate side effect of volatilizing low vapor-pressure actinides, particularly americium element [27], leading to potentially difficult contamination control problems.

While UN has many properties that make it an excellent reactor fuel, it has thus far failed to make the leap to practical systems due to the difficulty in its synthesis. In particular, the inclusion of carbon from the currently favored carbothermic reduction routes to UN is a major issue in the production of UN with favorable fuel properties [28, 29]. Therefore, it is important to identify alternate routes that could minimize these problems in synthesizing actinide nitrides. Given that a versatile route is found to synthesize AnN at general laboratory conditions without carbide impurities and with minimum oxide contaminations, it will provide the opportunity to study the chemistry of these compounds and fill some of the areas lacking chemical details.

1.4 Low-Temperature Fluoride Route

There are a number of previous techniques that have been used to remedy the difficulties encountered with the carbothermic reduction in synthesizing the actinide nitrides. Reaction of the metal hydride or metal with nitrogen gas [30] and the ammonolysis of the metal or metal carbide to the nitride [31] are two of those examples that could be found. However, these methods also consist of some disadvantages including the difficulty of making the reactants and the impurity levels of the final products. Use of AnO₂ as the precursor would, therefore, make it easy to deal with the reaction compared with the metal or the metal carbide. The conversion of actinide oxides to nitrides through a low-temperature fluorination route may address these issues [32]. In

this method, the metal oxides serve as the precursor compound to fabricate actinide mononitrides via three steps is presented. The method is based upon an initial reaction of oxide starting materials with a fluorinating agent. The resulting fluoride species is then further reacted to produce the nitrides, eventually yielding the mononitride species.



Here, the first step involves mixing the oxide with excess ammonium bifluoride (equation 1.3). AnO_2 and NH_4HF_2 solids were first ground in a mortar and pestle. Once they are ground well, the powders were weighed and mixed in the mortar and pestle for 10 to 15 minutes. The first step for both uranium and thorium compounds were done in this manner. The neptunium compounds were ground and mixed in a polyvinyl vial inside a gloveless glove box. Here, the $\text{NpO}_2(\text{s})$ was first weighted and added into the vial (Figure 1.5). Excess ground NH_4HF_2 was then added into the same vial and mixed for 10 min with the spatula. In the case of mixed uranium-thorium system, the two compounds were first added together and mixed for 10-15 min to make them powdered. The ground NH_4HF_2 was then admixed with the sample. More details on thorium, neptunium, and uranium-thorium mixed systems are given in Chapters 4, 5, and 6, respectively. The first step for the uranium system was not performed in this current work because another group under the supervision of same PI did the study on this step [33]. However, ammonium uranium fluorides were synthesized as a collaborative work with the above

mentioned group and UF_4 was used as the reactant for the second step in process of synthesizing UN.

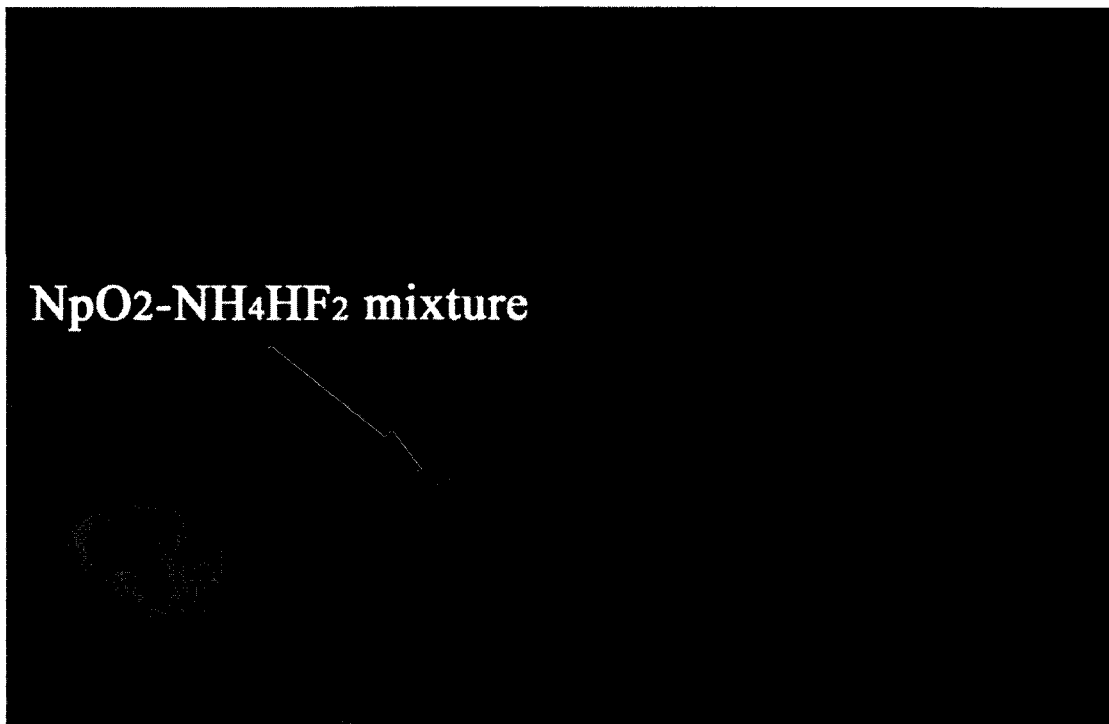


Figure 1.5 $\text{NpO}_2/\text{NH}_4\text{HF}_2$ solid mixture in the polyvinyl vial.

Reaction progress of this first step was checked with X-ray powder diffraction. Uranium system displayed fast reaction while thorium and neptunium took weeks depending on the sample size and/or the temperature used to complete the reaction described in equation 3. For example, NpO_2 reaction with NH_4HF_2 was fast at 100 °C. More details are discussed in the relevant chapter. In the second step, the resulting ammonium-actinide-fluoride $\{(\text{NH}_4)_x\text{AnF}_y\}$ was heat treated under ammonia gas (equation 1.4). Depending on the actinide been evaluated, a 2 to 50 mg quantity of the powder sample was added on to a Pt sheet and placed inside a two open end quartz tube.

The quartz tube was then placed inside a tube furnace as demonstrated in Figure 2.1 in Chapter 2. Ammonia gas was purged and flowed continuously while heating the sample with the expected temperature (typically 800°C). Gas flow was stopped when the sample was ready to remove from the reaction chamber.

Once the second step of the reaction was completed, the sample was removed and tested for chemical phases with XRD. Further heating of the product at elevated temperatures up to 1100 °C was performed under an inert atmosphere to decompose the higher actinide nitrides into the mononitride in the third step (equation 1.5). 1100 °C was typical for the UN_x decompositions to produce UN, but the temperatures for Th and Np systems were different. Because the terminal product of this step was ThNF for the thorium system, further heating at greater temperatures than 1100 °C may be needed to remove the extra fluorine and force Th⁴⁺ to reduce into Th³⁺ making the ThN. On the other hand, 900 °C was enough for the NpN_x decompositions. Detailed information on the experimental procedures can further be found in Chapter 2.

This process is particularly of interest due to the low temperatures required to convert the metal oxides to the nitride compared to the carbothermic reduction route. Research showed that the use of actinide fluorides such as UF₄ can also be used as the reactants which are heated under NH₃(g) to obtain the nitrides [34]. Synthesis and its related issues have been discussed in detail in C. B. Yeaman's Ph.D. thesis [33]. Here, the optimization of the experimental conditions of making UN was performed and Chapter 3 discusses these results. Furthermore, a detailed study on the decomposition kinetics of UN_x into UN in an inert atmosphere is also presented. Scanning (SEM) and transmission electron microscopy (TEM) were utilized in revealing the morphology and

micro/nanostructures of UN_2 , U_2N_3 , and UN . All these results on UN_x are discussed in Chapter 3. The optimized experimental conditions found for UN synthesis were further used in discovering the feasibility of making thorium and neptunium nitrides.

Chapter 4 consists of two major parts. The first part provides details on the products formed applying the fluoride route to thorium system. ThO_2 reaction with NH_4HF_2 together with the detailed characterization of ThNF , which was the terminal product of the ammonolysis step, is presented in this section. Second part of the chapter demonstrates a new method of synthesizing Th_2N_3 in a solid state reaction. Moreover, microscopic characterization of this compound to answer the question of why or where the ThO_2 secondary chemical phase was formed in the Th_2N_3 samples was performed and given in this section.

Complete discussion of the work performed on neptunium system using the fluoride route is presented in Chapter 5. Again, two main parts in the results section can be found in this chapter too. The reaction of $\text{NpO}_2\text{-NH}_4\text{HF}_2$ solid compounds were determined to be slower than uranium system. One new compound of the ammonium neptunium fluoride system was identified in this reaction. Using the knowledge of this new compound a reaction mechanism was proposed for the production of the terminal ammonium neptunium fluoride. The first part of the chapter is thus consisted of characterization of the new compound $\{(\text{NH}_4)_4\text{NpF}_8\}$ and the terminal product $\{(\text{NH}_4)_2\text{NpF}_6\}$. Final part of the chapter provides a thorough investigation of the reactions and products involved in the ammonolysis of these ammonium neptunium fluorides. This involves complete characterization of neptunium compounds of five novel chemical compositions.

Modifications to the method in synthesizing mixed actinide oxides together with remediation of the problems encountered in each system when synthesizing the oxide solid solutions of uranium and thorium are also presented in this work. Chapter 6 provides these investigations. Feasibility of making mixed U-Th-Nitrides is also discussed in the same chapter. The final chapter concludes the most important findings of each system. Thus, the final goal of the thesis work is to determine the feasibility of the low-temperature fluoride route in synthesizing the mononitrides and mixed oxides/solid solutions of actinides along with the characterization of these compounds to promote the field of actinide chemistry. Use of actinide mononitrides in the next generation reactor systems, on the other hand, needs to be supported by studying the chemistry of these compounds at laboratories. Because the use of carbothermic reduction is challenging at laboratories without a considerable effort on the experimental setups, it is mandatory to study novel techniques to synthesize the actinide nitrides to study their chemistries. This thesis is an effort to support these causes.

References

- (1) The need for nuclear power: <http://world-nuclear.org/why/biosphere.html>.
- (2) Minato, K.; Akabori, M.; Takano, M.; Arai, Y.; Nakajima, K.; Itoh, A.; Ogawa, T. *J. Nucl. Mater.* **2003**, *320*, 18.
- (3) Streit, Marco; Ingold, Franz. *J. Euro. Ceramic Soc.* **2005**, *25(12)*, 2687-2692.
- (4) Ganguly C. and Hedge, P.V. *J. Sol-Gel Sci Tech*, **1997**, *9*, 285-294.
- (5) Blank, H.; Richter, K.; Coquerelle, M.; Matzke, Hj.; Campana, M.; Sari, C.; Ray, I.L.F.; *J. Nucl. Mater.* **1989**, *166*, 95-104.

- (6) Morss, L.R.; Edelstein, N. M.; Fuger Eds., J. *The Chemistry of the Actinides and Transactinide Elements*; Springer Press: 3rd Edition, Vol. 1, 2006.
- (7) Tagawa, H. *J. Nucl. Mater.* **1974**, 51, 78.
- (8) Tagawa, H.; Masaki, N. *J. Inorg. Nucl. Chem.* **1974**, 36, 1099.
- (9) Berthold, H. J.; Hein, H. G. *Angew. Chem. Internat. Edit.* **1969**, 8, 891.
- (10) Rundle, R.E.; Baenziger, N.C.; Wilson, A.S.; McDonald, R.A. *J. Am. Chem. Soc.* **1948**, 70, 99.
- (11) Berthold, H. J.; Delliehausen, C. *Angew. Chem. Internat.* **1966**, 5, 726.
- (12) Sasa, Y.; Atoda, T. *J. Amer. Chem. Soc.* **1970**, 53, 102.
- (13) Serizawa, H.; Fukuda, K.; Ishii, Y.; Morii, Y.; Katsura, M. *J. Nucl. Mater.* **1994**, 208, 128.
- (14) Cordfunke, E.H.P. *J. Nucl. Mater.* **1975**, 56, 319.
- (15) Benz, R.; Zachariasen, W. H. *Acta Cryst.* **1966**, 21, 838-840.
- (16) Zachariasen, W. H. *Acta Cryst.* **1949**, 2, 388-390.
- (17) Chiotti, P. *J. Am. Ceram. Soc.* **1952**, 35, 123-130.
- (18) Gerward, L.; Olsen, J. S.; Benedict, U.; Itie, J. P.; Spirlet, J. C. *J. Appl. Cryst.* **1985**, 18, 339-341.
- (19) Sheft, I.; Fried, S. *J. Am. Chem. Soc.* **1953**, 75 (5), 1236-1237.
- (20) Olson, W. M.; Mulford, R. N. R. *J. Phys. Chem.* **1966**, 70 (9), 2932-2934.
- (21) Greenhalgh, W. O: Kinetic measurements for the carbothermic synthesis of uranium nitride, plutonium nitride, and (uranium, plutonium) nitride. *J. Amer. Cer. Soc.* **1973**, 56(11), 553-7.
- (22) Arai, Y.; Minato, K. *J. Nucl. Mater.* **2005**, 344, 180-185.

- (23) Agarwal, R.; Venugopal, V.; Sood, D. D. Calculation of thermodynamic parameters of U-Pu-N system with carbon and oxygen impurities. *J. Nucl. Mater.* **1999**, *270(3)*, 301-308.
- (24) Arai, Y.; Morihira, M.; Ohmichi, T.: The effect of oxygen impurity on the characteristics of uranium and uranium-plutonium mixed nitride fuels. *J. Nucl. Mater.* **1993**, *202(1-2)*, 70-8.
- (25) Muromura, T.; Tagawa, H. *J. Nucl. Mater.*, **71**, 1977, 65-72.
- (26) Muromura, T.; Tagawa, H. *J. Nucl. Mater.*, **80**, 1979, 330-338.
- (270) Ward, J. W.; Kleinschmidt, P. D.; Haire, R. G. *J. Chem. Phys.* **1979**, *71(10)*, 3920-5.
- (28) Pautasso, G., Richter, K. Sari, C., *J. Nucl. Mater.* ., **1988**, *158*, 12–18.
- (29) Bardelle, P.; Warin, D., *J. Nucl. Mater.* ., **1992**, *188*, 36–42.
- (30) Anselin, F. *CEA report R.2988* **1965**.
- (31) Katsura, M.; Hirota, M.; Miyake, M. *J. Alloy Compd.* **1994**, *213/214*, 440.
- (32) Yeamans, C. B.; Silva, G. W. C.; Cerefice, G. S.; Czerwinski, K. R.; Hartmann, T.; Burrell, A. K.; Sattelberger, A. P. *J. Nucl. Mater.* **2008**, *374*, 75.
- (33) Yeamans, C.B.; “Synthesis of Uranium Fluorides from Uranium Dioxide with Ammonium Bifluoride and Ammonolysis of Uranium Fluorides to Uranium Nitrides.” Ph.D. Dissertation, University of California, Berkeley, December 2008.
- (34) Funk, H.; Böhland, H. *Z Anorg. Allg. Chem.* **1964**, *334*, 155.

CHAPTER 2

METHODOLOGY AND INSTRUMENTATION

2.1 Introduction

This Chapter consists of information on the chemicals and experimental methods used. A brief introduction to the each instrumentation used in analyzing the samples will also be included. Section 2.2 consists of details on the reagents and the cover gases used in this research. A description on the general experimental procedure employed in the following chapters is given in section 2.3. Further details on using the procedure for each system (U, Th, Np, and U-Th mixture) are given in separate chapters 3, 4, 5, and 6. Final sections starting from §2.4 include introductions on each analytical method used to characterize samples synthesized.

2.2 Reagents

Table 2.1 Cover gases used for the experiments.

Gas	Purity (%)	Manufacturer
Ar	99.999	Praxair
NH ₃	99.999	Praxair
N ₂ /H ₂ (8%)	99.999	Praxair

Table 2.2 Chemicals used in the research work.

Solid chemical	Manufacturer
UO ₂	International Bio-Analytical Industries, Inc.
UF ₄	International Bio-Analytical Industries, Inc.
ThO ₂	STREM Chemicals, 99.99 %
ThF ₄	STREM Chemicals, 99.99 %
NpO ₂	Argonne National Laboratory
NH ₄ HF ₂	Fisher Scientific, 99.99 %

2.3 Experimental Procedures

2.3.1 Synthesis of ammonium actinide fluorides

Four and 10 to 20% excess moles of powdered NH₄HF₂ was added into the actinide oxide and mixed for 10 to 15 minutes in a polyvinyl or a Teflon vial. Depending on the actinide that was being used, the mixture was heated up to 100 °C for a week or higher. Further details on each actinide system are also presented in each relevant chapter of this report.

2.3.2 Synthesis of Actinide Nitrides

Ammonolysis of the resulting ammonium actinide fluorides was performed in this step of the reaction. Actinide fluorides such as UF₄ and ThF₄ were also used and are reported in each chapter. First, the actinide fluorides were loaded in a quartz boat wrapped with platinum foil or placed on a platinum sheet and placed inside a 25.4 mm diameter quartz tube. The quartz tube was capped with 25 mm Solv-Seal fittings (Andrews Glass Co., Inc.) at the both ends. In order to produce a controlled atmospheric condition for the reaction, the quartz tube was sealed with Pyrex Solv-Seal caps fitted

with 15 mm high-vacuum Teflon stopcocks. The quartz tube was then placed inside a tube furnace (Figure 2.1). Cover gas was introduced for 5 to 10 min to obtain the expected atmosphere and the furnace was ramped up to the temperature required. The cover gas was flowed through (1 atm) the sample over the entire time period of the synthesis. The sample was held at the selected temperature for the required time period before cooling down. Furnace door was opened for fast cooling during the process and it took about 90 min for a temperature of 1100 °C to come down to room temperature. These thermal treatments were performed under NH₃, Ar, or N₂/H₂(8 %) covering gases. The NH₃ gas was used in the first step of the heat treatments to make the starting actinide nitrides for the final actinide mononitride. The Ar(g) and N₂/H₂(8%) cover gases were used in the second step of the heat treatments to make mononitrides or to determine the reaction mechanism of higher actinide nitride decomposition.

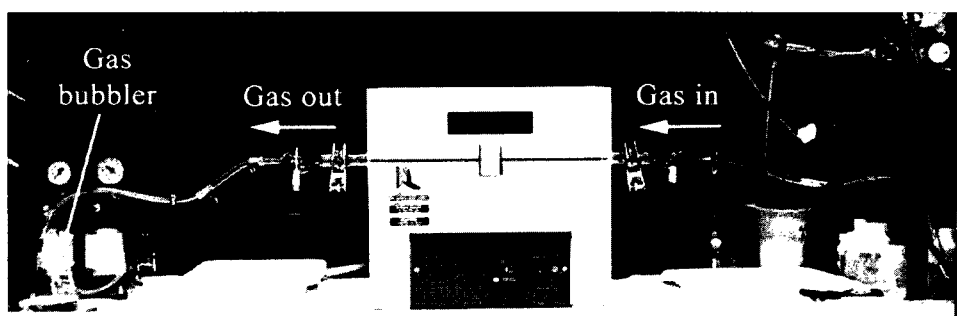


Figure 2.1 Experimental setup used to heat the samples.

2.4 X-ray Powder Diffraction (XRD)

2.4.1 Introduction and Sample Analysis with X-ray Powder Diffraction

When a compound is irradiated with X-rays (or with any other electromagnetic radiation), the electrons around atoms of the compound interact with the electric field of

the X-rays [1]. These interactions accelerate or decelerate the electron. If the electron is accelerated, the extra energy imparted to it can be reradiated. This scattering phenomenon is known to be coherent when none of the energy is transferred to the electron. Diffraction occurs when these coherent scatterings from a periodic array of objects make constructive interference at specific angles. X-rays will be diffracted in a number of different directions when they interact with a crystal containing three-dimensional periodic relationships between atoms (atomic planes) that compose it. However, only specific reflections from these planes can have constructive interferences (Figure 2.2). According to the Bragg's equation (equation 2.1) the atomic planes having θ angle to the incident beam will have this condition.

$$n\lambda = 2d_{hkl}\sin\theta \quad (2.1)$$

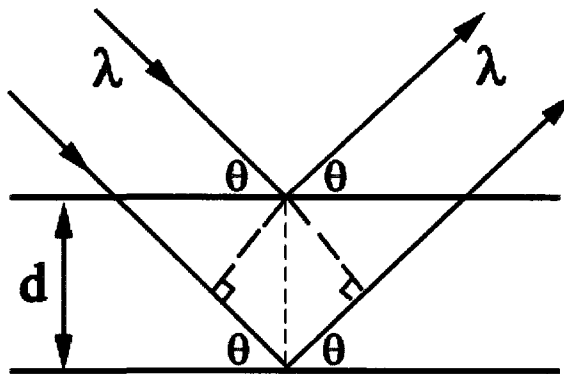


Figure 2.2 Bragg's Law reflection.

A powder sample or a polycrystalline aggregate can be a ground particle, a solid block of a metal, ceramic, polymer, glass or can even be a thin film or a liquid sample

and they consist of billions of tiny crystallites. These crystallites are randomly oriented and therefore all possible interatomic planes will be seen if the experimental angle of the X-ray diffractometer (2θ) is changed so that the characteristic diffraction angle (θ) of the planes hkl is compensated.

In this study, a slurry was made by applying few drops of ethyl alcohol onto the X-ray sample holder containing powder to be analyzed. The sample was then placed inside the powder X-ray diffractometer (Philips PANalytical X'Pert Pro). The diffractometer was operated using a 40 mA current and a 40 kV tension. The X-ray generated in the instrument is from Cu K_{α} (1.54 Å) radiation separated out from the K_{β} radiation using a Ni filter. The powder pattern was then analyzed against ICDD (International Centre for Diffraction Data) database files using X'Pert HighScore Plus software. XRD powder pattern refinements were done utilizing Rietveld method [2] for structure parameter refinement and for phase content determination. Pattern calculation was done assuming the chemical phase details identified with X'Pert HighScore Plus. Academic version of the TOPAS was used in these refinements.

2.4.2 Powder XRD Analysis Software: TOPAS

The software named 'TOPAS' is a XRD powder pattern refinement program. It uses Rietveld refinement to determine structures from powder data. Most importantly, structure determination does not include any methods that require integrated intensity extraction because it is done in direct space using step intensity data. Structure determination is done in TOPAS by estimating the cell parameters, using a rough knowledge about the cell content, and deducing the space group of the structure [3]. If the structural details of the compound are known, crystallographic databases such as ICDD

and ICSD (Inorganic Crystal Structure Database) can be used in finding these details for the refinement. Most of the compounds synthesized in the current work have been characterized and the single crystal data are present in the crystallographic databases. Therefore, these available details were used in structure refinements using TOPAS.

In the process of these analyses, first fit was calculated assuming these crystallographic data available and further calculations were made by refining different variables including lattice parameters. Chemical phases present in the samples were also calculated refining the XRD powder patterns applying the Rietveld method in TOPAS. As another function of the program, it selects the best refinement result when bond lengths and bond angles are to be calculated.

2.4.3 Application of Electron Density Maps

For new compounds synthesized, electron density maps were also used to confirm the crystallography. Powder XRD patterns were first refined with the software Jana2000 [4] which uses the Le Bail fit [5] when a structure model is not present. The LeBail fit assigns an optimal value to the intensity of each reflection found in the experimental diffraction pattern, and the lattice parameters and profile parameters will be refined. As the first step of calculating electron density maps of the sample, Le Bail decomposition was used to extract the individual observed structure factor amplitudes (F_{obs}) in Jana2000. These observed structure factors were then used to calculate the electron density maps of the compound by the charge-flipping algorithm [6] using Superflip [7] program. The calculated electron density maps were visualized using UCSF Chimera [8]. Electron density map obtained from the UCSF Chimera website [9] is presented in Figure 2.3.

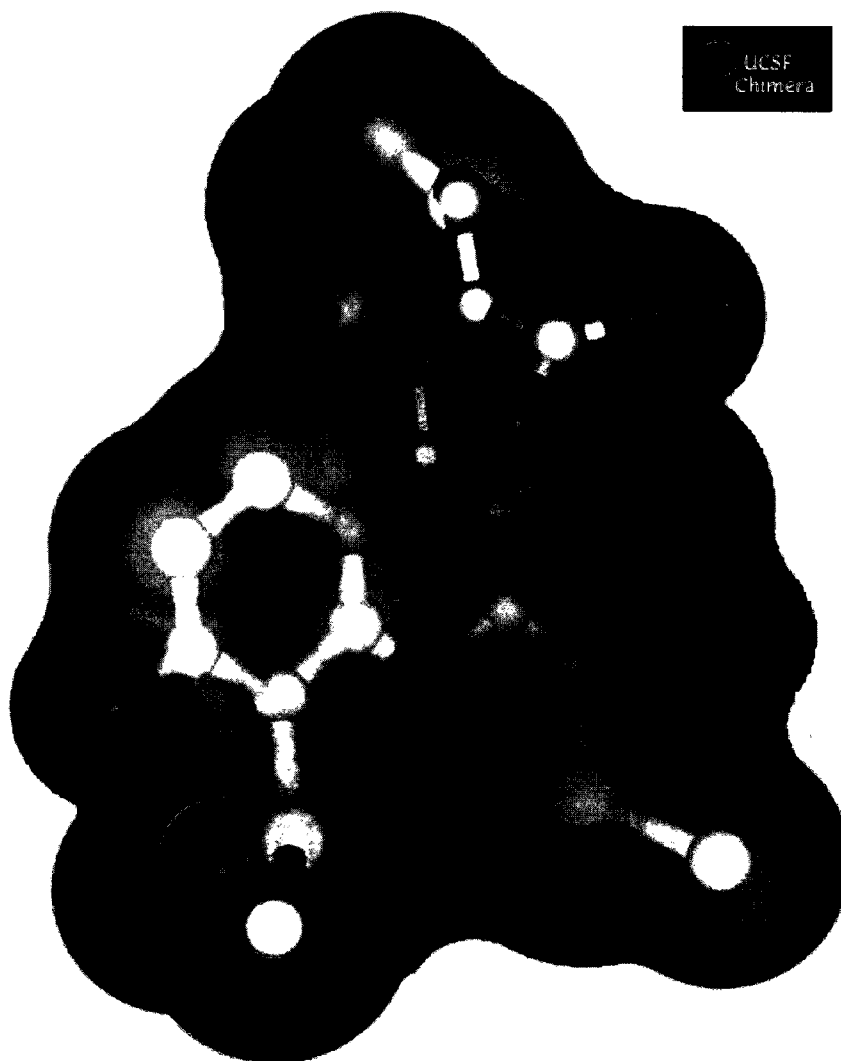


Figure 2.3 Example of an electron density map obtained from UCSF Chimera website.

2.5 Transmission Electron Microscopy (TEM)

2.5.1 Introduction to TEM and Instrumentation

Transmission electron microscopy is an important technique because of its different uses in various fields of science. It can be used to study morphology [10, 11], microstructure [12], and as well as nanostructures [13] of compounds. With the use of high resolution TEM (HRTEM) and selected area electron diffraction (SAED) difficult

structures can be solved [14]. Electron energy-loss spectrometry (EELS) is another mode of TEM that is being used to answer questions in science [15]. Another useful technique to solve unknown atomic structures is the scanning transmission electron microscopy (STEM) [16]. In this study, bright-field (BF) TEM, HRTEM, SAED, STEM/X-ray energy dispersive spectrometry (XEDS), and EELS mapping were used. Applications of each of these modes are described below. TEM studies were performed in all the samples synthesized here. However, the modes of the TEM used in samples were different depending on what type of information was needed to answer a particular question. The following chapters present and discuss these matters in detail for each case.

In TEM, a beam of electrons is focused on the specimen, and the transmitted beam is used in image forming. In this process, a TEM instrument uses a number of lenses to focus the incident beam on to the sample and the diffracted beam on to the screen or to the detector (Figure 2.4) [17]. There are two basic TEM imaging operations; bright-field (BF) and dark-field (DF) imaging. BF imaging uses the direct beam which passes through the specimen to make the image while DF utilizes the scattered beam. Therefore, the intensity of the image is high in BF while the contrast is high in DF. Also, BF and DF imaging are complementary to each other while both give similar information in most cases. Moreover, TEM imaging is easier with BF than with the DF mode both at low and high resolutions. The BF mode of energy-filtered transmission electron microscopy (EFTEM) was used in this study. TEM BF is useful in studying morphology, any impurity-phase related dislocations or other defects, and microstructure of the samples. BF TEM was also used to identify interesting locations for further investigations using high resolution mode (HRTEM).

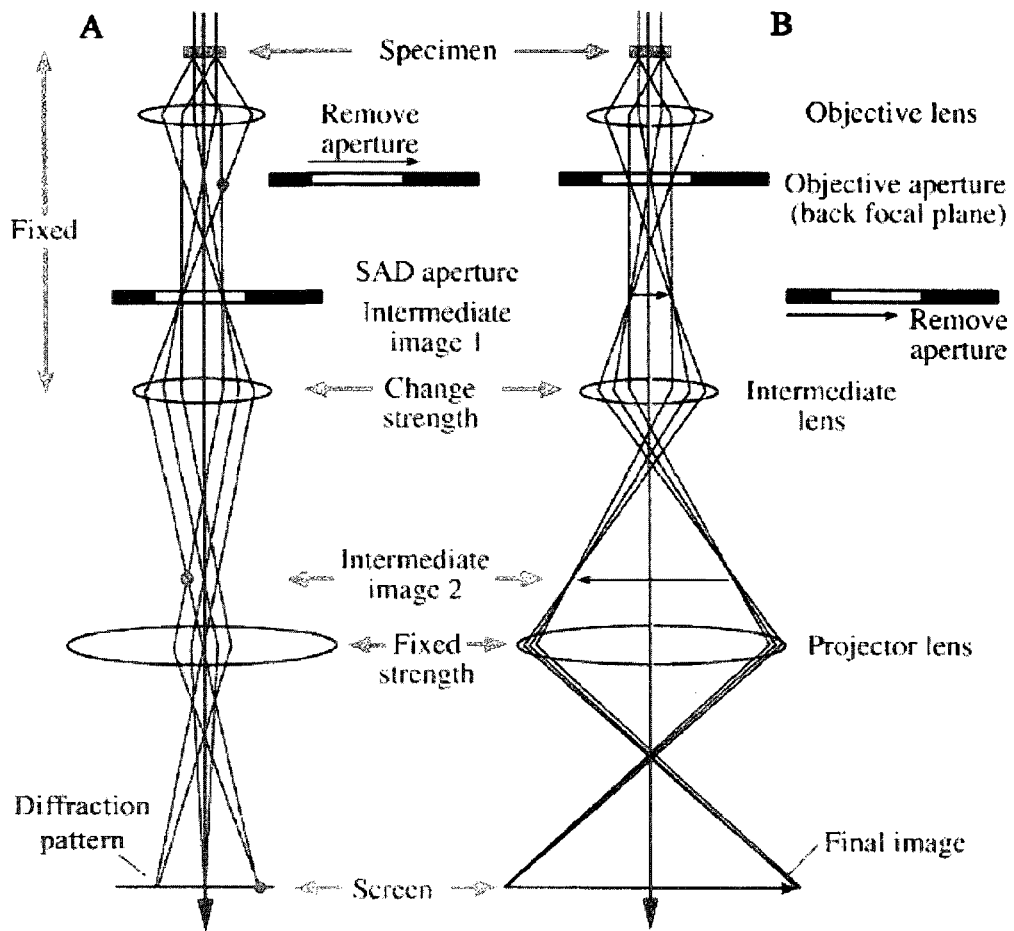


Figure 2.4 Diagrams displaying the two basic operations of the TEM: (A) viewing diffraction pattern and (B) viewing image.

Other than the BF and DF, TEM includes a number of important modes that have been mentioned before. One of such modes is the HRTEM. At high resolution, the nanostructures were studied in detail. Orientations and the interatomic planes relate to lattice fringes in HRTEM images were determined by the use of crystallographic details of the compounds being investigated. First, the spacing between lattice fringes in HRTEM images was correlated with the interplanar d -spacing of the structure. SAED or local Fast Fourier Transformed (FFT) patterns were also used in the above process of determining orientations and the interatomic planes present in the HRTEM images.

Calculated HRTEM images (Bloch Wave presentations) were applied in some of the analyses to confirm the nanostructural properties identified at high resolution. Bloch Wave simulated images were calculated using EMAPS software package [18] and an example is given in Figure 2.5.

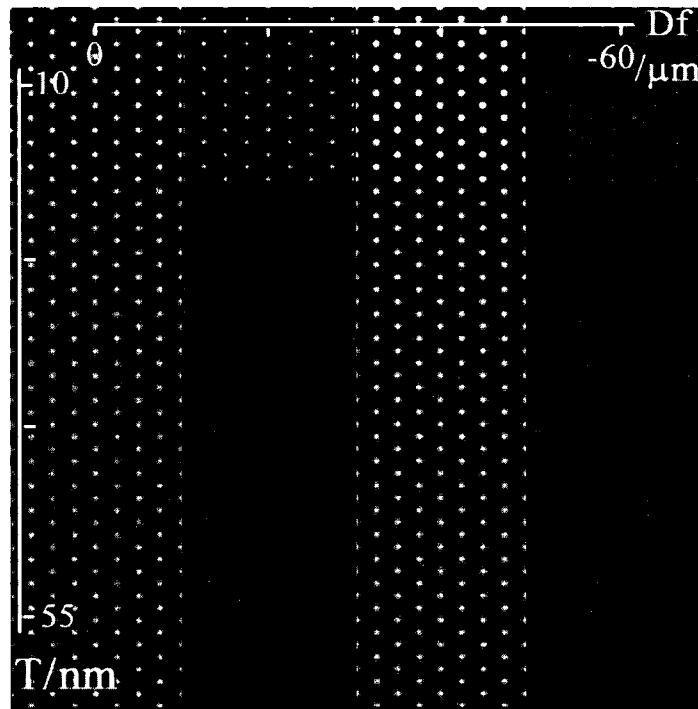


Figure 2.5 Calculated HRTEM image of UO_2 correspond to (10-1) planes along [111] zone axis.

As a supporting method, SAED can be used to observe the diffraction pattern of a sample. It also helps to identify crystalline particles of the sample being investigated. In TEM operation, objective lens takes diffracted electrons from the sample to disperse them into a diffraction pattern and to recombine them into an image. This diffraction pattern is not useful since it contains electrons from the whole area of the specimen. However, it can be used by reducing the intensity of the diffracted pattern by selecting an

area of the specimen which is of interest. For this reason, SAED is the diffraction pattern of the sample in TEM. Furthermore, SAED facilitates shorting out the presence of impurity phases. SAED will contain strong spots for primary chemical phase (Figure 2.6a) while extra diffraction spots represent secondary phases or sometimes grain boundaries with diverse orientations. Such a grain boundary can be separated out by tilting the TEM specimen few degrees from its original position (Figure 2.6b). If a sample is polycrystalline, rings will be formed in a diffraction pattern.

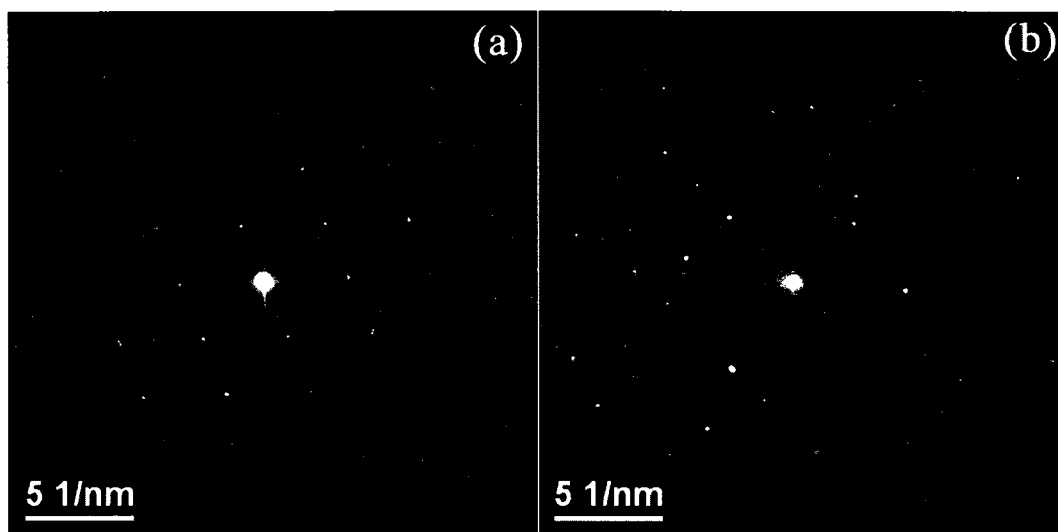


Figure 2.6 Tilting effect on SAED patterns (NpF_3): (a) strong diffraction spots for a single crystalline chemical phase and (b) after tilting the sample 20° .

XEDS and EELS mapping were some other modes of TEM that have been applied in sample characterization in this work. For XEDS, the sample image was obtained under STEM mode first and the electron beam was focused on the particle which is needed to be analyzed. The resulting spectrum gives information on the elements that the sample possesses. The spectrum gives peaks (Figure 2.7) and their relative intensities can be used to quantify elements of the sample. EELS mapping is also important in some cases where

the elemental distribution of a complete set of particles is required. XEDS give elemental distribution of one point whereas EELS mapping analyze the whole particle area. Therefore, sometimes the EELS mapping is more useful than XEDS. Figure 2.7 displays the difference of these two techniques.

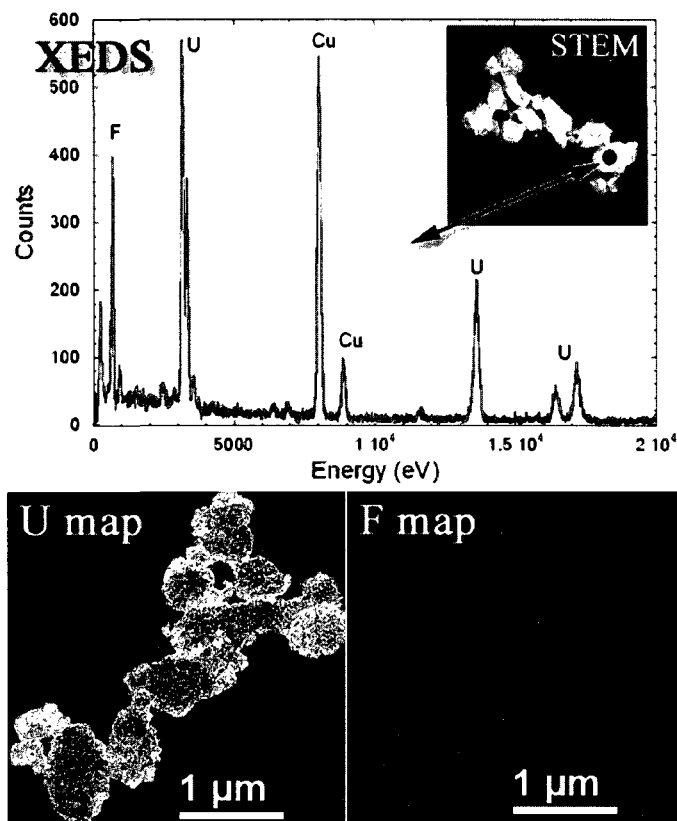


Figure 2.7 Comparison of XEDS and EELS mapping of UF_4 .

The TEM instrument (Figure 2.8) used in the current research uses a Tecnai-G²-F30 super-twin (S-TWIN) transmission electron microscope system with a 300 keV Schottky field emission gun. A Tecnai-G²-F30 S-TWIN is a powerful instrument for high resolution imaging, and it can go up to 1,000,000 times magnifications. Spherical and chromatic aberrations of the instrument are 1.2 and 1.4 mm, respectively. At high

resolution, the atomic scale details could be obtained with a 0.20 nm point-to-point resolution. The highest line resolution can be obtained is 0.10 nm. All TEM images were recorded using a slow scan CCD camera attached to a Gatan GIF 2000 energy filter.

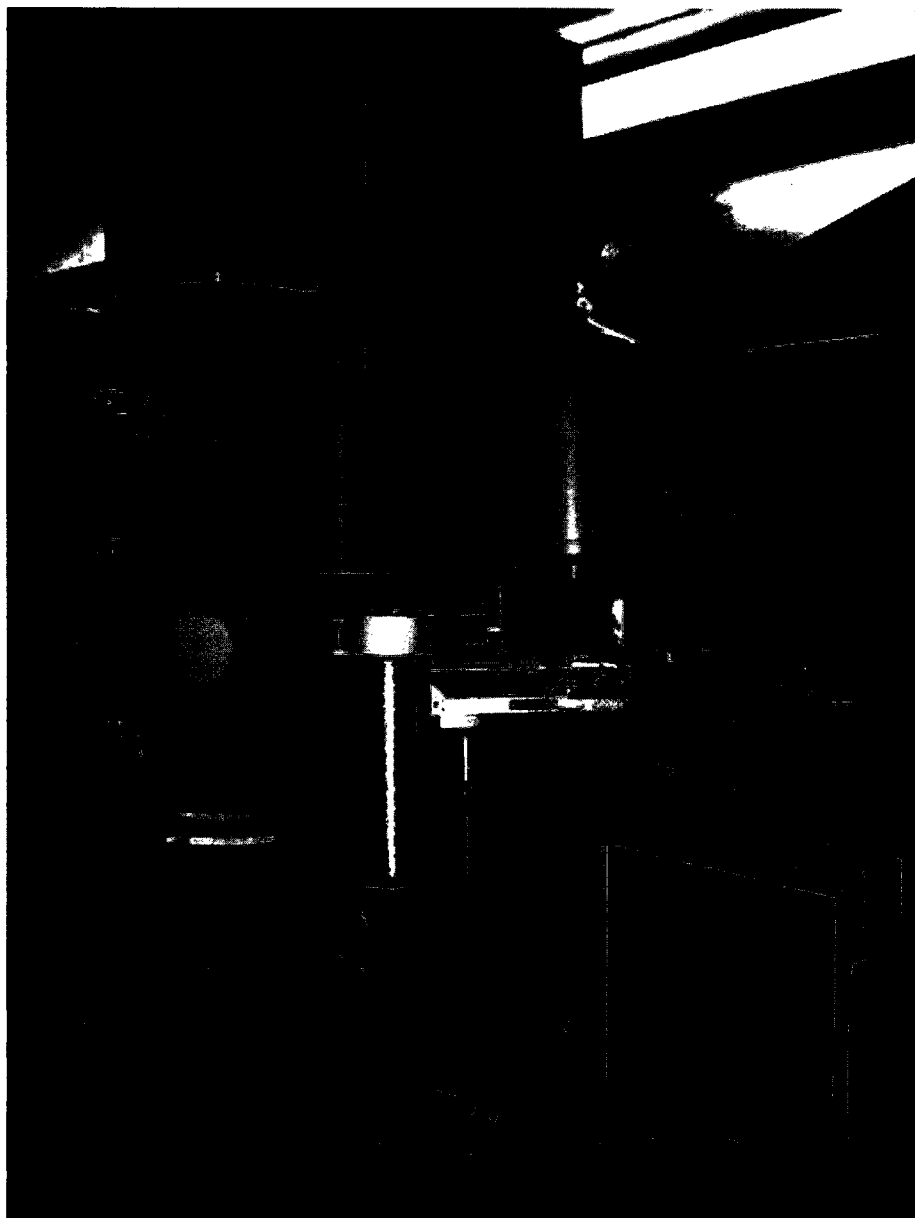


Figure 2.8 A picture of the TEM instrument used in this study [19].

2.5.2 Sample Preparation

Sample preparation involves several steps for TEM analysis because of the thickness required for specimens. Since a beam of electron has to go through the specimen, less than a 100 nm thickness is required. Three different sample preparation techniques were therefore tested with two selected for the current research project. Low-angle ion milling and polishing was tested for zirconium-based nitrides. In this method, sample was first made out of 3 mm diameter disk. This disk was then polished up to a thickness less than 150 μm . The center of the sample disk was then dimpled using a dimpler. Once a thickness less than 10 μm was achieved at the center of the sample, it was ion-milled up to a thickness of about 100 to 10 nm using a low-angle ($\sim 15^\circ$) ion milling and polishing system. Though, this method was not used here as it involves a number of steps that are difficult to use in radioactive sample preparations.

The primary method used for TEM sample preparation here is solution-drop method. In this method, the sample was first ground and a small amount (~ 0.5 mg) was added into a 5 mL solution of ethyl alcohol. The suspension was homogenized in an ultrasonicator for 5 minutes. Two to four drops of the solution were placed on a TEM sample holder (3 mm diameter copper grids of carbon type-B with 300 mesh size from TED Pella, Inc.), and the sample dried at ambient conditions before inserting in the TEM.

While the solution drop was the primary sample preparation technique applied here, microtome cutting method was occasionally used. In microtome cutting, the sample was first embedded in a hard spurr-resin (Table 2.3) and dried at 60 $^\circ\text{C}$ overnight. The sample embedded in the resin was cut into slices with a thickness of 20 to 50 nm using a Leica EM UC6rt microtome. The resulting samples were loaded onto a 3mm copper grid for

TEM analysis. With solution-drop method, bulk morphology of the particles can be observed while microtome cutting is important for cross sectional view. At high resolutions, sometimes it was difficult to examine bulk particle areas away from the edges due to thickness variances and high scattering effects from high-Z actinides. In such cases, microtome cutting was applied in specimen preparations [20].

Table 2.3 Chemical composition of hard Spurr-resin

Chemical component	Mass (g)
ERL 4206	10.0
DER 736	4.0
NSA	26.0
DMAE	0.4

2.6 Scanning Electron Microscopy (SEM)

2.6.1 Introduction

Scanning electron microscopy and the corresponding energy dispersive spectroscopy (EDS) were used extensively in this research project to characterize samples with respect to their morphology and elemental analyses, respectively. In SEM, an electron beam is focused on to a spot of the sample using electromagnetic lenses. Depending on the acceleration voltage, atomic number of the material and angle of the incident beam, the interaction volume (spot size) will vary from about 10\AA to couple of μm [21] (usually $3\ \mu\text{m}$). Once the electron beam strikes the sample, it can emit photon and electron signals. These signals include X-rays, Auger electrons, primary backscattered electrons, and secondary electrons (Figure 2.9).

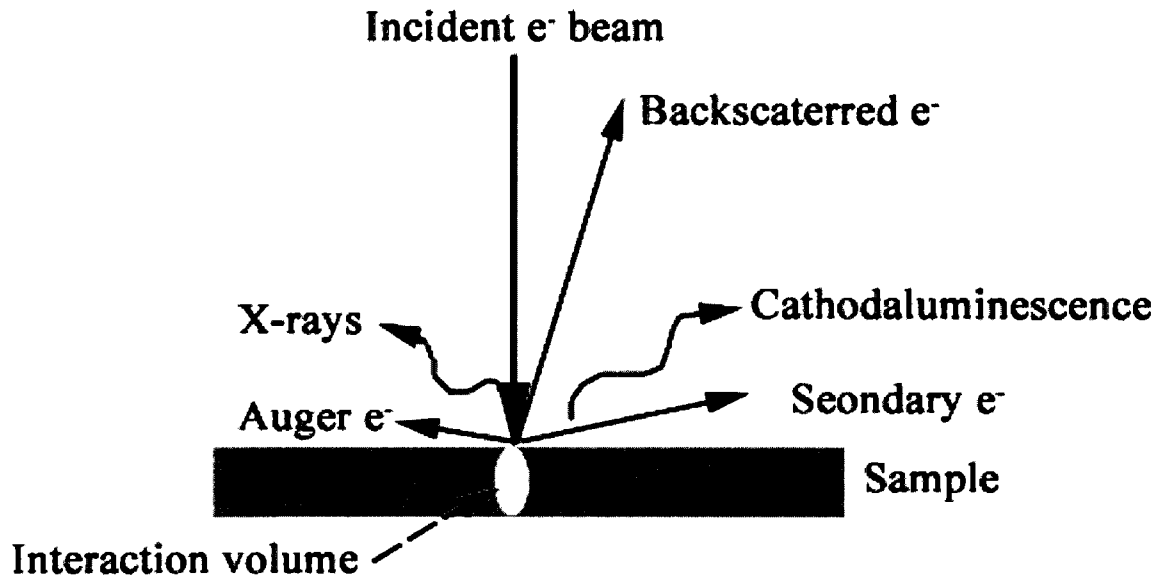


Figure 2.9 Various reactions occur in electron interactions with specimen.

If the X-rays are detected, elemental distribution of the sample can be semi-quantitatively determined (EDS). The primary backscattered electrons and secondary electrons will give information about the surface of the sample (topography) [22]. Use of backscattering electrons in SEM however has an advantage over the use of secondary electrons. The secondary electrons have low energy, 5eV, and therefore can only be used to examine the topography of the sample. On the other hand, backscattered SEM mode can be used to differentiate elements with different average atomic numbers since the backscattered electrons depend on atomic number of the specimen. Therefore, elements with higher atomic numbers will be brighter than low atomic numbered elements in the backscattered mode of SEM. Figure 2.10 shows a typical example of difference in information that can be gathered using SE and BE modes [23]. The SEM BE image gives more information on the different phases present in the sample than by SE.



Figure 2.10 Comparison of SE and BE SEM images of $(U_4Th_2Zr_9)H_{1.5}$ sample.

2.6.2 Instrumentation

The SEM imaging was performed on a JEOL scanning electron microscope model JSM-5610 (Figure 2.11a) equipped with secondary electron (SE) and backscattered electron (BE) detectors and an Oxford ISIS EDS (energy dispersive spectrometer) system with an acceleration voltage of 15 kV [24]. Gold-coated powder samples mounted on double-sided carbon tapes were used to investigate the bulk particle morphology of the samples using SE imaging mode of SEM.

2.7 Electron Microprobe Analysis

Electron microprobe can be used to both qualitatively and quantitatively analyze elements distributed in a solid sample. It has accuracy up to $\pm 1\%$ for the quantitative measurements and about $1 \mu m$ spatial resolution in the line profiles or two-dimensional maps of the samples [25]. The sample has to be well-polished after embedding it with epoxy and should contain an evolution area of 1 to $3 \mu m$. In electron microprobe, a high

energy (usually 15 keV) electron beam is impinged on the sample and the constituted elements will ionize after absorbing the correct energy. Electrons of inner shells will release the extra energy as characteristic X-ray of the element being detected. Depending on the wavelength of the X-ray, the element can be identified. Quantitative measurement of the element could be performed using the intensity of the characteristic wavelength and with the help of calibration plots of standard materials [26]. For the current study, a JEOL electron probe micro-analyzer model JXA-8900 (Figure 2.11b) equipped with 4 wavelength dispersive X-ray spectrometers (WDS) and an EDS was used to quantitatively analyze the elemental distributions in the samples.

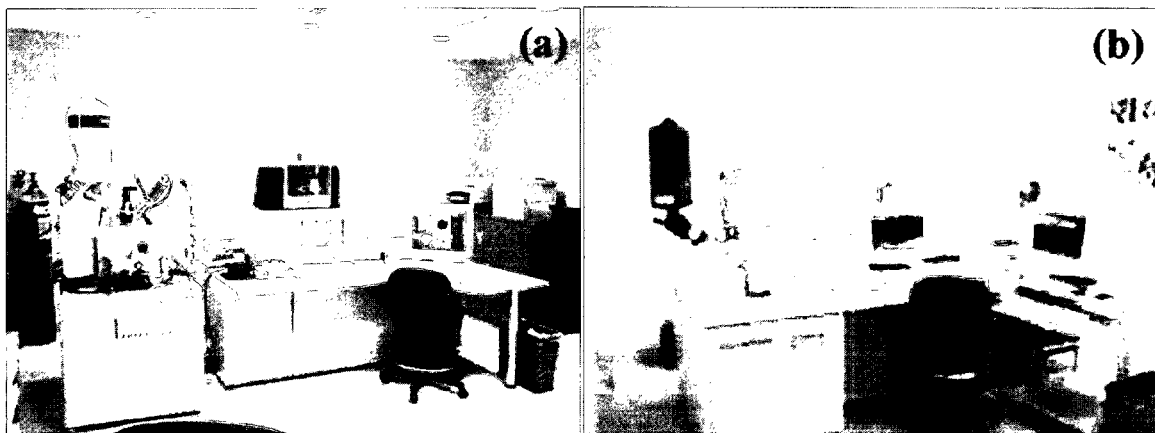


Figure 2.11 (a) SEM and (b) EMPA instruments.

References

- (1) Jenkins, R.; Synder, R. L. *Introduction to X-ray Powder Diffractometry*. John Wiley & Sons, Inc. Vol. 138.
- (2) Reitveld, H. M. *J. Appl. Cryst.* **1969**, 2, 65.

- (14) Baerlocher, C.; Gramm, F.; Massüger, L.; McCusker, L. B.; He, Z.; Hovmöller, S.; Zou, X. *Science* **2007**, *315*, 1113-1116.
- (15) Buck, E. C.; Finn, P. A.; Bates, J. K. *Micron* **2004**, *35*, 235-243.
- (16) Ferrer, D.; Blom, D. A.; Allard, L. F.; Mejía, S.; Pérez-Tijerina, E.; José-Yacamán, M. *J. Mater. Chem.*, **2008**, *18*, 2442-2446.
- (17) Williams, D. B.; Carter, C. B. *Transmission Electron Microscopy: A Textbook for Materials Science*, 1st edition, Springer (August 31, 2004).
- (18) Zuo, J. M.; Mabon, J. C. Web-based Electron Microscopy Application Software: Web-EMAPS, *Microsc. Microanal.* **2004**, *10* (Suppl. 2), URL: <http://emaps.mrl.uiuc.edu>.
- (19) <http://nstg.nevada.edu/TEM/TEMPic.htm>.
- (20) Silva, G. W. C.; Yeaman, C. B.; Ma, L.; Cerefice, G. S.; Czerwinski, K. R.; Sattelberger, A. P. *Chem. Mater.* **2008**, *20*, 3076.
- (21) <http://www.unl.edu/CMRAcfem/volume.htm>.
- (22) www.unl.edu/CMRAcfem/interact.htm.
- (23) Terrani, K. A.; Silva, G. W. C.; Yeaman, C. B. Y.; Balooch, M. *J. Nucl. Mater.* **2009**, *Accepted*.
- (24) <http://www.unlv.edu/centers/emil/sem.htm>.
- (25) Reed, S. J. B. *Electron Microprobe Analysis and Scanning Electron Microscopy in Geology*, 2nd Edition, Cambridge University Press.
- (26) <http://www.stanford.edu/group/snl/empa.htm>.

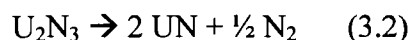
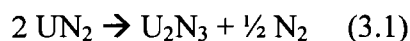
CHAPTER 3

SYNTHESIS AND CHARACTERIZATION OF URANIUM NITRIDES

3.1 Introduction

This chapter includes the synthesis of UN_x using UF_4 as the precursor compound, optimization of experimental conditions to decrease secondary impurity phases of the final UN samples, kinetics studies of the decomposition of UN_2/U_2N_3 under an inert atmosphere, and the characterization of each uranium nitride chemical phase using microscopic techniques. The relative concentration of uranium species in the solids were determined by Rietveld method [1] of the X-ray powder diffraction patterns.

Even though the presence of uranium nitrides of different compositions is reported under different experimental conditions, there is little information available on the reaction kinetics associated with the formation of UN from UN_2 or $\alpha-U_2N_3$. UN is the lowest-stoichiometry nitride of the U-N solid system (UN_2 , U_2N_3 , and UN) [2], and the following reactions could be used to represent the decomposition of higher nitrides towards the mononitride:



The research work that has been performed here focuses on confirming the above reaction mechanism and optimizing the reaction conditions to decrease the formation of impurity chemical phases such as UO_2 . Formation temperatures of $\alpha\text{-U}_2\text{N}_3$ and UN were identified by carefully decomposing UN_2 at various temperatures under an inert argon atmosphere. Determination of the relevant kinetic parameters and activation energies, which were calculated assuming a pseudo-first-order model and Arrhenius plots, will also be presented in this chapter.

Previous analyses by X-ray powder diffraction [3], neutron powder diffraction [4], nuclear magnetic resonance [5], transmission electron microscopy [6, 7], and x-ray photoelectron spectroscopy [8] can be found on uranium nitrides at different scales. However, the microscopy studies [6, 7, 9] have focused primarily on sintered pellets of UN and no microscopic studies on UN_2 and U_2N_3 were reported other than the current work [10]. Because microcrystalline properties influence the sinterability of UN, and because a fuel-quality sintered UN pellet is the ultimate goal of any nitride fabrication process for nuclear fuel, it is important to characterize the starting nitride material in sufficient detail. The work of Le et al., [6] and Sole and Van der Walt [7] reports the TEM characterization of UN specimen prepared using ion-thinning and electropolishing. In the current study, a solution-drop method and microtome cutting method, which can produce samples less than 25 nm thick [11] were used in sample preparations for the TEM analysis. Microtome cutting has been found to produce high quality TEM sample specimens in observing the cross-sectional as well as microstructural characterization [11].

3.2 Experimental details

3.2.1 Synthesis of Uranium Nitrides

The direct ammonolysis of UF_4 was used to synthesize UN_2 as described in Chapter 2 section 2.3.2. About 500.0 mg batches of UF_4 were heated at 800 °C for 60 minutes under ammonia gas to make the UN_2 samples required for the study. Different batches of the synthesized UN_2 were heat treated under an inert atmosphere (ultra-high purity argon, 99.9999%, Praxair) at temperatures ranging from 500 through 1100 °C (Table 3.1) for different time periods to study reaction mechanism, kinetics, and to optimize the experimental conditions for high phase purities of the final UN product. A batch of U_2N_3 was also synthesized by heating UN_2 at 700 °C under Ar(g) for the decomposition studies of the compound to synthesize UN.

3.2.2 Characterization Methods

X-ray powder diffraction (XRD) patterns were obtained using $\text{Cu-K}\alpha$ radiation. Phase composition and lattice parameter refinements were done assuming the crystallographic information of ICDD database for the Rietveld method: UN_2 (01-073-1713), U_2N_3 (01-073-1712), UN (00-032-1397), and UO_2 (00-041-1422). An internal LaB_6 standard from NIST (SRM 660a) was admixed with the uranium nitride samples to allow for precise lattice parameter refinement and to optimize the quality of each Rietveld analysis as performed. The morphology of the nitride samples was studied by SEM and TEM. Electron probe micro-analysis was also performed to determine elemental distributions in the samples. Both techniques described in §2.5.2 were used for TEM specimen preparation: solution-drop and microtome cutting. The solution-drop method was utilized

to explore the morphology of the nitrides samples. Microtome cutting was used to prepare samples for cross-section analysis and HRTEM imaging.

3.3 Mechanism and Kinetics of UN₂ Decomposition

3.3.1 UN₂ Decomposition Mechanism and Chemical Phase Characterization by XRD

XRD powder pattern refinement of the as-synthesized UN₂ sample is shown in Figure 3.1. The observed (top continuous line) and the calculated (highlighted continuous line for UN₂) patterns for the XRD powder refinement are shown. The lower curve is for the difference between the observed and calculated patterns. Allowed line positions for the UN₂ and LaB₆ are marked as vertical lines at the bottom. Square root of counts was used as the scale of Y-axis for proper display.

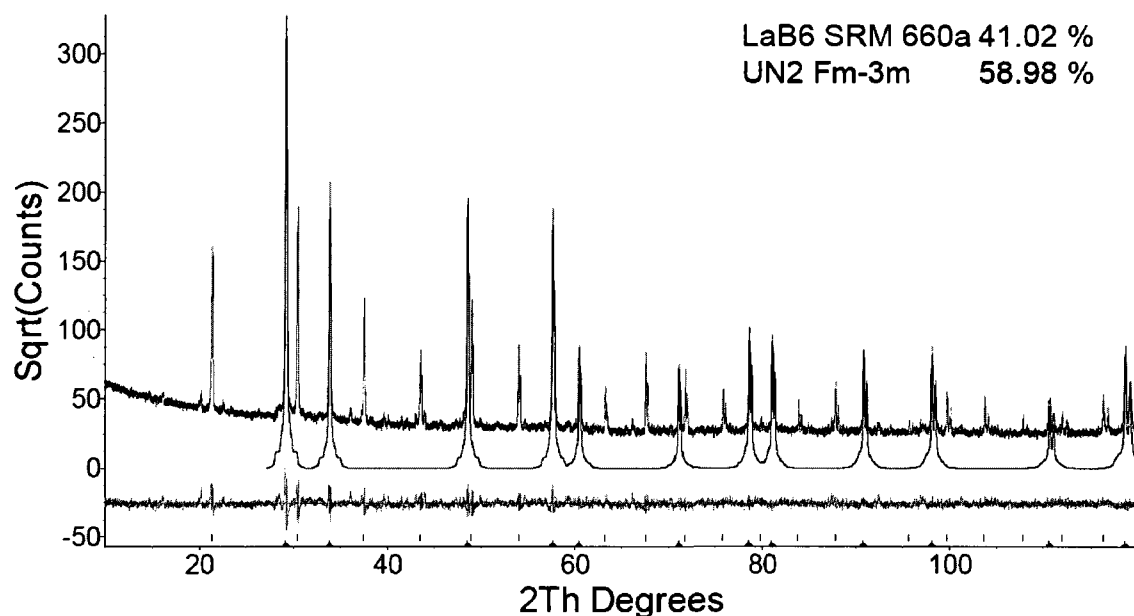


Figure 3.1 XRD powder pattern of UN₂ together with the calculated patterns.

Table 3.1 Lattice parameters and X-ray phase densities of the uranium nitrides calculated from experimental patterns using Rietveld analysis.

Sample	Lattice parameter (nm)		X-ray phase density (g cm ⁻³)	
	Calculated	Reference	Calculated	Reference ^[3]
UN ₂	0.53027(1)	0.531(1) ^[3]	11.8516(2)	11.73
U ₂ N ₃	1.06691(1)	1.0678-1.0580(5) ^[3, 12]	11.3340(2)	11.24
UN	0.48899(1)	0.48899(2) ^[13]	14.3175(5)	14.32

The lattice parameters refined show a good match with the values reported previously. These values are presented in Table 3.1. The XRD pattern consists of narrow, well-defined, high intensity peaks indicating the sample to be crystalline [14]. The observed pattern matches the calculated pattern for UN₂ with a relatively reasonable weighted pattern residual error (R_{wp}) of 10.8%, considering the impurity peaks found in the experimental pattern. Based on the other UN₂ samples prepared varying the amount of UF₄ used, the as-synthesized UN₂ samples consisted of 0.5 to 1.0 (3) wt % secondary oxide phase. The impurity peaks are significant at positions such as 20.2° and 36.1° 2theta values (Figure 3.1), and the peaks have some resemblance to the peaks identified in the U₂N₃ XRD pattern (Figure 3.2), but are not accounted for by the UN₂ structure. In order to investigate these peaks further, another UN₂ sample was synthesized under the same NH₃(g) atmosphere and temperature (800 °C) for 390 minutes.

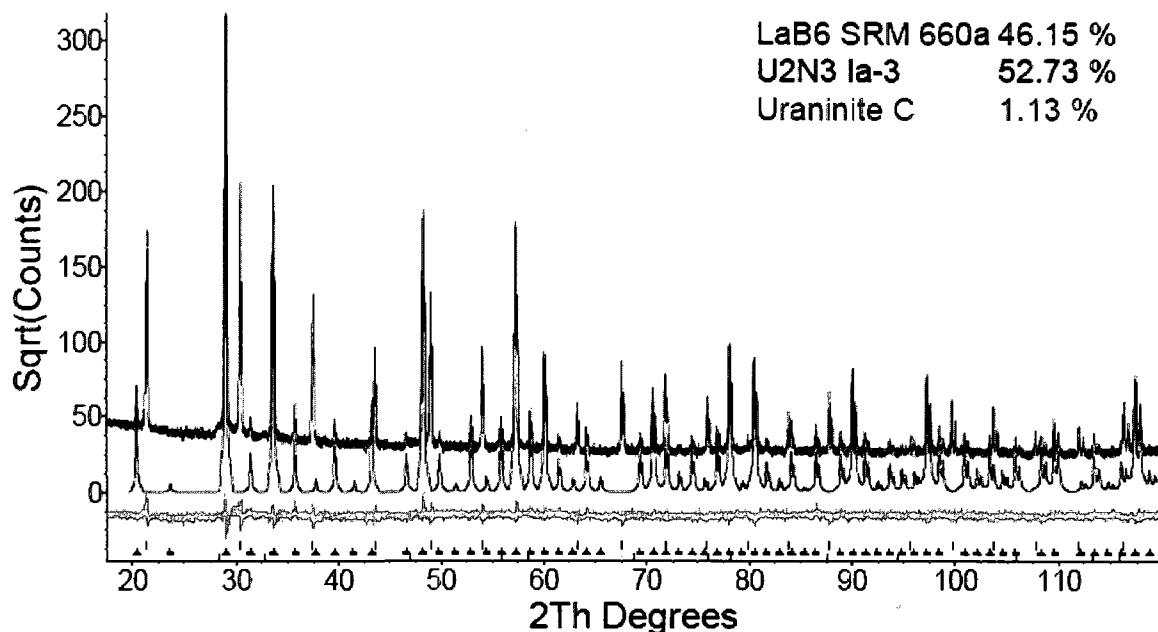


Figure 3.2 Rietveld refinement of U_2N_3 sample. The displayed patterns are as of UN_2 in Figure 3.1. Calculated pattern of U_2N_3 is highlighted. UO_2 impurity phase content of 2.1 (1) wt.% was identified and the $R_{wp} = 9.6\%$.

The Rietveld analyses of the sample held at this temperature for 60 minutes and the sample held for 390 minutes are shown in Figure 3.3a and 3.3b, respectively. The peaks at 20.2° and 36.1° 2theta values have been disappeared for the sample made after heating for 390 minutes. Incomplete conversion, with the material still slightly sub-stoichiometric UN_2 , could account for these peaks since UN_2 and U_2N_3 are known to have wide range of continuous stoichiometry [12, 15] and the supersymmetries that cause weak reflections to show in the XRD pattern. Thermal behavior of UN_2 in an inert atmosphere was studied by heating three UN_2 samples of approximately 50 mg of each at 500, 700, and 1100 °C under flowing high-purity argon (99.999 %) for 30 minutes. Heating the first sample at 500 °C resulted in no measurable decomposition of the UN_2 . At 700 °C, UN_2 was completely converted to U_2N_3 (Figure 3.2). After heating at 1100 °C for 30 min, the only uranium nitride phase identified in the sample was UN.

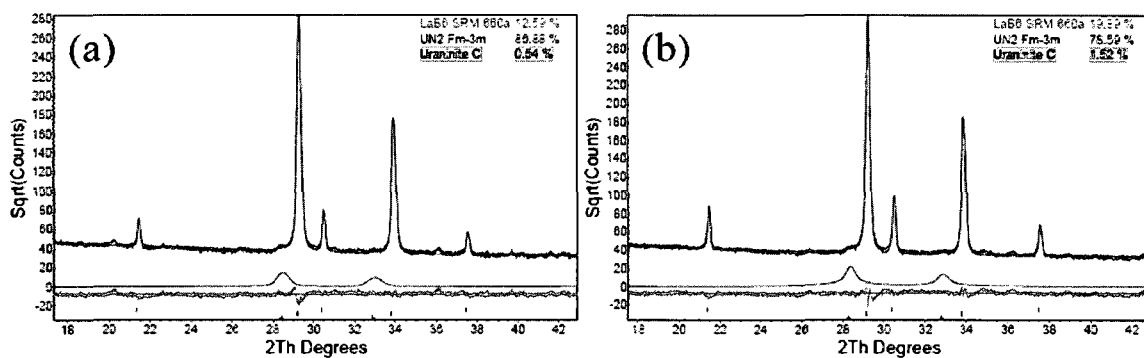


Figure 3.3 Observed patterns of UN₂ samples showing the impurity peaks in the low 2theta angles: (a) synthesized by heating UF₄ at 800 °C for 1 hour; (b) synthesized by heating at 800 °C for 6.5 hours. Calculated pattern of UO₂ is highlighted.

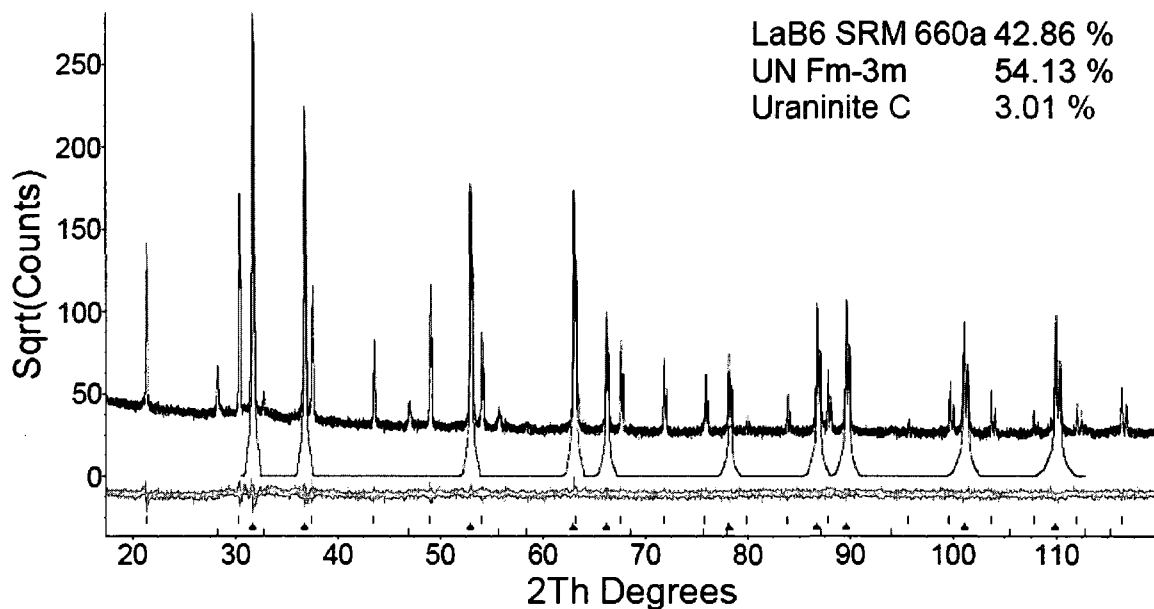


Figure 3.4 XRD powder refinement of the as-synthesized UN sample using Rietveld method. Highlighted is the calculated pattern of UN. $R_{wp} = 8.6\%$.

The UN sample was determined to consist of two chemical phases, the primary UN phase and a 5.3 (1) weight percent UO₂ impurity phase (Figure 3.4), most likely due to trace oxygen contamination attributable to the experimental setup. Table 3.1 further shows the cubic lattice parameters determined for U₂N₃ and UN using Rietveld

refinement and the X-ray densities of each nitride calculated from the experimental XRD patterns. Lattice parameters of U_2N_3 and UN_2 have a reasonable match to the literature values, but UN has a much better match to that of literature value comparatively. The variable stoichiometry of the $UN_{1.5 \leq x < 2}$ phase likely lead to the departure from the pure compound lattice parameter and density for synthesized U_2N_3 and UN_2 .

Table 3.2 Elemental compositions determined by electron microprobe studies.

Sample	Elemental %		
	U	N	O
UN_2	89.02 ± 1.72	10.68 ± 0.20	0.29 ± 0.38
U_2N_3	90.77 ± 1.64	8.26 ± 0.10	0.97 ± 0.30
UN	93.17 ± 1.94	5.14 ± 0.13	1.69 ± 0.41

Chemical analysis performed on these three samples with electron microprobe showed that there are considerable amounts of oxygen impurities in U_2N_3 and UN (Table 3.2) samples confirming the presence of UO_2 secondary phase. The oxygen level is highest in UN and lowest in UN_2 . The error in the oxygen quantity measurement for UN_2 sample is large because the oxygen level is near the lower detectable limit of this technique.

Further experiments were carried out in order to optimize the time of thermal decomposition of UN_2 at 1100 °C to increase the phase purity of UN. Experiments were performed from 1 min to 30 min time periods and the results are displayed in Figure 3.5. Thermal decomposition of UN_2 performed at 1100 °C for 23 min under Ar(g) produced a

UN sample of 97 wt% phase purity with the help of Zr-sponges as an oxygen getter. These experimental conditions were then further used for additional UN sample synthesis for characterization purposes.

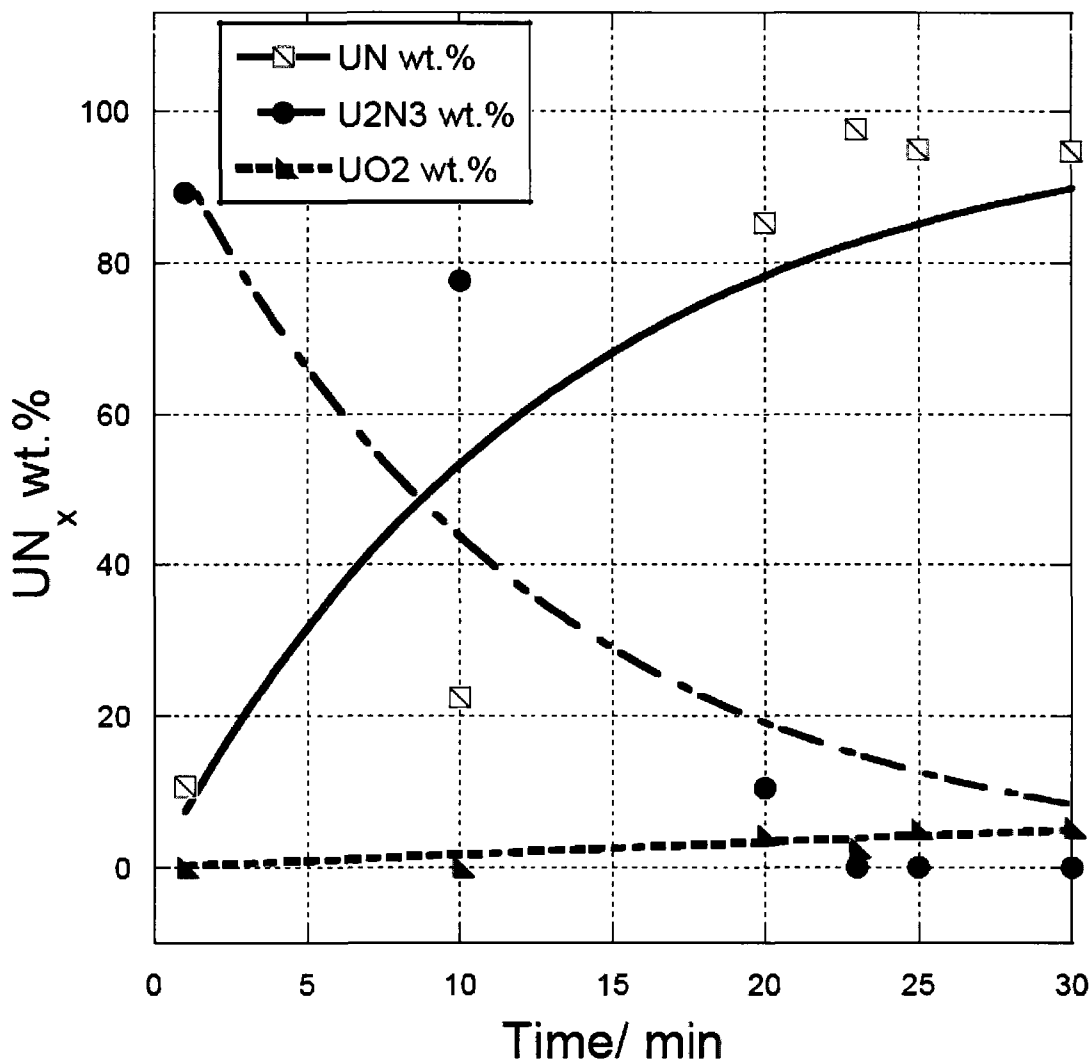


Figure 3.5 Decomposition of UN₂ under Ar(g) at 1100 °C as a function of time.

Subsequent experiments were conducted in two different temperature ranges, viz., 500 – 700 °C and 700 – 1100 °C (Table 3.3) in order to refine the temperature ranges in

which the decomposition reactions in equations (1) and (2) occur. At each of these temperatures, the reactants were heated for 30 min initially to determine where the decomposition reactions occur. These experiments showed that the UN_2 decomposition to U_2N_3 starts at about 675 °C, and the second decomposition to UN begins at about 975 °C. Therefore, the decompositions at the temperatures 650 and 950 °C were studied further with up to 60 min of heating. These two experiments showed neither formation of U_2N_3 at 650 °C nor formation of UN at 950 °C. Heating of UN_2 at 600 and 900 °C was also conducted for up to 240 min to see how the time of heating would affect the UN_2 decomposition. At 600 °C, no U_2N_3 formation occurred. Likewise, no UN formation was seen at 900 °C. Also, over the temperature range from 975 °C to 1100 °C, both U_2N_3 and UN were observed in the product depending on the time of heating.

Another sample was synthesized to check the presence of any other intermediate chemical phases of the formation or the decomposition of UN_2 . A sample of UF_4 was heat treated up to 1000 °C for 30 min under $\text{NH}_3(\text{g})$ and the temperature was raised to 1100 °C in 10 min time period after changing the covering gas to $\text{Ar}(\text{g})$. Sample heating at 1100 °C was done for another 30 min. Ammonolysis was done at 1000 °C in order to complete the UN_2 formation under a reduced time period (30 min instead of 60 min at 800 °C). This experiment show that the UF_4 undergoes a reaction with $\text{NH}_3(\text{g})$ to form UN_2 via an intermediate phase, UNF, which was not identified with previous experiments conducted here. Figure 3.6 shows the XRD powder pattern observed for this sample with the UNF calculated pattern being highlighted. A complete formation of UN_2 and decomposition into UN was not observed in this sample because the UF_4 amount used here was large

(close to 1g) so that the sample surface exposed to NH_3 was decreased reducing the reaction kinetics.

Table 3.3 Products observed after heating UN_2 at different temperatures and time intervals under argon atmosphere.

Temperature/ °C	Time of heating (min)	Products observed
500	30	UN_2
600	30	UN_2
	240	UN_2
650	30	UN_2
	60	UN_2
675	30	U_2N_3
700	30	U_2N_3
750	30	U_2N_3
800	30	U_2N_3
900	30	U_2N_3
	240	U_2N_3
950	30	U_2N_3
	60	U_2N_3
975	30	$\text{U}_2\text{N}_3, \text{UN}$
1000	30	$\text{U}_2\text{N}_3, \text{UN}$
1050	30	$\text{U}_2\text{N}_3, \text{UN}$
1100	30	UN

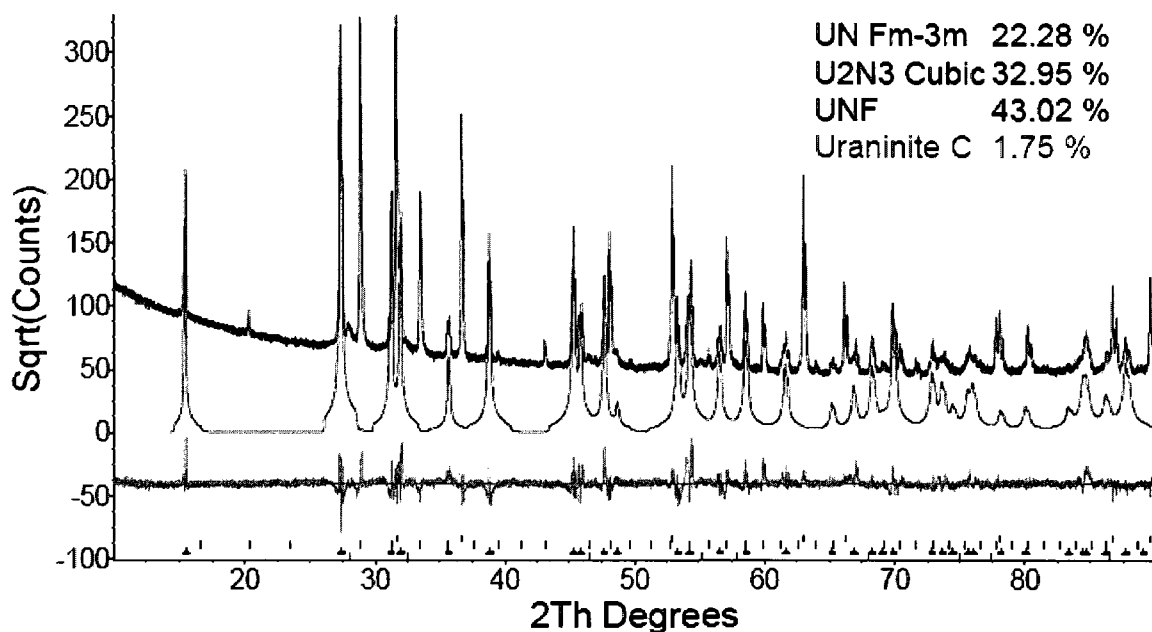


Figure 3.6 Observed XRD powder pattern of UF₄ after heating 30 min at 1000 °C and 1100 °C under NH₃(g) and Ar(g), respectively. Only the calculated pattern for UNF is highlighted for clarity ($R_{wp} = 11.1\%$).

Linear change of the refined lattice parameters of UN₂ and U₂N₃ as a function of temperature was also observed (Figure 3.7). The slope of U₂N₃ lattice parameter change in Figure 3.7 is larger than that of the UN₂ indicating a larger lattice parameter change in the intermediate chemical phase compared to the precursor compound. Further analysis showed that there is a 10-fold increase in the U₂N₃ lattice parameter change compared to the change of the UN₂. Furthermore, the N/U molar ratios of these UN_x samples were estimated by correlation plots for UN₂ and U₂N₃ as depicted in Figure 3.8 [3, 12, 15, 16, 17, 18, 19, 20, 21, 22]. A value of 0.521 nm was taken as the lattice parameter of the stoichiometric UN₂ by assuming behavior analogous to that of AmO₂ [12]. The lattice parameter values of the UN₂ samples synthesized and annealed up to 650 °C correlated with those found for samples with N/U molar ratios of 1.75 to 1.8. However, a lack of data for the UN_x system in the $1.8 \leq x \leq 2.0$ region of the plot in Figure 3.8 may imply a

higher error in the N/U molar ratio estimates compared to the $1.45 \leq x \leq 1.75$ region. Lattice parameters of U_2N_3 samples synthesized in this study show variations comparable to that seen by other authors as shown in Figure 3.8.

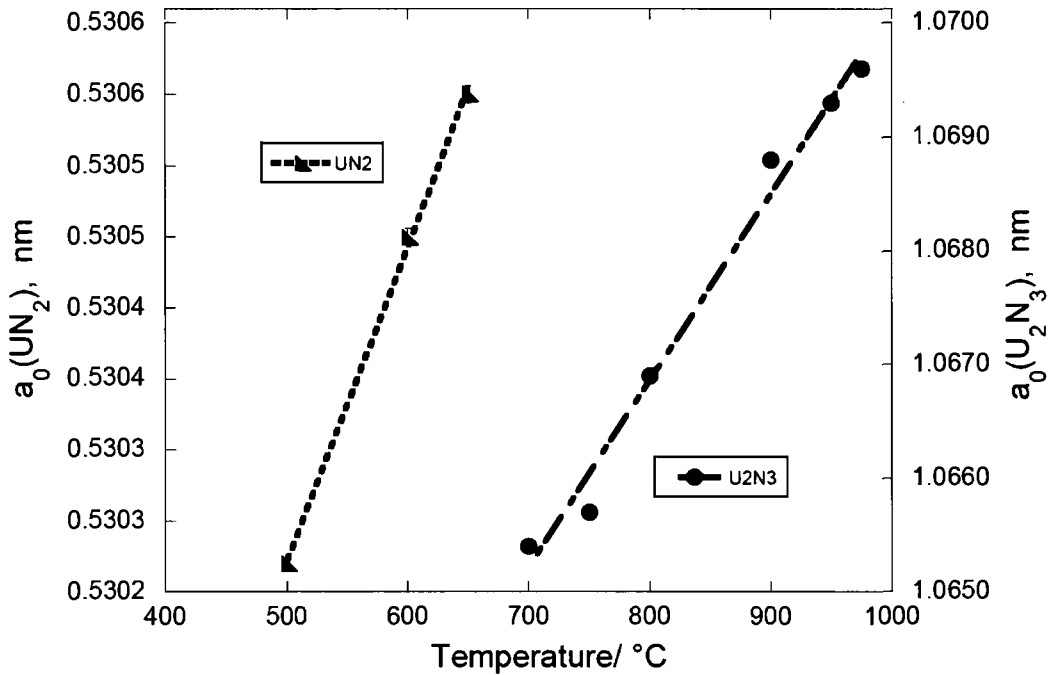


Figure 3.7 Lattice parameters of UN_2 and $\alpha-U_2N_3$ as a function of the temperature used for decomposition.

A number of additional UN samples were synthesized by decomposing UN_x at different temperatures. Secondary chemical phases, including a UO_2 impurity phase (<10 wt %) and the incompletely-decomposed U_2N_3 phase were observed in these samples. The UN samples prepared by decomposition of the UN_2 at 1050 and 1100 °C showed greater phase content than the samples made at 975 and 1000 °C temperatures due to the presence of larger amounts of incompletely decomposed U_2N_3 phase at the lower temperatures. The UO_2 phase impurity was typically less than 5 wt % at 1100 °C (Figure 3.5). A plot of the lattice parameters of these UN samples as a function of temperature is

shown in Figure 3.9, and reveals a distribution of the UN lattice parameter over a considerably wide range even at one particular temperature, as was reported elsewhere [12]. Another experiment showed that heating UN₂ under a N₂-H₂ mixture (8% H₂) for 30 min at 1100 °C, for an effective nitrogen pressure of about 92 kPa, produced U₂N₃ with no trace of UN.

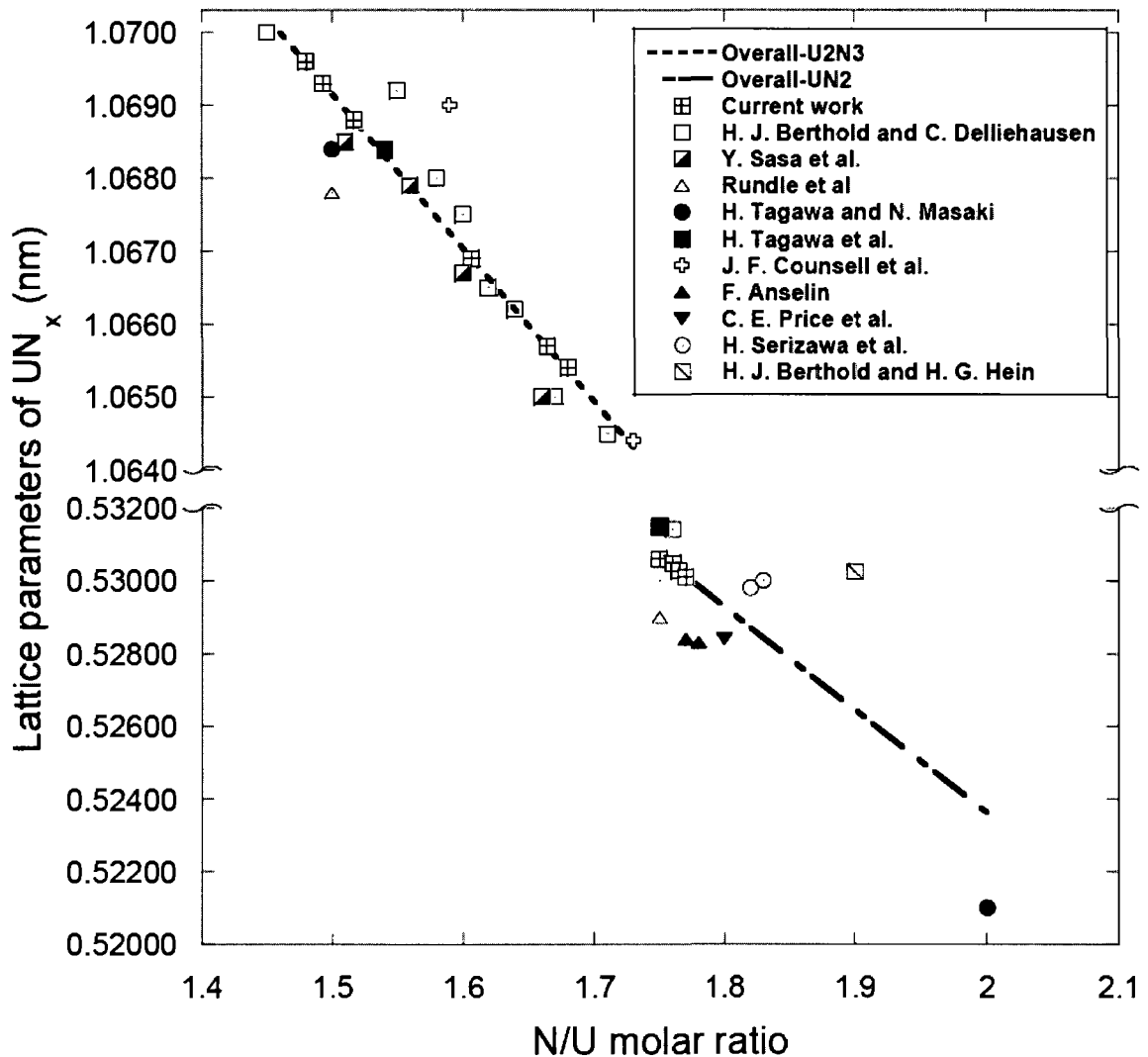


Figure 3.8 Change in the lattice parameter of the UN₂/α-U₂N₃ system with respect to the N/U molar ratio.

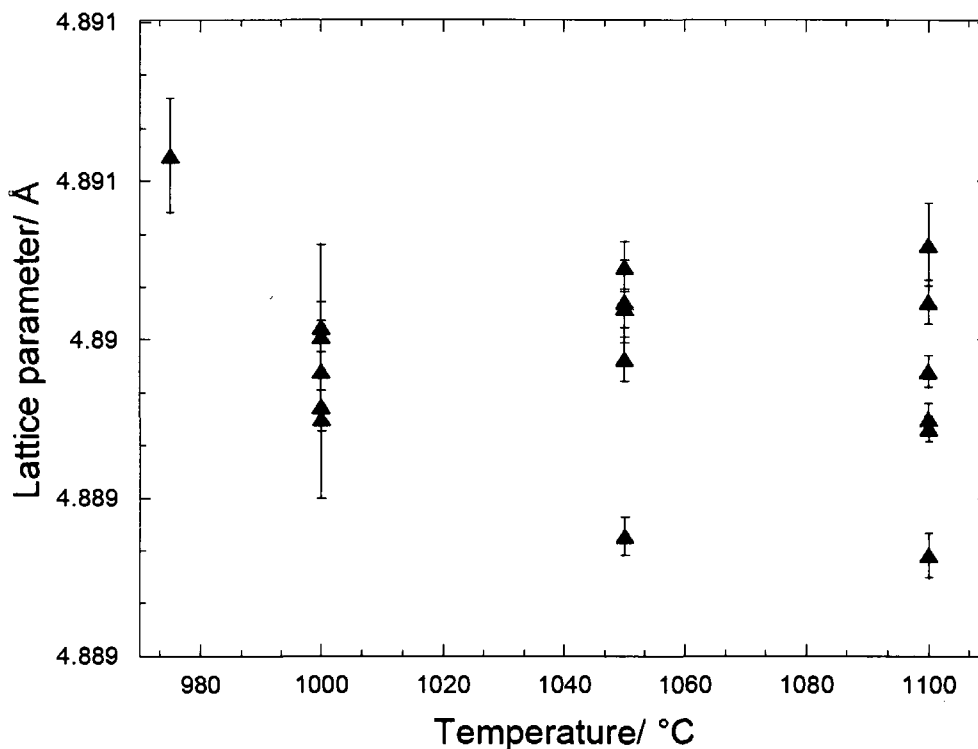


Figure 3.9 Lattice parameter of UN as a function of the temperature used for UN_x decomposition.

3.3.2 Kinetics of UN_2 decomposition

UN_2 decomposition studies revealed that U_2N_3 formed at temperatures between 675 °C and 975 °C. Due to the solid solution behavior of UN_2 and U_2N_3 and overlapping peaks in the XRD, the kinetics of the decomposition of UN_2 to U_2N_3 reaction could not be determined. For the conversion of UN_2/U_2N_3 to UN, the reaction kinetics were evaluated at temperatures of 1000, 1050, and 1100 °C. The kinetic data associated with this unimolecular reaction at 1050 °C is shown in Figure 3.10a, and shows an approximate match between the growth of UN and the decay of U_2N_3 . The slight deviation observed in this comparison is due to the formation of the secondary UO_2 chemical phase. These observations are consistent with an intermediate chemical phase of

U_2N_{3-x} , likely having the uranium-rich boundary composition of $UN_{1.54}$ that reaches a steady-state concentration close to zero. Similar behavior was found for the samples decomposed at 1000 and 1100 °C. Figure 3.10b displays the Arrhenius plot for this decomposition reaction, for which an activation energy of 423.8 ± 0.3 kJ/mol was determined. Table 3.4 summarizes the rate constants determined in the experiment.

Table 3.4 Rate constants of the UN_x decomposition reaction at 1000, 1050, and 1100 °C temperatures.

Temperature/ °C	Rate constant ($s^{-1} \times 10^{-3}$)
1000	0.07 ± 0.01
1050	0.21 ± 0.02
1100	1.3 ± 0.3

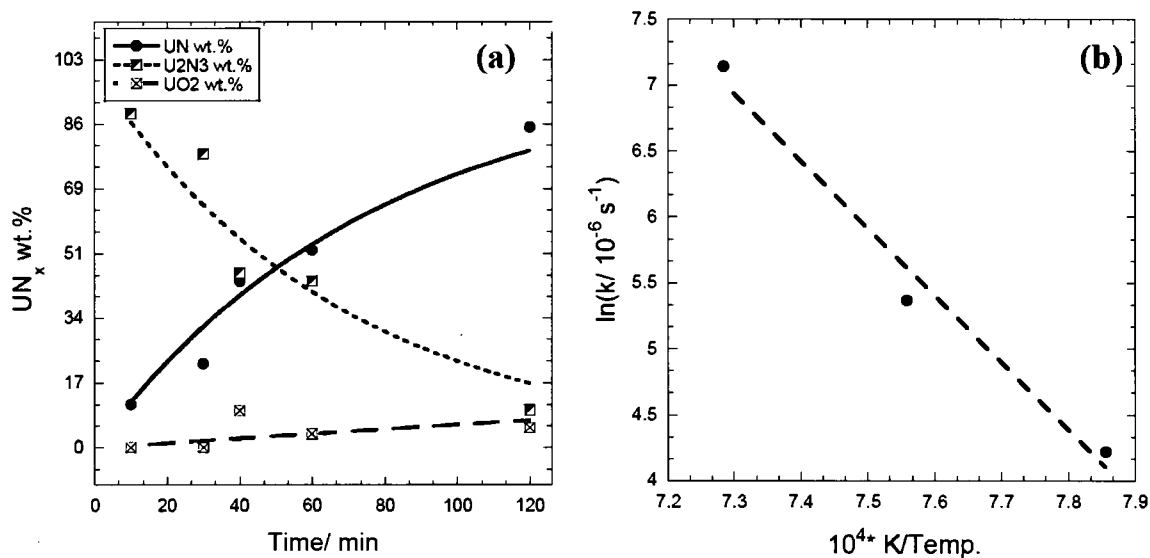


Figure 3.10 Pseudo-first-order kinetics of UN_x decomposition at 1050 °C (a) and the Arrhenius plot for the reaction (b).

3.4 Microscopic Evaluation of UN_x

3.4.1 Microscopy of UN₂

SEM micrographs in Figure 3.11 show significant morphological changes between the reactant (UF₄) and the product (UN₂). SEM micrographs of commercial and synthesized UF₄ have particles of agglomerated grains with less crystallinity without any particle shape. On the other hand UN₂ particles show grains with some discrete flat faces. The observed particle characteristic length distribution ranges from 0.1 to 6 μm, with incompletely-crystallized particle faces making it difficult to measure the particle sizes accurately. However, the morphological comparison indicates a definite chemical phase change in the product compared to the reactant.

HRTEM image of a well-crystallized particle area of the cross-section in the inset of Figure 3.12 (BF) is displayed in Figure 3.12. The fringe details of the image shows that the beam direction corresponds to the image is [111]. Image implies a high crystallinity of the sample at the nanoscale. The sample used in this imaging was prepared by microtome cutting of 50 nm thickness. Figure 3.13 shows the TEM imaging of two other UN₂ particles prepared using solution-drop method. The BF image (inset) in Figure 3.13a displays a set of scattered particles where as the BF image in Figure 3.13b shows a well-packed single particle. Also, the sharp particle edges in the inset of Figure 3.13b imply a higher crystallinity of the particle than the particles in Figure 3.13a. However, the HRTEM imaging of this sharp-edged particle could only be obtained at the thin edge areas due to high thickness of the particle at the middle. HRTEM in Figures 3.13a and 3.13b show some domains with two-directional fringe details, but some amorphous characteristics are also observable in both images. Especially, the amorphous

characteristics found in the sample (Figure 3.13a) other than particle surfaces (Figure 3.13b) suggest incomplete crystallization of some of the UN₂ particles.

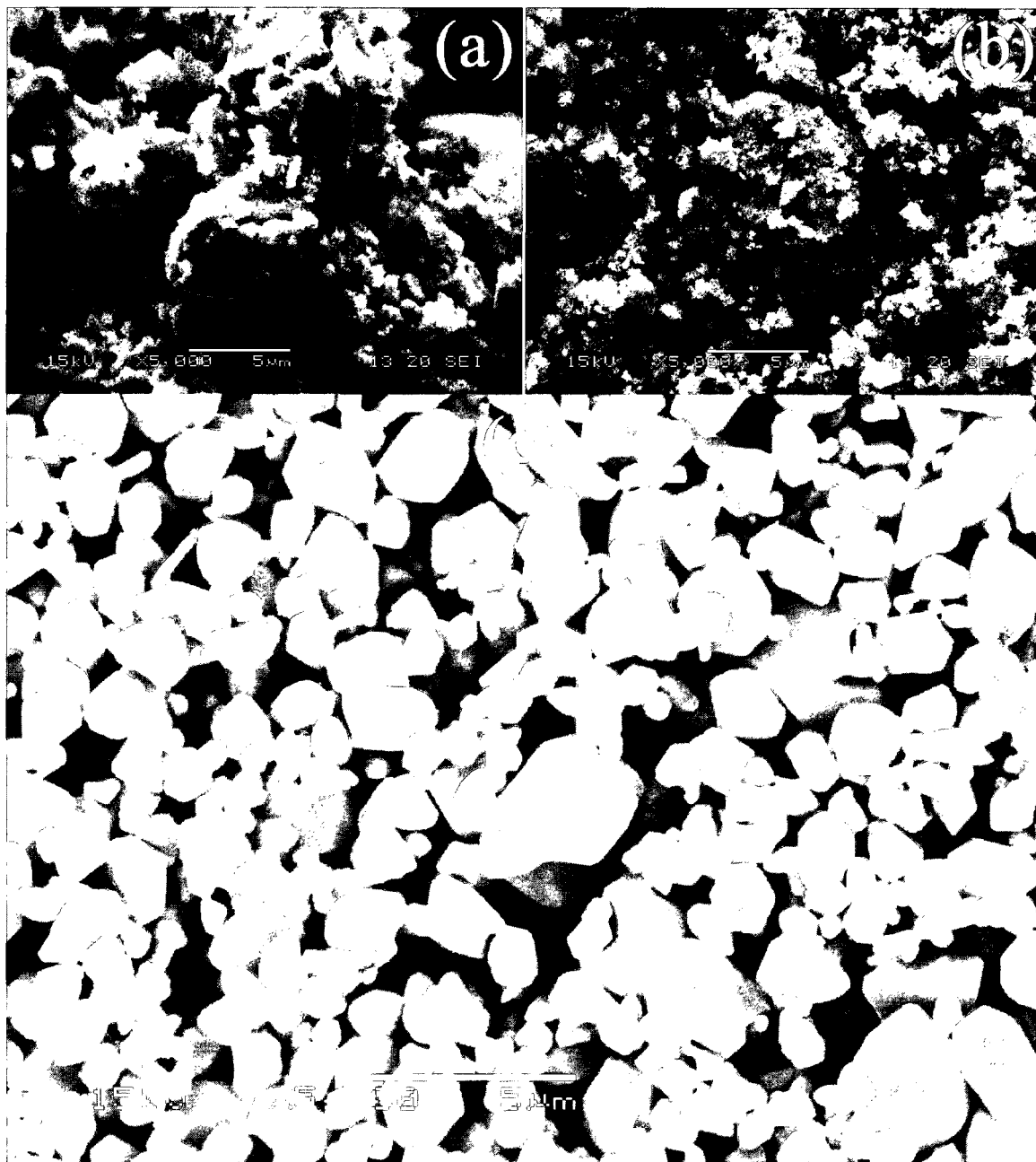


Figure 3.11 SE-SEM micrographs of UF₄ {(a) commercial; (b) as-synthesized} and (c) as-synthesized UN₂.

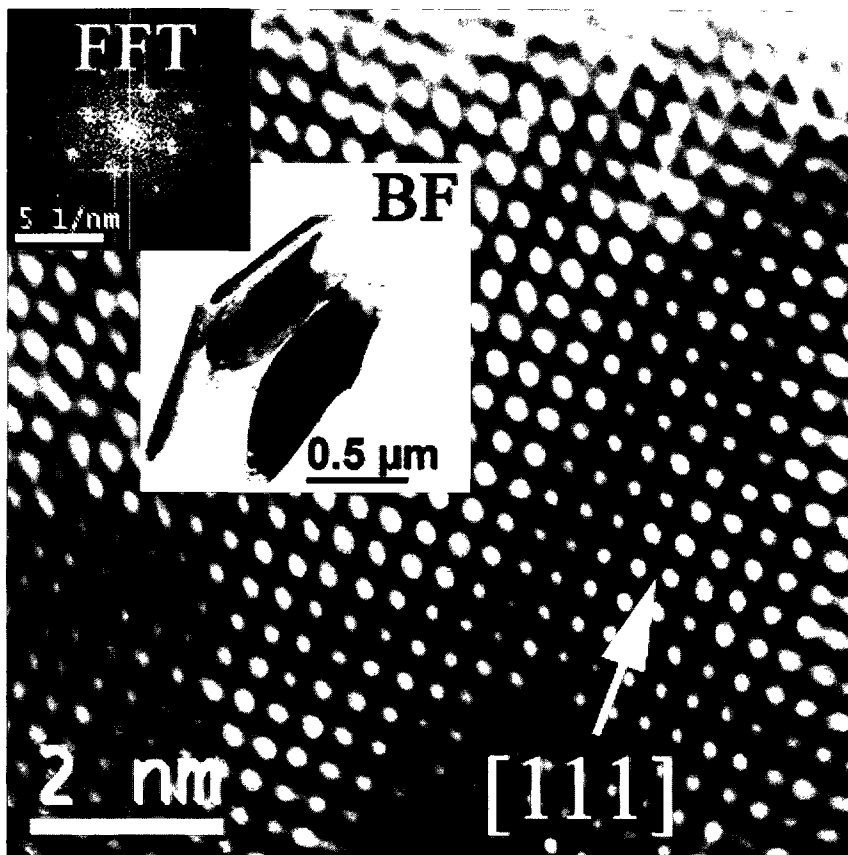


Figure 3.12 HRTEM image of UN₂ in [111] beam direction. Two insets are the FFT of the image and the BF image of the particle used to obtain the HRTEM image.

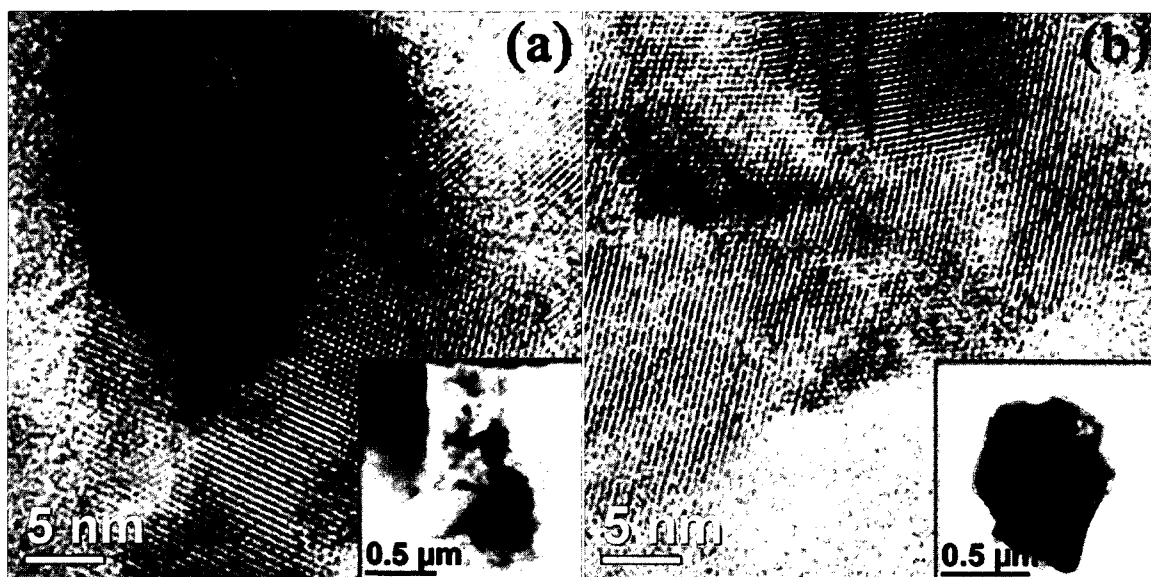


Figure 3.13 HRTEM images of two UN₂ particles (insets) prepared using solution-drop method.

3.4.2 Microscopy of U_2N_3

SE-SEM image and a line scan across the BF image (inset of Figure 3.14b) of U_2N_3 sample are shown in Figure 3.14. The morphology of the sample is similar to that of the UN_2 sample. Particles have irregular shapes with incompletely-crystallized faces (Figure 3.14a). The particle sizes range from 0.1 to 6 μm , also similar to the UN_2 sample. The line scan was obtained to determine how the oxygen distributes throughout the sample. At each position, when the beam hits a sample particle, a prominent peak for U element can be detected. By observing the U peak, therefore, elemental distribution of the UN_2 across the sample with respect N, O, and as well as U can be qualitatively analyzed. The line scan graph in Figure 3.14b shows that N distribution throughout the sample is uniform, but the O distribution is random depending on the particle which is being scanned. This property is prominent in particles at about 8 and 54 μm distances. Also, the O peak intensities are close to that of the background intensities. These observations imply a minor O contamination as well as a random oxidation of the sample particles probably due to environmental oxygen.

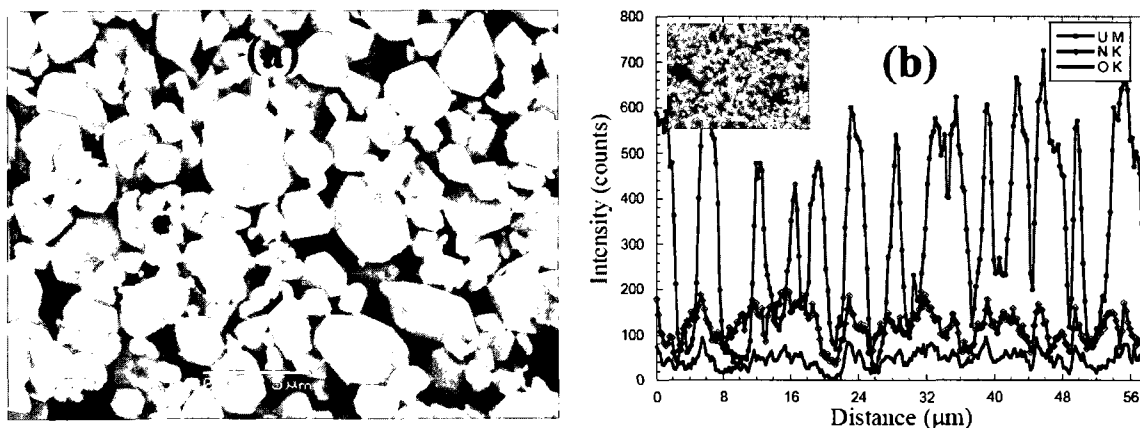


Figure 3.14 SE-SEM micrograph (left) and the line scan across A – B (right) of U_2N_3 .

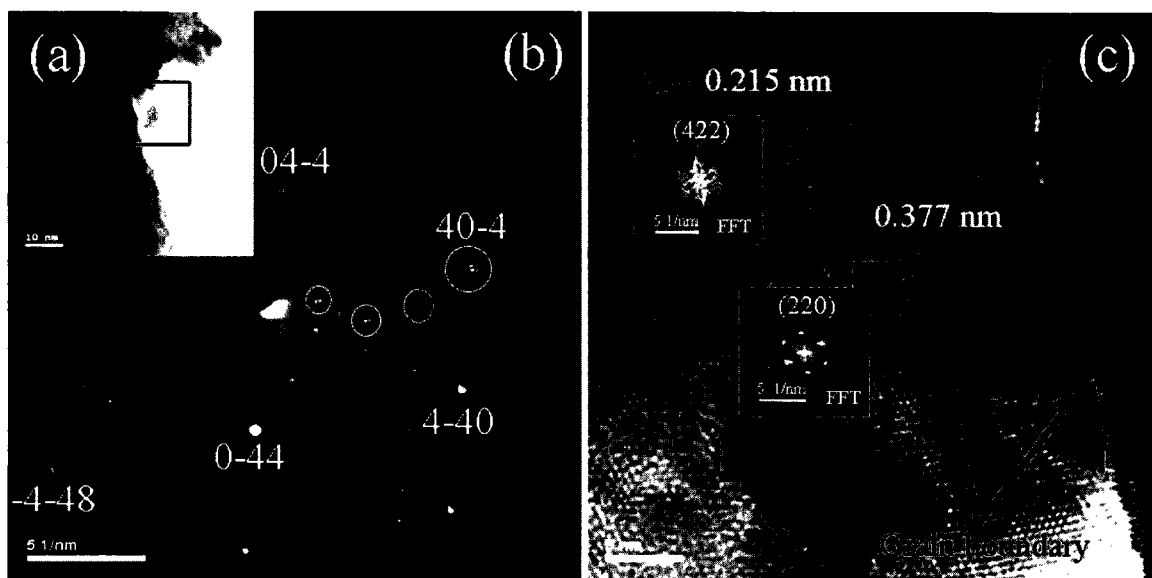


Figure 3.15 TEM images of U_2N_3 : (a) TEM BF image; (b) SAD pattern in $[111]$ zone axis; (c) HRTEM image.

The TEM BF image of a microtome cut U_2N_3 sample is shown in Figure 3.15a. The black spots in this image are due to mass contrast contributed by multiple overlapping U_2N_3 particle layers. Because of these layers, most of the region in the bulk of the TEM BF image is too dense to see a clear picture of U_2N_3 morphology. However, the thickness decreases at the edge of the sample, which allows for quality imaging. No secondary phase-precipitates or defects in U_2N_3 are visible in these thin edge areas. The SAD pattern shown in Figure 3.15b shows the zone axis is along $[111]$. The weak diffraction spots, as well as some stronger spots possibly corresponding to double diffractions (circled in the image), are due to minor secondary phases (UO_2) and grain overlapping. Grain boundaries can also be observed in the HRTEM image (Figure 3.15c), which shows lattice fringes in different orientations correspond to (220) and (422) diffracting planes.

3.4.3 Microscopy of UN

A similar size distribution to that of UN₂ and U₂N₃ samples can be seen for UN samples as well (Figure 3.16a). However, the UN particle faces appear noticeably less sharp. While the higher nitride samples show a majority of the larger particles having discrete-sharp faces, very few of the similarly-sized UN particles have observable flat sharp faces. This observation suggests that either the image is out-of-focus a little or the UN sample is less crystalline than the higher nitride precursor species. SE-SEM image in Figure 3.16b is from a UN sample embedded in a spur resin, and the line scan in Figure 3.16c was obtained by scanning across this image. The O and N distributions throughout the UN sample are more discrete than that of the U₂N₃ in Figure 3.14b. The O distribution though has a similar distribution to that of U₂N₃, especially of the particles at about 38 and 48 μm distances.

The TEM BF micrograph in Figure 3.17a shows several UN particles prepared for imaging by the solution drop method. Magnified TEM BF images focused on two thin edges, B and C, of one UN particle are shown in Figure 3.17b and 3.17c, respectively. The particles shown in this image range from 100 to 150 nm in length, which is in the lower end of the particle size distribution observed in the SEM image. The lack of contrast in the bright field image caused by the high electron scattering factor of UN tends to suppress the detailed structure information, making it difficult to detect the presence of any secondary phases in the BF mode image shown in Figure 3.17a. However, the magnified images of the selected particles in Figure 3.17b and 3.17c show no indication of morphological changes corresponding to a secondary phase. The same

two particles in Figure 3.17b and 3.17c were used to obtain the HRTEM images shown in Figure 3.18 and Figure 3.19, respectively.

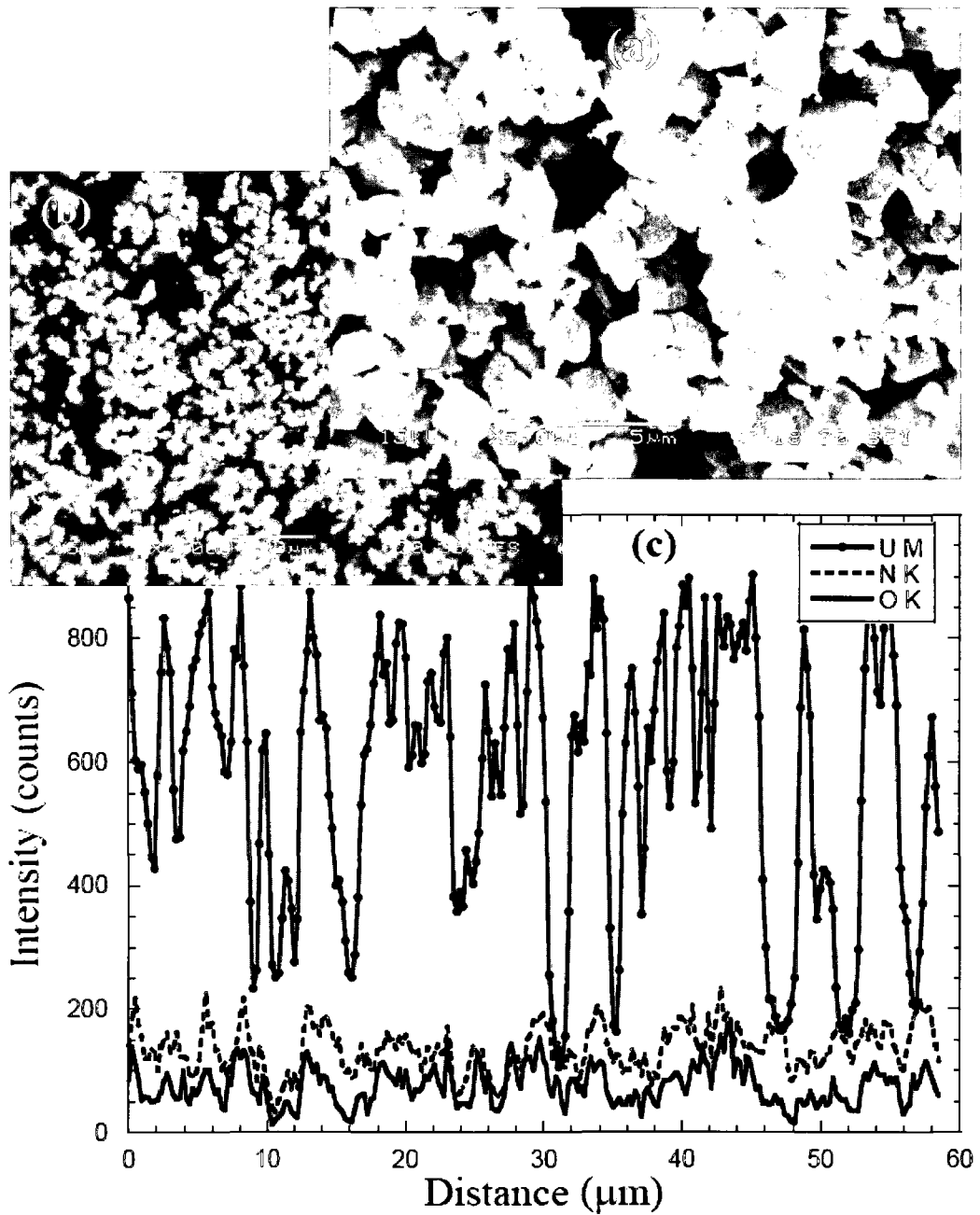


Figure 3.16 (a), (b) SE-SEM images of UN, and the line scan across the image in (b).

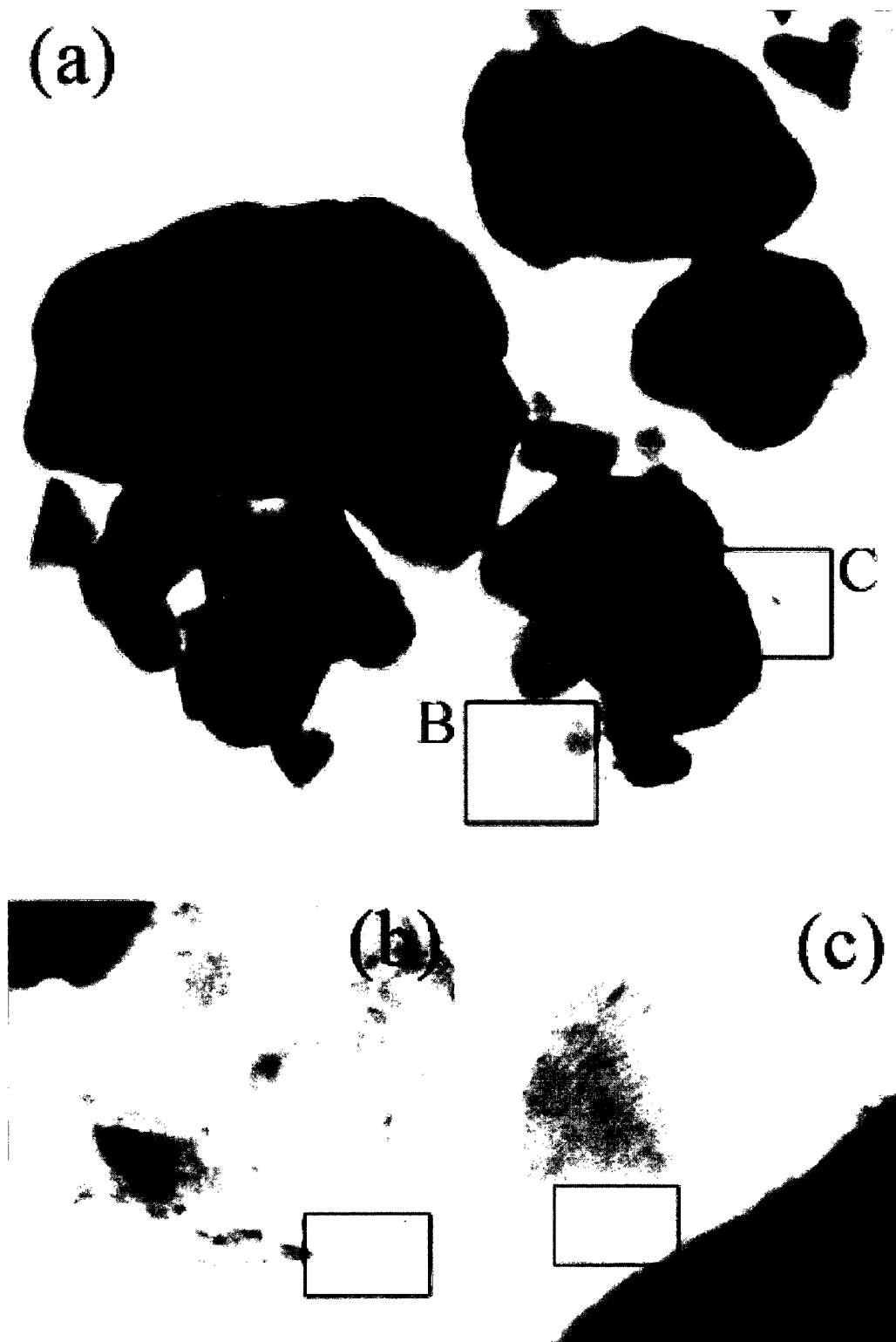


Figure 3.17 (a) TEM BF image of UN particles embedded on a C-Cu grid using solution-drop method. (b) and (c) are the magnified particle images corresponding to areas B and C in Figure (a), respectively. Highlighted areas in Figure (b) and (c) are used in obtaining the HRTEM images in Figure 3.18 and 3.19, respectively.

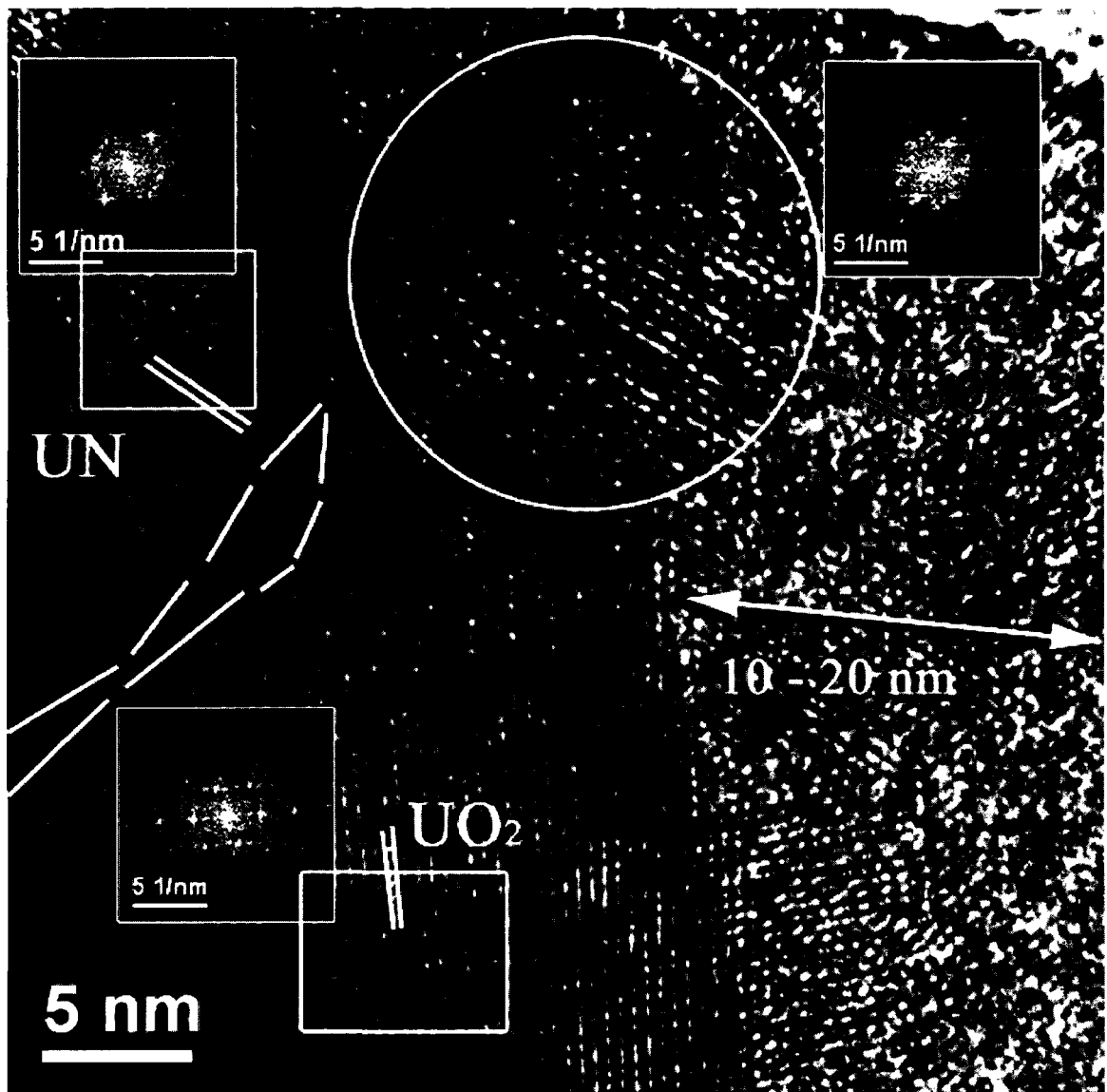


Figure 3.18 HRTEM image of the highlighted area of the particle in Figure 8b.

HRTEM image in Figure 3.18 shows a major grain boundary on another grain beneath it. This grain resides on the main particle from a distance of 10 – 20 nm from the edge of the particle. UO_2 fringe formation could be determined at the surface of this particle. The UO_2 fringes extend up to about 20 nm from the edge of the grain. At this distance a thin layer (indicated by lines in the figure) of amorphous characteristics are

found. The presence of UN fringes can be seen after this amorphous layer. This UN phase is disrupted at the top of the grain at which the particle edge is seen. The fringes are affected by the formation of UO_2 (circled area) making them larger than the fringes found at the area of the UN phase.

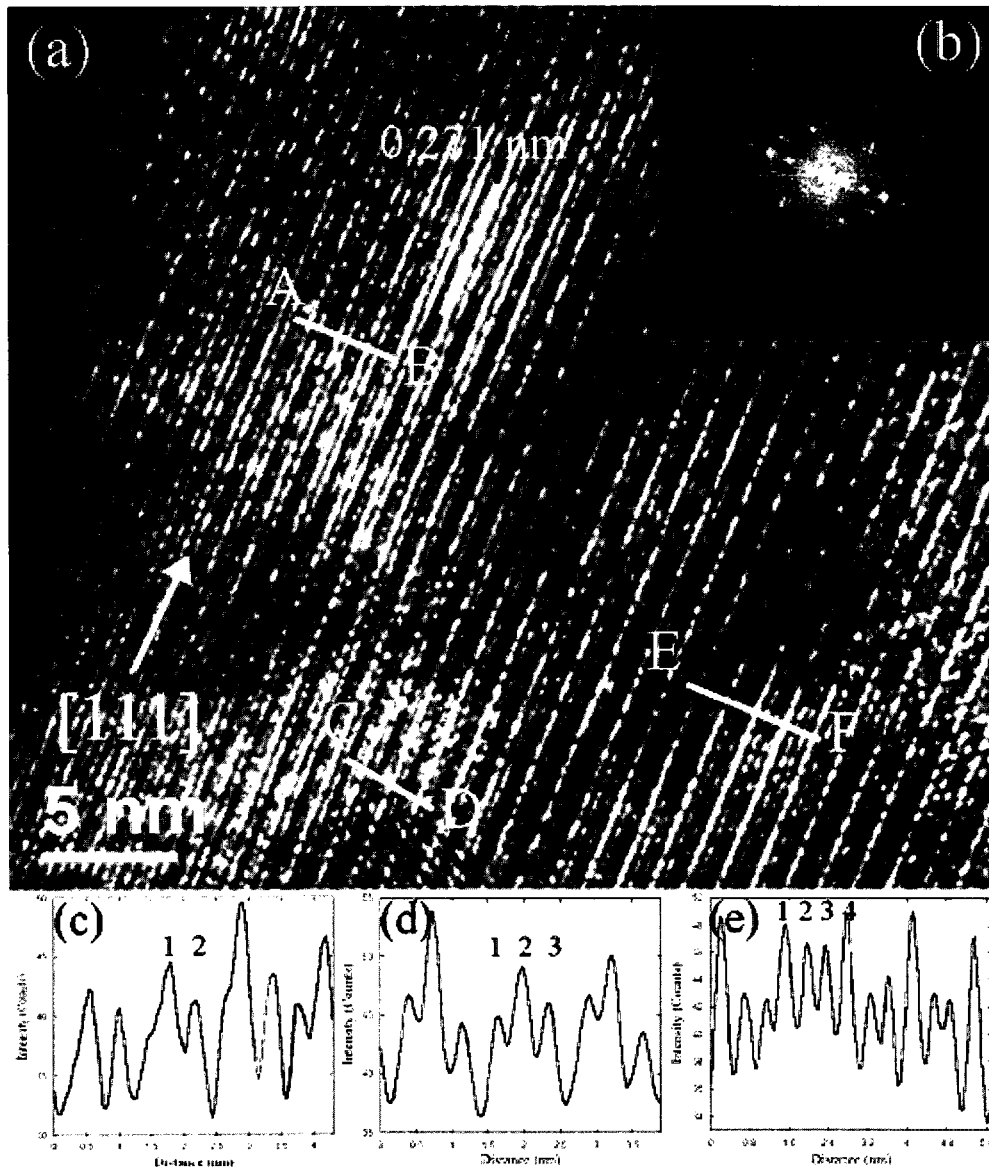


Figure 3.19 (a) HRTEM image of the particle shown in Figure 3.14c in $[111]$ direction and (b) FFT micrograph. Figures (c), (d), and (e) indicate the intensity profiles of three different regions shown in (a) denoted by the lines AB, CD, and EF, respectively.

The HRTEM image shown in Figure 3.19 was obtained by focusing on a thin area of the middle of the particle in Figure 3.17c highlighted with a box. This image shows no indication of the presence of UO_2 as a secondary phase in this area, supporting the hypothesis that the oxide present in the sample is due to environmental oxidation at the particle surface rather than UO_2 inclusions nucleated within the bulk of the UN phase. On the other hand, this figure shows that lattice fringes of UN parallel to the (111) planes are continuously grown farther way from the particle edge. These lattice fringes show a long-range order with different multiplicities of tunnel rows. There are three different tunnel rows; two, three, and four-fold. The experimental intensity profiles shown in Figure 3.19c, 3.19d, and 3.19e were obtained along the lattice fringes normal to line segments AB, CD, and EF, respectively. These profiles confirm the tunnel multiplicities (2, 3, and 4-fold) of the long-range order in the lattice fringes. The FFT micrograph (Figure 3.19b) also indicates the presence of well resolved lattice fringes.

Microtome cut UN sample of 25 nm thick was also used in studying the nanostructure of UN. A cross-sectional TEM BF image of a UN particle is shown in Figure 3.20 together with the HRTEM images of two particle areas as donated in the TEM BF image. In the inset HRTEM image, the well-crystallized UN lattice fringes can be identified along [011] direction. This grain is also surrounded by few more grains in which the lattice fringes of UO_2 are prominent at the surfaces of those grains. One such grain, which is displayed with 0.335 nm fringe spacing, can be seen in the inset HRTEM image. HRTEM image on the background of Figure 3.20 consists of UN lattice fringes at bulk, but the circled particle area is disrupted by the UO_2 formed around most of the grains as described before. These observations further confirm the formation of UO_2 as a

secondary phase due to the oxidation of UN from the environmental oxygen impurity after it was made.

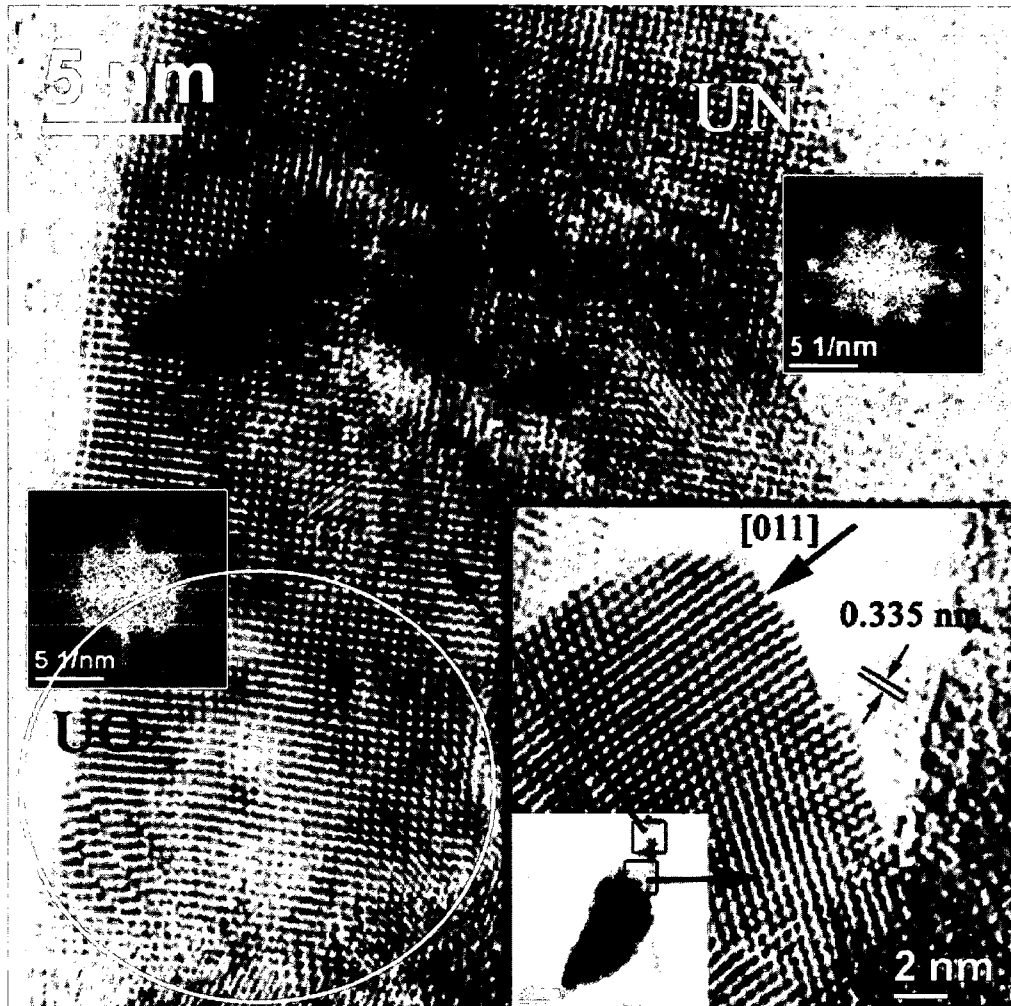
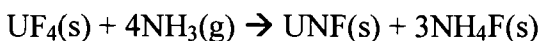


Figure 3.20 HRTEM images of two thin areas of a 25 nm thick UN nano particle (cross-sectional TEM BF image is shown) prepared using the microtome cutting method. In HRTEM image, the area indicated by A shows both sets of reflections due to (200) UN planes. Lattice fringe spacing (0.335 nm) due to UO_2 phase was found at one edge of the particle as indicated.

3.5 Discussion

The terminal product of the ammonolysis of UF_4 was identified to be UN_2 . Further heating of UN_2 under a nitrogen environment did not produce any UN except a chemical

composition (U_2N_3) of lower nitrogen concentration than UN_2 . The results observed on the ammonolysis of UF_4 using different experimental conditions further suggested the following reaction mechanism



Decomposition of UN_2 under inert atmosphere conditions forms U_2N_3 and UN. XRD patterns obtained for UN_2 and U_2N_3 showed high phase purity of the product, with possible contaminations of UN_{2-x} incompletely crystallized impurities plus a minimal secondary UO_2 phase. Although the XRD patterns indicated the presence of impurity phases in minimal quantities, impurity levels were below those observable by either TEM BF or HRTEM imaging. It was also found that some of the peaks in UN_2 XRD pattern can be reduced by heating for longer time periods under NH_3 atmosphere. However, the longer heating time increased the oxide contamination levels, which in turn would affect the phase purity of the final UN sample. Based on the results obtained through this work, the production of high-purity UN does not appear to require reacting the fluoride starting material past the point at which it is fully converted to a uranium nitride, even though the intermediate UN_2 product may be slightly hyper-stoichiometric.

The UN product, however, showed significant phase impurities, with secondary phase levels of UO_2 up to 10 wt %. Depending on the decomposition time and conditions, UN_x phases, due to incomplete decomposition, were also present, up to 80 wt %. Given a time of heating of at least 30 min and up to 240 min, three primary temperature stability

regions for the UN_x were identified. UN_2 is the only phase present at temperatures below 675 °C. In the second temperature region, 675–975 °C, UN_2 quickly decomposes to α - U_2N_3 . Between 975 and 1100 °C, both UN and U_2N_3 were detected depending on the temperature and time of heating, with UN being the stable phase in this temperature region.

Above 675 °C, the lattice parameter in the UN_x system changes rapidly. Stated another way, the reduction of the N/U ratio through decomposition of the UN_x system is kinetically-favorable at elevated temperatures. The effect is large enough that even though UN is thermodynamically favorable at a lower temperature, higher-composition UN_x phases are kinetically stable up to 675 °C. A linear increase of the lattice parameters of both UN_2 and U_2N_3 as a function of reaction temperature was observed. This indicates a continuous removal of nitrogen from the UN_x system, lowering the N/U molar ratio per the correlation reported in Figure 3.7. Heating UN_2 under N_2 -8% H_2 for 30 min, even at 1100 °C, produces only U_2N_3 , with no formation of UN, further supporting the reaction model presented in Equations 1 and 2.

In contrast to the U_2N_3/UN_2 samples, UN showed no variation in lattice parameter as a function of reaction temperature. This is consistent with the knowledge that UN has a very narrow range of compositions at temperatures below 1200 °C [23]. Also, considerable levels of uranium oxide impurity (up to about 10 wt %) had only a small effect on the lattice parameter of the UN phase. Because oxide phases are known to have a very low solubility in UN [24], this consistency in the lattice parameter supports the conclusion that lattice parameter of UN will not vary significantly as a function of oxide impurity levels across a large composition range of the UN/ UO_2 system.

The activation energy for the formation of UN under argon atmosphere starting from UN_x with a composition of UN_{1.80} was determined to be 423.8 ± 0.3 kJ/mol. A theoretical study reported -504.2 kJ/mol as the amount of stabilizing energy for nitrogen atom occupying a lattice site in α -U₂N₃ with a 1.75 N/U molar ratio [25], indicating about 504.2 kJ/mol activation energy requirement to decompose the material into UN according to the equation 2, provided the freeing of nitrogen from the lattice and the creation of a vacancy is the rate-determining step. This result provides reasonable agreement with the activation energy calculated for the decomposition of the higher nitrides to UN (423.8 ± 0.3 kJ/mol) determined in this study.

HRTEM analysis of the UN samples confirmed that the bulk of the particle consist of UN, as suggested from the XRD pattern, with a UO₂ secondary phase forming on the surface of particles observed (Figure 3.18 and 3.20). The large interior region of the UN lattice fringes, corresponding to the (200) plane (Figure 3.20), is uninterrupted by UO₂ inclusions. This supports the conclusion that oxide impurities are likely to be formed by a diffusive process from the synthetic environment, and thus are also likely to form along particle surface. Given the high reactivity of UN in any environment not completely devoid of oxygen, contamination from the experimental apparatus is likely to be the source of these oxide impurities. Subsequent analysis of the UN sample after it had been allowed to age for three months shows the ingrowth of oxide contamination, lending support to this initial hypothesis. The quantitative analysis performed on the XRD patterns of both these samples showed that the UO₂ level increases from 5.0 (1) to 14.8 (1) wt % over this time period [10]. In fact, the determination of oxygen levels in the

samples by line scans also confirmed the presence of UO_2 at minimal quantities in U_2N_3 and UN.

The stoichiometry between uranium and nitrogen in uranium nitrides is known to be a continuous variable from $\text{UN}_{1.75}$ to $\text{UN}_{2.0}$ for UN_2 and $\text{UN}_{1.45}$ to $\text{UN}_{1.75}$ for U_2N_3 [13, 16]. However, for the lower nitrides the stoichiometry range is smaller, $\text{UN}_{0.995}$ - $\text{UN}_{0.999}$, than that of the higher nitrides. The refined lattice parameters of UN_2 and U_2N_3 synthesized samples show a match to the reference values only up to the second decimal point (Table 3.1). The X-ray densities of these two nitrides also vary accordingly. However, the lattice parameter and x-ray density of the synthesized UN matches with the reference value within the confidence intervals reported. Thus the lattice parameter variance in the higher uranium nitrides (UN_2 and U_2N_3) likely indicates the vast range of stoichiometry identified by other authors. The absence of variance in the lattice parameter for the synthesized UN confirms its phase-purity to expectations, given the narrow range of stoichiometry reported for UN.

As-synthesized uranium mononitride particles appeared to fall within a particle size distribution of 0.1-6 μm . Furthermore, the particle sizes estimated by SEM were verified by TEM. This particle size range is consistent with the previously reported microscopic data [26], and it is similar to the particle size distribution observed for the UN_2 and U_2N_3 precursor phases. The surface area measurements of the nitride species also show no significant change as the UN_2 is converted to the U_2N_3 and UN products, suggesting that the conversion of the higher nitrides to the mononitride does not significantly impact particle size or morphology.

3.6 Conclusions

Uranium nitrides synthesized using the oxidative ammonolysis of UF_4 were successfully characterized by means of XRD and electron microscopy. Formation of UN was identified to be occurring through first forming UNF. Further ammonolysis produced UN_2 as found before. UN_2 decomposes into UN via U_2N_3 . The UN samples could be synthesized from UN_2 up to a 97 (1) weight percent phase purity. The decomposition of UN_2 samples progressed slowly below 675 °C, but showed a rapid rate increase above that temperature. An intermediate U_2N_3 phase was seen at temperatures greater than or equal to 675 °C under inert atmosphere with a negligible nitrogen pressure. UN was formed at 975 °C and above. A continuous removal of nitrogen was observed in the UN_2 decomposition process to U_2N_3 and to UN with continues crystal structure changes from fcc to bcc and from bcc to fcc. The complete decomposition of about 50 mg of UN_x sample to pure UN could be completed in less than 30 minutes at 1100 °C. The lattice parameter of UN did not vary significantly with changing reaction temperature or purity of the bulk sample. The activation energy for the formation of UN via U_2N_3 decomposition under inert atmospheric conditions was determined to be 423.8 ± 0.3 kJ/mol.

The TEM observations of this UN sample showed that UN has long-range order in its microstructure. Furthermore, the HRTEM images of microparticle surface and cross-section made by solution-drop and microtome-cutting methods respectively showed the secondary oxide phase formed primarily on the UN particle surface. Given the absence of an oxide phase in the UN_2 and U_2N_3 samples in large quantities, the oxide contamination appears to form during the final stage of the process, most likely due to oxygen

contamination in the experimental system used for this synthesis. Observed increases in uranium oxide levels in UN after long term exposure to air support the conclusion. Better oxygen control during the final decomposition reaction, such as replacement of the quartz furnace tube and the addition of oxygen getters for the cover gas, may be sufficient to reduce the oxide levels within the UN product, as well as storage of the UN samples under inert atmosphere.

References

- (1) Reitveld, H. M. *J. Appl. Cryst.* **1969**, 2, 65.
- (2) Morss L. R.; Edelstein N. M.; Fuger J.; Katz JJ (Eds.) *The Chemistry of the Actinides and Transactinide Elements*; 3 ed.; Chapman & Hall: New York, 2006; Vol. 1.
- (3) Rundle, R.E.; Baenziger, N.C.; Wilson, A.S.; McDonald, R.A. *J. Am. Chem. Soc.* **1948**, 70, 99.
- (4) Mueller, M.H.; Knott, H.W. *Acta Cryst.* **1958**, 11, 751.
- (5) Kuznietz, M. *Phys. Rev.* **1969**, 180, 476.
- (6) Le, T.N.; Lorenzelli, N.; Zuppiroli, L. *J. Nucl. Mater.* **1991**, 184, 230.
- (7) Sole, M.J.; Van der Walt, C.M. *Acta Metall.* **1968**, 16, 501.
- (8) Black, L.; Miserque, F.; Gouder, T.; Havela, L.; Rebizant, J.; Wastin, F. *J. Alloy Compd.* **2001**, 315, 36.
- (9) Minato, K.; Akabori, M.; Takano, M.; Arai, Y.; Nakajima, K.; Itoh, A.; Ogawa, T. *J. Nucl. Mater.* **2003**, 320, 18.
- (10) Silva, G. W. C.; Yeaman, C. B.; Ma, L.; Cerefice, G. S.; Czerwinski, K. R.; Sattelberger, A. P. *Chem. Mater.* **2008**, 20, 3076.

- (11) Silva, G. W. C.; Ma, L.; Hemmers, O.; Lindle, D. *Micron* **2008**, *39*, 269.
- (12) Tagawa, H.; Masaki, N. *J. Inorg. Chem.* **1974**, *36*, 1099.
- (13) Cordfunke, E.H.P. *J. Nucl. Mater.* **1975**, *56*, 319.
- (14) Jenkins, R.; Synder, R. L. *Introduction to X-ray powder Diffractometry*, John Wiley & Sons, Inc: Vol. 138, 1996.
- (15) Tagawa, H. *J. Nucl. Mater.* **1974**, *51*, 78.
- (16) Serizawa, H.; Fukuda, K.; Ishii, Y.; Morii, Y.; Katsura, M. *J. Nucl. Mater.* **1994**, *208*, 128.
- (17) Berthold, H. J.; Dellihaüsen, C. *Angew. Chem. Internat.* **1966**, *5*, 726.
- (18) Sasa, Y.; Atoda, T. *J. Amer. Chem. Soc.* **1970**, *53*, 102.
- (19) Counsell, J. F.; Dell, R. M.; Martin, J. F. *Trans. Faraday Soc.* **1966**, *62*, 1736.
- (20) Anselin, F. *J. Nucl. Mater.* **1963**, *10*, 301.
- (21) Price, C. E.; Warren, I. H. *Inorg. Chem.* **1965**, *4*, 115.
- (22) Berthold, H. J.; Hein, H. G. *Angew. Chem. Internat. Edit.* **1969**, *8*, 891.
- (23) Hoenig, C. L. *J. Am. Chem. Soc.* **1971**, *54*, 391.
- (24) Benz, R.; Balog, G.; Baca, B. H. *High Temp. Sci.* **1970**, *2*, 221.
- (25) Fujino, T.; Tagawa, H.; *J. Phys. Chem. Solids* **1973**, *34*, 1611.
- (26) Le, T.N.; Lorenzelli, N.; Zuppiroli, L. *J. Nucl. Mater.* **1991**, *184*, 230.

CHAPTER 4

EVALUATION OF THORIUM SYSTEM

4.1 Introduction

Compared to the UN_x system, only a few thorium nitrides have been reported and studied. Among them, Th_3N_4 is the most common nitride of thorium [1, 2]. Th_3N_4 has been synthesized using a number of routes: heating thorium metal [3], heating thorium hydride [4, 5] under ammonia or nitrogen, or reacting $ThCl_4$ with $LiNH_2$ in liquid ammonia and then heating under nitrogen gas [6]. Two other common thorium nitrides that have been reported are Th_2N_3 [4, 7] and ThN [3, 4]. Synthesis of thorium mononitride (ThN) is achieved by thermally decomposing higher thorium nitrides such as Th_2N_3 [3, 4] and Th_3N_4 [1, 5, 7, 8]. The phase purity of ThN depends on a number of factors such as heating atmosphere, temperature, and time [5, 8]. If the temperature is not high enough decomposition of Th_3N_4 will not be completed, resulting in ThN with secondary chemical phases. At high temperatures, at which Th_3N_4 can be completely decomposed, other secondary chemical phases like ThO_2 and Th_2N_2O form in addition to ThN . Formation of these secondary phases, especially ThO_2 , has also been found in synthetic routes of higher thorium nitrides (Th_xN_y) [3]. Formation of a ThO_2 contaminated phase in Th_3N_4 at room temperature is also reported [5]. The presence of ThO_2 could also lead part of the ThN to convert into Th_2N_2O , reducing the phase-purity of ThN even under inert atmospheric conditions [5]. Some of these issues have been

investigated in kinematical and as well as thermodynamic aspects [5, 8]. However, only very few microscopic studies have been conducted and reported to explain the phase-purity issues found in all these thorium nitrides.

Chiotti et al reported the formation of Th_2N_3 when the thorium metal is heated up to 750 °C under NH_3 . Synthesis of the same compound was also reported in 1965 by thermally decomposing thorium hydride at temperatures below 1500 °C under nitrogen or ammonia [4]. Identification of Th_2N_3 in the late nineties was controversial due to its crystallographic structure resemblance to $\text{Th}_2\text{N}_2\text{O}$ compound. R. Benz et al., [9] reported Th_2N_3 to be equivalent to $\text{Th}_2\text{N}_2\text{O}$ which was synthesized by reacting ThN with ThO_2 at 1700 °C under nitrogen atmosphere. Another study reports Th_2N_3 to be unstable at temperatures higher than 1500 °C under nitrogen or ammonia atmospheres [4]. Therefore, these Th_2N_3 and $\text{Th}_2\text{N}_2\text{O}$ can be considered as two separate compounds. Although there are few publications related to the chemistry of these two compounds to the best of our knowledge, microscopy has never been used to confirm the chemical structure determined by crystallography or to investigate the secondary phase contamination problems found in these thorium nitrides.

In this chapter, evaluation of the low-temperature fluoride route in producing ThN_x is presented. It was found that the desired ThN_x was not produced from the initial ammonium-thorium-fluoride starting material. However, the reactions and intermediate species in the formation of ThNF from ThO_2 using the described experimental conditions are provided. A complete study on the thermal behavior of ThNF up to 1400 °C under different environmental conditions is also presented. In addition, a possible reaction mechanism for the formation of ThNF from ThF_4 under ammonia gas is proposed.

Microscopy is used to characterize the morphological and nanostructural changes occurring during the complete reaction. Structural details are used in explaining the kinetics of different reactions and their final product formations.

Furthermore, a new method is presented to synthesize Th_2N_3 under NH_3 with a secondary oxide phase using a simple experimental setup after making some changes to the fluoride route. Identification of Th_2N_3 naturally leads questioning the oxidation state of Th in the compound. Because the electronic configuration of Th is $[\text{Rn}] 6d^2 7s^2$, it has a stable tetravalent state. In the Th_2N_3 compound, with a nominal oxidation state of 4.5+, implies a mixture of tetravalent and pentavalent oxidation states. The reliance on the identification of the compound as Th_2N_3 is based on existing literature. The microscopic studies of this material synthesized here showed no oxygen in the nitrogen rich areas of the sample particles that could lead to the formation of $\text{Th}_2\text{N}_2\text{O}$, where tetravalent Th would be expected. Further details on this system are discussed in the results section (4.6), in discussion (4.7), and also be discussed in Chapter 7 as future work. Reactions of different thorium fluorides with lithium amide (LiNH_2) under NH_3 were studied, and the sample synthesized with the lowest impurity was used for the characterization. Electron microscopy was used to study the morphology and microstructure of Th_2N_3 . These microscopic observations were included in this study to discuss how the morphological and nanostructural characteristics of Th_2N_3 induce the formation of a ThO_2 impurity phase which is common in all the nitride systems of thorium. The general goal of this chapter is thus to shed light on the chemistry of thorium nitride systems by means of characterization of the underlying crystal structure and nanostructure.

4.2 Experimental Details and Characterization Methods

4.2.1 Synthesis of Ammonium Thorium Fluoride

A solid state reaction was utilized in synthesizing ammonium thorium fluorides. Two batches of ThO₂ of weights 100 mg and 1000 mg were used in these experiments. The ThO₂ (STREM Chemicals, 99.99 %) powder was added into a polyethylene vial with ground NH₄HF₂ (Fisher Scientific, 99.99 %) in a 1:4 molar ratio with 10 mol. % excess NH₄HF₂. The sample was then mixed with a spatula for about 10 min. The reaction was allowed to progress in the closed vial at room temperature until completion. Reaction progress was evaluated time to time by removing a small amount from the mixture for X-ray diffraction.

4.2.2 Ammonolysis of (NH₄)₄ThF₈ and Heating of ThNF.

The resulting (NH₄)₄ThF₈ product was added onto a sheet of platinum and the platinum sheet with the sample was inserted into a 25 mm diameter quartz-glass tube. The tube was closed on either end with a 25 mm quartz Solv-Seal (Andrews Glass Co., Inc.), and sealed using Pyrex Solv-Seal caps fitted with 15 mm high vacuum Teflon stopcocks. Ammonia gas (high-purity 99.999%, Praxair) was flushed through the tube for 5 minutes to cover the inside of the tube with NH₃ gas. Then the system was heated to 800 °C under a constant flow of ammonia gas at 1 atm. The gas flow was constant throughout the experiment and was used as a cover gas. Total heating time was varied up to a maximum of 5 hours and then cooled to room temperature. Once the samples cooled, the ammonia gas flow was terminated and the product was removed for analysis. The reaction was also performed at 1000 °C for 45 minutes and at 1100 °C for 15 minutes. All other heating of the products were done under high-purity (99.999%) Ar, Ar/H₂ (5%),

N₂, and N₂/H₂ (5%). Zr-sponge was also used as a getter in some experiments where elevated temperatures such as 1100 °C were used.

4.2.3 Synthesis and heat-treatment of Th₂N₃

Reactions involving three thorium fluorides were tested in synthesizing Th₂N₃. These fluorides were (NH₄)₄ThF₈, ThF₄, and ThNF, which can be synthesized at low-temperatures as described in above sections. Each of these thorium compounds of 25–50 mg batches were mixed with LiNH₂ (95%, Alfa Aesar) at 1:1 or 1:4 molar ratio. The mixed sample was added on to an open platinum foil and placed inside a quartz tube. The mixture was then heated at 800 °C for 30 min under a flowing NH₃ gas. Studies of the thermal behavior of the as-synthesized Th₂N₃ samples were performed under inert atmosphere (high-purity argon). These thermal studies were done at four different temperatures (800, 900, 1000, and 1100 °C) for 30 min each. Th₂N₃ was initially identified with X-ray powder diffraction and its refinement was performed by using the ICSD pattern number 76467.

4.2.4 Characterization Methods

X-ray powder diffraction was used to identify phase distributions of the synthesized samples using Cu-K_α radiation. Morphological studies of the samples were done using SEM and TEM. Energy dispersive spectrometry (EDS) was used to determine the elemental distributions. The conventional bright field (BF) diffraction contrast mode and the high resolution (HR) TEM modes coupled with selected area electron diffraction (SAD) patterns were utilized to characterize the samples.

4.3 Synthesis and Characterization of $(\text{NH}_4)_4\text{ThF}_8$

The XRD patterns of the samples showed that the terminal product of the reaction of NH_4HF_2 with ThO_2 is $(\text{NH}_4)_4\text{ThF}_8$ with a triclinic unit cell and $P\bar{1}$ space group. Further analysis confirmed the formation of an intermediate $(\text{NH}_4)_3\text{ThF}_7$ chemical phase of an orthorhombic unit cell and $Pnma$ space group in the reaction. Figure 4.1 is a graphical view of the kinetics of ThO_2 (100 mg batch) solid state reaction with NH_4HF_2 at room temperature. After one day of mixing the two reactants, a new chemical phase was formed according to the XRD pattern in Figure 4.1. This XRD pattern has some similarities to the pattern of the terminal $(\text{NH}_4)_4\text{ThF}_8$ chemical phase even though refinement assuming similar crystallography was not successful. The intermediate chemical phase which was identified as $(\text{NH}_4)_3\text{ThF}_7$ was formed after two days. The XRD pattern of the sample after 5 days displays some of the peaks correspond to $(\text{NH}_4)_3\text{ThF}_7$ as indicated by arrows. These peaks start to diminish with the formation of new set of peaks at 2θ values of 12.6, 15.1, and 15.5°. The XRD pattern formed with these peaks was prominent and was believed to be another intermediate phase that was not identifiable as the known ammonium fluorides of thorium or any other actinides such as uranium and neptunium. This new and unknown chemical phase remained until it completely changed into the terminal $(\text{NH}_4)_4\text{ThF}_8$ chemical phase after 22 days at room temperature.

Wani et al [10] describes the reaction of solid ThO_2 with solid NH_4HF_2 at room temperature to be quick (two hours) in forming $(\text{NH}_4)_4\text{ThF}_8$. However, they reported an absence of the reflection at $d = 0.815$ nm in the XRD pattern of this product. Furthermore, they did not identify or matched their XRD pattern to $(\text{NH}_4)_3\text{ThF}_7$ which has some

similar reflections to that of $(\text{NH}_4)_4\text{ThF}_8$ with the absence of the peak at $d = 0.815$ nm (Figure 4.2). Further comparison on this work cannot be done because the experimental parameters such as reactant weights or XRD patterns of the products are not reported in their article.

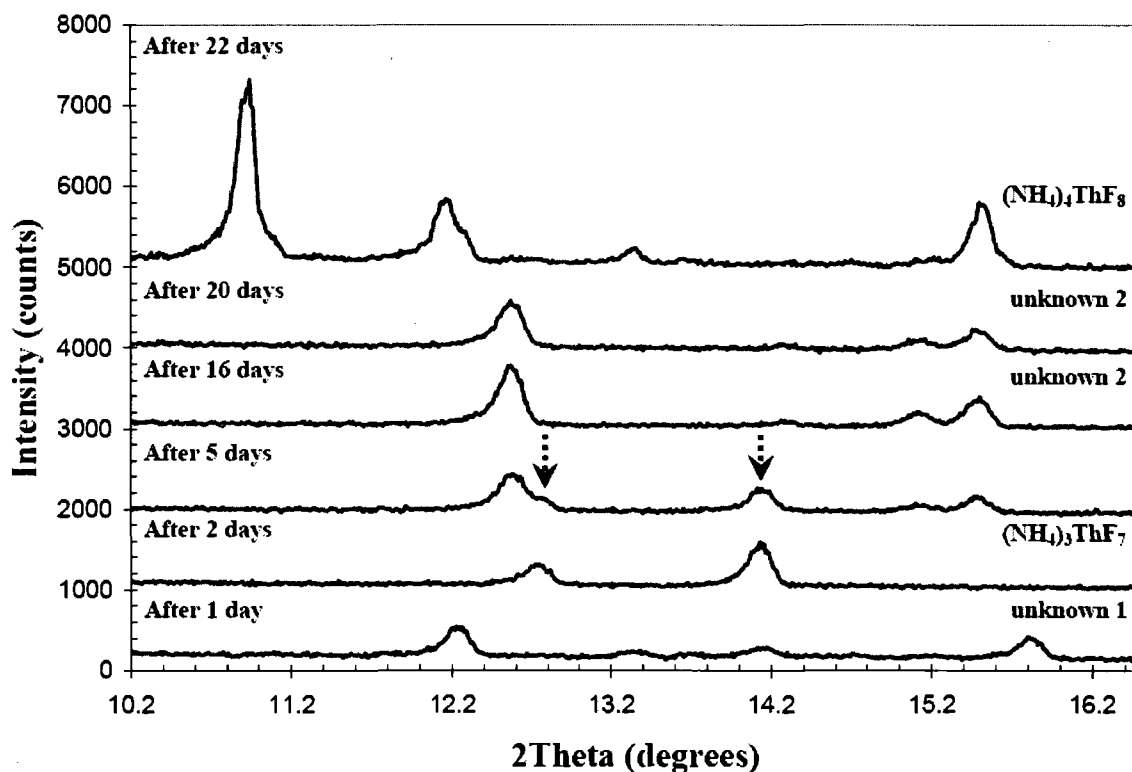


Figure 4.1 XRD patterns indicating the reaction progress of ThO_2 mixed with excess NH_4HF_2 . Only a part of the XRD patterns are shown for clarity of the comparison.

The observed and the calculated patterns of $(\text{NH}_4)_4\text{ThF}_8$ and a sample containing $(\text{NH}_4)_3\text{ThF}_7$ phase are shown in Figure 4.2a and 4.2b, respectively. The patterns of both $(\text{NH}_4)_4\text{ThF}_8$ and $(\text{NH}_4)_3\text{ThF}_7$ matched well with the reference patterns in the ICSD of numbers 9889 and 14128, respectively. Few impurity peaks in both samples were identified especially at about 0.68 nm d-spacing value in $(\text{NH}_4)_4\text{ThF}_8$ sample. These

impurity peaks together with the amorphous characteristics of the samples can be accounted for the excess $\text{NH}_4\text{F}/\text{NH}_4\text{HF}_2$ salts. The refined triclinic unit cell parameters of $(\text{NH}_4)_4\text{ThF}_8$ compound after applying Rietveld method are $a = 8.5041(7)$, $b = 8.3667(7)$, and $c = 7.3372(6)$ Å. Lattice parameters of orthorhombic $(\text{NH}_4)_3\text{ThF}_7$ with a space group of *Pnma* were refined to be $a = 0.3952(9)$, $b = 0.7932(5)$, and $c = 0.70462(5)$ nm.

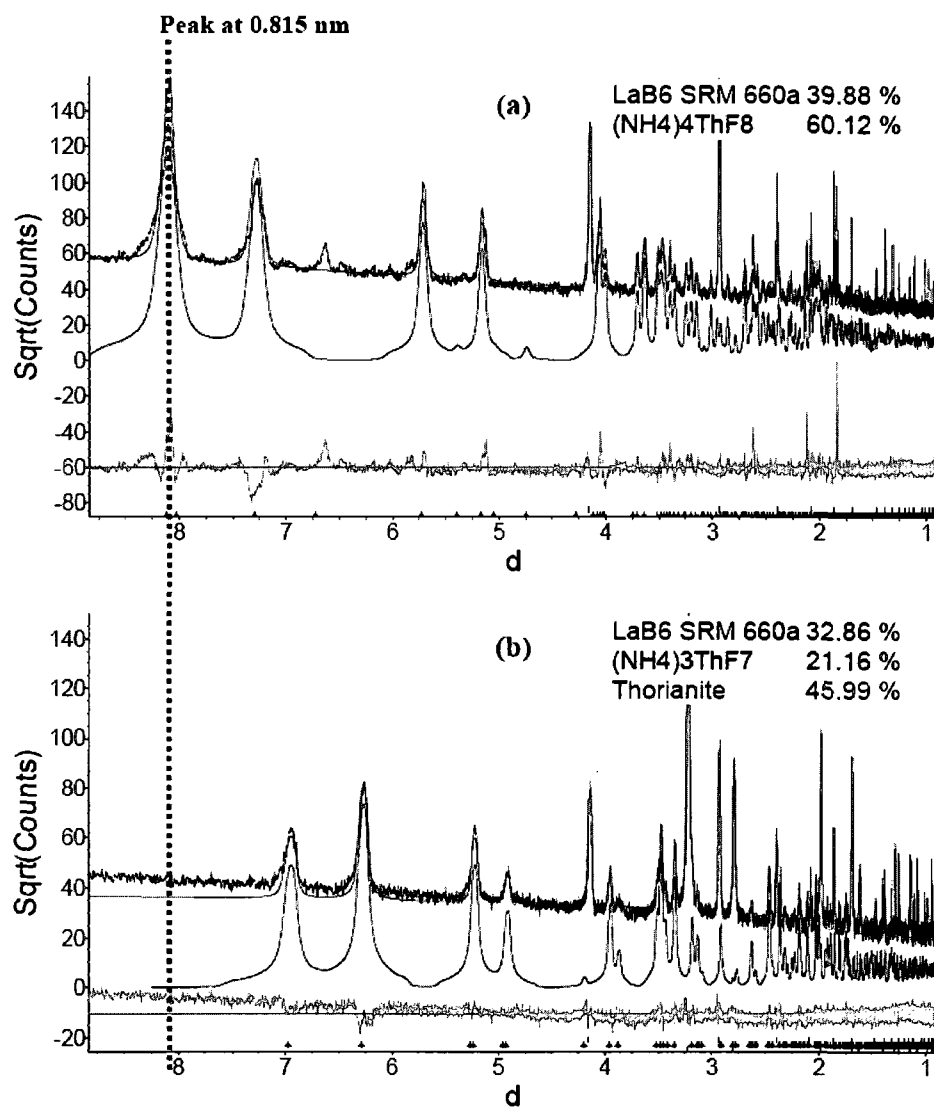


Figure 4.2 XRD powder refinements of (a) $(\text{NH}_4)_4\text{ThF}_8$ and (b) $(\text{NH}_4)_3\text{ThF}_7$ samples. Calculated patterns of both $(\text{NH}_4)_4\text{ThF}_8$ and $(\text{NH}_4)_4\text{ThF}_8$ are highlighted in the corresponding figure. X-axes are in 10^{-1} nm units.

The secondary electron SEM image of the $(\text{NH}_4)_4\text{ThF}_8$ sample (Figure 4.3a) indicates well-crystallized sample particles with an acicular shape (Figure 4.3a) compared to the plate-like shape of the reactant, ThO_2 , (Figure 4.3c). Furthermore, the acicular crystals that Penneman et al [11] described can also be clearly seen in this figure. The elemental distribution of the $(\text{NH}_4)_4\text{ThF}_8$ sample obtained using the EDS (Figure 4.3b) also shows the presence of the expected components in the sample.

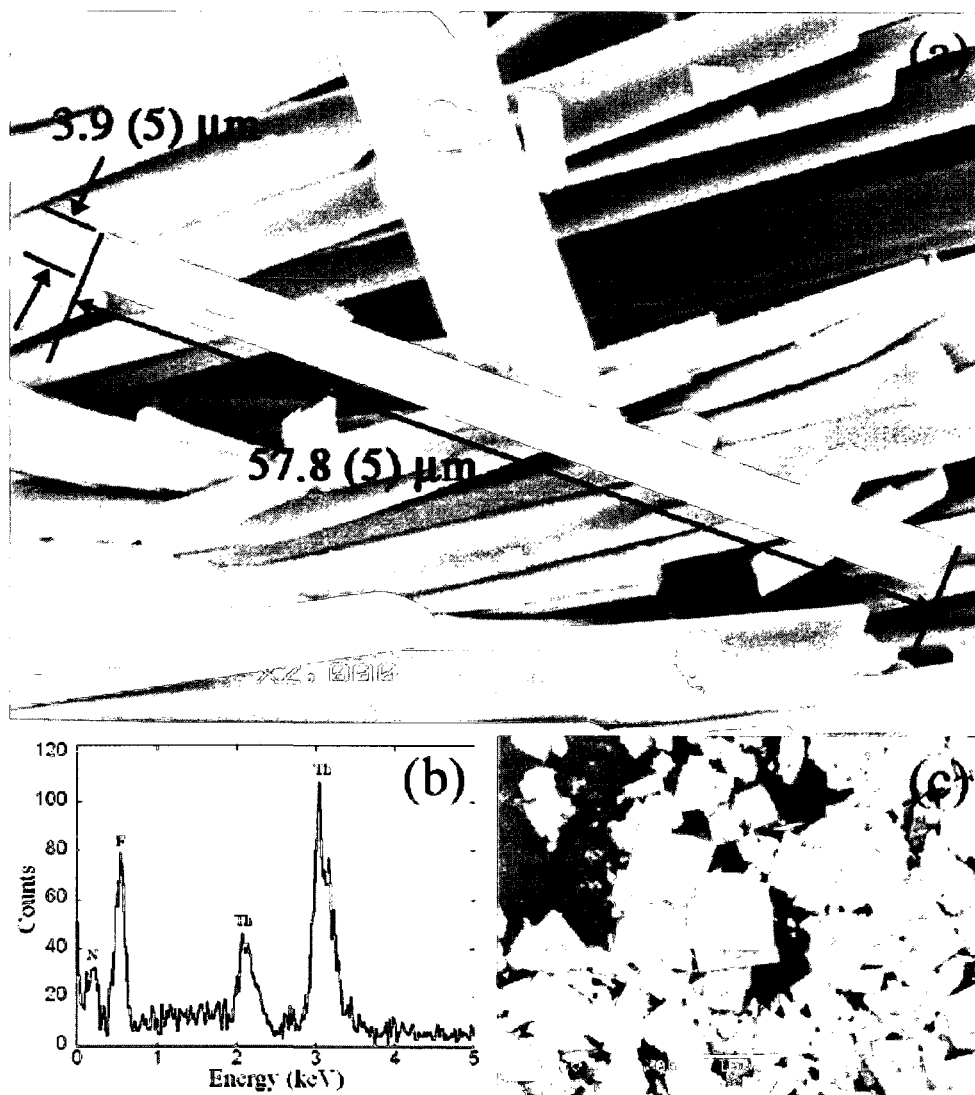


Figure 4.3 Secondary-electron SEM image (a) and the corresponding EDS spectrum (b) of the synthesized $(\text{NH}_4)_4\text{ThF}_8$ and the SEM image of ThO_2 (c).

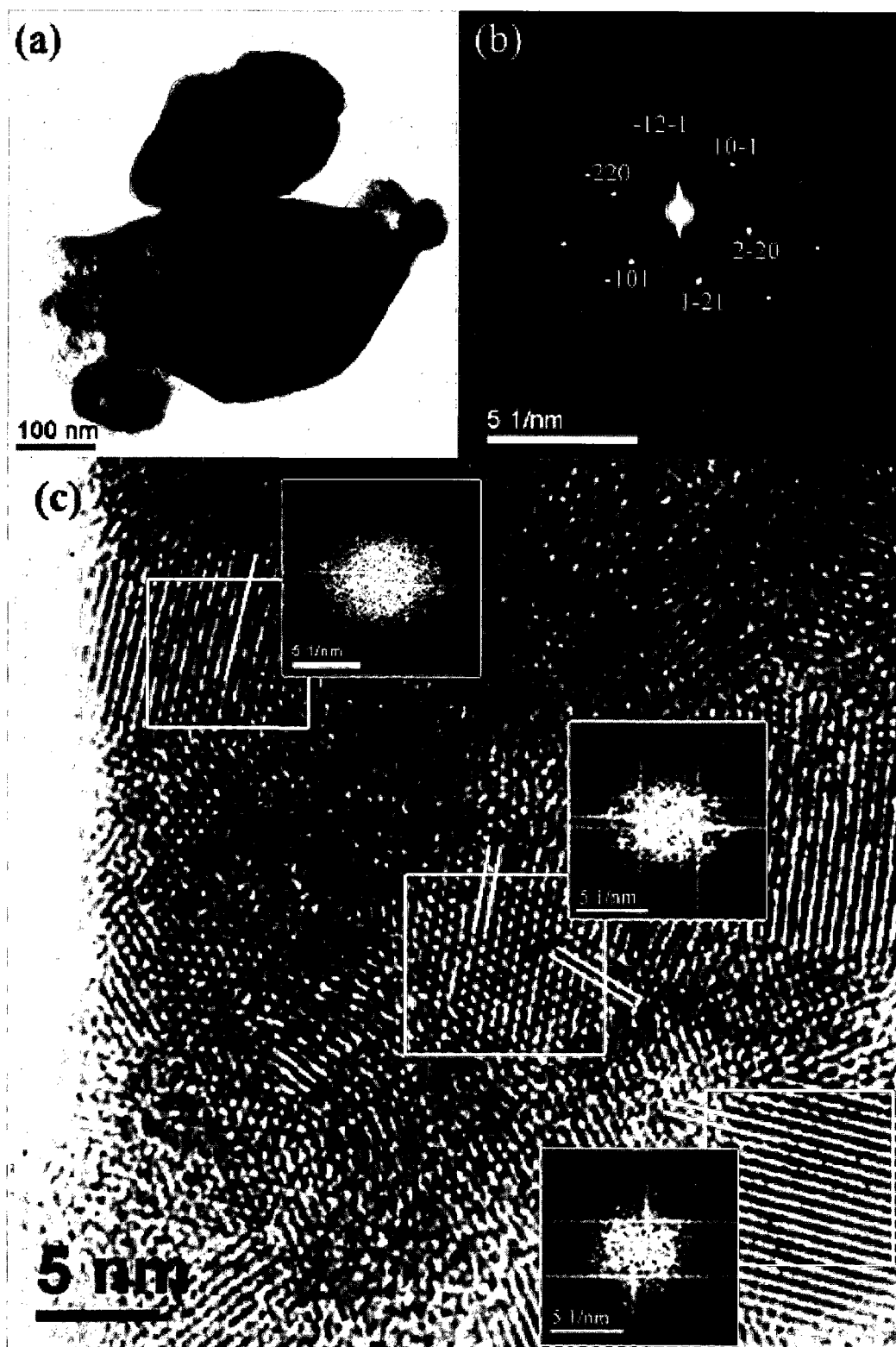


Figure 4.4 (a) TEM BF image, (b) [111] electron diffraction pattern, and (c) HRTEM image of $(\text{NH}_4)_4\text{ThF}_8$ ground particle.

TEM BF image of the $(\text{NH}_4)_4\text{ThF}_8$ particles from a ground sample is shown in Figure 4.4a. The SAD pattern in Figure 4.4b was obtained by focusing on an area of the large particle seen in the bottom half of Figure 4.4a, and this pattern is in $[111]$ zone axis. Figure 4.4c is a HRTEM image of the same particle displaying lattice fringes in several different orientations as indicated in the image. Some of these domains have high point resolution in two directions while others exhibit either one or none directional fringe properties. This observation suggests that the $(\text{NH}_4)_4\text{ThF}_8$ obtained is a polycrystalline material.

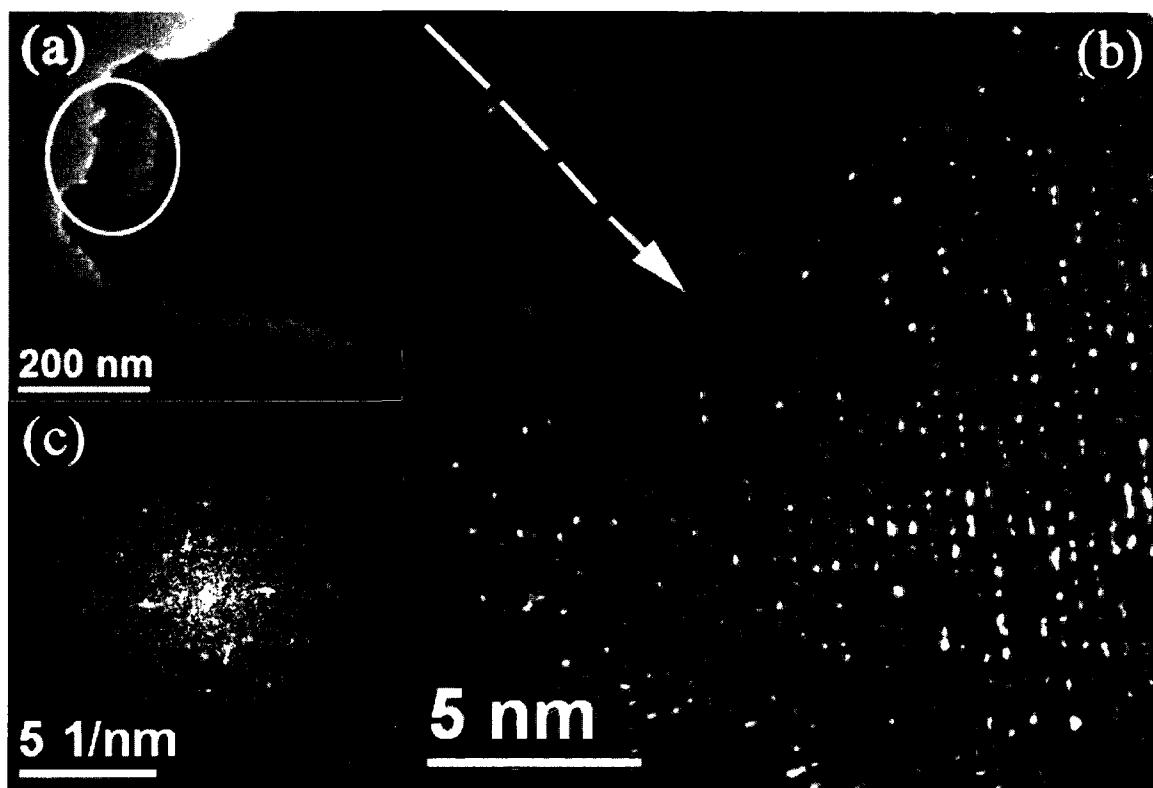


Figure 4.5 (a) TEM BF image of another ground $(\text{NH}_4)_4\text{ThF}_8$ particle. (b) The HRTEM image of the circled area of (a) and (c) the corresponding FFT.

On the other hand, Figure 4.5b shows a well-oriented set of lattice fringes of $(\text{NH}_4)_4\text{ThF}_8$ corresponding to (1-11) lattice plane distributed in a larger area than in the nanocrystalline areas found in Figure 4.4c. This set of lattice fringes are also disturbed though by another set of similar sized nanoparticle domain which has being grown from the other side of the particle as indicated by an arrow. This feature further implies a polycrystalline characteristic of the sample even though this area consists of comparatively large nanoparticles.

4.4 Synthesis and Characterization of ThNF

Ammonolysis of $(\text{NH}_4)_4\text{ThF}_8$ or the heat-treatment of the sample under ammonia atmosphere at three different temperatures up to 1100 °C (Table 4.1) showed that the final product of this reaction step is ThNF. At 800 °C, 300 minutes were required to synthesize this terminal product. Increasing the reaction temperature resulted in a significant decrease in reaction time, with sample heating at 1100 °C for 15 minutes optimal for synthesis of ThNF.

Table 4.1 Temperature effect on the ammonolysis of $(\text{NH}_4)_4\text{ThF}_8$.

Temperature/ °C	Time/ min	Products			
		1° phase	Weight %	2° phase	Weight %
800	300	ThNF	79.0(6)	ThO ₂	21.0(6)
1000	45	ThNF	100	-	-
1100	15	ThNF	100	-	-

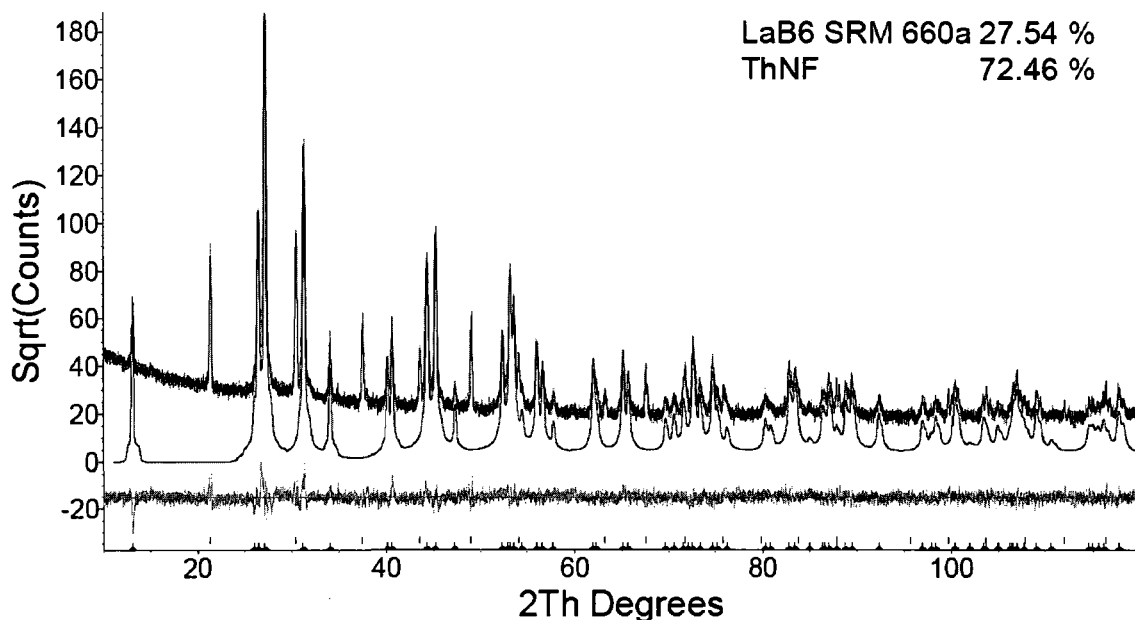


Figure 4.6 XRD powder refinement of ThNF synthesized by heating $(\text{NH}_4)_4\text{ThF}_8$ at 1100°C for 15 min under NH_3 .

The XRD pattern of the ThNF sample synthesized by ammonolysis of $(\text{NH}_4)_4\text{ThF}_8$ at 1100°C for 15 minutes (Figure 4.6) confirms the sample is single-phased. The refined lattice parameter of the rhombohedral unit cell was $0.71312(5)$ nm which agrees well with the literature value of $0.7130(3)$ nm [12]. The phase density of ThNF was calculated to be $9.369(2)$ g/cm^3 .

The secondary SEM image of ThNF sample (Figure 4.7a) shows plate-like particle shapes. The 15,000 times magnified SEM image (Figure 4.7b) further displays pitted and porous characteristics of the ThNF particle surface. Size of these pore spaces vary from about 50 to 200 nm in width. Furthermore, the corresponding EDS spectrum (Figure 4.7c) of this sample confirms the presence of thorium, fluorine, and nitrogen. The nitrogen peak partially overlaps with the background peak from carbon tape that was used to mount the sample. SEM image of ThF_4 is also shown in Figure 4.7d for the comparison purposes.

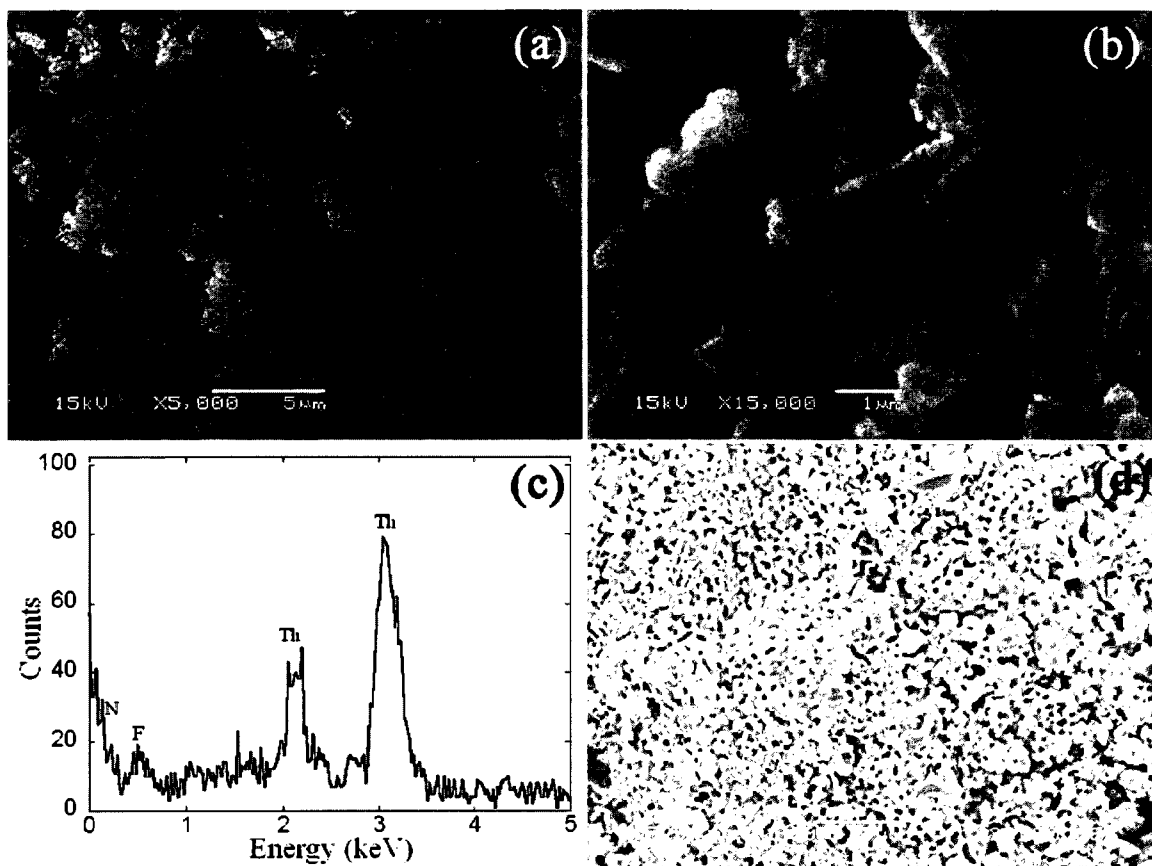


Figure 4.7 Secondary electron SEM images of the ThNF sample, (a) showing the morphology at x5,000 magnification and (b) at x15,000 magnification, (c) the corresponding EDS spectrum of ThNF, (d) and the SEM image of ThF₄.

Table 4.2 Elemental analysis of the as-synthesized ThNF by EDS.

Element	Averaged atom percentages (%)
N K (± 1.25)	39.0
F K (± 1.26)	21.6
Th K (± 1.47)	39.4
Th:N:F molar ratio	1:0.99:0.60

The elemental analysis of this sample determined by EDS is shown in Table 4.2. The Th:N:F molar ratio of the compound is approximately 1:1:0.6. Based on the error

associated with the EDS on quantification and because EDS is considered a semi-quantitative method, the stoichiometry of the compound can be considered close to 1:1:1 (ThNF). In the sample heated for 300 minutes at 800 °C, a secondary ThO₂ phase was identified due to prolonged exposure to minute oxygen impurities in the system.

A 50 nm thick sample of ThNF was microtome cut for the TEM imaging. Figure 4.8a shows a low resolution TEM BF image of few ThNF particles thus prepared. Since the microtome cutting was applied for the specimen preparation, the cross sectional view of the sample at HRTEM is supposed to show a uniform intensity across a focused area. However, most of the areas investigated showed intensity variance of the images at high-resolution. HRTEM of one such area is shown in Figure 4.8b. The area in this image shows a continuous set of lattice fringes of ThNF correspond to (0-11) planes under [100] beam. Most of the area displays lattice fringes only in one direction except for some lattice fringes in the area depicted by B – C. A line scan across the image on a randomly selected lattice fringe from A through D (Figure 4.8d) showed that the intensity of the image changes considerable. The intensities from A to B do not vary much, but it is highest in the region denoted by B – C. From C to D, the intensities start to change abruptly and approach a minimum at the end of the line. This observation suggests a thickness variance across the scanned area forming a thinner region of about 6 nm long given the length of the line scanned to be 36 nm. The pore spaces of the ThNF particles detected by SEM imaging were 50 to 200 nm in width. This implies a continuation of the pore spaces up to nano-scale of the ThNF compound.

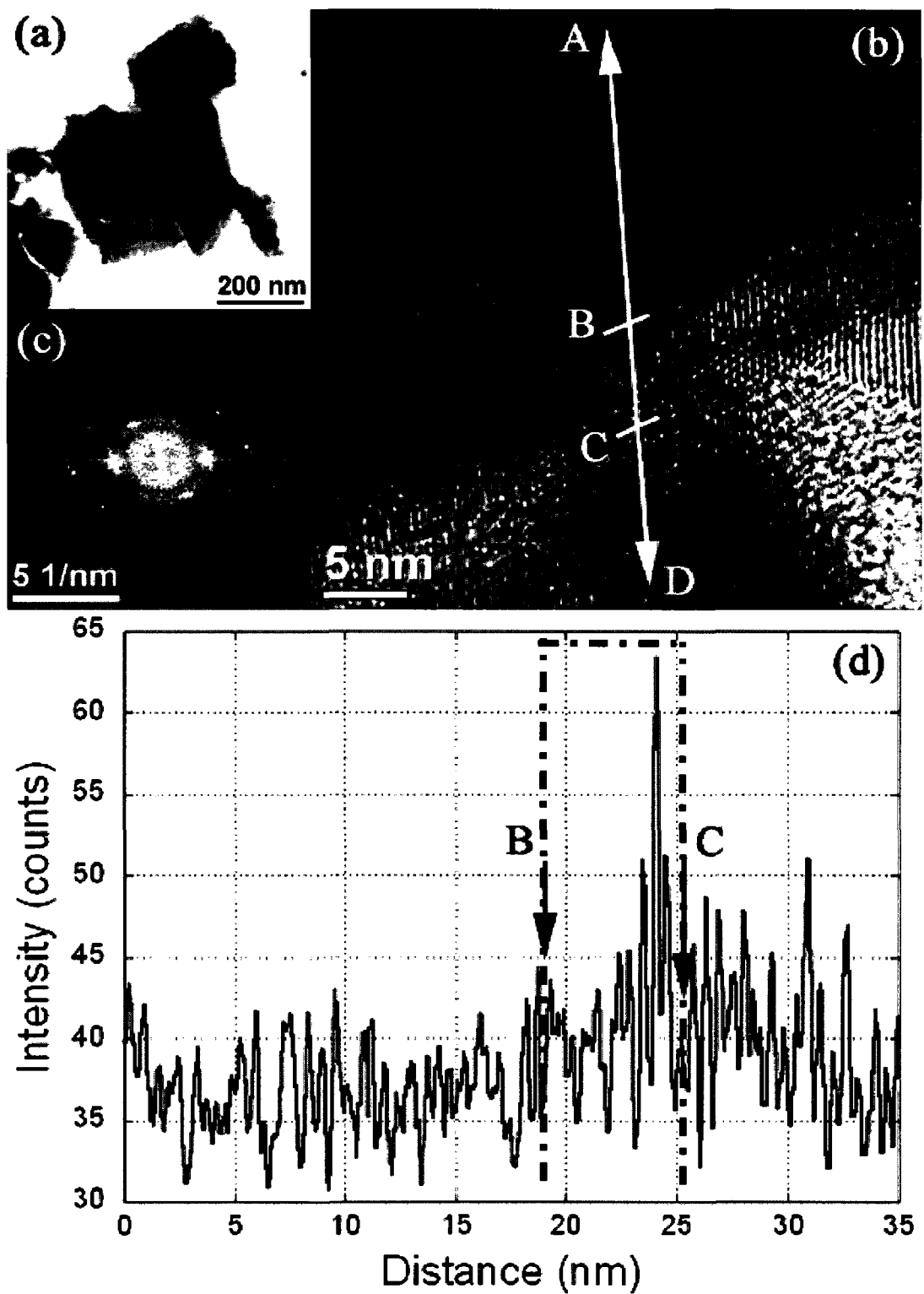


Figure 4.8 (a) TEM BF of a microtome cut ThNF sample, (b) HRTEM image, (c) FFT of HRTEM, and (d) experimental intensity profile along A – B in HRTEM.

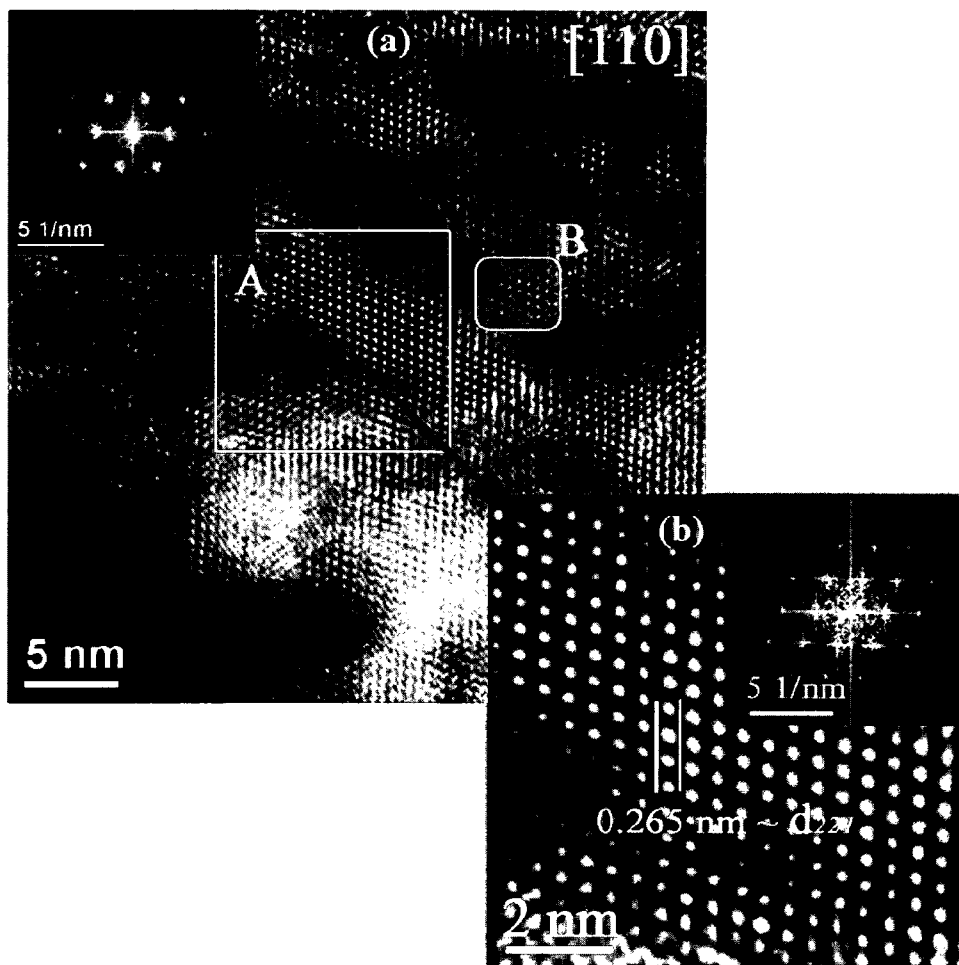


Figure 4.9 (a) HRTEM of another area of the particle in Figure 4.8a. (b) Enlarged image of area denoted by letter A with a rectangle. The area B denoted by a rounded rectangle is used in Figure 4.10. Onsets of each image are the corresponding FFT micrographs.

HRTEM of another area of the same particle in Figure 4.8a is displayed in Figure 4.9. Two rectangle areas of Figure 4.9 were enlarged using a smooth spatial filter to obtain HRTEM images in Figure 4.9b and Figure 4.10. The beam direction of these HRTEM images is $[110]$. Lattice fringes in Figure 4.9b provide a width of 0.265 nm for a single layer of fringes corresponding to a reflection plane of (221). Intensity difference between areas A and B reveals more intuitive structural detail of ThNF as depicted in Figure 4.10. Thickness variance as identified previously is the probable reason for such a difference in

intensities of two areas within 30 nm. Lattice fringes in area B as shown in Figure 4.10 show more details than area A. Spacing between two layers of lattice fringes in Figure 4.10 is 0.225 nm which is close to the d-spacing of (333) lattice plane of ThNF. Furthermore, this spacing is less than the width of a single layer of lattice fringes in area A (0.265 nm) demonstrating a shift in the planes that attribute to the lattice fringes of the HRTEM images.

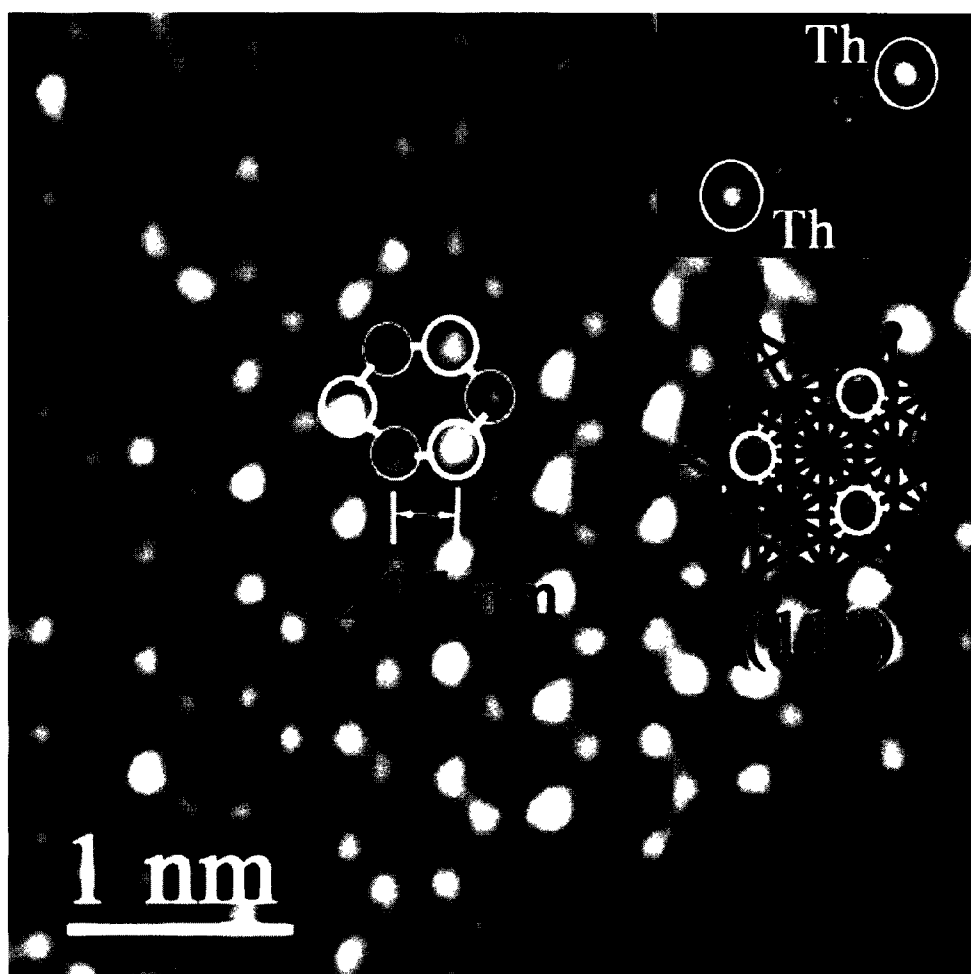


Figure 4.10 HRTEM of the particle area denoted by letter B in Figure 4.9. Inset to the upper right side is the electron density map calculated by ThNF XRD pattern using charge flipping. A model of the molecule in (111) direction is also inserted.

The electron density map, which is the inset of Figure 4.10, of ThNF calculated from XRD pattern utilizing charge flipping also confirms the structural details observed with HRTEM imaging. Electron density map indicated a high electron density at locations where Th atoms reside within the crystal structure of ThNF. Therefore, the HRTEM imaging will only show the intensities due to Th atoms. Repetition of such structural units will give a well-ordered nanostructure as in Figure 4.10. Atomic resolution of the hexagonal-like order of atoms in the HRTEM image is different from point-to-point as indicated by circles in the image. The atomic planes in (111) direction of the packed rhombohedral unit cells are in and out of plane slightly such that the depth of the imaging can change as indicated in the inset of the Figure 4.10. All these observations confirm the presence of single-phased ThNF in the sample.

4.5 Ammonolysis of ThF₄ and the Thermal Behavior of ThNF

Heating of the (NH₄)₄ThF₈ sample at 800 °C for 60 min formed ThF₄ in agreement with the work done by Wani et al [10]. The XRD powder pattern together with the Rietveld analysis of ThF₄ chemical phase identified is shown in Figure 4.11. The lattice parameters, $a = 13.049$ (3), $b = 11.120$ (2), $c = 8.538$ (2) published by G. Benner and B. G. Mueller [13] for the monoclinic ThF₄ agree fairly well with the refined lattice parameters, $a = 13.0444$ (7), $b = 11.0118$ (6), $c = 8.5343$ (5) of the ThF₄ sample synthesized here.

After identifying ThF₄ as an intermediate of the conversion of (NH₄)₄ThF₈ into ThNF, ThF₄ was heated under varying experimental conditions (Table 4.3) to determine the reaction mechanism. Removal of fluorine atoms from the ThF₄ and incorporation of

nitrogen to fill those vacant sites can be observed as the low-stoichiometric chemical phases of thorium nitride fluorides start to appear in the samples (Table 4.3).

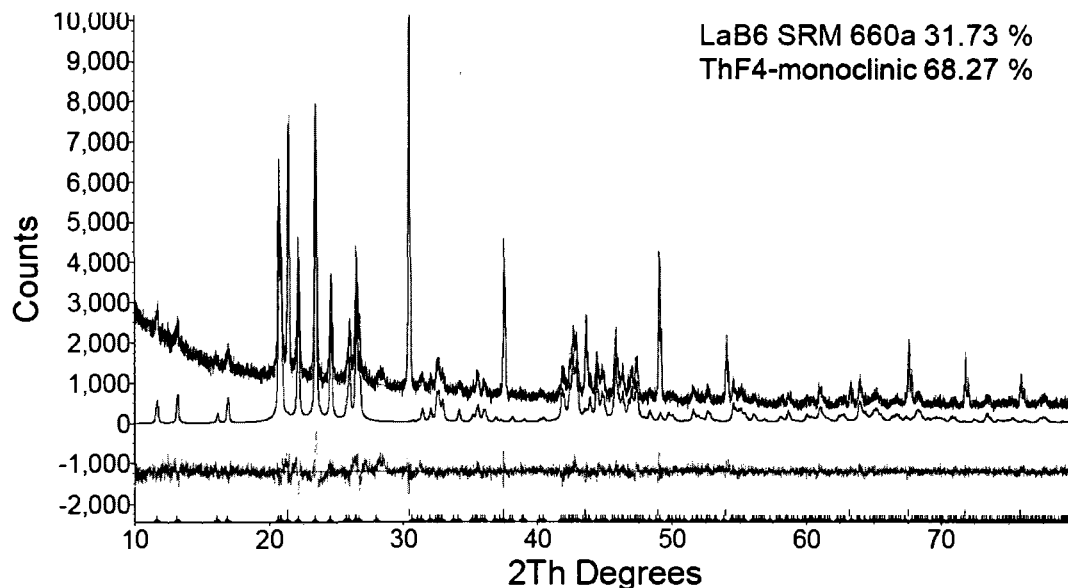


Figure 4.11 XRD refinement of the sample synthesized heating $(\text{NH}_4)_4\text{ThF}_8$ at 800 °C for 60 min under NH_3 .

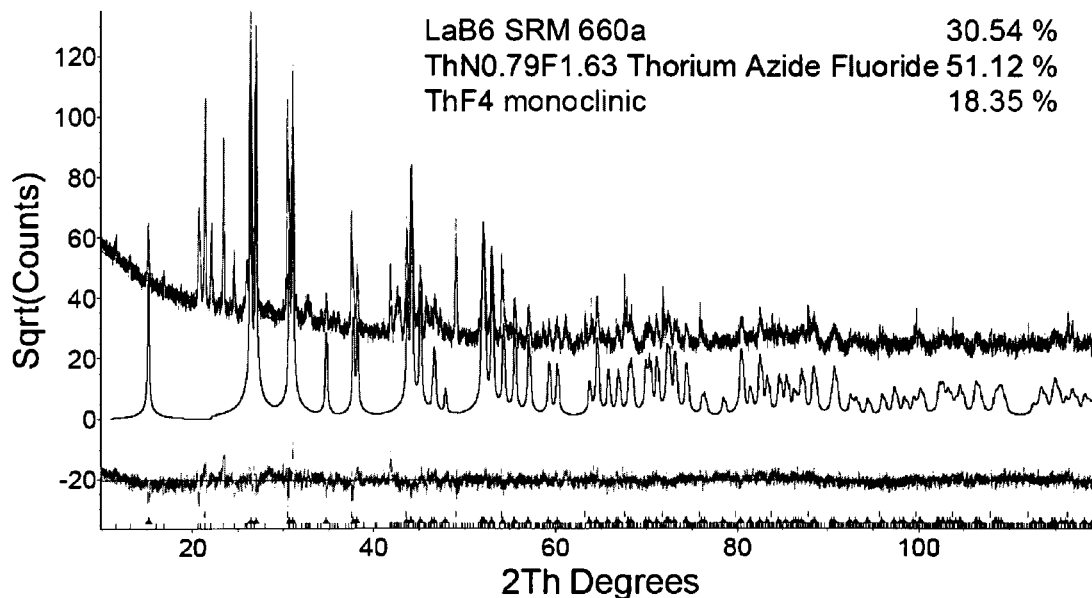


Figure 4.12 XRD powder refinement of the ThF_4 sample after the ammonolysis at 800 °C for 1 hour.

Table 4.3 Ammonolysis of ThF₄.

Temp./ °C	Time/ min	Product			
		Primary phase	Weight %	Secondary phase	Weight %
800	60	ThN _{0.79} F _{1.63}	73.6(2)	Unreacted ThF ₄	26.4(2)
800	240	ThNF	79.0 (1)	ThN _{0.9} F _{1.3}	21.0 (1)
800	300	ThNF	79.0(6)	ThN _{0.9} F _{1.3}	21.0(6)
800	600	ThNF	100	-	-
1000	45	ThNF	100	-	-
1000	75	ThNF	82.4 (6)	ThO ₂	17.6 (7)
1100	15	ThNF	100	-	-

Figure 4.12 shows the XRD powder pattern refinement of the ThN_{0.79}F_{1.63} sample which was synthesized by heating ThF₄ at 800 °C for 60 min. Heating ThF₄ for 300 min under NH₃ further removed the fluorine content from the reactant producing ThNF (79 wt%) and some ThN_{0.79}F_{1.63} (21 wt%). XRD powder refinement of this sample is displayed in Figure 4.13 with highlighting the calculated pattern for ThN_{0.79}F_{1.63}. A complete formation of ThNF was observed after 600 min with no ThO₂ impurities (Figure 4.14a). However, a 17.6(7) wt% ThO₂ secondary phase was detected on heating ThF₄ at 1000 °C for 75 min (Figure 14b) whereas a 45 min heating did not show any impurity phase. These three observations suggest that prolong heating at elevated temperatures form a ThO₂ secondary chemical phase due to the oxygen partial pressure produced by quartz tube used to insert the sample for the experiment.

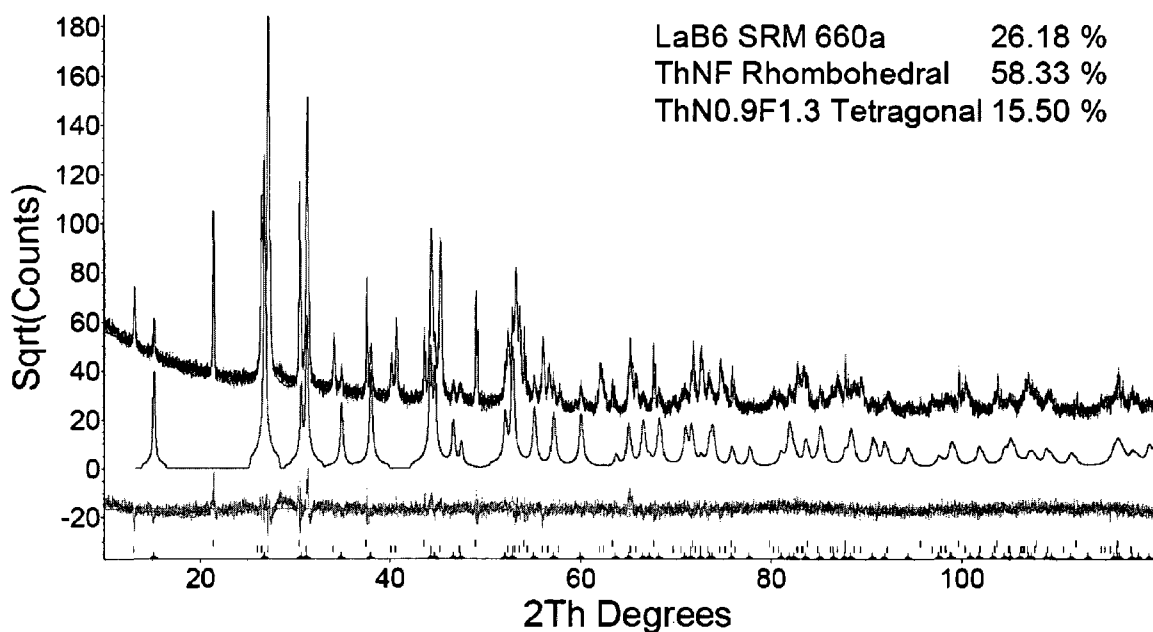


Figure 4.13 XRD powder refinement of the ThF₄ after the ammonolysis at 800 °C 300 min.

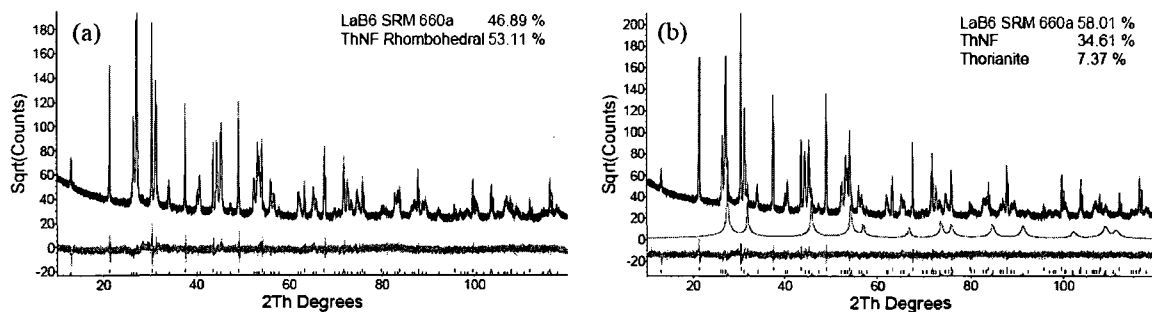


Figure 4.14 XRD powder refinements of ThF₄ after the ammonolysis at 800 °C for 600 min (a) and at 1000 °C for 75 min (b). Square root of counts was used as the scale of Y-axis for proper display of the calculated patterns.

Thermal stability of ThNF under different atmospheres was tested as well, and the results are summarized in Table 4.4. Under high-purity argon (99.999 %) at 1100 °C, ThNF decomposes into ThN_{0.79}F_{1.63} with a formation of a minor secondary ThO₂ phase probably due to minor oxygen impurities formed in the experimental setup at 1100 °C.

Under N₂ and N₂-H₂ (5 %) environments, ThNF decomposed into another low-stoichiometric thorium-nitride-fluoride (ThN_{0.90}F_{1.30}).

Table 4.4 Thermal behavior of ThNF under different atmospheric conditions.

Atmosphere	Temperature/ °C	Time/ min	Product	Secondary phases
Ar	1100	60	ThN _{0.79} F _{1.63}	ThO ₂
Ar-H ₂ (5%)	1100	60	ThO ₂	-
N ₂	1100	60	Th _{0.90} F _{1.30}	ThNF, ThO ₂
N ₂ -H ₂ (5%)	1100	60	ThN _{0.90} F _{1.30}	ThO ₂
N ₂ -H ₂ (5%)	1100	120	ThO ₂	-

4.6 Synthesis and Characterization of Th₂N₃

Table 4.5 summarizes some of the products observed after heating different thorium fluorides under NH₃ after mixing with LiNH₂. These temperatures were randomly selected and 800 °C was found to be sufficient to make Th₂N₃. At low temperatures, ThF₄ was observed as the major chemical species. At elevated temperatures, three chemical phases were identified in the sample made from (NH₄)₄ThF₈, while only two phases were identified in the samples made from ThF₄ and ThNF. The sample which contained LiF was made by mixing ThF₄ and LiNH₂ at 1:4 molar ratio. All the samples made at elevated temperatures contain ThO₂ as the major second phase and the Th₂N₃. A few more samples were made by heating ThNF/LiNH₂ mixture at 800 °C under NH₃ for 30 min and then by consecutive heating of the sample under N₂ and N₂/H₂ (5%) up to 900 °C for 30 min. Further heating under different atmospheres did not change the chemical phase even though the weight percentages of each phase seem to change.

Further heat-treatment of Th_2N_3 samples at different temperatures under high-purity argon atmosphere is shown in Table 4.6. At 800 and 900 °C, Th_2N_3 phase was almost diminished, while at 1000 and 1100 °C a complete oxidation of the compound could be identified.

Table 4.5 Results obtained after heating different thorium fluorides with LiNH_2 under ammonia.

Sample	Temperature/ °C	Time/ min	Products		
$(\text{NH}_4)_4\text{ThF}_8$	100	60	ThF_4	-	-
$(\text{NH}_4)_4\text{ThF}_8$	900	60	Th_2N_3	ThO_2	Impurities due to ThF_xO_y
ThF_4	100	60	ThF_4	-	-
ThF_4	800	30	Th_2N_3	ThO_2	LiF
ThF_4	800	60	Th_2N_3	ThO_2	-
ThNF	800	30	Th_2N_3	ThO_2	-

Table 4.6 Results obtained after heating $\text{Th}_2\text{N}_3/\text{ThO}_2$ sample at different temperatures under high-purity argon for 30 min.

Temp. /°C	Products			
	Primary	Wt. %	Secondary	Wt. %
800	ThO_2	97.16	Th_2N_3	2.84
900	ThO_2	97.74	Th_2N_3	2.26
1000 & 1100	ThO_2	100	-	-

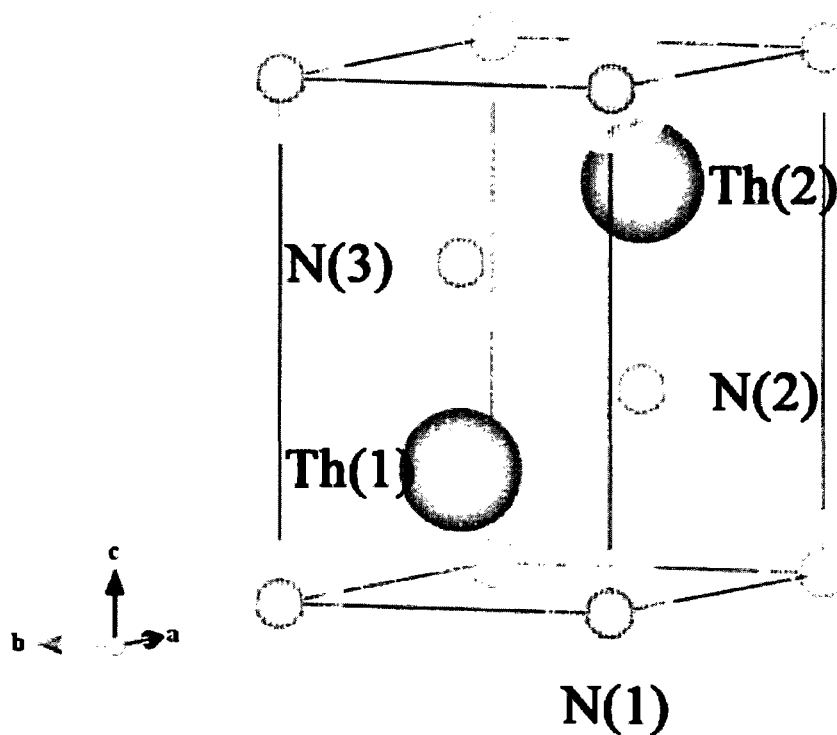


Figure 4.15 Crystal unit cell of Th₂N₃ with La₂O₃-type hexagonal $P\bar{3}m1$ structure.

The Th₂N₃ phase investigated in this study crystallizes in the La₂O₃-type hexagonal system (Figure 4.15) with $P\bar{3}m1$ space group symmetry [9]. Figure 4.16a shows the XRD pattern of the Th₂N₃ sample synthesized by heating a mixture of ThNF/LiNH₂ at 800 °C for 30 min under NH₃. The refined lattice parameters of the hexagonal Th₂N₃ are $a = b = 3.8843(1)$ and $c = 6.1853(3)$ Å ($c/a = 1.59238$). These values have a match up to the third decimal point of the lattice parameter values of Th₂N₃ of the ICSD pattern number 76637 which is calculated from Zachariasen et al [9] and the lattice parameters reported by Chiotti et al [3]. Interatomic distances of the crystal unit cell refined by XRD pattern of the Th₂N₃ are summarized in Table 4.7.

Table 4.7 Interatomic distances for Th₂N₃ with La₂O₃-type hexagonal $P\bar{3}m1$ crystal structure.

Bonds	Distances (Å)
N(1)-N(2)	3.20418 (8)
N(1)-N(3)	4.4960 (2)
N(1)-Th(1)	2.67246 (8)
N(1)-Th(2)	5.2363 (2)

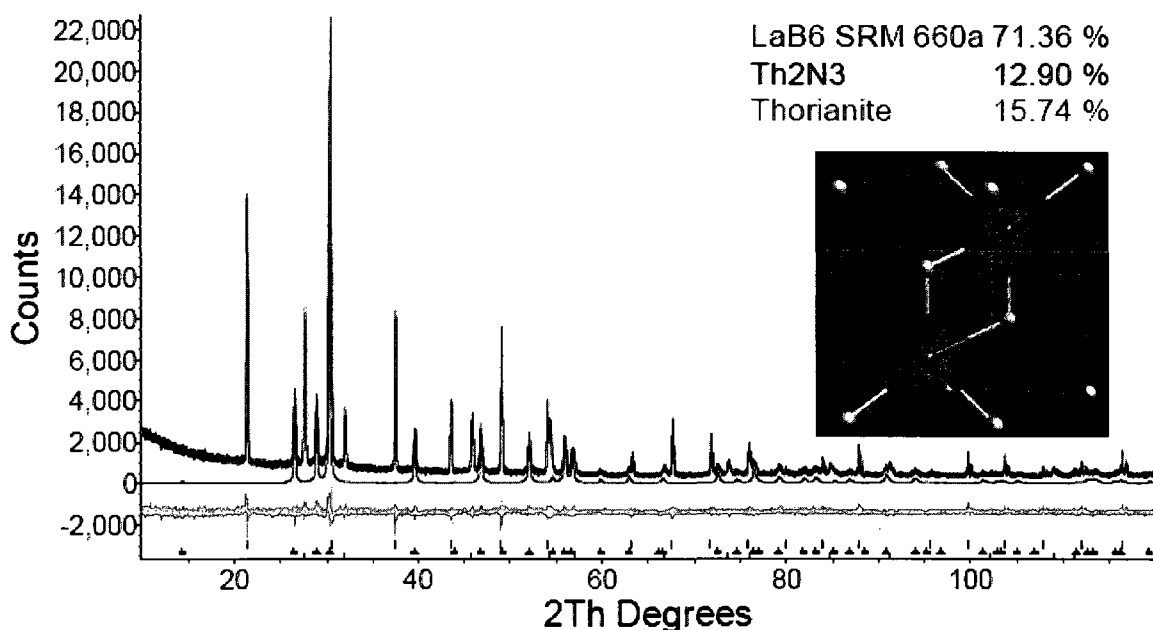


Figure 4.16 XRD powder refinement using Rietveld method. The calculated Th₂N₃ pattern is highlighted. Inset is the corresponding Fourier map of Th₂N₃. The sample contains 56 wt% ThO₂ as a second chemical phase.

SEM micrographs presented in Figure 4.17 show the morphology of Th₂N₃ sample the ThO₂ source sample used to synthesize fluorides of thorium. Thin-square particles of about 10 μm in length can be seen in ThO₂ (Figure 4.17b). Particles of incompletely crystallized faces can be observed for the sample synthesized (Figure 4.17a).

Multibranched characteristics of Th_2N_3 particles are also visible in Figure 4.17a. These dendrites contain bulk areas (anhedrals) agglomerated with subhedral (Figure 4.18b) and needlelike (Figure 4.18c) grains. The EDS spectrum in Figure 4.18a shows Th, N, and O present in the sample. Figure 4.18a also reveals that the sample consists of some F impurities. Quantitative analysis in Table 4.8 further shows that F represents the lowest elemental distribution in the sample. Absence of any ThF_4 , ThNF , or any other crystalline fluoride chemical phases in the XRD pattern indicates that the fluorine is in an amorphous phase of the sample.

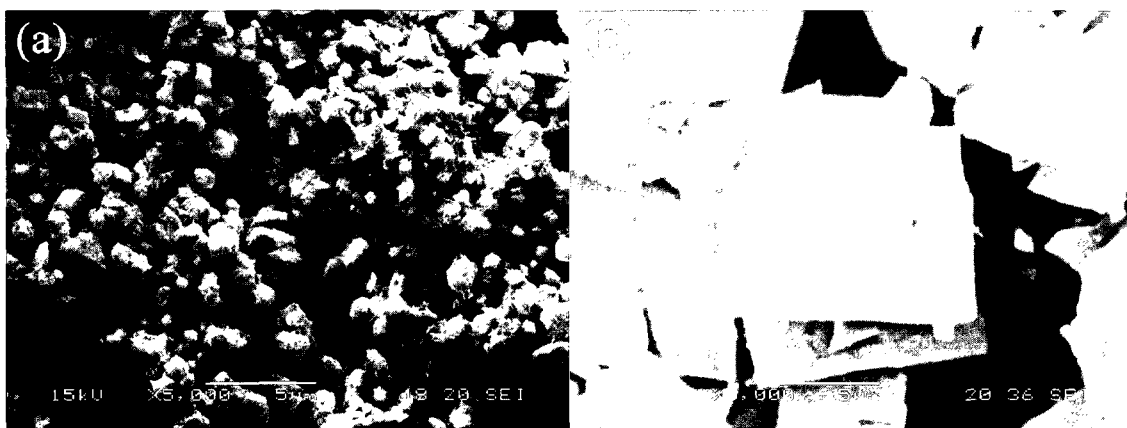


Figure 4.17 SEM micrographs of the (a) synthesized Th_2N_3 sample and (b) ThO_2 .

Table 4.8 Elemental distribution of the as-synthesized Th_2N_3 sample.

Element	Wt. %	Error %
N	6.28	0.86
O	11.19	0.59
F	4.04	0.56
Th	78.49	1.02

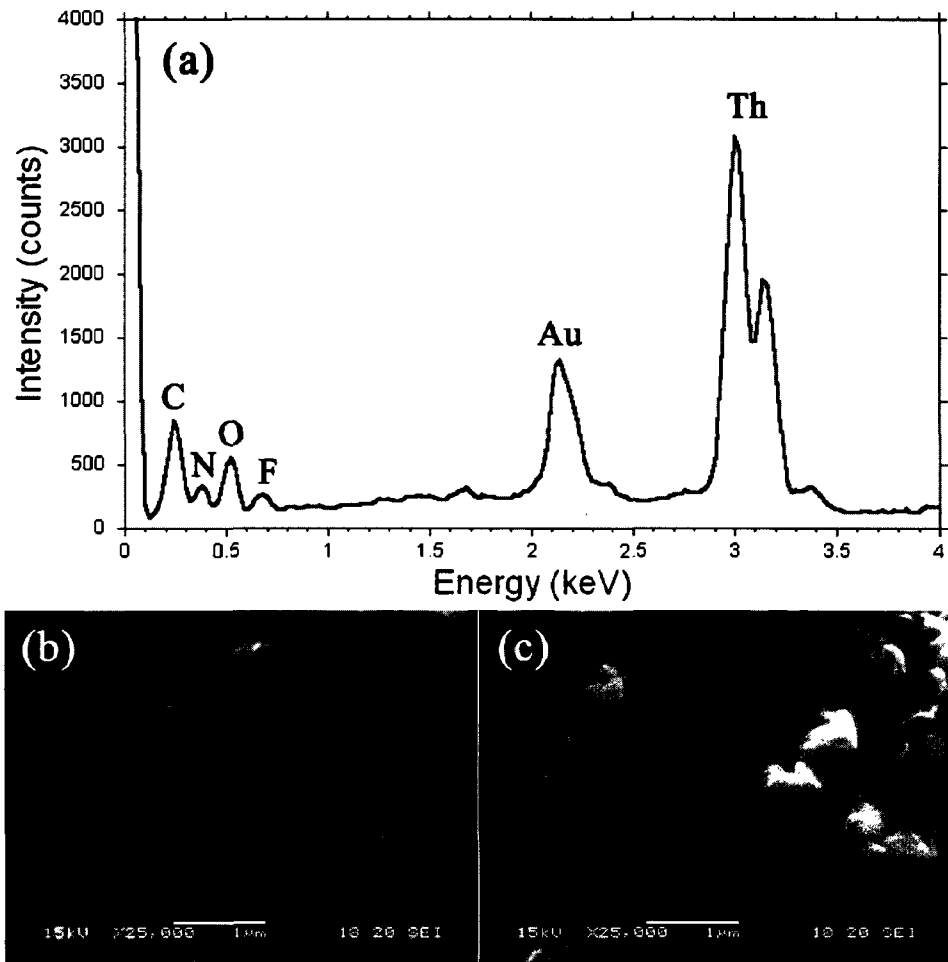


Figure 4.18 (a) EDS spectrum and (b), (c) SEM micrographs of the Th_2N_3 sample at different area of the sample. C and Au are from the tape used to mount the sample and gold coating, respectively.

EELS elemental mapping of a cluster of reasonably separated particles (Figure 4.19a) of the synthesized sample are shown in Figure 4.19b through 4.19e. Distribution of thorium (Figure 4.19b) is most likely uniform throughout the grain edges where thickness is less. Figure 4.19c shows the amount of nitrogen distributed in two particle areas (bright white) is higher than in all other regions. Therefore, the region to the left bottom was further focused in obtaining HRTEM in Figure 4.20. On the other hand, a uniform distribution of oxygen can be observed throughout all the particles in Figure 4.19d.

Oxygen is also deficient in particles where nitrogen is rich. Such large particle area is highlighted with a circle in Figure 4.19c and 4.19d. Similar characteristics can be seen on the fluorine map in Figure 4.19e, except for one bright area with more amorphous characteristics (highlighted in Figure 4.19a and 4.19e) than other particle areas. This observation explains the presence of F in amorphous particles mainly.

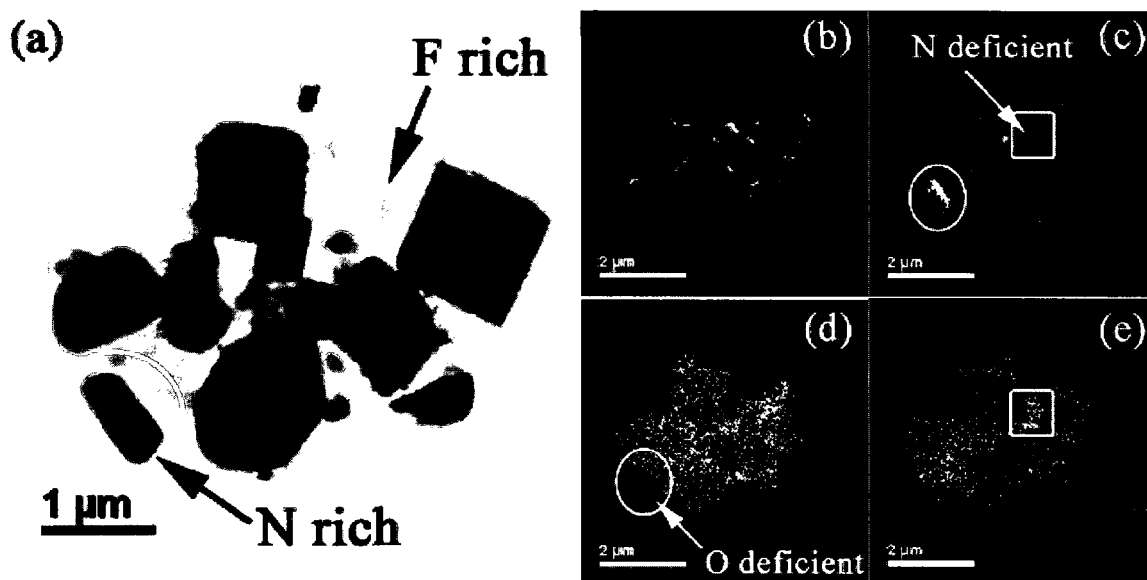


Figure 4.19 EELS elemental maps of Th_2N_3 sample. (a) Zero energy-loss image, (b) Th map, (c) N map, (d) O map, and (e) F map.

HRTEM images of the Th_2N_3 particle in Figure 4.20a and 4.20b indicate that these lattice fringes are from (100) plane reflections aligned in [010] beam direction. Most of the areas in Figure 4.20a do not contain lattice fringe details clearly due to thickness contrast of the particle. However, the magnified area in Figure 4.20b consists of 2-directional lattice fringes corresponding to (100) reflections. This area also shows to contain amorphous domains of < 2 nm length. Furthermore, some of the lattice fringes (along AB) display disorientations in their atomic distributions. Corresponding

experimental intensity profiles within one set of lattice fringes normal to [100] direction indicate a disruption of atomic positioning along AB at point C at which the atomic layer starts continuing along CB after about 0.1 nm shift normal to AB.

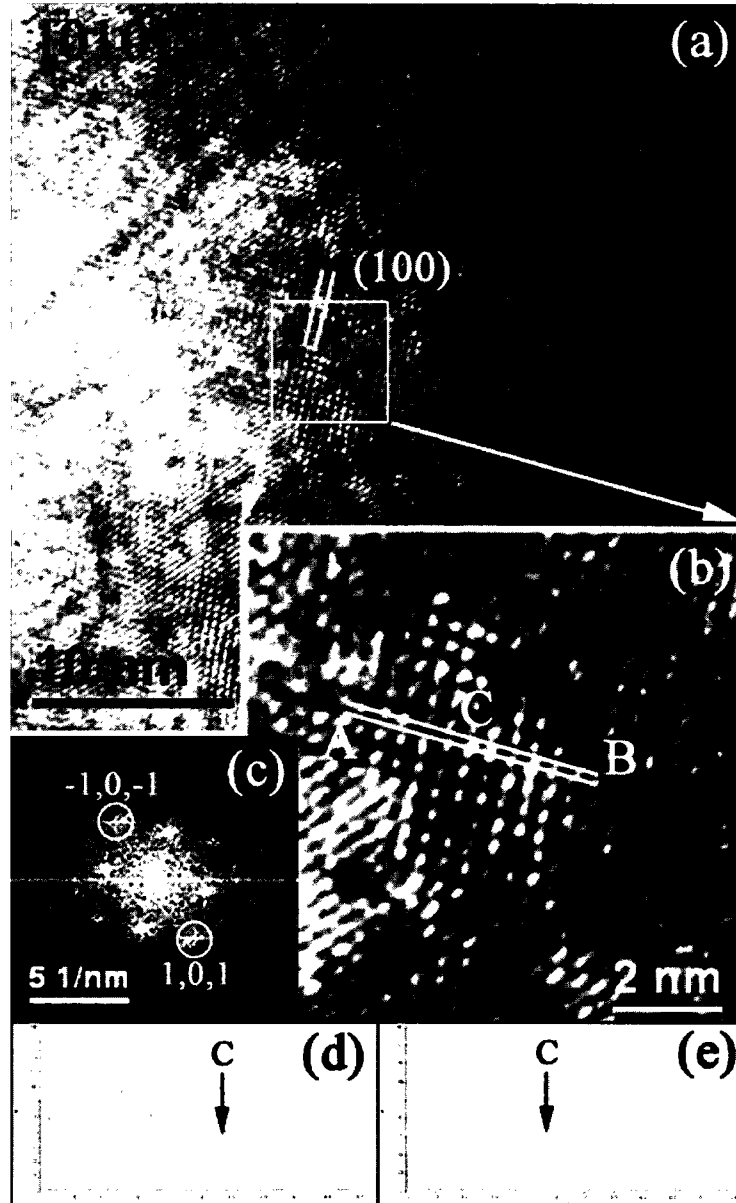


Figure 4.20 (a) HRTEM image of Th_2N_3 sample, (b) magnified image of the square area in (a), (c) FFT of (b), (d) and (e) are the experimental intensity profiles of the HRTEM image in (b) along AB.

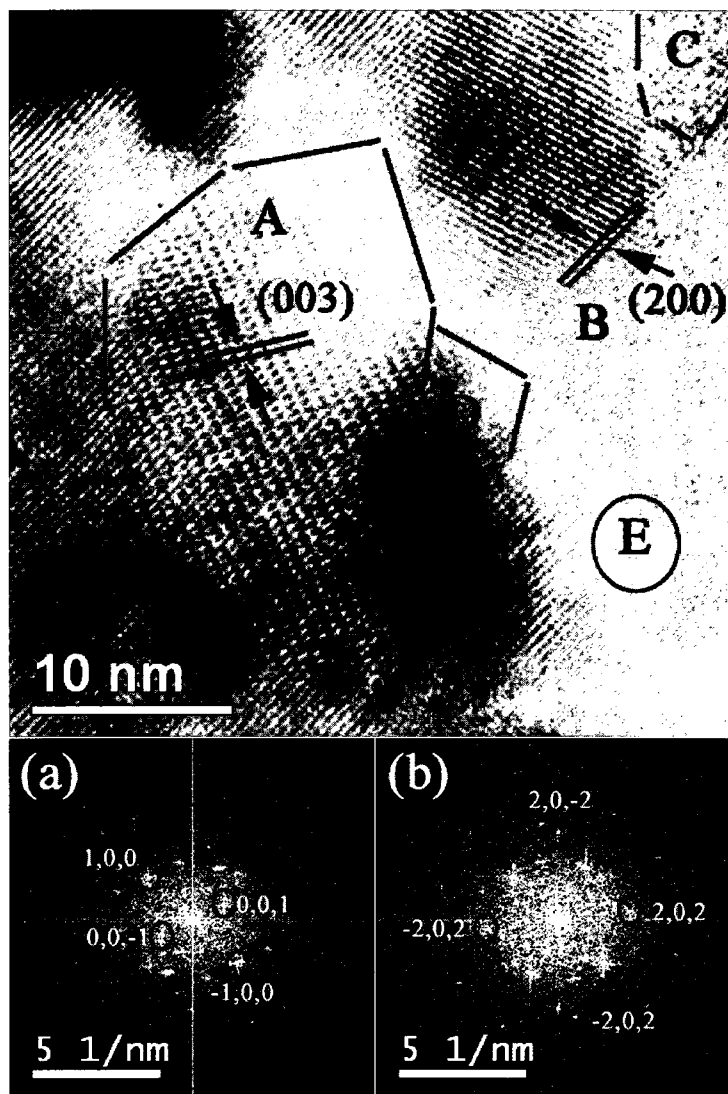


Figure 4.21 (a) HRTEM and (b), (c) the corresponding FFT micrographs of the synthesized Th_2N_3 sample. FFT in (a) and (b) are corresponding to the areas A and B, respectively.

The HRTEM image of another sample area in Figure 4.21a contains lattice fringe details of Th_2N_3 (area A) as well as of ThO_2 (area B). The corresponding localized FFT micrographs of the areas A and B in HRTEM are also shown in Figure 4.21a and 4.21b, respectively. These FFT micrographs and the lattice fringe details show that area A corresponds to the (003) reflections of Th_2N_3 and area B corresponds to the (200) reflections of ThO_2 phase in [010] beam direction. HRTEM image of the particle imaged

in Figure 4.21a also consists of amorphous domains (areas C, D, and E), confirming the findings of XRD and SEM.

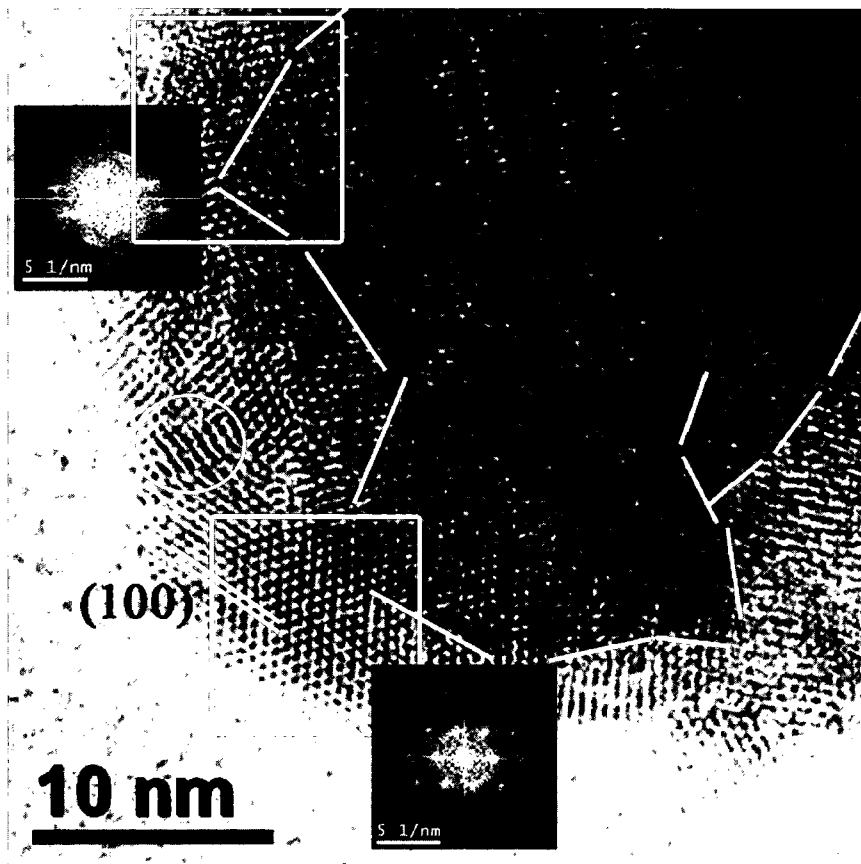


Figure 4.22 HRTEM image of another particle area of Th₂N₃ sample.

HRTEM image of another nitrogen rich particle area of the as-synthesized Th₂N₃ sample is shown in Figure 4.22. The region with detailed lattice fringes and the corresponding FFT micrograph displayed that the particle exhibits lattice fringes due to (100) lattice planes of Th₂N₃ in [001] beam direction. This HRTEM image also contains some distorted areas with speckled diffraction patterns. In another area, which is indicated by a circle, close to the well-oriented lattice fringes contains one-directional

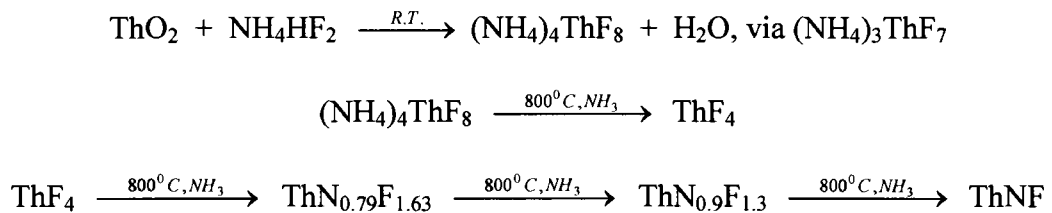
lattice fringes of abrupt distortions. Furthermore, this particle area is accumulated with another grain which is displayed by lines. This new grain however blended with the first grain quite well although some regions are affected by lattice fringe twisting.

4.7 Discussion

The terminal product of ThO₂ reaction with NH₄HF₂ at ambient conditions was (NH₄)ThF₈ as was reported earlier [10]. We found that this reaction proceeds through an intermediate chemical phase (NH₄)₃ThF₇ that was formed after few hours of mixing ThO₂ with NH₄HF₂. Further reaction of the unreacted ThO₂ with NH₄HF₂/NH₄F and the transformation of (NH₄)₃ThF₇ into the terminal (NH₄)₄ThF₈ took up to two months at room temperature. Wani et al reported that (NH₄)ThF₈ to be formed after two hours based on the XRD pattern they obtained for the sample. They also did not report the size of the sample because the sample size might also affect the kinetics of terminal product formation. However, they mentioned that this XRD pattern did not include the peak at about $d = 0.815$ nm which determines the chemical composition of the sample to be (NH₄)₃ThF₇ or (NH₄)₄ThF₈. In this current work, we found that (NH₄)₃ThF₇ forms quickly after mixing ThO₂ and NH₄HF₂ whereas (NH₄)₄ThF₈ takes up to few months depending on the sample size.

Ammonolysis of (NH₄)₄ThF₈ at 800 °C produced ThNF through ThF₄. Therefore, further studies of the thorium system was performed using ThF₄. Heat treatment of ThF₄ under NH₃ at different temperatures demonstrated a ThF₄ decomposition through removing some of the fluorine atoms in the crystal system. Nitrogen incorporation into those vacant sites of the ThF_{4-x}, resulting in new phases with the chemical formula of

ThN_{1-x}F_{4-y}. Removal of fluorine and the incorporation of nitrogen to those vacancies stopped after the Th:N:F molar ratio of ThN_{1-x}F_{4-y} chemical phases reached 1:1:1, resulting a ThNF terminal product. Further heating of ThNF up to 1100 °C under ammonia and other atmospheres examined in this work resulted only in the formation of low-stoichiometric thorium nitride fluorides and an impurity phase ThO₂ due to minor oxygen pressure coming from the quartz tubing used in the experiment at elevated temperatures. In each of these experiments the cover gas used was high purity of 99.999%. Therefore, formation of ThO₂ was probably due to minute quantities of oxygen present in the cover gas and the experimental setup or due to the decomposition of ThNF under these experimental conditions. Although variation of the experimental conditions impacted the stoichiometry of ThNF, no conditions yielded a pure thorium nitride (ThN_x) phase under these experimental conditions. Observation of all these thorium-nitrogen-fluorides however inferred a possible reaction mechanism for the formation of ThNF starting from ThO₂ as shown below:



SEM imaging showed that the morphology of the samples involved in the reactions changed considerably. Plate-like morphology of the starting ThO₂ turned into an acicular particle shape upon conversion to (NH₄)₄ThF₈. The acicular (NH₄)₄ThF₈ particles became flat and agglomerated with partially crystallized facets upon thermal decomposition to

ThF₄. Particles of ThNF produced by the ammonolysis of ThF₄ consist of plate-like particles with porous surfaces. The average particle size and shape of (NH₄)₄ThF₈ shown in the SEM image (Figure 4.3) are much different than that of the starting ThO₂, implying a difficulty in ThO₂ conversion to (NH₄)₄ThF₈ at room temperature. Formation of ThF₄, on the other hand, was reasonable based on the high gap in the crystalline character between (NH₄)₄ThF₈ and ThNF according to SEM imaging. Morphology of ThF₄ is at an intermediate position with respect to the change of acicular shape of (NH₄)ThF₈ to a thin plate-like particle shape of ThNF. The porous characteristics of the ThNF particles have relatively large surface areas. This increase is likely the explanation for ThNF reactions with minute oxygen content in the experimental setup. A longer exposure of ThNF to minute quantities of oxygen at elevated temperatures such as 1100 °C thus produces the ThO₂ contaminant.

Transmission electron microscopy also showed some prominent differences in the nanostructures of (NH₄)₄ThF₈ and ThNF. Bulk area of the micro particles of (NH₄)₄ThF₈ exhibited polycrystalline characteristics with nano-scale crystalline patches. Some of these patches had fringe details in two directions while others showed fringe details either in one direction or none, showing the bulk of the particle to be low in crystallinity. Even in areas of high crystallinity, continuation of such crystallinity was disturbed by other polycrystalline characteristics. Therefore, the (NH₄)₄ThF₈ with its low-ordered crystal structure is vulnerable for attacks by other agents and is easy to decompose into other compounds given the enough energy to break the bonds.

In the case of ThNF, most of the microparticle areas imaged showed well-oriented fringes with two-directional details implying a high crystallinity. The porous

characteristics identified from SEM imaging were also found at nanoscale. The nanostructure of ThNF was observed well with the HRTEM and the crystal structure could also be confirmed. ThNF consisted with high-ordered nanostructure. Therefore, even at elevated temperatures it was difficult to change the chemical properties of the well-crystallized low-energy stable chemical phase. This is the likely reason for the difficulty of removing further fluorine from ThNF to produce ThN_x. However, the overall thermodynamic favorability of the oxide phase may still drive the ThNF susceptible to oxygen to form other crystalline chemical phases such as ThO₂.

Heating of thorium fluorides like (NH₄)₄ThF₈, ThF₄, and ThNF after mixing with LiNH₂ under NH₃ produced Th₂N₃ of a unit cell with lattice parameters of $a = b = 3.8843(1)$ and $c = 6.1853(3)$ Å. However, ThF₄ and ThNF seem to be more suitable in synthesizing Th₂N₃ under the experimental conditions examined. Synthesis of single-phased Th₂N₃ is difficult according to the XRD results due to the formation of secondary ThO₂. Th₂N₃ was identified based on the XRD powder patterns of the samples based on results in the literature. However, the same XRD pattern could be matched with Th₂N₂O. One of the experimental and calculated XRD patterns of Th₂N₂O and Th₂N₃ are shown in Figure 14.23a and 14.23b, respectively. These refinements do not include the ThO₂ pattern for the clarity. The calculated patterns using both Th₂N₂O and Th₂N₃ crystallographic data match quite well with the experimental XRD. In both these compounds, the two Th atoms reside in (1/3 2/3 0.235) position. Two N atoms in Th₂N₃ are in (000) and (1/3 2/3 0.631) positions. O and N atoms have similar positions in Th₂N₂O, i.e. (000) and (1/3 2/3 0.631) causing similar diffraction pattern to that of Th₂N₃ [10].

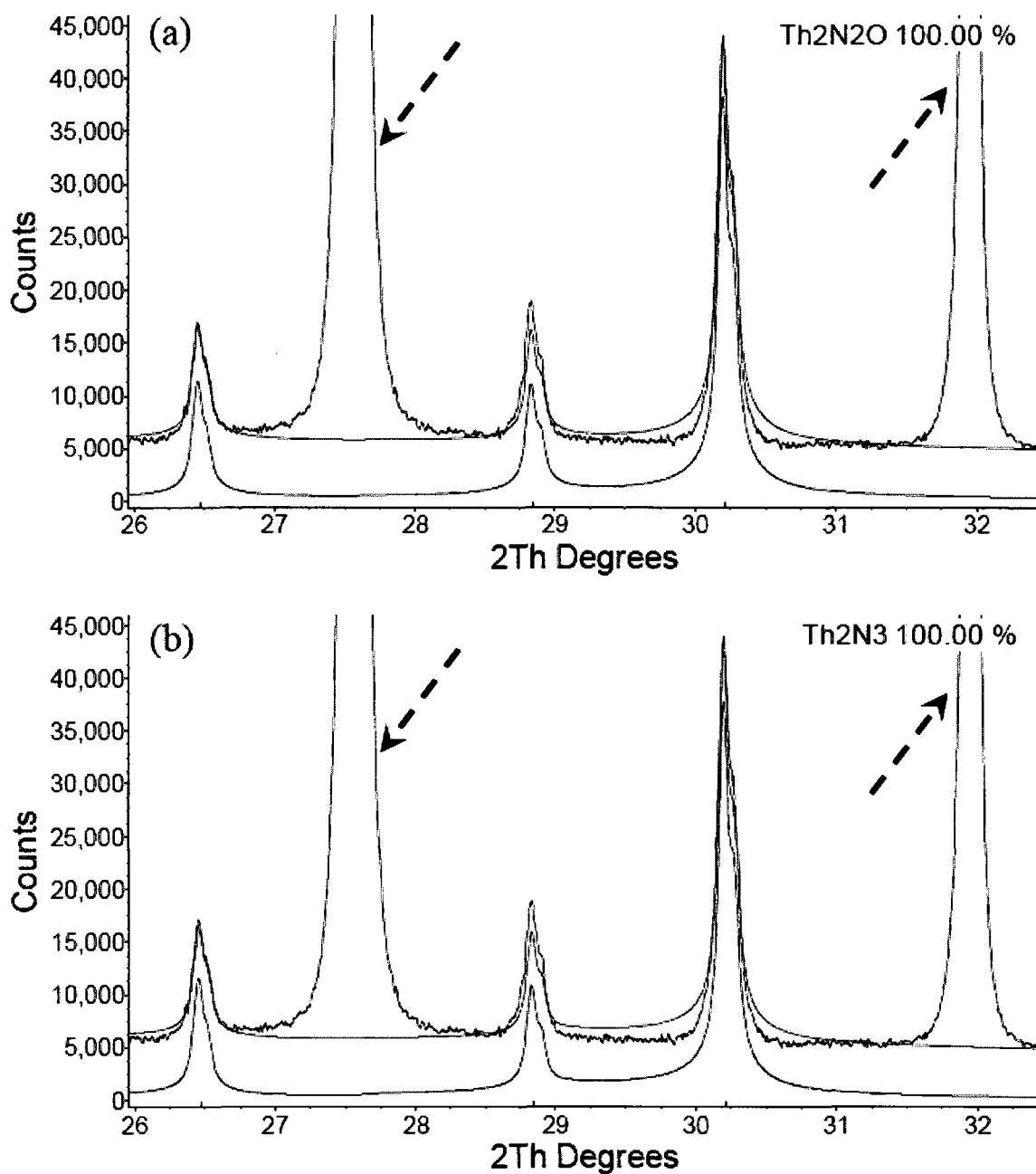


Figure 4.23 XRD powder refinements of the sample synthesized by heating a mixture of ThNF and LiNH₂ at 800° 30min under NH₃. (a) Using only Th₂N₂O and (b) using only Th₂N₃ crystal data. ThO₂ (peaks highlighted with arrows) was not used in the refinement for clarity.

Morphological evaluations completed on the as-synthesized samples showed that Th_2N_3 was highly susceptible to oxygen because ThO_2 forms within Th_2N_3 particles and not as a separate chemical phase or after the synthesis due to oxygen contamination from air like in the case of UN. Possible oxygen contamination of LiNH_2 due to its high reactivity [14] with moisture can also be another reason for oxide formation. The presence of another amorphous chemical species was also suspected since fluorine was detected in the sample by EDS studies. Fluorine was present in the sample up to 4 wt% with about 6 wt% of nitrogen. This observation could be explained by the presence of bulk amorphous particle areas in the sample as detected in the SEM images. Furthermore, the fluorine could be present as an amorphous LiF phase since crystallized LiF was seen in one sample where ThF_4 was mixed with LiNH_2 of 4 molar ratio (Table 4.5).

Elemental mapping showed that nitrogen is distributed throughout the sample although a few N-rich areas also exist. Oxygen distribution was uniform suggesting a surface driven reaction of minute quantities of oxygen with Th_2N_3 particles. This is because thickness of the particles did not affect the elemental mapping results obtained for oxygen like in the case of thorium and nitrogen in Figure 4.19b and 4.19c, respectively. These N rich areas of large particle showed no O suggesting an absence of $\text{Th}_2\text{N}_2\text{O}$ and presence of Th_2N_3 . The nitrogen rich areas of the sample showed single-phased Th_2N_3 characteristics according to HRTEM even though amorphous patches could be found within the imaged particle area. Also, the crystallization of these areas was affected by randomly distributed disorientations of the atomic layers of lattices. These observations indicate a disruption of the Th_2N_3 formation by amorphous characteristics and ThO_2 which is trying to form within Th_2N_3 grains. Figure 4.21 is

another example of ThO_2 interferences on Th_2N_3 crystallization. Here, ThO_2 seems to be the major phase while Th_2N_3 plays the secondary phase characteristics. Successful formation of ThO_2 crystals within the crystalline Th_2N_3 grains and thus in majority of particles was also detected by HRTEM (Figure 4.22). These observations further show that Th_2N_3 and ThO_2 are interchangeably formed in the nanostructure of each species, and thus unraveling the failure to dominate strong ionic bonding of Th_2N_3 in the increment of its stability.

Heat treatments of Th_2N_3 at temperatures > 800 °C under inert atmosphere showed Th_2N_3 is unstable at these temperatures. Th_2N_3 converted completely into ThO_2 on sufficient heating even under inert atmosphere of high-purity Ar(g) of 99.999% and a getter (Zr sponge). Presence of ThO_2 within the Th_2N_3 crystallized particles could be a dominant reason for this conversion. However, the initial formation of ThO_2 in the Th_2N_3 sample even under NH_3 , which is a nitrogen agent at elevated temperatures, confirms the fact that the complete conversion of Th_2N_3 into ThO_2 is due to its oxygen scavenging property. Presence of ThO_2 within the Th_2N_3 particles and the uniform distribution of oxygen on the particle surfaces can be related as the main reasons for Th_2N_3 to be easily affected by oxygen. These observations further explain why the thorium nitrides as general always consist with a ThO_2 secondary phase.

4.8 Conclusions

Solid-state reaction of ThO_2 with NH_4HF_2 at room temperature showed to form two products: $(\text{NH}_4)_3\text{ThF}_7$ and $(\text{NH}_4)_4\text{ThF}_8$. The first compound was produced quickly while the second formed slowly over time. The $(\text{NH}_4)_4\text{ThF}_8$ was the terminal product of the

overall reaction. The final product of the ammonolysis of $(\text{NH}_4)_4\text{ThF}_8$ at temperatures ranging from 800 to 1100 °C was found to be ThNF. Attempting to further react the material under NH_3 , N_2 , or N_2/H_2 (5%) to produce ThN_x chemical phases instead resulted in the formation of low-stoichiometric ThNF chemical phases with minor ThO_2 phase. Formation of ThO_2 was most likely due to the trace oxygen in the experimental system, often formed at elevated temperatures over common laboratory equipment materials like the quartz. Thermal decomposition of $(\text{NH}_4)_4\text{ThF}_8$ to ThNF occurred through a ThF_4 intermediate and following a slow nitridization of ThF_4 under NH_3 through low-stoichiometric thorium-nitrogen-fluoride ternary chemical phases. Thermal behavior of ThNF under different chemical environments confirmed that the stoichiometric thorium nitrogen fluoride (ThNF) is the preferable chemical composition of all thorium nitride fluorides produced during the $(\text{NH}_4)_4\text{ThF}_8$ ammonolysis above 800 °C.

Distinct morphologies of the starting materials and final products of the reactions studied confirmed the chemical transformations identified by XRD. Polycrystalline characteristics were identified in the nanostructure of the $(\text{NH}_4)_4\text{ThF}_8$ whereas in ThNF, long-ranged single crystal characteristics were observed over a wide range of the particles. Despite the appearance of the larger particles shown by SE SEM, HRTEM demonstrated the final ThNF product to be more crystalline than its precursors explaining the high stability of ThNF towards substitution of fluorine with nitrogen.

Synthesis of Th_2N_3 was possible by heating a solid mixture of thorium fluorides/ LiNH_2 under NH_3 at 800 °C temperature. Formation of a secondary ThO_2 chemical phase was identified in the synthetic process. Further heating of Th_2N_3 samples produced ThO_2 by converting Th_2N_3 completely or partially depending on the

temperature and time of heating. Powder XRD revealed each Th₂N₃ sample synthesized contain ThO₂ phase up to > 50 wt%. SEM images showed that the morphology of ThO₂ is dominant with respect to the bulk of the sample even though the particles showed less crystallinity than the ThO₂ crystalline particles. TEM imaging also indicated ThO₂ morphology to be more prominent in the isolated particle clusters of small size.

Multibranched grains seen in SEM imaging and the presence of lattice fringes correspond to both Th₂N₃ and ThO₂ together with amorphous patches in HRTEM indicated that the Th₂N₃ particles are not present as a separated chemical phase in most of the areas but as a chemical phase branched with ThO₂ especially at micro-scale. These observations infer that the Th₂N₃ is difficult to synthesize as a single-phased compound by this particular method. Furthermore, the Th₂N₃ reactivity with oxygen could be reasoned by microscopic evaluation of the morphology and microstructure of the samples. These microscopic observations could also be used to explain why other thorium nitrides such as Th₃N₄ and ThN are susceptible to oxygen as observed in the literature.

References

- (1) Benz, R.; Hoffman, C. G.; Rupert, G. N. *Phys. Inorg. Chem.* **1967**, *89*, 191-197.
- (2) Auskern, A. B.; Aronson, S. *J. Phys. Chem. Solids* **1967**, *28*, 1069-1071.
- (3) Chiotti, P. *J. Am. Ceram. Soc.* **1952**, *35*, 123-130.
- (4) Olson, W. M.; Mulford, R. N. R. *J. Phys. Chem.* **1965**, *69*, 1223-1226.
- (5) Uno, M.; Katsura, M.; Miyake, M. *J. Less-Comm Metals* **1986**, *121*, 615-619.
- (6) Brese, N. E.; Disalvo, F. J. *J. Solid State Chem.* **1995**, *120*, 378-380.
- (7) Aronson, S.; Auskern, A. B. *J. Phys. Chem.* **1966**, *70*, 3937-3941.

- (8) Uno, M.; Katsura, M.; Miyake, M. *Inorg. Chim. Acta.* **1987**, 140, 123-126.
- (9) Benz, R.; Zachariassen, W. H. *Acta Cryst.* **1966**, 21, 838-840.
- (10) Wani, B. N.; Patwe, S. J.; Rao, U. R. K.; Venkateswarlu, K. S. *J. Fluorine Chem.* **1989**, 44, 177-185.
- (11) Penneman, R. A.; Ryan, R. R.; Rosenzweig, A. *Chem. Commun.* **1968**, 16, 990-991.
- (12) Juza, R.; Sievers, R. *Z. Anorg. Allg. Chem.* **1968**, 363, 258-272.
- (13) Benner, G.; Muller, B. G. *Z. Anorg. Allg. Chem.* **1990**, 588, 32-42.
- (14) MSDS sheet, CAS No. 7782-89-0.

CHAPTER 5

SYNTHESIS AND CHARACTERIZATION OF NEPTUNIUM NITRIDES

5.1 Introduction

As previously described (section 1.1), actinide mononitrides have preferable properties for fast reactors when compared to oxides [1]. Mononitrides have also been considered as using a fuel for reactors to burn minor actinides [2]. For this reason most of the studies on actinide nitrides have focused on aspects related to nuclear reactors. For NpN few reports are available describing physical and chemical properties of the material [3-5]. In fact, there are no publications on microscopic evaluation of the NpN system. Synthesis and characterization of neptunium mononitride along with information on a number of related neptunium-based compounds are presented in this chapter.

Synthesis of NpN have been reported by several authors using a range of methods. NpN can be synthesized by reacting Np metal with $N_2/H_2(0.5\%)$ gas mixture at 600 °C [6]. However, this process involves further heating of the product to 1500 °C in order to remove any unreacted Np metal and to decompose produced NpH_3 . Also, the production of the Np metal and avoidance of oxidized involves effort. Therefore, this route is difficult to follow as a common laboratory procedure. Irving et al [7] reported the synthesis of NpN using NpH_3 with NH_3 vapor. The reaction was conducted at 750 – 775 °C. They further reported the NpN to be isostructural to UN and PuN. Another attempt to produce NpN utilizing a reaction of $NpCl_4$ with $NH_3(g)$ by the same group was

failed and instead formed NpCl_3 . The reaction was repeated up to a temperature of 1000 °C. The most commonly used method to fabricate actinide mononitrides is the carbothermic reduction [8], and it has been used to synthesize NpN [3]. Using carbothermic reduction of NpO_2 , NpN could be synthesized after heating to 1550 °C for 10 hrs.

The fluoride route, which is described in this work, has fewer difficulties in forming NpN compared to the methods using Np metal or its hydrides as starting materials. The temperatures used in the carbothermic reduction are often too high, resulting in secondary chemical phases without specific methods in place. The fluoride route to fabricate NpN and other neptunium-based compounds presented in this chapter was examined to overcome issues related to the high temperature from the carbothermic reduction. Synthesis of NpN at 900 °C was successful. It is expected lower temperatures, such as 700 to 800 °C, should also form the desired product.

X-ray powder diffraction together with electron density maps are used to determine chemical phases of both novel and known compositions. Powder diffraction refinement was used successfully to describe the crystallography of these new compounds. Section 5.3.1 through 5.3.3 consists of the characterization of ammonium neptunium fluorides. Structure refinement and microscopic evaluation of two distinct compounds are presented. One of the compounds is reported here for the first time. Even though the other compound has a known crystallography [9], a new crystal system was introduced with an accurate refinement.

Section 5.3.4 describes the reactions and products involved in the heat treatment of ammonium neptunium fluorides in two different atmospheres (NH_3 and Ar). Compounds

identified for the first time were characterized using XRD and were refined using Rietveld method using proposed crystal systems. Further characterization of the compounds was carried out using electron microscopy in Section 5.3.5. Moreover, the morphological observations coupled with nanostructural evaluation of the neptunium system are reported for the first time. Presence of secondary oxide chemical phase such as NpO_2 is always a problem due to the oxidation potential of nitride compounds. Therefore, the kinetics involved in the NpN reaction with oxygen in air is also presented. Nanostructural characterization was used to answer the question of why or how the oxidation of NpN occurs, producing the secondary NpO_2 chemical phase. The optimization of the experimental conditions was done only up to a point at which the phase purity of NpN is adequate for microscopic characterization. Future work on the synthesis of NpN with the experimental conditions reported here are suggested under high purity conditions such as in a glove box of inert atmosphere.

5.2 Experimental Details and Characterization Methods

5.2.1 Synthesis of Ammonium Neptunium Fluorides ($(\text{NH}_4)_x\text{NpF}_y$)

Five batches of ammonium neptunium fluorides were made for the ammonolysis of the step to synthesize NpN. All the powder manipulations were performed inside a glove box. NpO_2 powder masses used in these batches were 132, 11, 78, 113, and 28 mg. In the preparation of ammonium neptunium fluorides, first the NpO_2 solid was added to a polyvinyl vial with solid NH_4HF_2 . The mixture was then ground with a spatula for 10 min. The polyvinyl vial was then sealed with a cap and left at room temperature for about two months. Because no known chemical composition was identified in the sample with

initial XRD, the sample was heated at 80 °C in an oven. After 4 months of heating the first known compound was identified in the sample. Another sample with similar mass ratio of NpO_2 and NH_4HF_2 was heated in the oven for a week at 100 °C to evaluate kinetics. A third sample with same mass ratio was prepared, but the sample was kept at ambient conditions to check the feasibility of formation of a second compound of the chemical composition $(\text{NH}_4)_4\text{NpF}_8$ at room temperature.

5.2.2 Ammonolysis of $(\text{NH}_4)_x\text{NpF}_y$

Samples containing $(\text{NH}_4)_2\text{NpF}_6$, $(\text{NH}_4)_4\text{NpF}_8$, or a mixture of both were heated in the quartz tube as described in section 2.3.2 under $\text{NH}_3(\text{g})$. Because of the high activities of the neptunium bearing samples and the limited quantities available, a mass of 2 to 30 mg of the $(\text{NH}_4)_x\text{NpF}_y$ sample was used in each of these experiments. A few experiments were performed at the beginning of the evaluation of neptunium system with a covered platinum sheet used to hold the sample. An opened sheet of platinum was used after determining proportionality between the reaction rates and sample exposure to the cover gas.

5.2.3 Heat Treatment of the Resulting NpN_x under an Inert Atmosphere

The resulting products from the ammonolysis of $(\text{NH}_4)_x\text{NpF}_y$ were further heated to an elevated temperature such as 1100 °C under argon atmosphere (99.999 % purity). Some of the samples were first ammonolyzed and the covering gas was changed to $\text{Ar}(\text{g})$ when further heating was performed to decompose the higher neptunium nitrides such as NpN_2 and Np_2N_3 into the final product; NpN .

5.2.4 Characterization Methods

Identification of the chemical phases in the synthesized samples was done by XRD powder patterns. Rietveld method was used in the structure refinements. Le Bail decomposition was also utilized in solving the structures of $(\text{NH}_4)_x\text{NpF}_y$ samples with Charge Flipping technique. Initial estimates of the structures of $(\text{NH}_4)_2\text{NpF}_6$ and $(\text{NH}_4)_4\text{NpF}_8$ was performed using isomorphous structure parameters of $(\text{NH}_4)_2\text{CeF}_6$ (ICSD # 9890) and $(\text{NH}_4)_4\text{UF}_8$ (ICSD # 9913), respectively. SEM and TEM were also used in characterizing the samples with respect to their morphology and nanostructures.

5.3 Results and Discussion

5.3.1 Structure Solutions of $(\text{NH}_4)_2\text{NpF}_6$ and $(\text{NH}_4)_4\text{NpF}_8$

Solid state reaction of NpO_2 with NH_4HF_2 at 80 °C produced $(\text{NH}_4)_2\text{NpF}_6$, which is isostructural with orthorhombic $(\text{NH}_4)_2\text{CeF}_6$ of *Pbcn* space group, after a 8 months (4 months at room temperature and another 4 months at 80 °C) time period. Profile fit of the X-ray powder diffraction of the sample is shown in Figure 5.1 and the refined lattice parameters are given in Table 5.1.

Table 5.1 Refined lattice parameters of $(\text{NH}_4)_2\text{NpF}_6$ and $(\text{NH}_4)_4\text{NpF}_8$ structures.

Compound	Space group	Refined lattice parameters					
		a (Å)	b (Å)	c (Å)	α	β	V
$(\text{NH}_4)_2\text{NpF}_6$	<i>Pbcn</i>	7.079(3)	12.133(5)	7.518(3)	90	90	645.8(4)
$(\text{NH}_4)_4\text{NpF}_8$	<i>C2/c</i>	13.054(4)	6.681(2)	13.676(5)	90	121	1020.9(6)

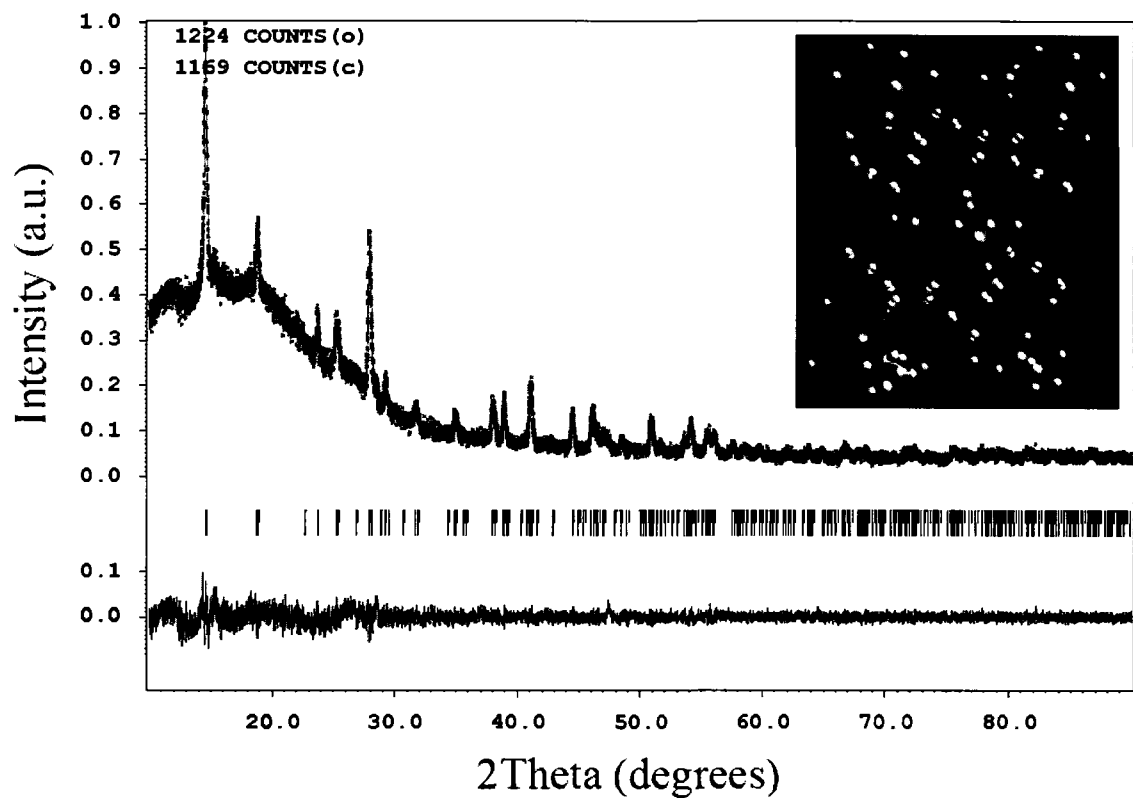


Figure 5.1 Profile fit to the $(\text{NH}_4)_2\text{NpF}_6$ XRD powder pattern using jana2000. Observed intensities are in dots, the overlapping continuous line is the calculated profile, and the continuous line at the bottom is the difference. Inset of the figure is a graphical interpretation of the unit cell of the compound.

Table 5.2 Structure parameters of $(\text{NH}_4)_2\text{NpF}_6$.

		X	y	z	g	B
N1	N	0.0168	0.343	0.4976	1	-0.2672
Np1	Np+4	0	0.0414	0.25	1	-0.10(45)
F1	F-1	0.2089	0.4816	0.2019	1	13.6866
F2	F-1	0.1885	0.1868	0.2867	1	7.1237
F3	F-1	0.9538	0.0979	0.5444	1	20

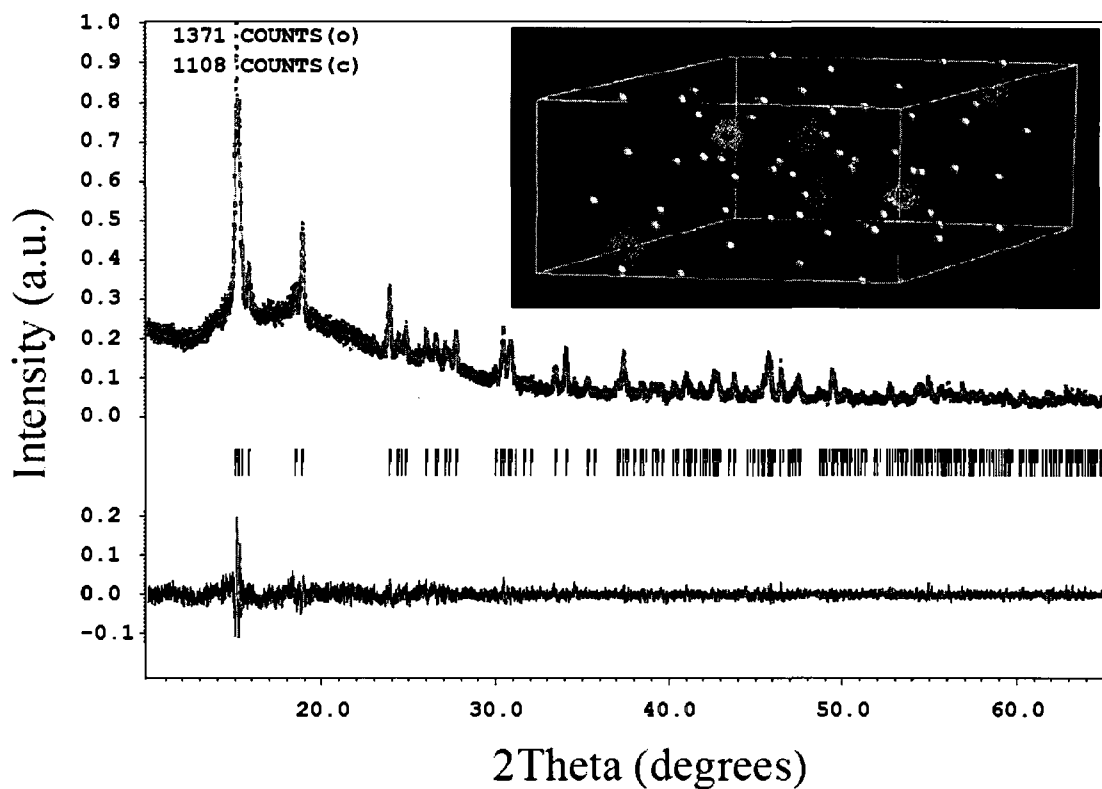


Figure 5.2 Profile fit to the $(\text{NH}_4)_4\text{NpF}_8$ XRD powder pattern using TOPAS. Inset of the figure is a graphical interpretation of a Fourier map of the compound.

Table 5.3 Structure parameters of $(\text{NH}_4)_4\text{NpF}_8$.

		x	y	z	g	B
N1	N	0.3824	0.1531	0.3921	1	-6.00(95)
N2	N	0.2115	0.1111	0.0836	1	-5.9(10)
Np1	Np+4	0	0.1682	0.25	1	-2.96(60)
F1	F	0.0243	0.0071	0.1166	1	4.9(14)
F2	F	0.1597	-0.0317	0.358	1	-0.7(11)
F3	F	0.1599	0.3237	0.2528	1	-2.20(89)
F4	F	0.0784	0.3952	0.3921	1	-1.1(10)

The structure parameters are also provided in Table 5.2. When the NpO_2 and NH_4HF_2 mixture was heated at $100\text{ }^\circ\text{C}$ for a week, a new compound of neptunium was observed. This new compound was isostructural with monoclinic $(\text{NH}_4)_4\text{UF}_8$ of the space group $C2/c$. Figure 5.2 displays the profile fit of the XRD powder pattern of the sample and a figure indicating the Fourier map calculated from the pattern. Refined crystallographic data of these two compounds are given in Table 5.1 and Table 5.3.

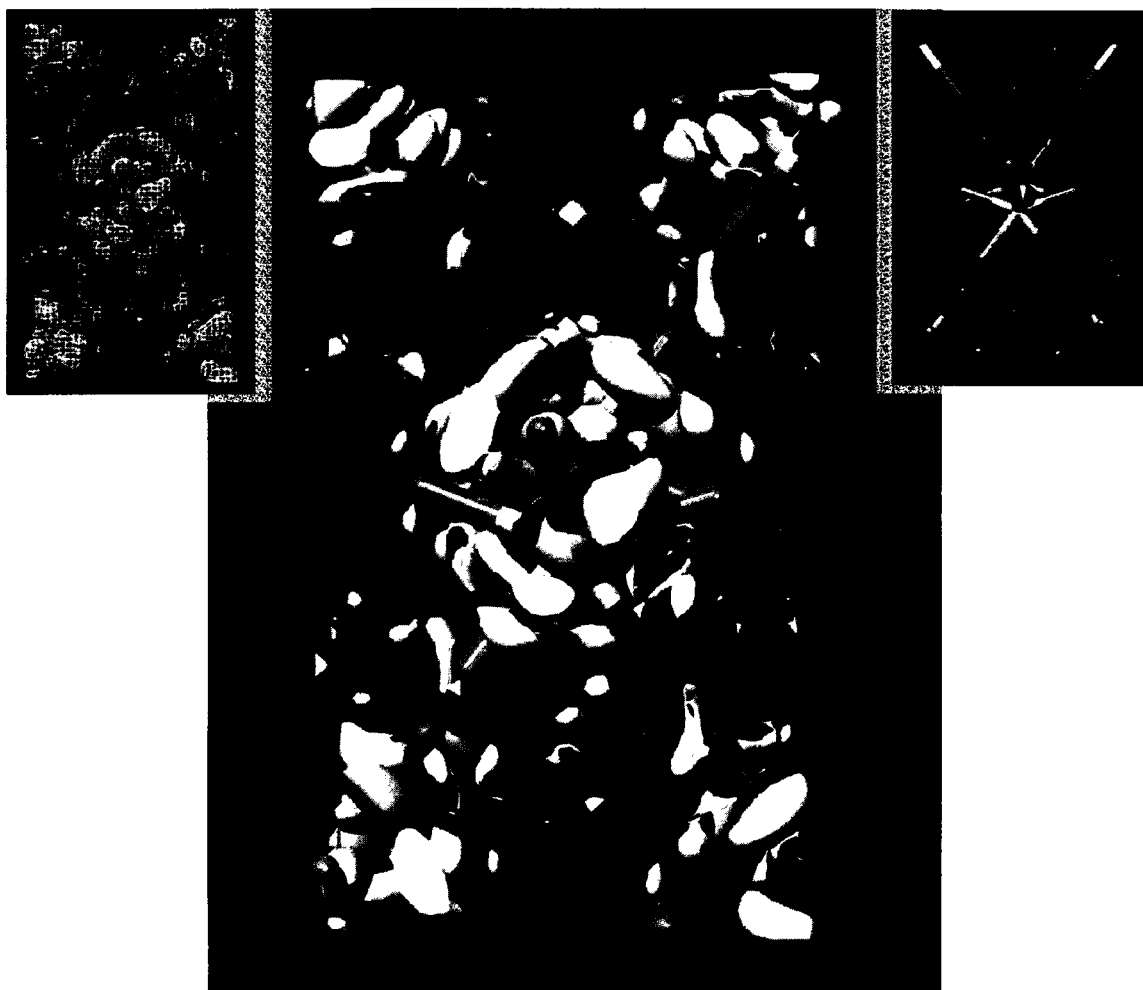


Figure 5.3 A structure fitting of $(\text{NH}_4)_2\text{NpF}_6$ using the electron density map calculated using charge flipping of the powder diffraction and a model of the crystal structure in $[001]$ direction. Insets in left and right are the electron density map and a structural model, respectively.

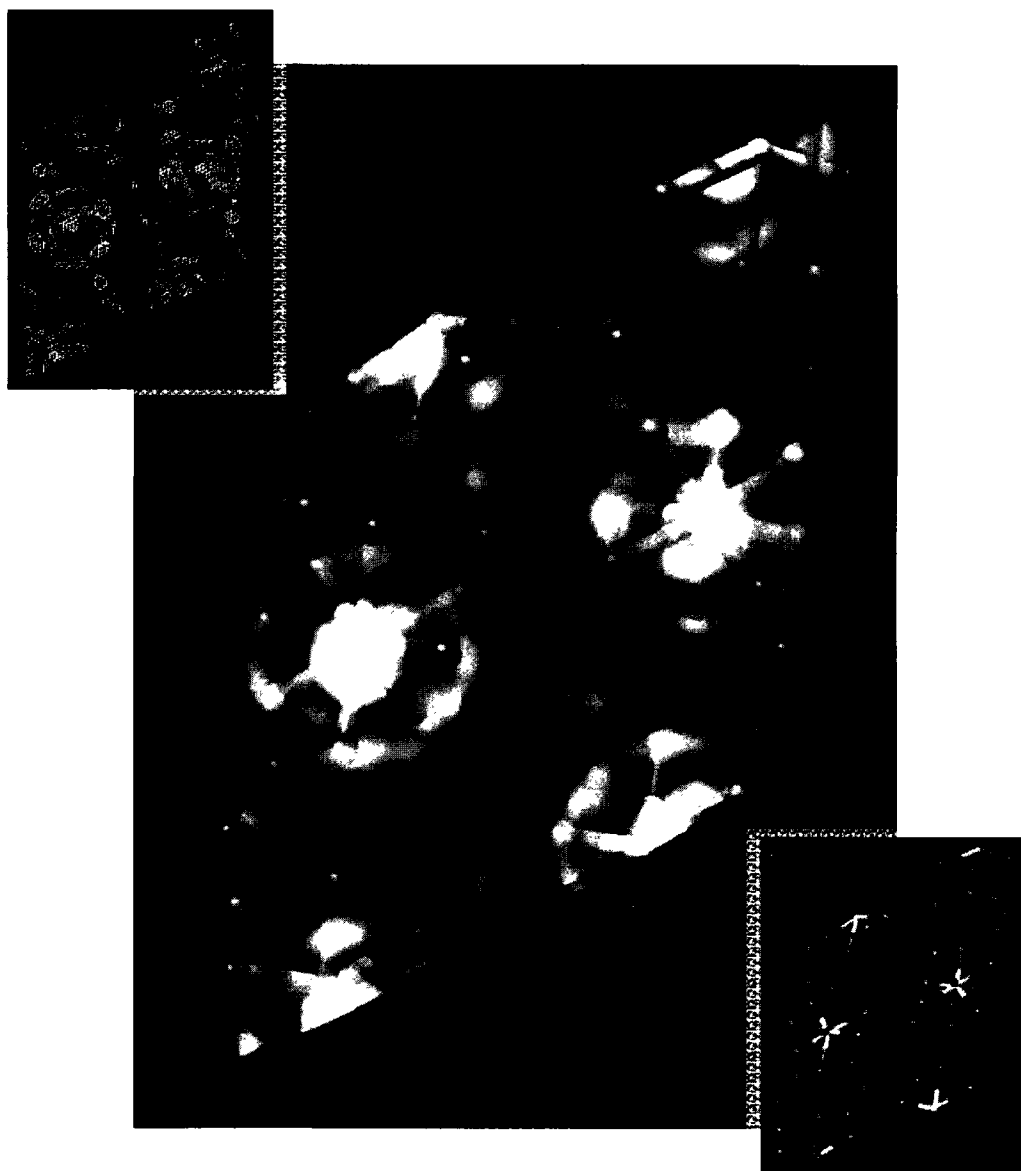


Figure 5.4 Structure fitting of $(\text{NH}_4)_4\text{NpF}_8$ using an electron density map (inset to left) and a model (inset to right) of the crystal structure in $[010]$ direction.

Crystal structure fitting of the two ammonium neptunium fluorides was also done using the experimental electron density maps calculated by performing the charge flipping on the XRD powder patterns of $(\text{NH}_4)_2\text{NpF}_6$ and $(\text{NH}_4)_4\text{NpF}_8$ (Figure 5.3 and 5.4). The calculated experimental electron densities of each compound were fitted against a model of the crystal structure in a particular direction. Both figures indicate high

electron densities at the Np sites of the crystal structures as expected. Thus, these electron densities confirm the crystallography of the structures used to perform the full profile fits of the XRD powder patterns in Figures 5.1 and 5.2.

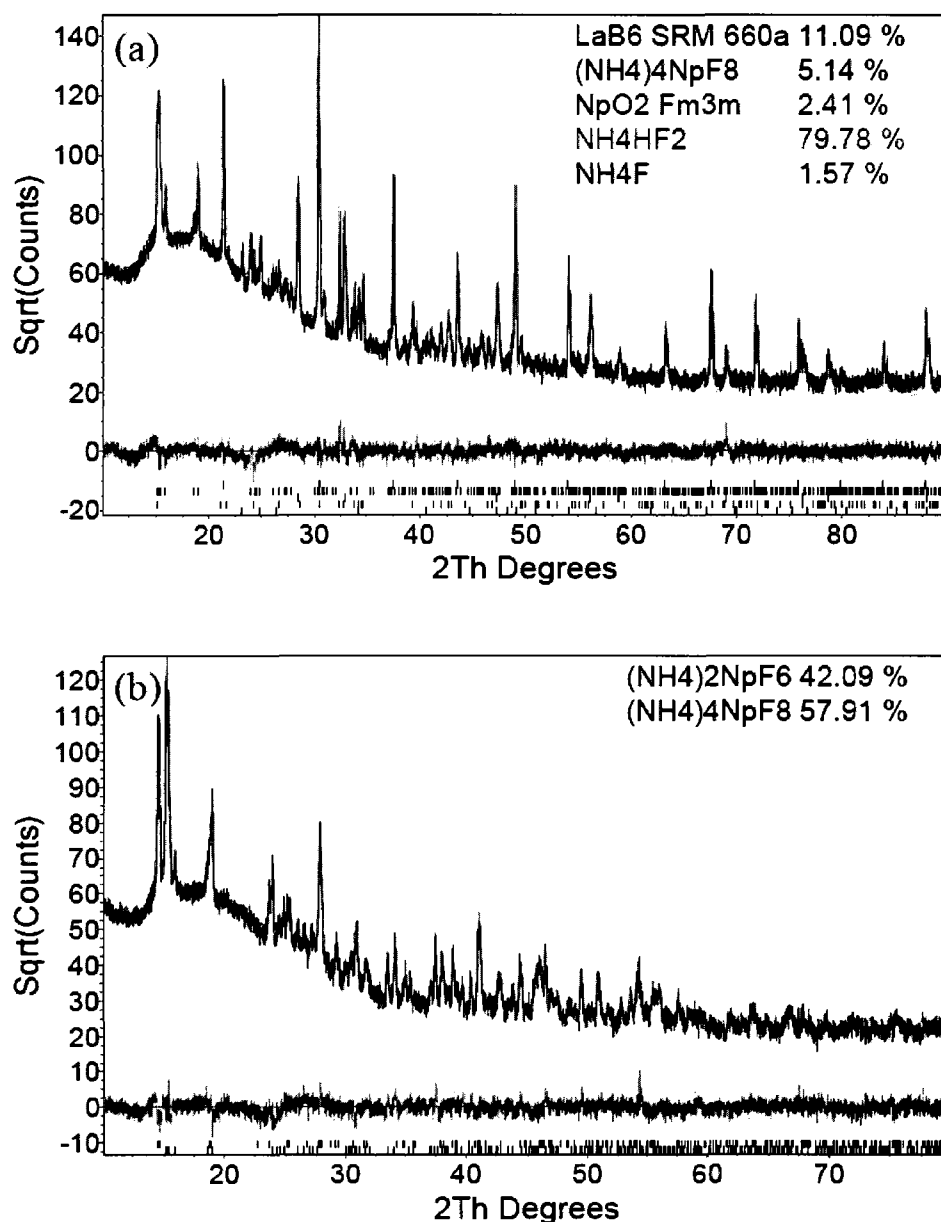
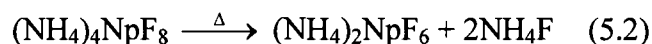
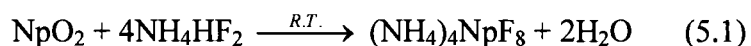


Figure 5.5 Profile fits of the XRD powder patterns of the NpO₂ and NH₄HF₂ mixture after 2 days at room temperature (a) and before completion of the conversion of (NH₄)₄NpF₈ into (NH₄)₂NpF₆ at 80 °C (b).

5.3.2 Reaction Mechanism of NpO₂ and NH₄HF₂

The sample prepared at room temperature to test the slow reaction of the NpO₂ together with NH₄HF₂ contain a small amount of (NH₄)₄NpF₈ after two days (Figure 5.5a) A mixture of (NH₄)₄NpF₈ and (NH₄)₂NpF₆ was also found in one of the samples after heating the NpO₂ and NH₄HF₂ mixture at 80 °C for about 3 months (Figure 5.5b). These observations suggest a possible reaction mechanism/sequence of NpO₂ and NH₄HF₂ as follows:



5.3.3 Microscopic Study of (NH₄)_xNpF_y Samples

SEM images of (NH₄)₄NpF₈ and (NH₄)₂NpF₆ samples in Figures 5.6a and 5.6b show different morphological characteristics. Even though both samples consist of agglomerated particles, (NH₄)₄NpF₈ show sharp edged particle characteristics (inset of Figure 5.6a) whereas (NH₄)₂NpF₆ showed no such sharp edged particles. Moreover, (NH₄)₂NpF₆ consists of particles of incompletely crystallized flat surfaces. Particle sizes of (NH₄)₄NpF₈ range from 2 to 50 μm depending on how well they are separated. This range varies from 1 to 20 μm in the case of (NH₄)₂NpF₆ sample. The chemical analyses of both samples are displayed in Table 5.4. These values were obtained by the corresponding EDS spectra of the SEM imaging. Experimental chemical analyses differ considerably from that of the theoretical amounts due to the errors relate to the EDS (semi-quantitative) method.

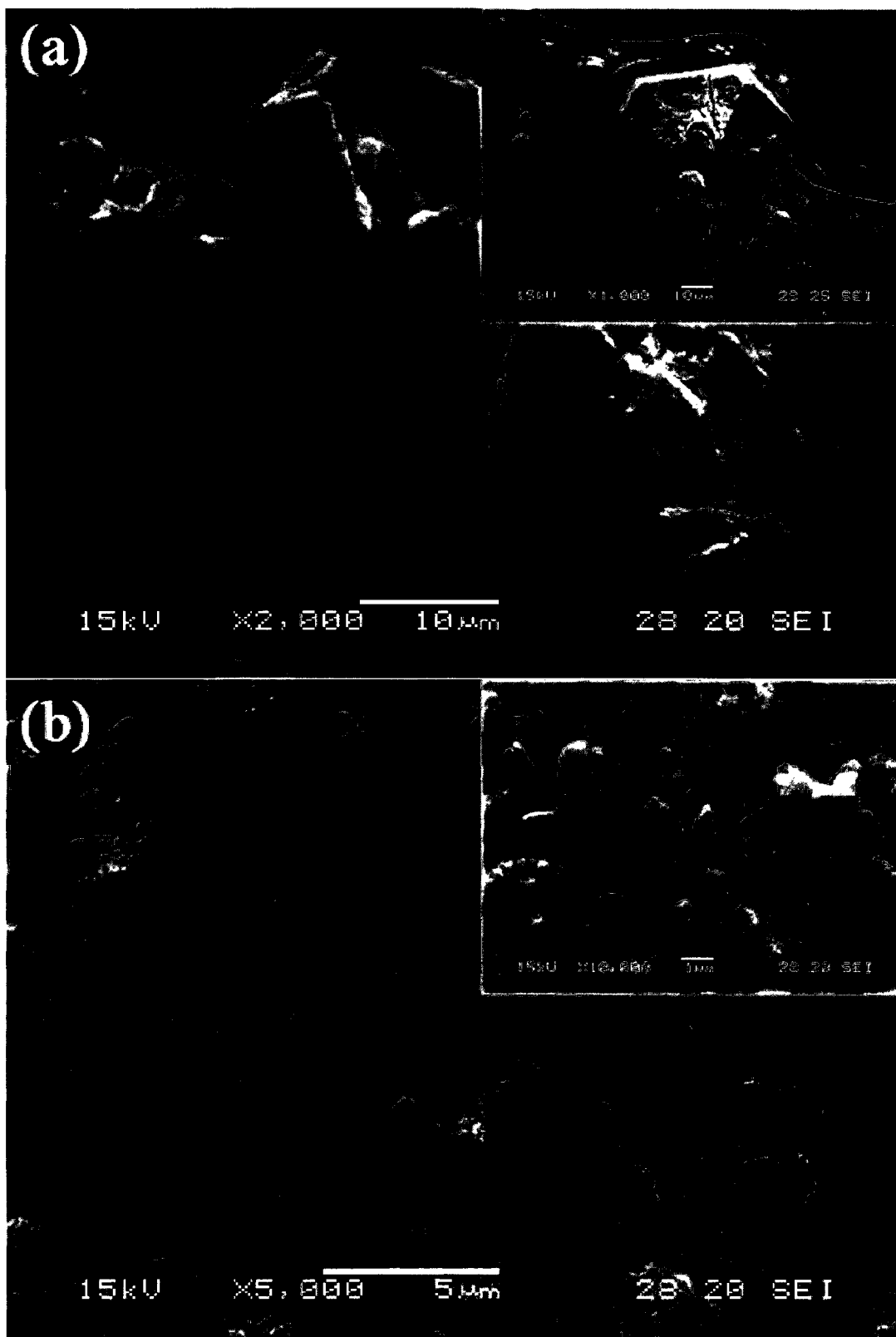


Figure 5.6 SEM images of (a) $(\text{NH}_4)_4\text{NpF}_8$ and (b) $(\text{NH}_4)_2\text{NpF}_6$. Insets of (a) and (b) are a sharp edged particle of $(\text{NH}_4)_4\text{NpF}_8$ and a magnified image of $(\text{NH}_4)_2\text{NpF}_6$.

Table 5.4 Chemical analyses of $(\text{NH}_4)_2\text{NpF}_6$ and $(\text{NH}_4)_4\text{NpF}_8$ samples. Standard deviations (S.D.) of each experimental value are also given.

Element	Weight %					
	$(\text{NH}_4)_4\text{NpF}_8$			$(\text{NH}_4)_2\text{NpF}_6$		
	Theoretical	Experimental	S.D.	Theoretical	Experimental	S.D.
N	12.1	6.08	2.03	7.2	6.55	1.38
F	33.0	37.21	5.57	29.5	33.93	4.52
Np	51.4	56.71	7.09	61.2	59.52	5.57
H	3.5	-	-	2.1	-	-
Total	100.0	100.00		100.0	100.00	

HRTEM imaging of both ammonium neptunium fluoride samples showed they have particle areas of different crystallinity. Figure 5.7 shows HRTEM of two particle areas of $(\text{NH}_4)_4\text{NpF}_8$. Particle in Figure 5.7a has crystalline domains of different orientations and the corresponding FFT (Fast Fourier Transformed) in Figure 5.7b of the whole image verifies the polycrystallinity of this particle area. This compound also consists of single crystal areas such as shown in Figure 5.7c. In this area, two grains of single crystal characteristics were identified.

$(\text{NH}_4)_2\text{NpF}_6$ also displayed similar nanostructural properties as shown in Figure 5.8. Particle in Figure 5.8a consists of crystalline domains whereas the particle in Figure 5.8c displays single crystals. Particle in Figure 5.8c has three single crystals of similar orientation. These three grains are overlapped on each other (dashed –lines) as observed by the corresponding FFT in Figure 5.8d. Thus, both samples have polycrystalline characteristics and as well as single crystal characteristics of large domain areas.

Furthermore, the corresponding FFT micrographs (Figure 5.7b and Figure 5.8b) of the polycrystalline particles of both compounds show that they have a similar discrete-like spots making rings implying a similar grain sizes.

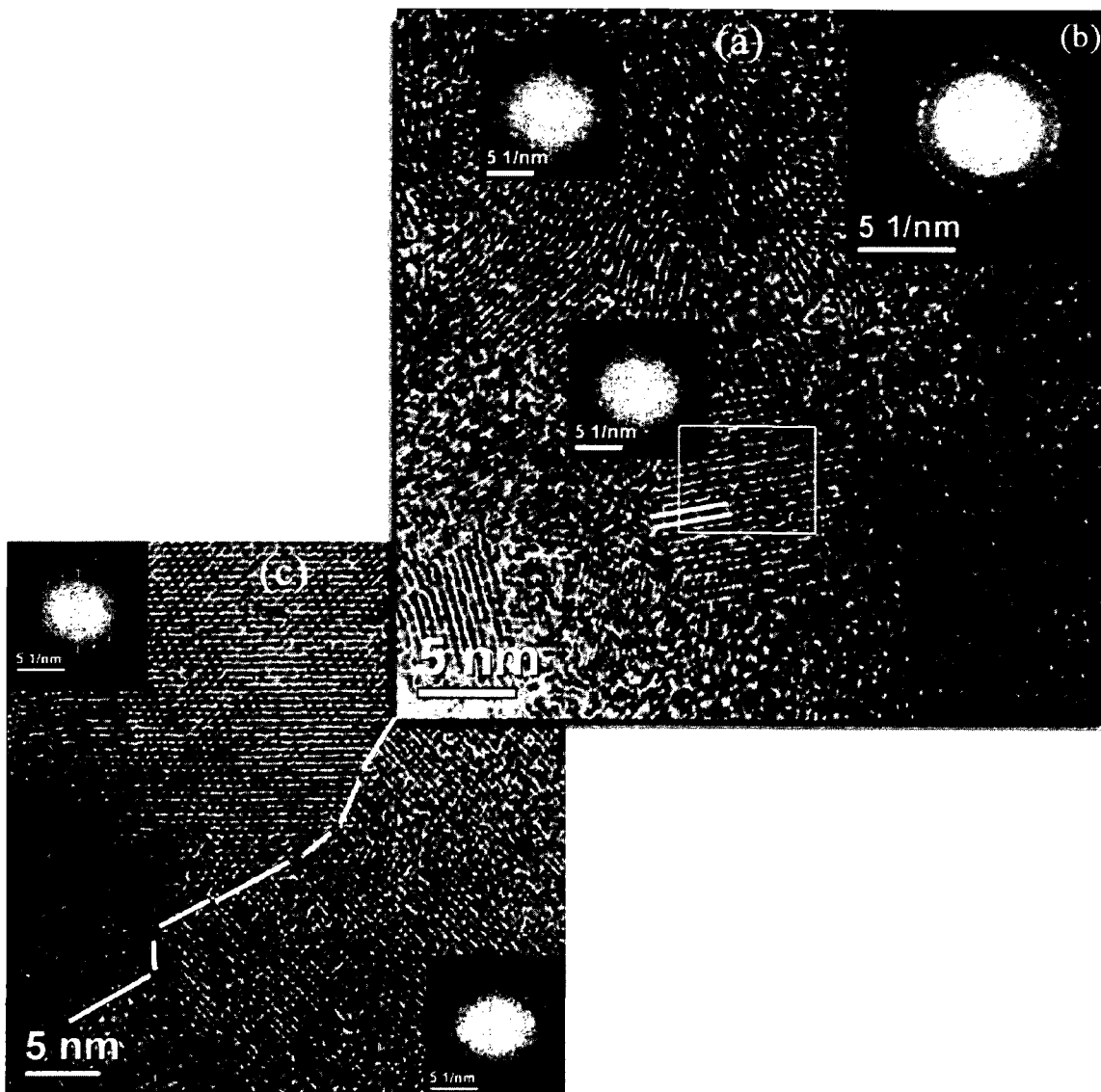


Figure 5.7 HRTEM image of $(\text{NH}_4)_4\text{NpF}_8$. (a) HRTEM showing polycrystalline character of the particle, (b) FFT of image (a), and (c) HRTEM of another area of two grains of single crystal.

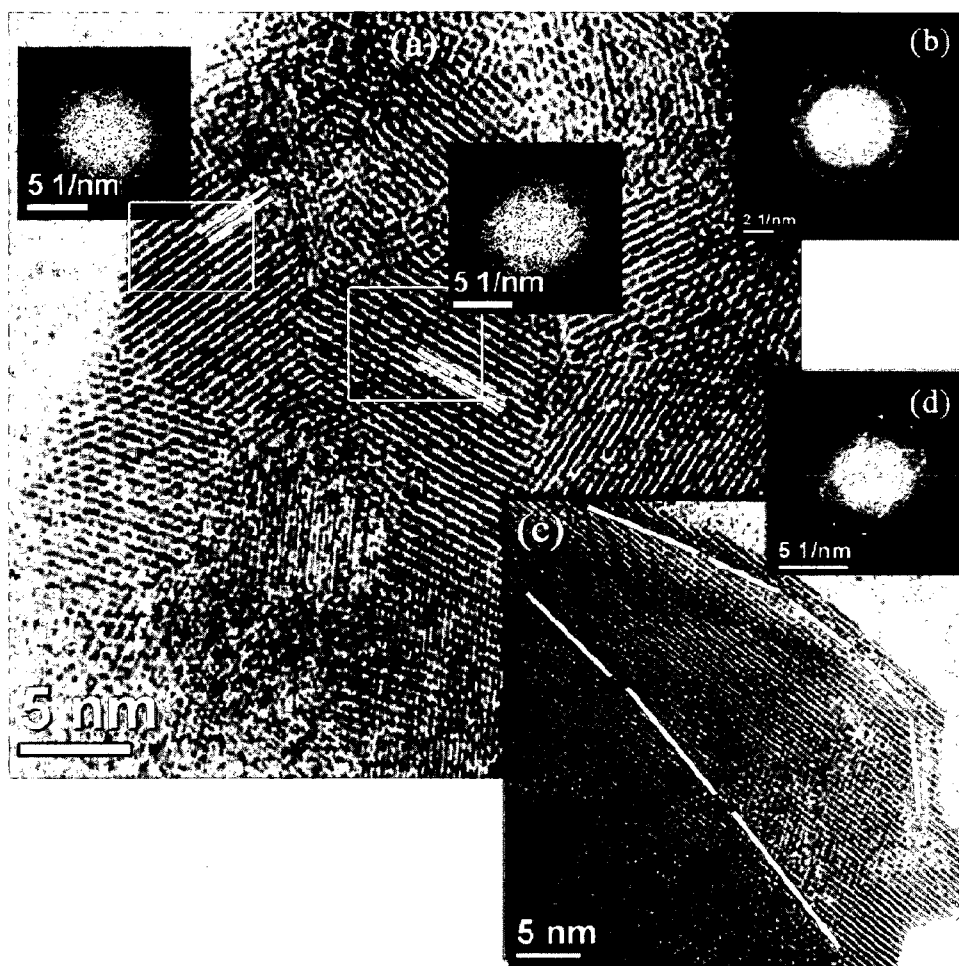


Figure 5.8 HRTEM of $(\text{NH}_4)_2\text{NpF}_6$. (a) HRTEM of a particle showing polycrystalline characteristics, (b) FFT of HRTEM in (a), (c) HRTEM of another particle area with three layers of single crystal, and (d) FFT of image in (c).

Figure 5.9 is a HRTEM image of the mixed $(\text{NH}_4)_x\text{NpF}_y$ sample mentioned earlier. In this area, a phase boundary was identified where the nanostructures of both $(\text{NH}_4)_4\text{NpF}_8$ and $(\text{NH}_4)_2\text{NpF}_6$ are observed. The FFT micrographs of the complete area and the areas where the phase boundary was seen are presented as insets of the figure. FFT of the phase boundary area represents a collection of spots of the two other FFTs of the separate chemical phases at the two sides of the phase boundary. Lattice fringes correspond to $(\text{NH}_4)_4\text{NpF}_8$ and $(\text{NH}_4)_2\text{NpF}_6$ phases are due to (110) and (112) lattice planes of the

compounds, respectively. These observations further confirm the identification of both compounds in the sample with XRD.

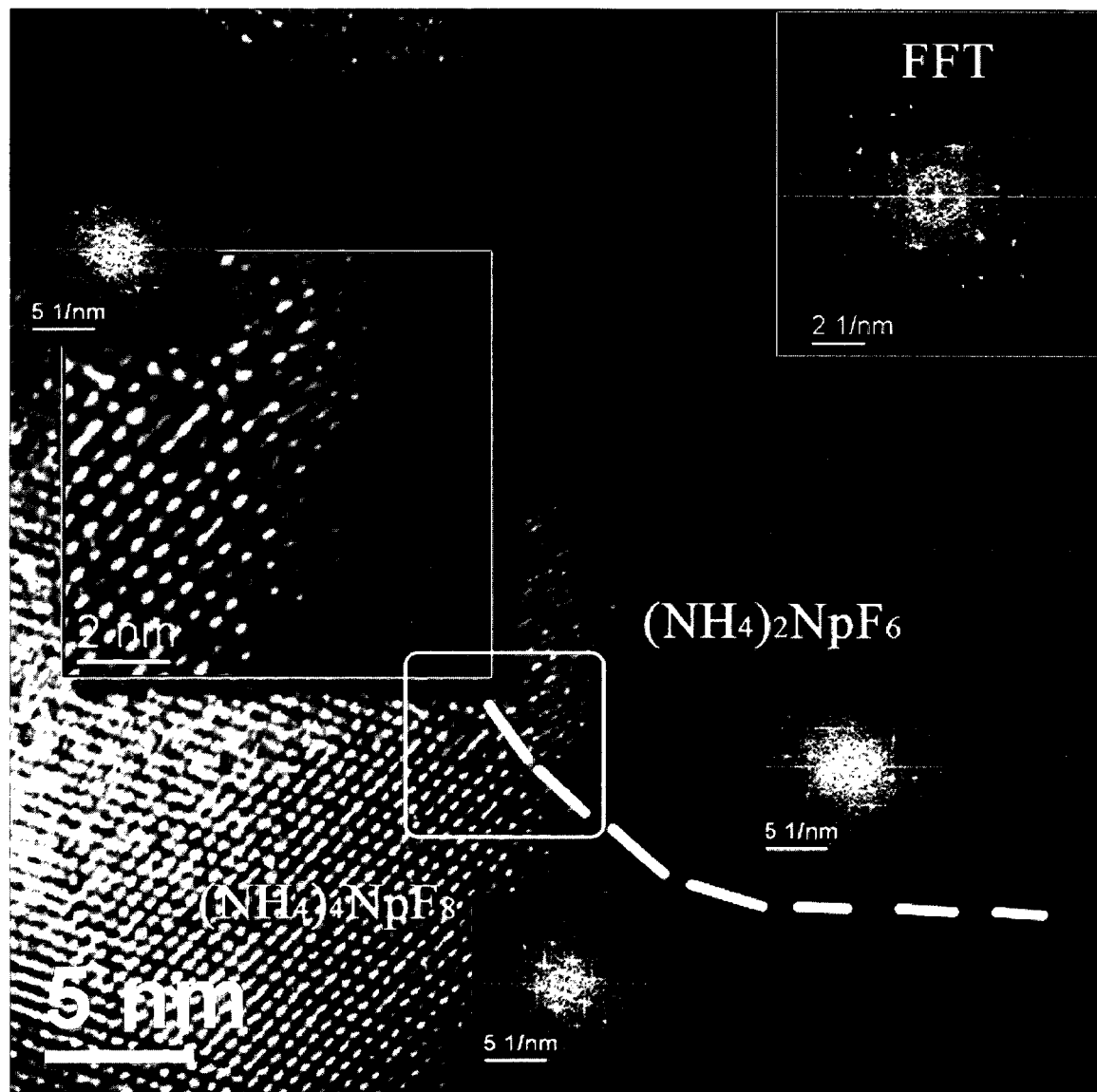


Figure 5.9 HRTEM of the mixed $(\text{NH}_4)_x\text{NpF}_y$ sample displaying a phase boundary of two chemical phases.

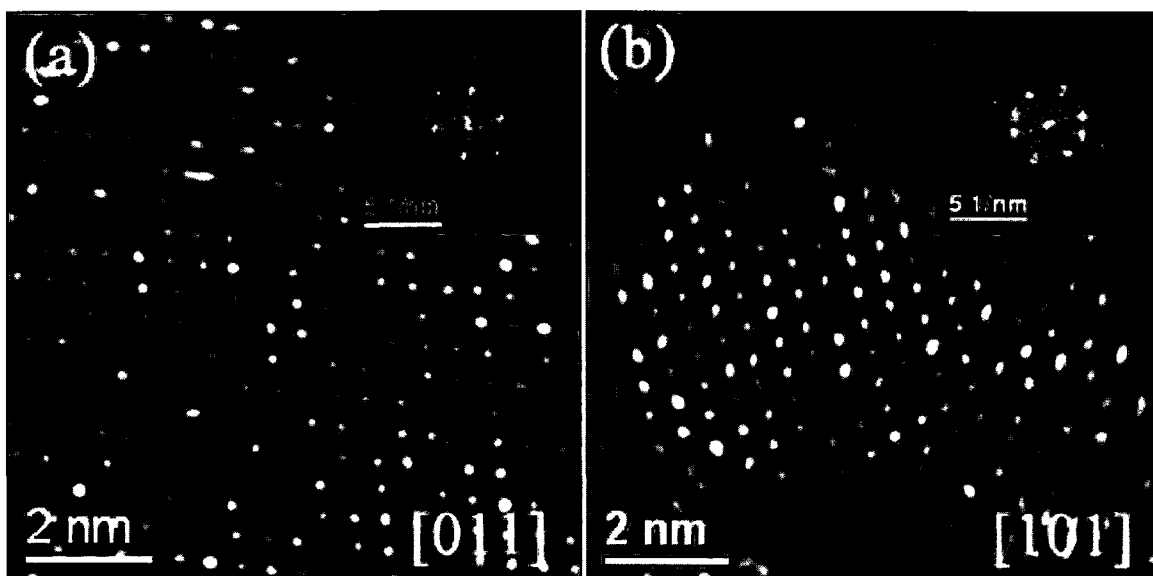


Figure 5.10 HRTEM images of (a) $(\text{NH}_4)_4\text{NpF}_8$ and (b) $(\text{NH}_4)_2\text{NpF}_6$. Lattice fringes of both compounds are found to be due to (111) lattice planes.

Lattice fringes of both $(\text{NH}_4)_x\text{NpF}_y$ compounds were studied using HRTEM and Figure 5.10 displays these images. The distance between two lattice fringes of $(\text{NH}_4)_4\text{NpF}_8$ was determined to be 0.464 nm. This value is close to the interplanar distance of d_{111} (0.468 nm) of the refined crystal structure of $(\text{NH}_4)_4\text{NpF}_8$. The FFT (inset of Figure 5.10a) also confirmed the lattice fringe orientation correspond to d_{111} along [011] beam direction. A lattice fringe distance of 0.476 nm in Figure 5.10b and the corresponding FFT pattern (inset) also indicated the (111) lattice reflections of $(\text{NH}_4)_2\text{NpF}_6$ in a beam of [101]. Thus, the HRTEM imaging also confirmed the crystallography of the two compounds synthesized.

5.3.4 Heat Treatment of $(\text{NH}_4)_x\text{NpF}_y$ under $\text{NH}_3(\text{g})$ and $\text{Ar}(\text{g})$

Heat treatment of solid $(\text{NH}_4)_x\text{NpF}_y$ under ammonia atmosphere was performed at different temperatures. Table 5.5 summarizes the products formed during these heat treatments of $(\text{NH}_4)_4\text{NpF}_8$ sample. At 250 °C, formation of $(\text{NH}_4)_2\text{NpF}_6$ was observed

together with some minor peaks that correspond to NH_4NpF_5 (Figure 5.11a). The major peak at 12.6° 2θ value is prominent of NH_4NpF_5 and all other peaks are negligible because of the amorphous character of the sample. NH_4NpF_5 isostructural with monoclinic NH_4UF_5 (ICSD # 2138) with a space group of $P 1 21/c 1$. The refined lattice parameters of the compound are $a = 0.7764(7)$, $b = 7.071(7)$, $c = 8.758(8)$ nm, and $\beta = 115.72(6)^\circ$.

Table 5.5 Heat treatment of ammonium neptunium fluorides under $\text{NH}_3(\text{g})$

Temperature ($^\circ\text{C}$)	Time (min)	Products			
		Primary	Wt. %	Secondary	Wt. %
250	60	$(\text{NH}_4)_2\text{NpF}_6$	66(1)	NH_4NpF_5	33(1)
400	60	$\text{NH}_4\text{Np}_3\text{F}_{13}$	93(2)	NpO_2	6(2)
450	60	NpO_2	-	Impurities	-
500	30	NpF_3	69(4)	NpO_2	30(4)
800	60	NpN_xF_y	96.2(2)	NpF_3	3.8(2)
800	90	NpN_xF_y	72(3)	$\text{NpN}_2, \text{NpO}_2$	15(2), 11(3)
800	90	Np_2N_3	57.0(6)	NpO_2	43.0(6)
800	120	NpO_2	57(1)	NpN_2	42(1)
1000 – 1100	30 – 75	NpO_2	76.5(3)	Np_2N_3	23.5(3)

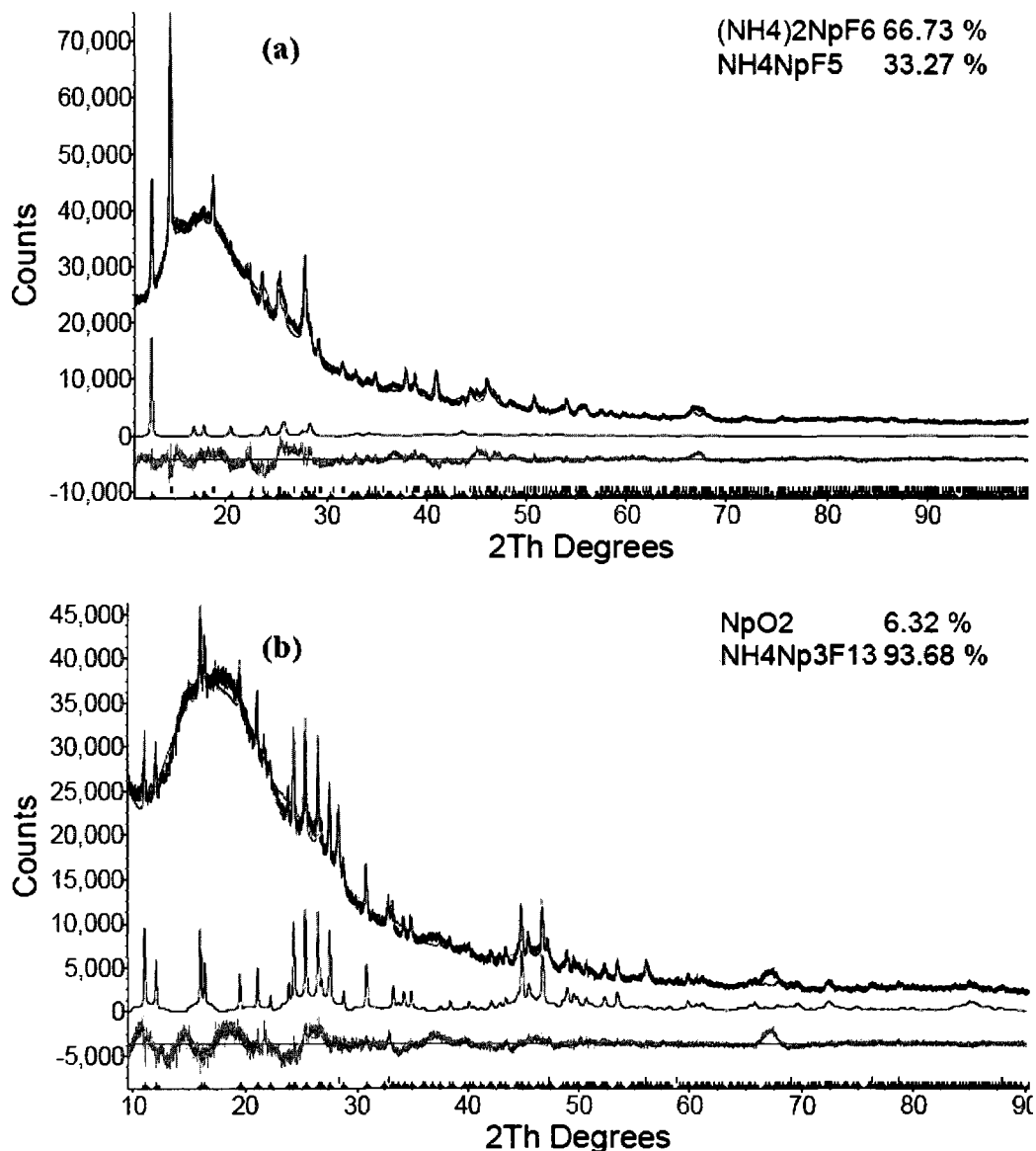


Figure 5.11 XRD patterns of the products obtained after heating $(\text{NH}_4)_4\text{NpF}_8$ at 250 °C (a) and 400 °C (b) for 60 min under $\text{NH}_3(\text{g})$.

When the temperature was increased to 400 °C, another ammonium neptunium fluoride was observed. The XRD pattern of the compound was analogous to $\text{NH}_4\text{U}_3\text{F}_{13}$ (ICSD # 16480). The $\text{NH}_4\text{U}_3\text{F}_{13}$ crystallizes in an orthorhombic unit cell with a space group of $Pm21b$ and $a = 0.7969(4)$, $b = 0.8406(5)$, and $c = 0.7312(4)$ nm lattice parameters. These two samples show a removal of NH_4F from the reactants increasing

the neptunium concentration as the temperature increases. Another sample which was made by heating a $(\text{NH}_4)_4\text{NpF}_8$ sample at 450 °C showed only the presence of NpO_2 and some impurity peaks in its XRD pattern.

However, the formations of NpF_3 and NpN_xF_y compositions (Figure 5.12) were observed at these temperatures 500 and 800 °C, respectively. At 500 °C, about 2 mg batch of $(\text{NH}_4)_2\text{NpF}_6$ was transformed into NpF_3 as the primary chemical phase with a secondary NpO_2 phase (Figure 5.12a). Refined lattice parameters of hexagonal NpF_3 unit cell are $a = 0.4117(2)$ and $c = 0.7287(3)$ nm. Its space group is $P\bar{3}1c$. Some impurity peaks at about 21.3°, 22.7°, and 24.1° 2θ values can be detected in the experimental XRD pattern. The first three peaks could be matched with the NpF_4 crystal structure. However, the refinement of NpF_4 was not included in the pattern in Figure 5.12a due to insufficient peak intensities in other 2θ values found for the ICSD (# 31672) file as indicated by an inset of Figure 5.12a. The impurity peak found at 30.2° was not identified with any known neptunium or uranium compounds. Formation of NpF_3 at 500 °C further confirms the release of NH_4F by $(\text{NH}_4)_x\text{NpF}_y$ reactants forming neptunium rich compounds. On the other hand, formation of NpN_xF_y (Figure 5.12b) at 800 °C suggests the reaction of neptunium fluorides such as NpF_4 or NpF_3 with $\text{N}_2(\text{g})$ due to its partial pressure from the decomposition of $\text{NH}_3(\text{g})$ at elevated temperatures. NpN_xF_y structure identified in this sample is isomorphous to that of tetragonal $\text{UN}_{0.95}\text{F}_{1.2}$ with a space group of $P4/nmmS$ [ICSD #21027]. The lattice parameters of the compound were refined and are $a = 0.3917(2)$, $b = 0.5676(3)$ nm. A model of the unit cell of NpN_xF_y identified in this study is presented in Figure 5.13.

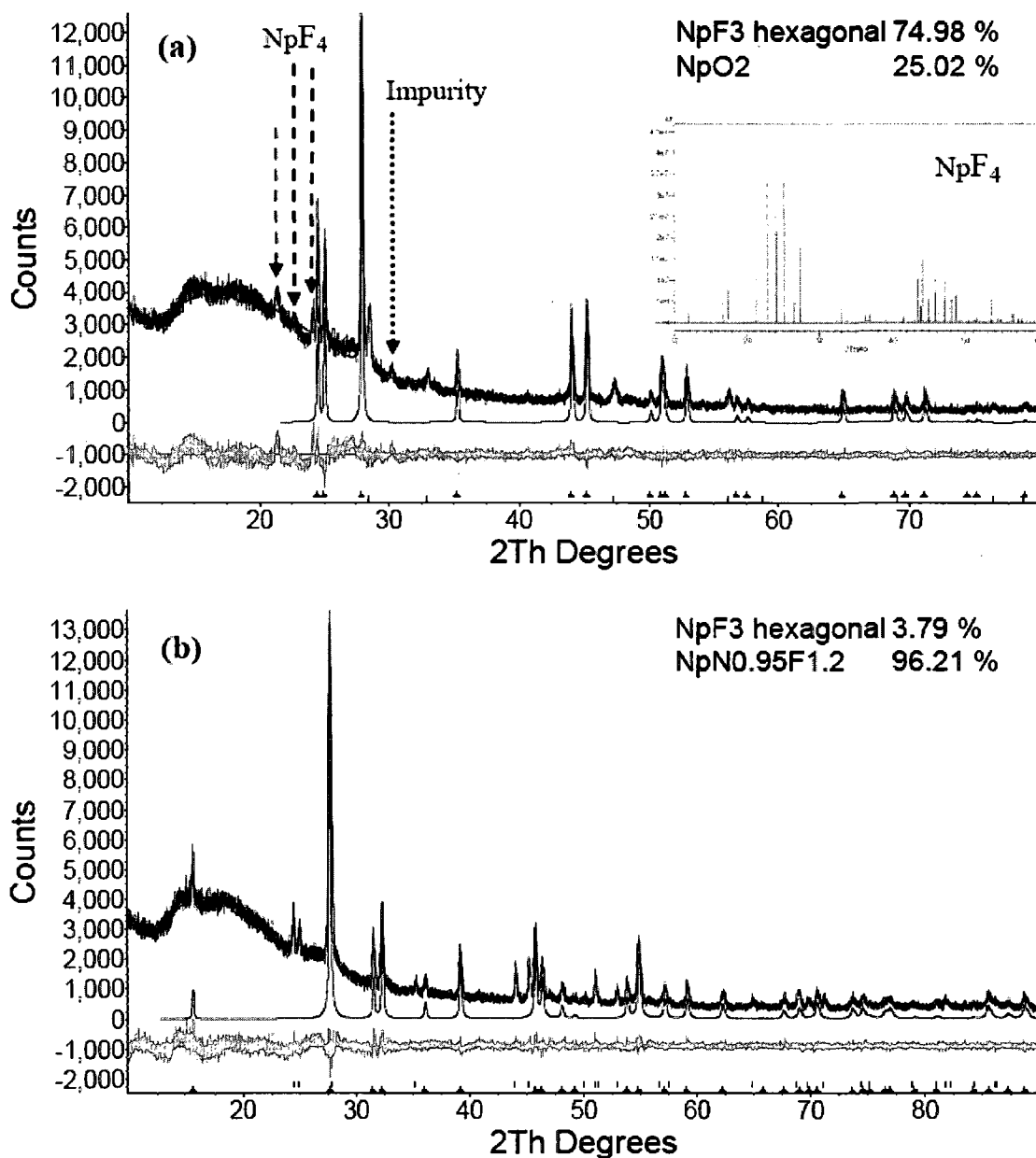


Figure 5.12 XRD patterns of the products formed after heating $(\text{NH}_4)_2\text{NpF}_6$ at 500°C for 30 min (a) and 800 °C for 60 min (b) under NH_3 . The highlighted patterns are the calculated patterns for NpF_3 and NpN_xF_y in (a) and (b), respectively. Some peaks for NpF_4 identified are also displayed together with an inset of a database (ICSD) powder pattern of the NpF_4 crystal structure in (a).

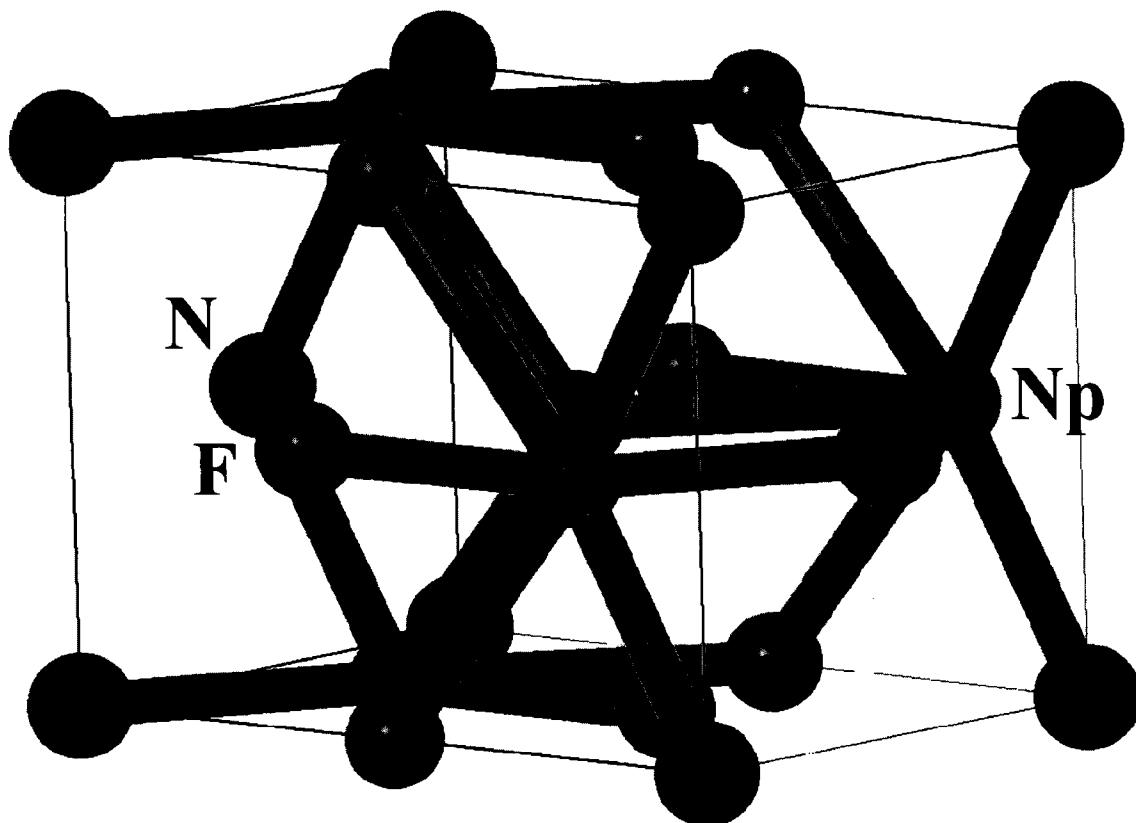


Figure 5.13 Unit cell of NpN_xF_y determined in this study.

Heating of $(\text{NH}_4)_x\text{NpF}_y$ at 800 °C for 90 min was done using two different methods. The first sample was made by heating the reactant wrapped in the Pt sheet. The second sample was made without wrapping the sample assuming it to have more reactivity with the cover gas than the first closed sample. These two samples led to the discovery of two new neptunium compounds of similar crystallography to UN_2 and U_2N_3 . Figure 5.14 displays the observed XRD patterns of these two samples together with the calculated patterns of the corresponding compounds. The first sample showed to contain NpN_xF_y as the major chemical phase with some NpO_2 impurity and a new compound NpN_2 (Figure 5.14a) which has an analogous XRD pattern to the cubic UN_2 structure with a space group of $Fm\bar{3}m$ (ICSD #24222). Its lattice parameter was refined to be 0.5331(6) nm. A

model of the NpN_2 unit cell obtained from the refined crystallography is shown in Figure 5.15.

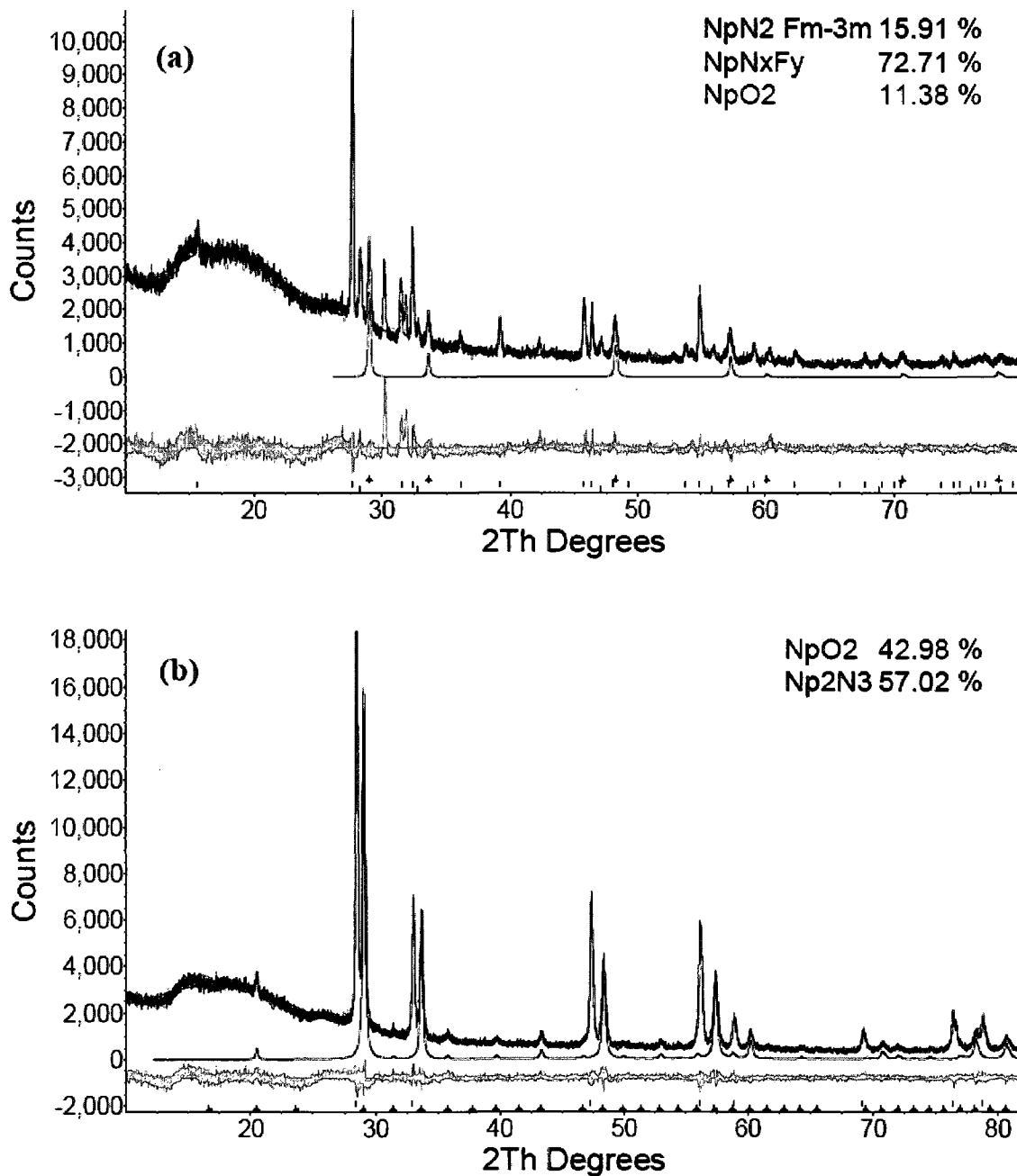


Figure 5.14 XRD patterns of the products formed after heating $\text{NH}_4\text{-Np-F}$ at 800°C for 90min using a closed Pt sheet (a) and an open Pt sheet (b).

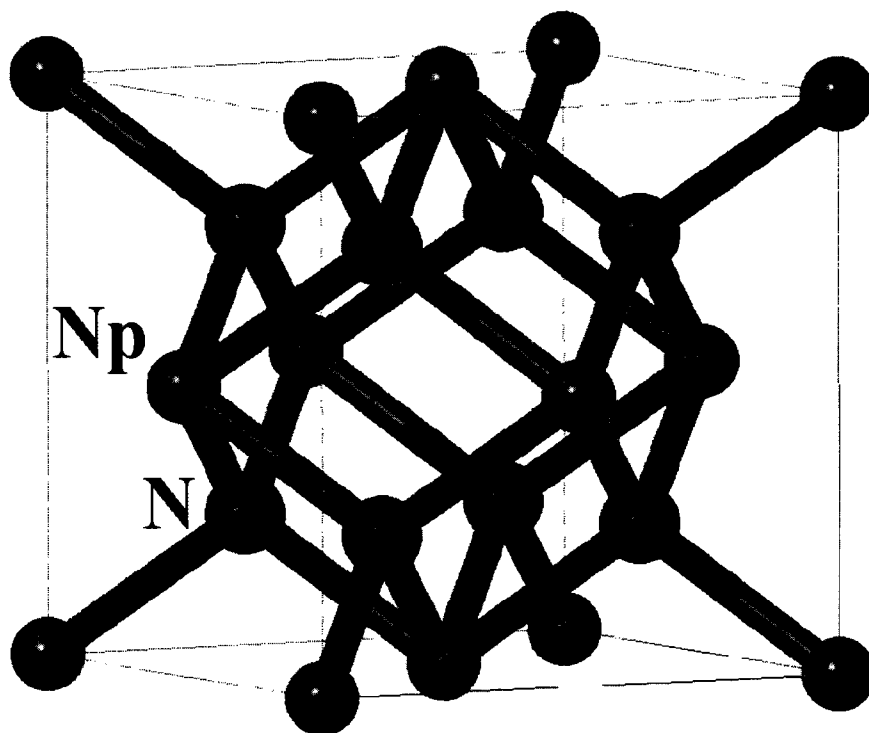


Figure 5.15 Unit cell of the newly discovered NpN_2 .

The second sample, which was heated in an opened Pt sheet, contained another new neptunium bearing chemical phase identified to be Np_2N_3 (Figure 5.14b), similar to the crystallographic parameters of U_2N_3 (ICSD #60415). The refined lattice parameter of this new compound was 1.0657(6) nm and the unit cell of the compound is shown in Figure 5.16. The N:Np molar ratio of NpN_2 and Np_2N_3 are 2 and 1.5, respectively. Once the NpN_2 is formed, further heating can remove some of the nitrogen from the compound forcing it to form nitrogen deficient chemical compositions such as Np_2N_3 . Thus, the open sample reacted with the covering gas quickly to form NpN_2 and decomposing it to Np_2N_3 within 90 min while the closed sample was able to perform only the first step (forming NpN_2) in the same time period. Moreover, the faster reaction has also promoted the formation of the impurity NpO_2 chemical phase.

A longer heating (120 min) of the $(\text{NH}_4)_4\text{NpF}_8$ sample at $800\text{ }^\circ\text{C}$ however produced NpN_2 with NpO_2 as the primary phase. Increased heating time of NpN_x under $\text{NH}_3(\text{g})$ thus did not remove further nitrogen from NpN_x system but it stabilized the NpN_2 chemical composition due to the nitrogen partial pressure. Heat treatments of $(\text{NH}_4)_x\text{NpF}_y$ samples at temperatures in the range of $1000 - 1100\text{ }^\circ\text{C}$ also produced only NpN_x suggesting a subsequent heating of these NpN_x samples under an inert atmosphere such as argon to form neptunium mononitride.

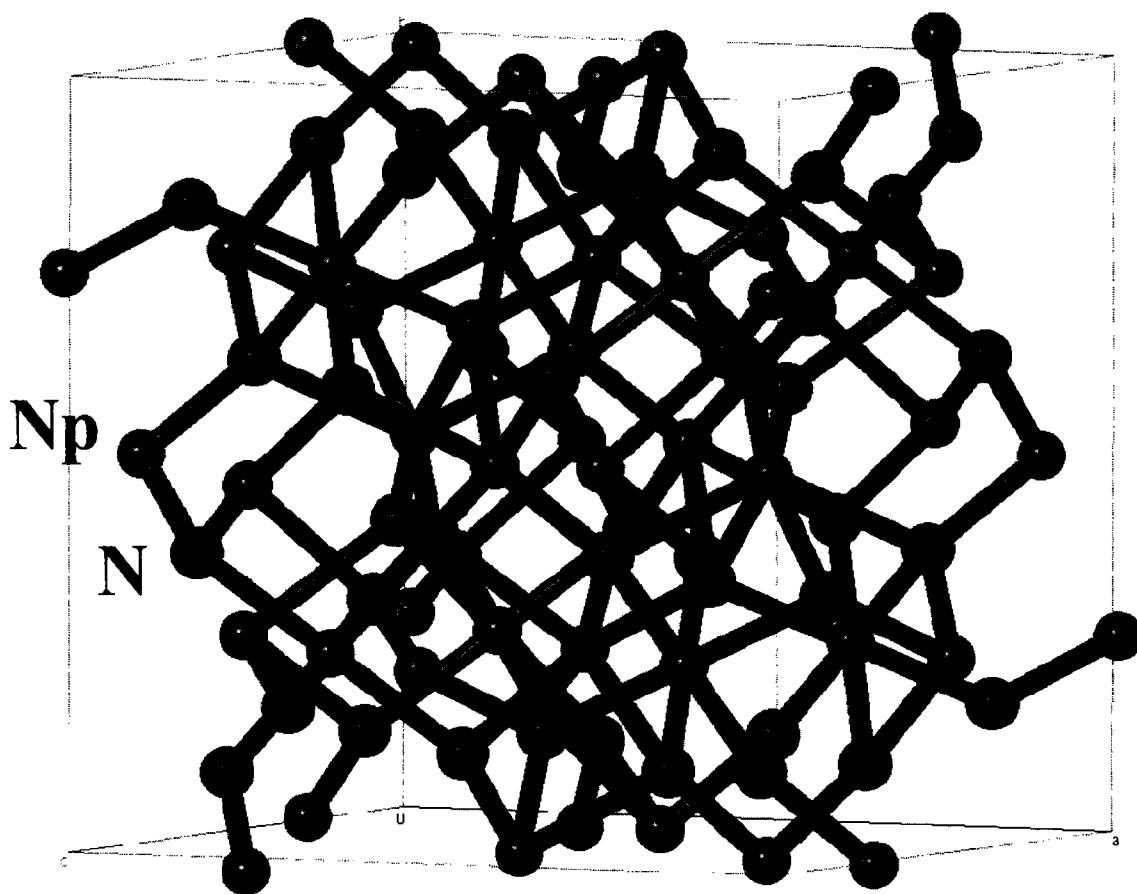


Figure 5.16 Unit cell of Np_2N_3 .

The neptunium mononitride sample was synthesized after continuously heating NpN_x , which was formed by heating $(\text{NH}_4)_x\text{NpF}_y$ at 800 °C for 90 min under $\text{NH}_3(\text{g})$. The NpN_x was treated under high-purity argon atmosphere at 1100 °C for 30 min (Figure 5.17). This sample contained only 15.03(1) wt% NpN while NpO_2 was identified as the major phase. This sample had a color of gold/yellow. NpN is known to be black in color. The gold/yellow color was probably due to the majority chemical phase (NpO_2). Formation of NpO_2 as the major phase in the sample is due to two factors, susceptibility of NpN_x compounds to oxygen impurities from the atmosphere and from the minute quantities forming in the quartz tubing at elevated temperatures.

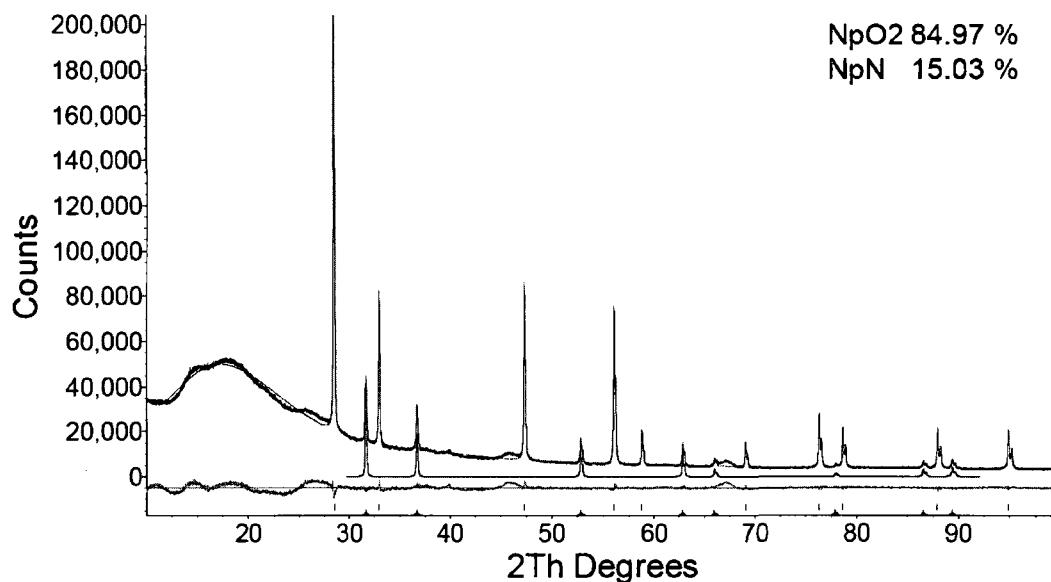


Figure 5.17 Observed and the calculated XRD patterns of the NpN sample synthesized by heating $(\text{NH}_4)_x\text{NpF}_y$ for 90 min at 800 °C under NH_3 and a continuous heating at 1100 °C for 30 min under high-purity argon. Peaks at 46° and 67.5° 2Theta values are due to the sample holder because of the kapton tape used to contain sample.

To minimize the amount of NpO_2 formation in the NpN synthesis, few samples were synthesized at temperatures 800 and 900 °C. A sample of $(\text{NH}_4)_4\text{NpF}_8$ was heated at

800 °C under NH₃ and the gas flow was changed into Ar after 90 min heating. Further heating of the sample was maintained for an additional 60 minutes under Ar(g). The resulting sample consisted of 46 wt% NpN_xF_y and a small amount (0.6 wt%) of NpN₂. The remainder of the sample was NpO₂. Since the temperature and the time of heating are not sufficient to produce NpN, another synthesis attempt was made by heating (NH₄)₄NpF₈ at 900 °C. Heating under NH₃(g) for 30 min and under Ar(g) for another 60 min made NpN with majority of the sample being NpO₂ (73 wt%). Therefore, the sample heating at 900 °C under Ar(g) was reduced to 30 min and found it was not enough to transform all the higher neptunium nitrides to the mononitride. This sample contained 38 wt% NpN_xF_y and 24 wt% NpN with a 38 wt% NpO₂ phase. The final sample was therefore made by heating (NH₄)₄NpF₈ at 900 °C for 30 min under NH₃(g) and 45 min under Ar(g) with a Zr sponge as a O₂ getter. Figure 5.18a displays the observed and calculated XRD patterns of the sample immediately after synthesis. XRD powder refinement showed a 62.70(1) wt% of NpN and a decrease of the phase to a 61.9 wt% after three days (Figure 5.18b).

Reaction of atmospheric oxygen with NpN was studied at room temperature. An NpN powder was placed on a XRD sample holder and obtained XRD patterns of the sample as a function of time. The powder refinement was performed for each XRD pattern to evaluate the amount of NpN and NpO₂ at different stages. Figure 5.19 displays the transformation kinetics of NpN determined by such a series of XRD powder pattern refinements. The fit obtained by first order exponential decay was also indicated and the rate constant was determined to be $1.6 \times 10^{-8} \text{ s}^{-1}$. The data could also be fitted to a second order reaction kinetics and the rate constant was $2.5 \times 10^{-7} \text{ s}^{-1}$. These data display a high

degree of oxidation of NpN with atmospheric oxygen further explaining the difficulty of making phase-pure NpN under ambient conditions.

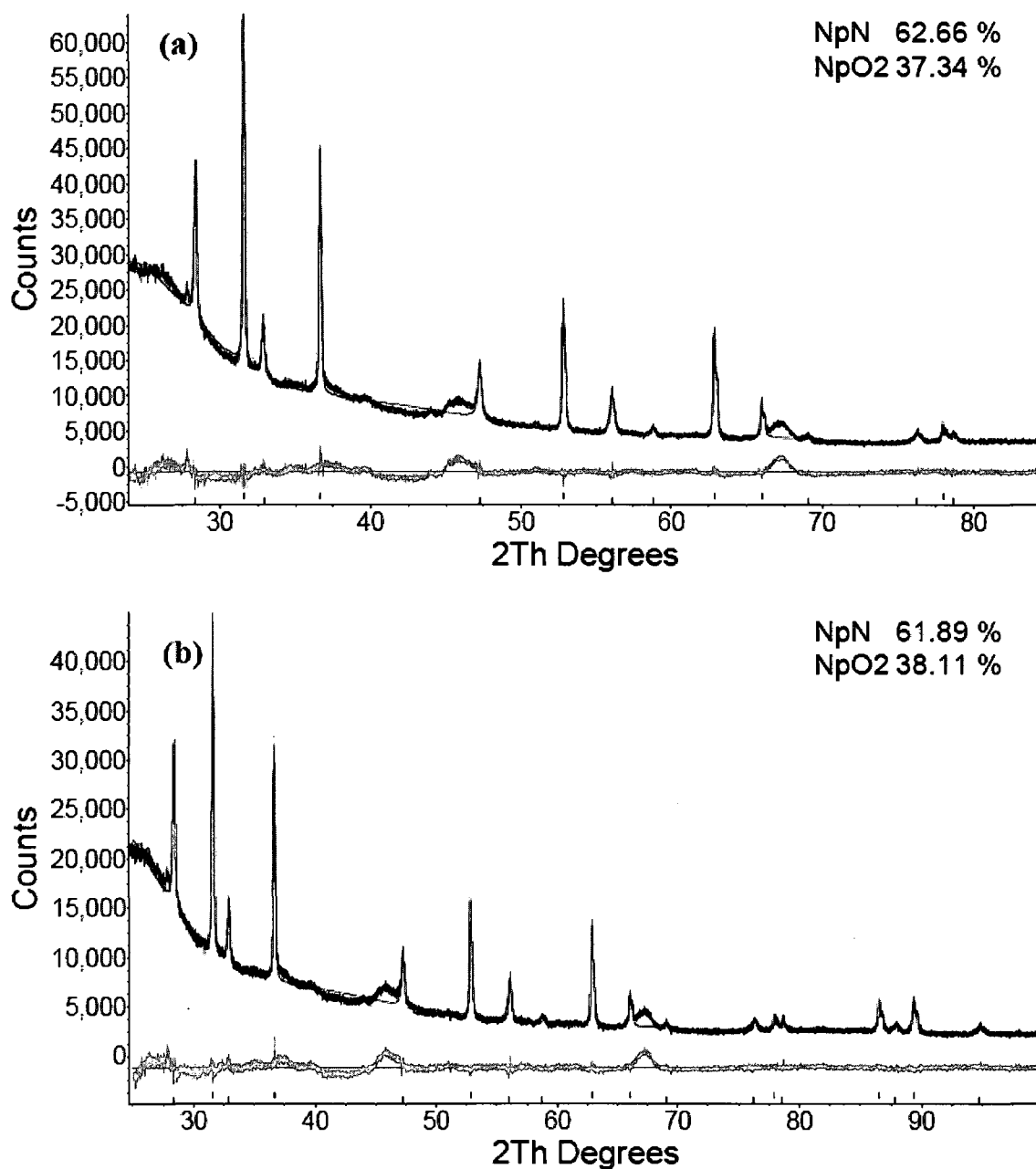


Figure 5.18 Observed and the calculated XRD patterns of the NpN sample synthesized by heating $(\text{NH}_4)_x\text{NpF}_y$ for 30 min under NH_3 and a continuous heating for another 30 min under high-purity argon at 900 °C. XRD pattern of the sample immediately after synthesis (a) and after three days (b).

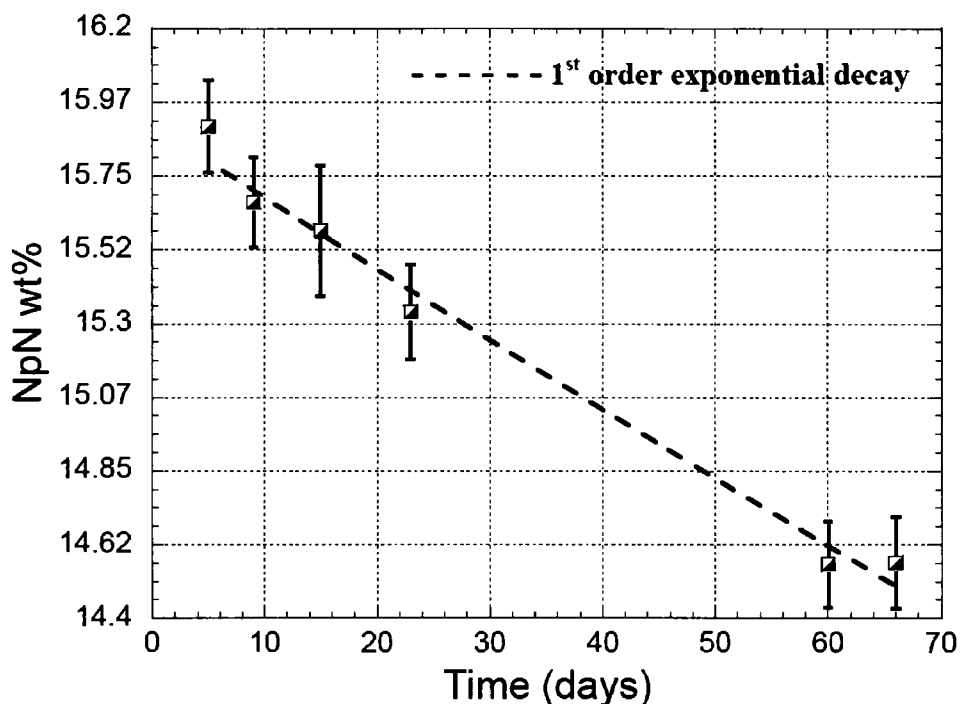


Figure 5.19 Decay kinetics of NpN at ambient conditions as a function of time due to NpN transformation into NpO₂.

5.3.5 Microscopic Characterization of NpN_x

5.3.5.1 Microscopic Characterization of NpN₂

Morphological observation of NpN₂ using SEM imaging showed that majority of it contains particles of needle shape (Figure 5.20). These particles have a width of approximately 0.2 μm whereas some particles elongate up to about 1 μm changing in to a flat shape. The inset of the figure consists of a cluster of particles of different morphology. The bulk of these particles have flat shapes, indicating a presence of a second phase (NpO₂) as found by XRD. Corresponding EDS also showed the presence of different nitrogen and oxygen weight percentages depending on the particle shapes analyzed (Table 5.6). EDS analyses done on different particles therefore suggest the NpN₂ particle expansion due to the formation or binding of NpO₂ grains within phase boundaries.

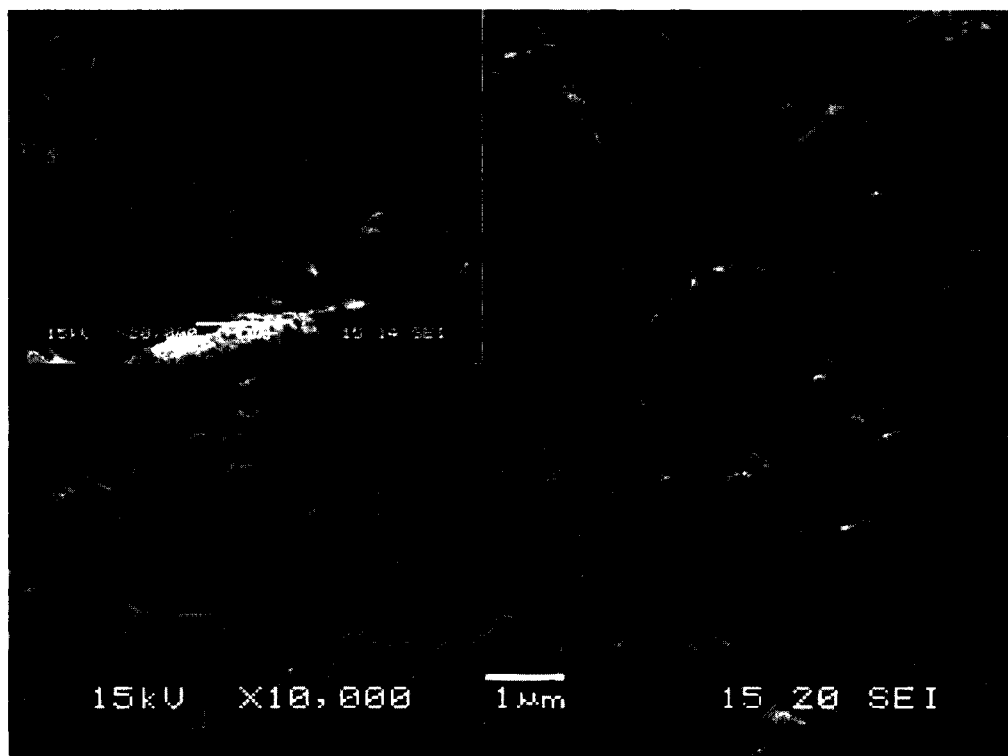


Figure 5.20 SEM images of NpN_2 . Inset is the SEM of another area containing a cluster of particles.

HRTEM images shown in Figure 5.21 confirmed the formation of NpN_2 at the nanoscale. Furthermore, each of these images shows a high crystallinity of the samples at this scale. Lattice fringes formed attributed to (002) interplanar d -spacing are found to be displayed in both images. Lattice plane reflections of the compound in Figure 5.21a are indicated by bright spots that congregate to form hexagonal-shaped image. In Figure 5.21b, on the other hand, each dark color spot is surrounded by bright, six membered rings suggesting an array of NpN_2 unit cells along [110] direction. These observations designate a high order in nanocrystals of the as-synthesized NpN_2 sample.

Table 5.6 Quantitative analysis of NpN₂ sample with respect to the particle shape.
Approximate error percentage is 1%.

Particle shape	Element wt. %		
	N	O	Np
Flat	10.2	10.1	79.7
Needle	17.9	-	82.1
Average	14.0	5.1	80.9

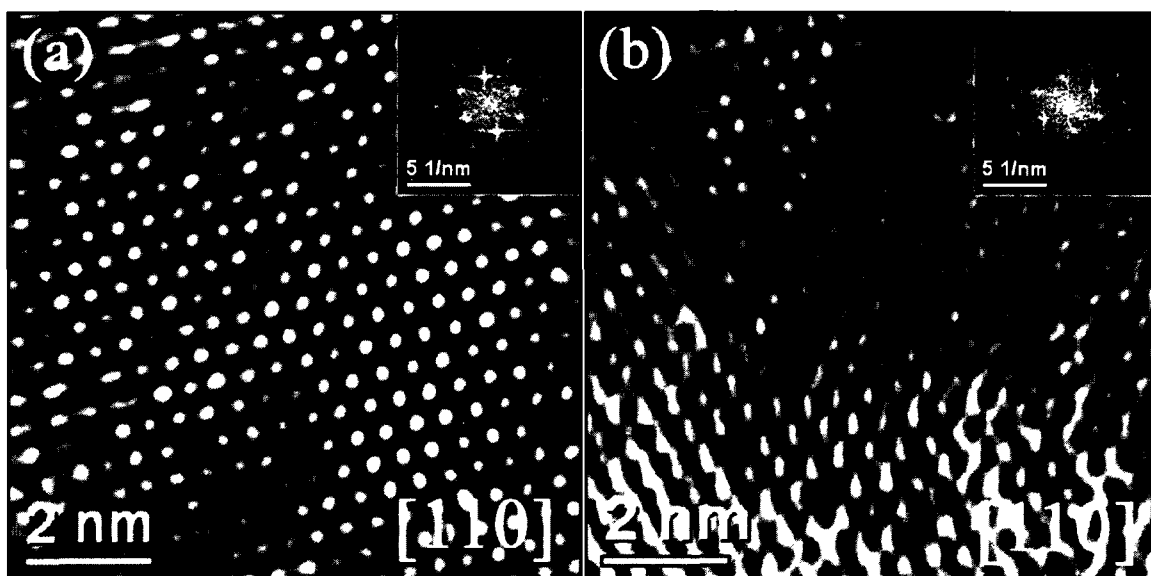


Figure 5.21 HRTEM images of two NpN₂ nanoparticle areas.

5.3.5.2 Microscopic Characterization of Np₂N₃

The bulk morphological characteristics identified in NpN₂ have been changed when it was transformed into Np₂N₃. Most of the particles of Np₂N₃ are plate like with elongated boundaries in different directions (Figure 5.22b). Clusters of particles can also be seen in some of the areas of the sample (Figure 5.22a). EDS analyses showed that most of the particles consist both oxygen (7.8 ± 0.8) and nitrogen (8.1 ± 0.8) representing a mixture

of Np_2N_3 and NpO_2 compounds. Figure 5.23 is the HRTEM of a well-crystallized Np_2N_3 nanoparticle. Lattice fringes of the image correspond to (022) lattice planes of the compound.

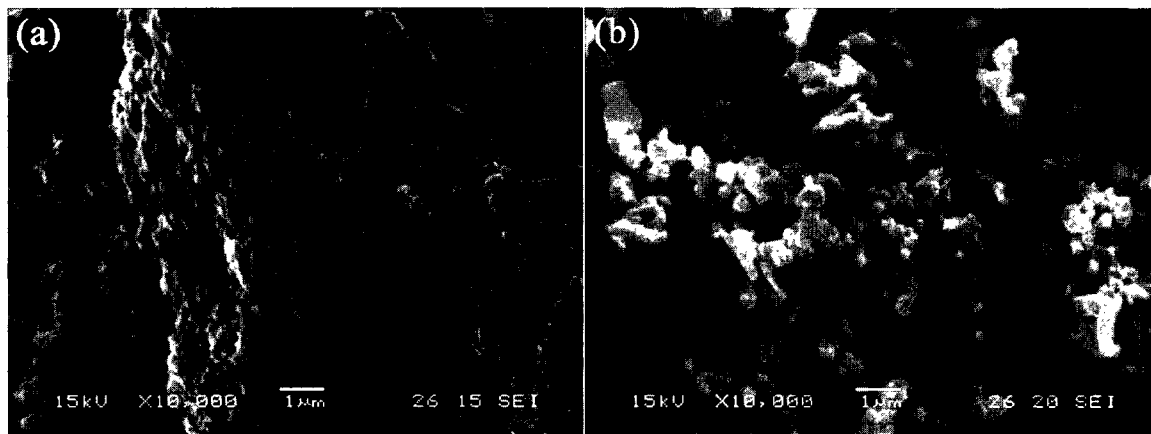


Figure 5.22 SEM micrographs of Np_2N_3 showing a cluster of particles (a) and a flat area containing some separated particles (b).

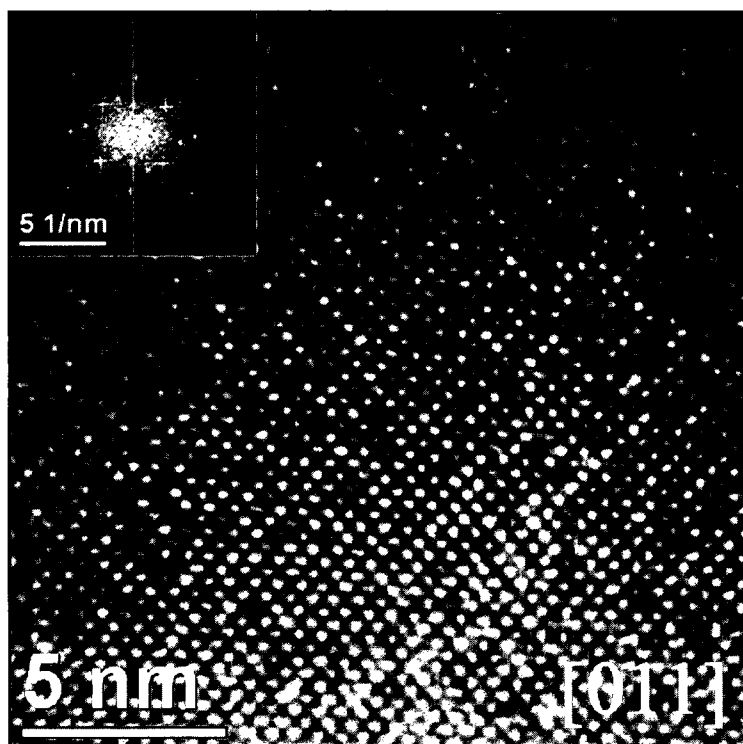


Figure 5.23 HRTEM image of Np_2N_3 .

5.3.5.3 Microscopic Characterization of NpN

SEM imaging and EDS analyses of two NpN samples were performed. The NpN sample with large NpO_2 content showed to contain separately formed NpO_2 particles (Figure 5.24a). SEM micrograph of the other sample containing NpN is displayed in Figure 5.24b. According to this image, morphology of the as-synthesized NpN sample is distinctively different from both NpN_2 and Np_2N_3 . The NpN particles (Figure 5.24b) appear to be large compared to the other two NpN_x . The circled particles in Figure 5.24a match to NpN compared to particles in Figure 5.24b and subsequent EDS analysis. Table 5.7 summarizes the chemical analysis of the sample containing 62.7(1) wt% NpN. The experimental weight percentages are deviated from the expected values due to the secondary chemical phase and errors associated with the technique.

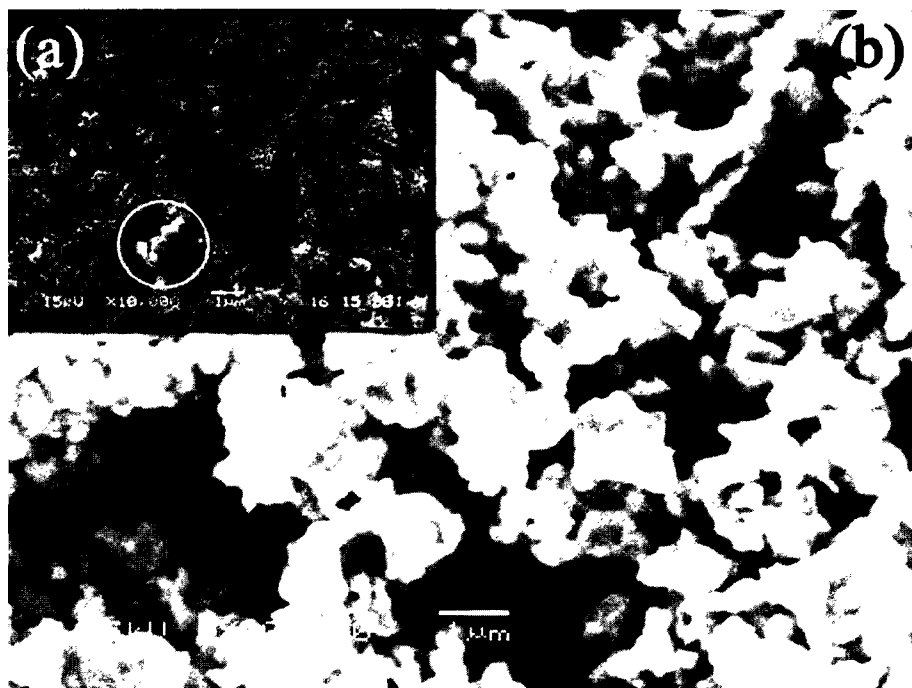


Figure 5.24 SEM micrographs of NpN samples. (a) NpN sample with a 15.03(1) wt% mononitride (Figure 5.17) and (b) the sample containing 62.70(1) wt% NpN (Figure 5.18).

Table 5.7 Chemical analysis of NpN sample.

Element	Weight %	
	Measured	Theoretical
N K	5.07 ± 0.85	5.6
O K	3.16 ± 0.56	-
Np M	91.76 ± 0.98	94.4
Totals	100.00	100

TEM was also utilized to characterize the synthesized NpN samples. Figure 5.25 display a set of particles of the 15.03(1) wt% NpN sample with XEDS spectra of two areas. One of these areas contained both nitrogen and oxygen whereas only oxygen was determined in the other area. Other particles shown in the TEM BF and STEM images were also evaluated with XEDS and found both N and O. Similar analyses were done on the sample containing 62.70(1) wt% NpN. Figure 5.26 shows one area where only nitrogen was detected in this sample. HRTEM images shown in Figure 5.27 were obtained by focusing on the N rich areas of the two samples. This figure represents nanostructure of NpN in a similar manner which was identified for NpN₂ in Figure 5.21. High crystallinity of the N rich areas and as well as the high ordered crystal structure can be observed. In addition, the crystallography of the as-synthesized sample was confirmed by the lattice fringe orientations.

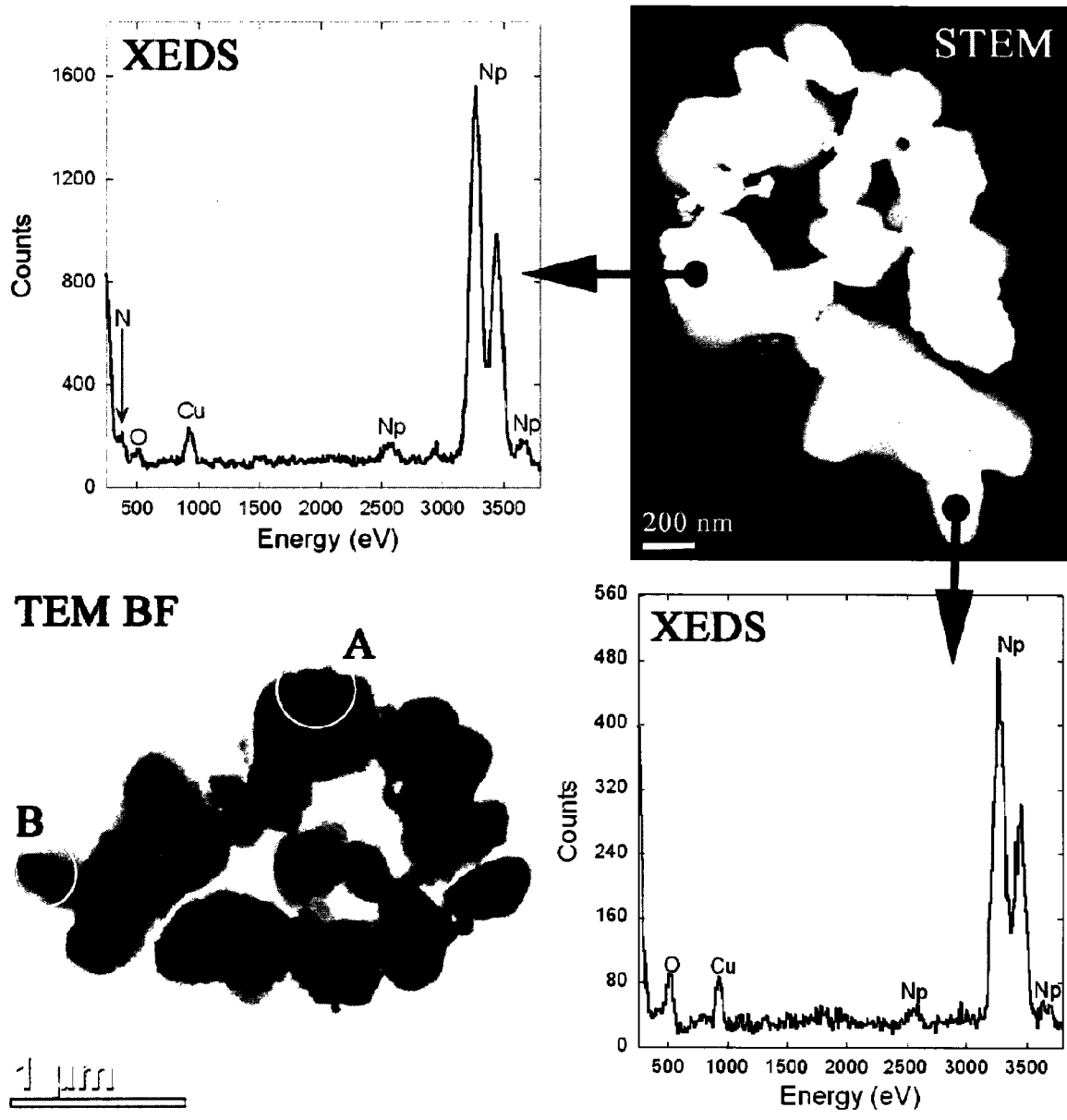
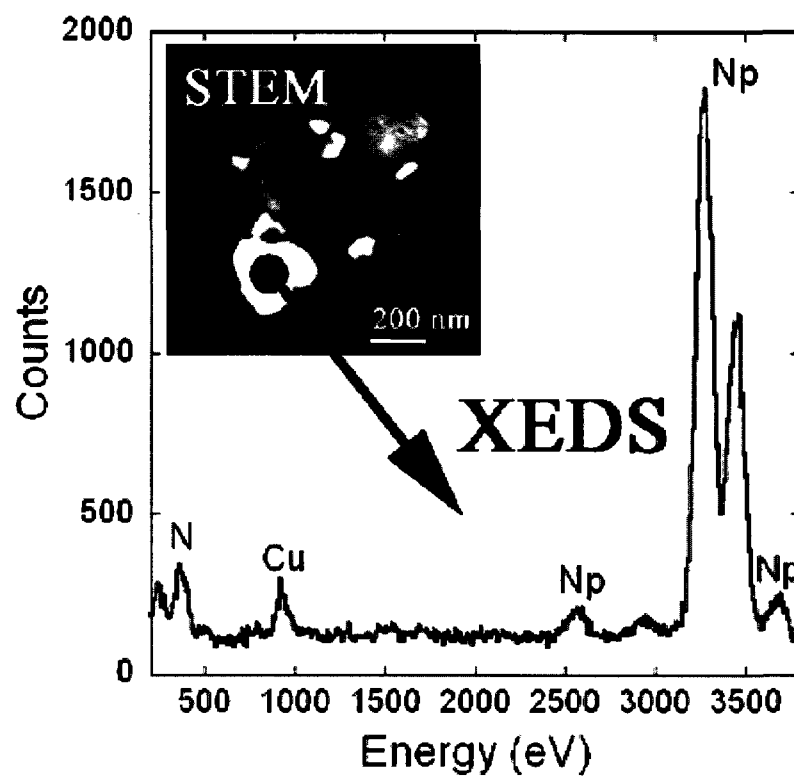


Figure 5.25 TEM BF and STEM images of few particles of NpN sample with a 15.03(1) wt% mononitride. XEDS profiles of two points rich with nitrogen and oxygen are also displayed.



TEM BF

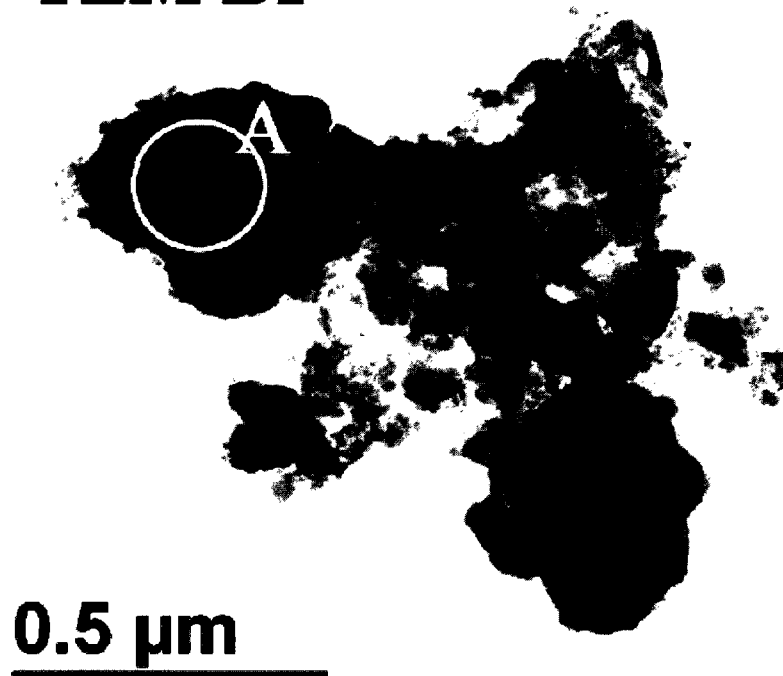


Figure 5.26 STEM and TEM BF images of the NpN sample containing 62.70(1) wt% NpN. XEDS spectrum of the particle highlighted in the STEM image is also displayed.

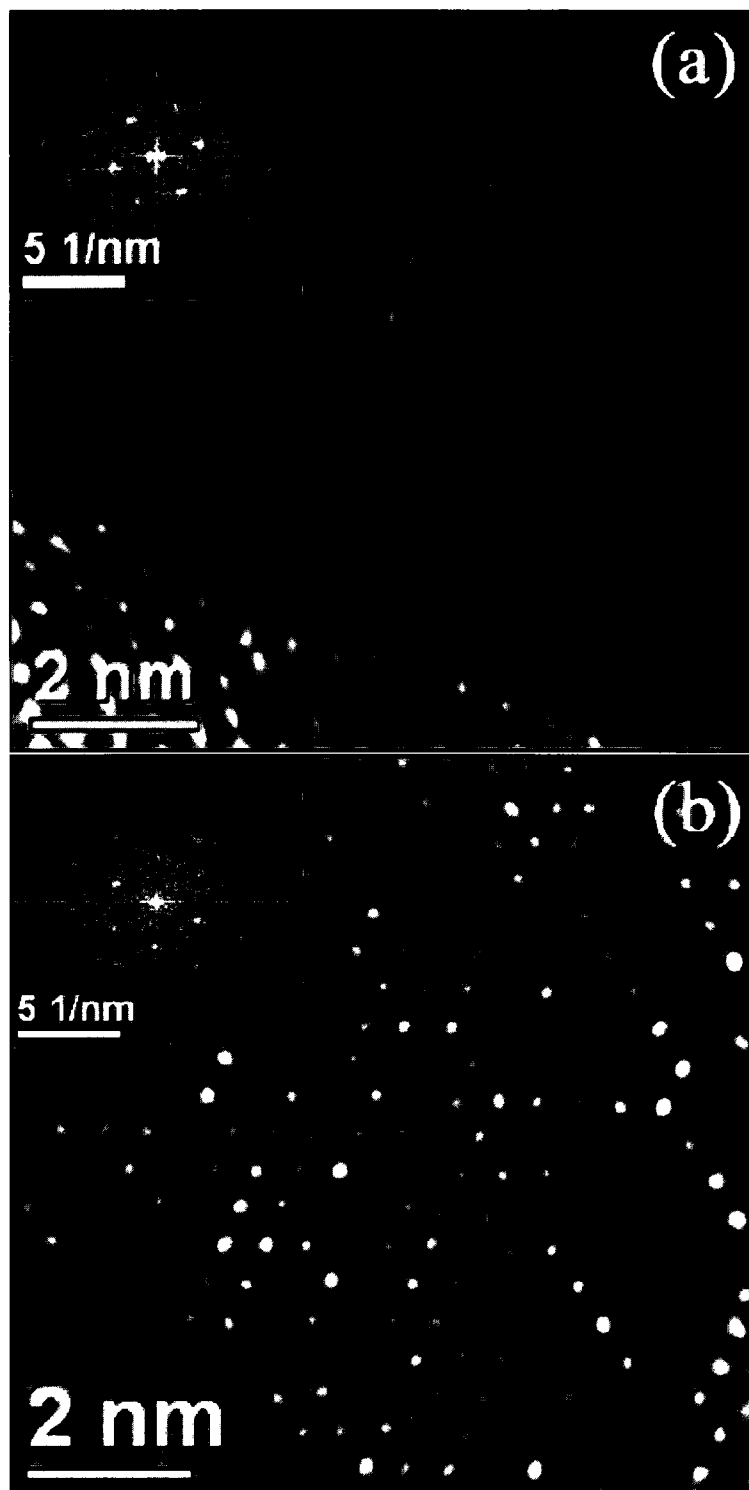


Figure 5.27 HRTEM images of NpN samples. (a) Particles from 15.03(1) and (b) 62.70(1) wt% NpN samples. Both images contain lattice fringes from (111) planes of NpN.

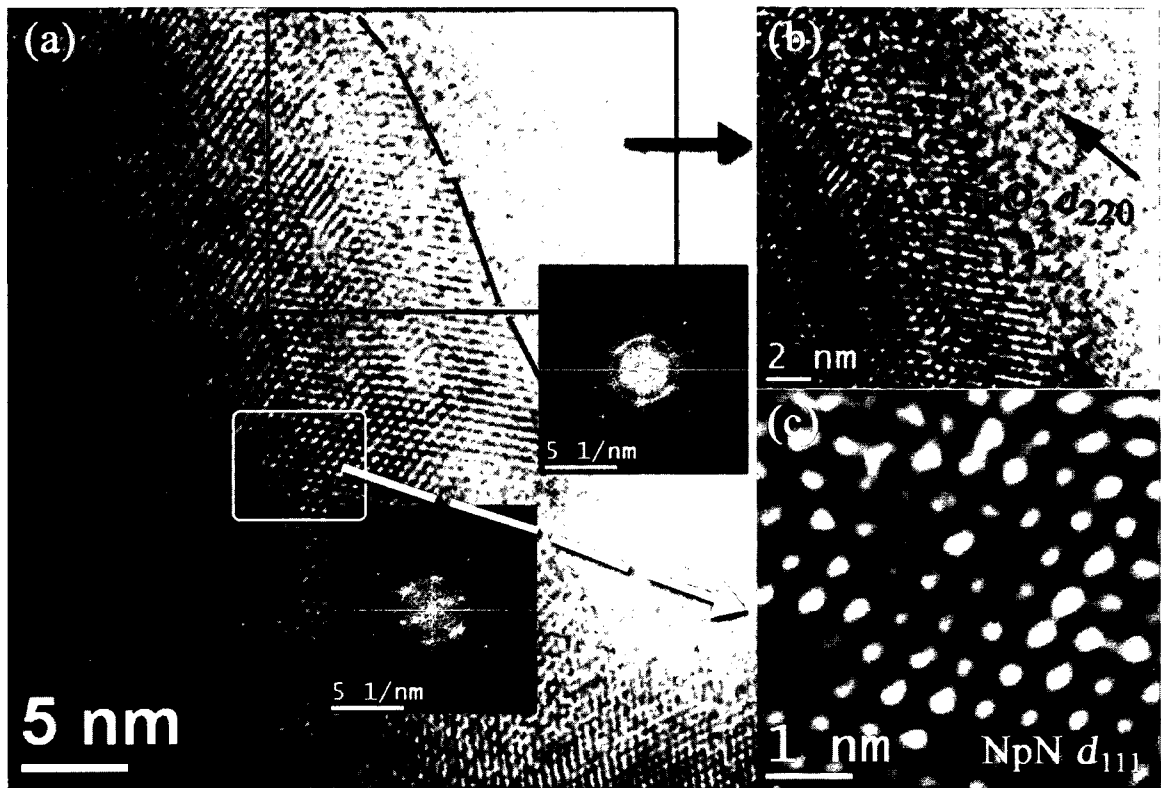


Figure 5.28 HRTEM of the N rich a particle as shown in Figure 5.25.

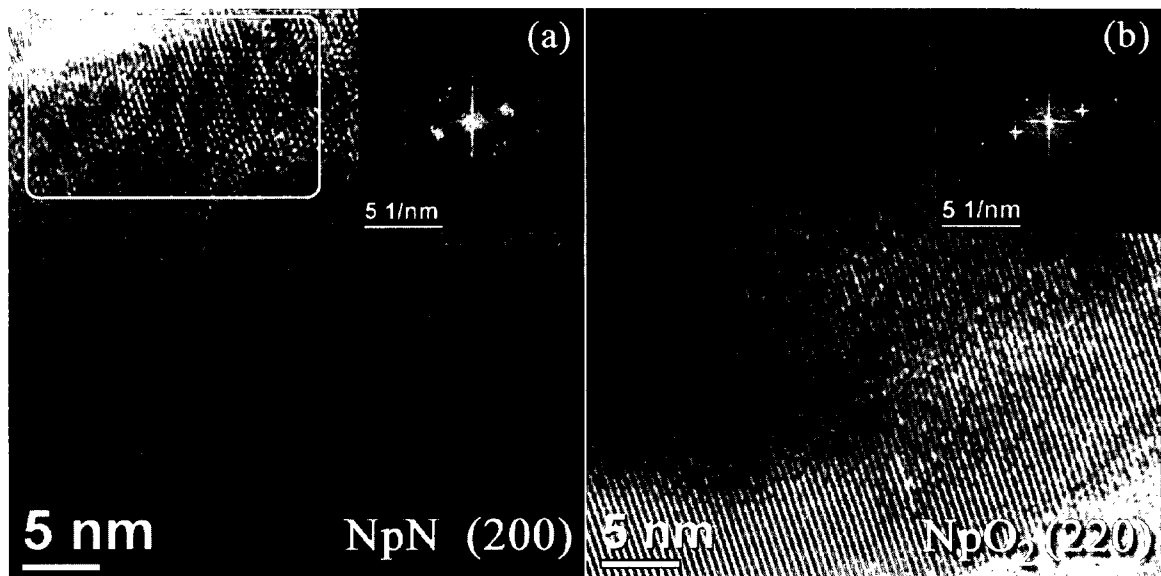


Figure 5.29 HRTEM of 15.03(1) wt% NpN sample. (a) Nitrogen rich and (b) oxygen rich areas. Area focused in (a) is about 40 nm into the particle from the edge of it.

Figure 5.28 and 5.29 are HRTEM images of NpN sample in Figure 5.25. Nitrogen rich areas showed to contain lattice fringes correspond to NpN (Figure 5.28c). Observation of other areas even with high N concentrations shows an oxidation at particle edges forming NpO_2 domains. Figure 5.28b indicates such area with NpO_2 present. Corresponding FFT micrographs of the two areas highlighted in Figure 5.28 confirm the formation of another phase. The FFT of the area with two phases display few ring patterns different from the FFT of the NpN area. Another area of the same sample (Figure 5.29a) contained lattice fringes from NpN crystals, but some deformations at the edge of the particle (highlighted with a rectangle) is observed, again suggesting a possible interference of a secondary phase. Figure 5.29b represents a well-formed single crystal of NpO_2 in an O rich area of the sample.

The area denoted by a circle and a letter A in Figure 5.26 TEM BF image was also used to obtain the HRTEM images of the sample containing 62.70(1) wt% NpN. The bulk of the area observed with HRTEM contained lattice fringes of NpN. In one area, however, a partially crystallized NpO_2 domain was identified. Figure 5.30 shows this observation in detail. This NpO_2 (highlighted) domain was detected about 36 nm from the edge of the particle from the right-bottom of the figure. Also, this domain has a length of about 22 nm from the starting point to the end where NpN (200) phase was found. Also another open area can be seen from bottom left of the figure. Therefore, formation of this NpO_2 domain can probably be due to the reaction of sample edge with oxygen in air. These observations further indicate that NpO_2 acts as a secondary chemical phase of the NpN particles after it is made and as a major chemical phase due to the oxygen

contaminations in the experimental setup at elevated temperatures. Further details of these observations are discussed in section 5.4 (Discussion).

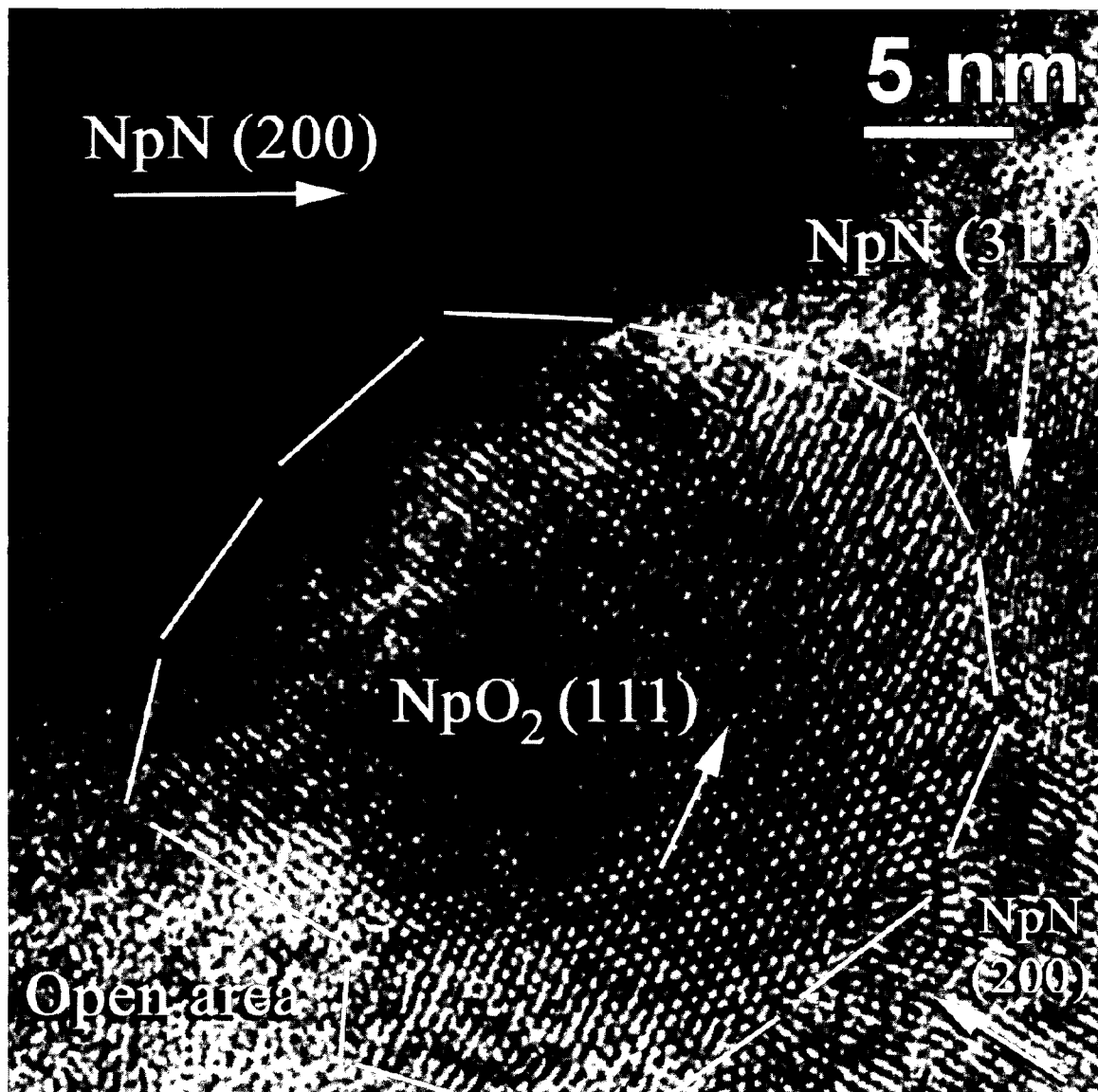


Figure 5.30 HRTEM of the area A displayed in Figure 5.26 TEM BF image.

5.4 Conclusions

The current work found six new neptunium compounds ($(\text{NH}_4)_4\text{NpF}_8$, NH_4NpF_5 , $\text{NH}_4\text{Np}_3\text{F}_{13}$, NpN_xF_y , NpN_2 , and Np_2N_3). Use of the fluoride route in the synthesis of NpN led to discover new compounds and a great deal of knowledge involved in their chemistry. $\text{NpO}_2(\text{s})$ reaction with excess $\text{NH}_4\text{HF}_2(\text{s})$ did not lead to any known compounds of ammonium neptunium fluorides after aging the mixture for about 4 months at room temperature. This observation directed to check the reaction between NpO_2 and NH_4HF_2 at a higher temperature than of the room (22 °C). Therefore, the mixed sample was heated at 80 °C and found no known compounds for another 3 months. Chemical phase determination which was done using powder XRD finally showed the formation of $(\text{NH}_4)_2\text{NpF}_6$ in the fourth month of heating at 80 °C.

The calculated XRD pattern of $(\text{NH}_4)_2\text{NpF}_6$ of the ICSD # 034-1367 showed some resemblance to the pattern of the above sample. However, the database pattern was calculated using a cubic crystal system. The sample XRD pattern was also tried by refining against a similar crystallography of $(\text{NH}_4)_2\text{UF}_6$ after Abazli et al [9], but the attempt failed because of the incorrect space group. $(\text{NH}_4)_2\text{CeF}_6$ compound has an orthorhombic crystal system with a *Pbcn* space group, and the compound the current study synthesized had similar crystallography. Therefore, an orthorhombic $(\text{NH}_4)_2\text{NpF}_6$ with a *Pbcn* space group and lattice parameters as shown in Table 5.1 is reported here as the terminal product of the NpO_2 and NH_4HF_2 solid-state reaction at 80 °C. The $\text{NpO}_2(\text{s})$ and $\text{NH}_4\text{HF}_2(\text{s})$ reaction at 100 °C was also evaluated and a new compound of ammonium neptunium fluoride was identified after 7 days. Further evaluation of the reaction showed that the compound can be made at room temperature as well. The new

compound, $(\text{NH}_4)\text{NpF}_8$, was isostructural to that of $(\text{NH}_4)\text{UF}_8$ with a monoclinic unit cell and $C2/c$ space group. Lattice parameters of the compound are presented in Table 5.1.

The formation of $(\text{NH}_4)\text{NpF}_8$ was rapid at 100 °C and it can also be made at room temperature. The terminal product of the $\text{NpO}_2(\text{s})$ and $\text{NH}_4\text{HF}_2(\text{s})$ reaction at room temperature for 4 months and 80 °C for another 4 months was $(\text{NH}_4)_2\text{NpF}_6$, the reaction mechanism was defined in equations 5.1 and 5.2.

Heat treatment of the ammonium neptunium fluorides under $\text{NH}_3(\text{g})$ at different temperatures demonstrated a formation of series of neptunium compounds together with some new species identified for the first time. As Table 5.5 summarizes, $\text{NH}_4\text{Np}_3\text{F}_{13}$ was the first compound to identify at lower temperatures than 800 °C. NH_4NpF_5 was also identified in the same sample. NH_4NpF_5 isostructural with monoclinic NH_4UF_5 with a space group of $P121/c1$ while $\text{NH}_4\text{Np}_3\text{F}_{13}$ was had similar crystallography to $\text{NH}_4\text{U}_3\text{F}_{13}$ with an orthorhombic unit cell with a space group of $Pm21b$. NpF_3 was the next compound to be identified in the reaction sequence. Some peaks in the XRD pattern of the sample contained probably due to some incompletely crystallized NpF_4 (Figure 5.12a). When the reaction temperature was increased beyond 800 °C, the XRD patterns of the powder samples matched with three more new compounds: NpN_xF_y , NpN_2 , and Np_2N_3 . XRD pattern of NpN_xF_y compound was analogous to the tetragonal $\text{UN}_{0.95}\text{F}_{1.2}$ with a space group of $P4/nmmS$. NpN_2 and Np_2N_3 were isostructural to UN_2 and U_2N_3 compounds, respectively.

Heating the $(\text{NH}_4)_x\text{NpF}_y$ up to temperatures such as 1000 or 1100 °C, however, did not produce any NpN by the decomposition of higher neptunium nitrides identified. Further heating of the NpN_x samples under an inert atmospheric conditions produced

NpN. Heating the NpN_x at 1100 °C produced NpN but with large amounts of NpO_2 (Figure 5.17). Nevertheless, heating at 900 °C under Ar(g) produced NpN with reasonable purity (Figure 5.18). Given the amount of neptunium sample being heated is small (4 – 10 mg) and the high susceptibility of NpN to oxygen in the air (Figure 5.18 and 5.19), a 100 % phase purity was not able to achieved. The suggested reaction sequence for the formation of the different Np species is shown in Table 5.8.

Table 5.8 Reactions and products identify in the neptunium system.

Reaction		Products
Reactant	Exp. Conditions	
$(\text{NH}_4)_4\text{NpF}_8 \{ \text{Np}^{+4} \}$	80 – 250 °C	$(\text{NH}_4)_2\text{NpF}_6 \{ \text{Np}^{+4} \}$ / or $\text{NH}_4\text{NpF}_5 \{ \text{Np}^{+4} \}$
$(\text{NH}_4)_2\text{NpF}_6 \{ \text{Np}^{+4} \}$	400 °C, $\text{NH}_3(\text{g})$	$\text{NH}_4\text{Np}_3\text{F}_{13} \{ \text{Np}^{+4} \}$
$\text{NH}_4\text{Np}_3\text{F}_{13} \{ \text{Np}^{+4} \}$	500 °C, $\text{NH}_3(\text{g})$	$\text{NpF}_3 \{ \text{Np}^{+3} \}$ /or $\text{NpF}_4 \{ \text{Np}^{+4} \}$
$\text{NpF}_3 \{ \text{Np}^{+3} \}$ /or $\text{NpF}_4 \{ \text{Np}^{+4} \}$	≤ 800 °C, $\text{NH}_3(\text{g})$	$\text{NpN}_x\text{F}_y \{ \text{Np}^{+4} \}$
$\text{NpN}_x\text{F}_y \{ \text{Np}^{+4} \}$	≥ 800 °C, $\text{NH}_3(\text{g})$	$\text{NpN}_2 \{ \text{Np}^{+6} \}$
$\text{NpN}_2 \{ \text{Np}^{+6} \}$	≥ 800 °C, $\text{Ar(g)}/ \text{NH}_3(\text{g})$	$\text{Np}_2\text{N}_3 \{ \text{Np}^{+4} \text{ and } \text{Np}^{+5} \}$
$\text{Np}_2\text{N}_3 \{ \text{Np}^{+4} \text{ and } \text{Np}^{+5} \}$	≥ 800 °C, Ar(g)	$\text{NpN} \{ \text{Np}^{+3} \}$

Microscopic observations of $(\text{NH}_4)_4\text{NpF}_8$ and $(\text{NH}_4)_2\text{NpF}_6$ showed the bulk of the particles of them have incompletely crystallized flat surface morphologies. HRTEM could be used to confirm the crystal structure details of these two compounds even though some differences such as crystallinity of the nanostructures were found. Slow crystal formation of $(\text{NH}_4)_2\text{NpF}_6$ was also detected with HRTEM imaging of a sample

containing mixture of both compounds. Morphology of NpN_x also displayed some differences. Especially, the NpN had significant morphological differences with respect to the morphology of NpN_2 and Np_2N_3 . A majority of the NpN_2 particles was needle-shaped with some particles being larger than others. The plate-like characteristics of the particles of Np_2N_3 and NpN were prominent. NpN had the largest particle sizes compared to other NpN_x compounds studied here.

Table 5.9 Microscopic observations of neptunium compounds.

Compound	Microscopic observation	
	Morphology	Nanostructure
$(\text{NH}_4)_4\text{NpF}_8$	Incompletely crystallized flat surface	Polycrystalline with crystalline domains
$(\text{NH}_4)_2\text{NpF}_6$	Incompletely crystallized flat surface	Polycrystalline with crystalline domains
NpN_2	Needle-shaped with some large particles	High lattice fringe order
Np_2N_3	Plate-like particles	High lattice fringe order
NpN	Plate-like particles larger than that of NpN_2 and Np_2N_3	High lattice fringe order with some defects in lattice fringes due to NpO_2

Single crystal areas with high lattice fringe orders were observed in all NpN_x samples by HRTEM. NpO_2 phase could be identified at edges (Figure 5.28) and as well as complete crystals (Figure 5.29b) in NpN samples. These observations suggested that the oxidation of NpN can occur due to the reaction of oxygen of two sources. Because

only a small amount of sample were used to synthesize NpN and the partial pressure of the oxygen generated inside the furnace/quartz tube is high enough to react with bulk of the NpN produced at elevated temperatures, conversion of NpN into NpO₂ is possible at the time the sample synthesis. This is why well-crystallized NpO₂ were found at nanoscales (Figure 5.29b). The second source of oxygen is the environmental oxygen which can readily react with the synthesized NpN as determined by XRD (Figure 5.19). This is the source that led some of the NpN particle edges or surfaces to become oxidized making NpO₂ at those locations (Figure 5.30).

References

- (1) Blank, H. *J. Nucl. Mater.* **1988**, *153*, 171.
- (2) Minato, K.; Akabori, M.; Takano, M.; Arai, Y.; Nakajima, K.; Itoh, A.; Ogawa, T. *J. Nucl. Mater.* **2003**, *320*, 18.
- (3) Takano, M.; Akabori, M.; Arai, Y.; Minato, K. *J. Nucl. Mater.* **2008**, *376*, 114.
- (4) Arai, Y.; Nakajima, K.; Suzuki, Y. *J. Alloys Compd.* **1998**, *271-273*, 602.
- (5) Suzuki, Y.; Arai, Y. *J. Alloys Compd.* **1998**, *271-273*, 577.
- (6) Olson, W. M.; Mulford, R. N. R. *J. Phys. Chem.* **1966**, *70(9)*, 2932.
- (7) Sheft, I.; Fried, S. *J. Am. Chem. Soc.* **1953**, *75(5)*, 1236.
- (8) Arai, Y.; Fukushima, S.; Shiozawa, K.; Handa, M. *J. Nucl. Mater.* **1989**, *168*, 280.
- (9) Abazli, H.; Jove, J., . *R. Seances Acad. Sci., Ser. C.* **1979**, *288(4)*, 157.

CHAPTER 6

EVALUATION OF URANIUM-THORIUM MIXED SYSTEM

6.1 Introduction

Current research work reported in the early chapters has shown that ammonium bifluoride can be used to convert uranium and thorium oxides to ammonium actinide fluorides. Conversion of each of these ammonium actinide fluorides into their actinide nitrides (UN_2) or to the nitride fluoride ($ThNF$) suggested an exploration of making mixed nitrides by the ammonolysis of mixed ammonium actinide fluorides. This chapter presents and discusses the feasibility of making $(U, Th)N_2$ and $(U, Th)O_2$ solid solutions as an added application of the low-temperature fluoride route used to investigate the synthesis of actinide nitrides.

Actinide oxide solid solutions of thorium and/or uranium with the higher actinides offer a number of advantages for the nuclear fuel cycle. Potential plutonium burning capability [1] and analogous crystal structures to other tetravalent actinide oxides make thoria-based oxide fuels to be considered as a potential fuel type. Direct disposal of the irradiated thoria-based oxide fuels due to high resistance to aqueous corrosion [2, 3] and reducing ability of the leaching rates under oxidizing conditions [4] are few other advantages of these thoria-based nuclear fuels.

Current synthetic routes for actinide oxide solid-solutions require significant time and effort to produce a well homogenized mixed oxide product. Two synthetic routes are commonly used for the synthesis of actinide oxide solid-solutions: the dry method and the wet method. In the dry method, the separate actinide oxides are mixed and heated at elevated temperatures such as 1700 °C or higher under reducing atmospheric (hydrogen or argon/hydrogen) conditions [5, 6] for up to 48 hours or more. The resulting products, even after these prolonged sintering efforts, often fail to meet the required degree of homogeneity, requiring that the product to be milled or ground and re-sintered, some times more than once, to produce a final product that meets the requirement. In the wet method, the actinides are dissolved in an aqueous system and co-precipitated. The resulting precipitate is then converted to the oxide at an elevated temperature (1650 °C) under reducing atmosphere in order to get the final oxide solid-solution [7]. An alternative approach to the co-precipitation method is the sol-gel wet method. In sol-gel methods, a number of steps such as sol preparation, gelation, washing, drying, heat-treatment at 300 °C for 3 hours, humidification, pelletization, and sintering at 1100 °C in Ar/H₂ atmosphere for another couple of hours (2-3 hrs) are involved in order to obtain the final oxide solid solution [8]. The sol-gel method requires lower sintering temperatures than either the dry method or co-precipitation method uses. However, the production of oxide solid solutions by the sol-gel method requires significant additional effort to produce a quality product. Furthermore, to produce homogenous samples with near-theoretical densities, additional sintering at high temperatures is often required [9]. It is therefore of great interest to investigate other possible routes to synthesize oxide solid solutions.

Recent efforts to synthesize actinide nitrides [10] have suggested that a low-temperature fluorination-defluorination synthetic route may have the potential to address a number of concerns with the current techniques for producing solid solutions of actinide oxides. Wani, et al [11] has demonstrated the conversion of uranium ammonium fluoride to UF_4 at 400 °C in air. The use of electrolysis to synthesize UO_2 by electroreduction of UO_2F_2 which can be made by UF_4 as the starting material [12], and the synthesis of UO_2 from ammonium diuranate, $(NH_4)_2U_2O_7$, which is an intermediate product of the decomposition of $(NH_4)_4UF_8$ [13] are important findings that have also been reported.

The first part of the chapter discusses the synthesis of the ammonium uranium-thorium fluorides $((NH_4)_4U_{1-x}Th_xF_8)$ and the second part discusses the mixed uranium-thorium nitride system. A versatile low-temperature route for actinide oxide solid solutions is presented at the end of the chapter. Furthermore, the method developed and tested for the $(U, Th)O_2$ solid solution is suggested for extending to include the higher actinides such as neptunium and plutonium as future work.

6.2 Experimental Methods

6.2.1. Synthesis of Ammonium Uranium- Thorium Fluorides $((NH_4)_4U_{1-x}Th_xF_8)$

UO_2 and ThO_2 powders (International Bio-Analytical Industries, Inc.) were mixed using different mass ratios as indicated in Table 6.1. NH_4HF_2 was added to the U/Th oxide powder in a 4-to-1 molar ratio, with a 10% excess of NH_4HF_2 , and mixed in a mortar and pestle for approximately 10 minutes. The resulting mixtures were transferred into polyethylene vials and sealed for two days in order to ensure that the conversion of

the oxide to the ammonium fluoride salt is complete before using the samples for the next step.

Table 6.1 Sample compositions and the products formed after reacting with NH_4HF_2 .

Sample	Weight %		Terminal products
	ThO ₂	UO ₂	
UT 1	10	90	$(\text{NH}_4)_4\text{U}_{0.9}\text{Th}_{0.1}\text{F}_8$
UT 2	20	80	$(\text{NH}_4)_4\text{U}_{0.8}\text{Th}_{0.2}\text{F}_8$
UT 3	30	70	$(\text{NH}_4)_4\text{U}_{0.7}\text{Th}_{0.3}\text{F}_8$
UT 4	40	60	$(\text{NH}_4)_4\text{U}_{0.6}\text{Th}_{0.4}\text{F}_8$
UT 5	50	50	$(\text{NH}_4)_4\text{U}_{0.5}\text{Th}_{0.5}\text{F}_8$
UT 6	60	40	$(\text{NH}_4)_4\text{U}_{0.4}\text{Th}_{0.6}\text{F}_8$
UT 7	70	30	$(\text{NH}_4)_4\text{UF}_8 / (\text{NH}_4)_4\text{ThF}_8$
UT 8	80	20	$(\text{NH}_4)_4\text{UF}_8 / (\text{NH}_4)_4\text{ThF}_8$
UT 9	90	10	$(\text{NH}_4)_4\text{UF}_8 / (\text{NH}_4)_4\text{ThF}_8$

6.2.2. Heat Treatment of the Ammonium Uranium-Thorium Fluorides

Heat-treatment of the resulting ammonium fluorides of mixed uranium and thorium was performed by three different experimental conditions.

6.2.2.1 Heating under $\text{NH}_3(\text{g})$

The mixed ammonium fluorides of uranium and thorium were heated under flowing NH_3 gas to determine the feasibility of making $(\text{U}, \text{Th})\text{N}_2$ and thereafter the mixed mononitrides. A number of different temperatures starting from 150 °C were used to study the reactions.

6.2.2.2 Heating under Flowing Air

Samples are first placed on a platinum foil inside the reacting quartz tube. The quartz tube with the sample was heated in a tube furnace. Compressed air (Industrial grade) flow was started before the sample heating. The covering gas was passed into a water container and the heating was done up to 1100 °C.

6.2.2.3 Heating in a Box Furnace under Static Air

Some of the experiments were also performed in a box furnace under ambient conditions. No inert cover gas was used for these experiments. Heating was done again up to 1100 °C.

6.2.2.4 Heating under Argon

Sample heating was done in a similar manner described in section 2.2.1 except the argon was purged through the quartz tube for 10 min before heating. For the experiments in which argon flow was started after reaching a particular temperature, however, this was not the case. Here, the sample was heated up to 600 to 700 °C temperature first and started flowing argon from that point. The maximum temperature used in the experiments was 1100 °C.

6.3 Characterization methods

X-ray powder diffraction (XRD) patterns were obtained Cu-K α radiation filtered with a Ni filter. The current and tension used were 40 mA and 40 kV, respectively. A LaB6 SRM 660a internal standard was admixed with the samples before acquisition of the XRD powder patterns in order to perform Rietveld refinement with high accuracy. Lattice parameters were refined by Rietveld method. The morphology of the samples was

studied by scanning electron microscopy (SEM) and transmission electron microscopy (TEM). Samples were prepared for SEM imaging by mounting the powder on double-sided carbon tape prior to gold-coating. Bulk particle morphology of the samples was examined using SE imaging mode of SEM. Particle morphology was analyzed using the conventional bright field (BF) mode and lattice structure was analyzed using the high resolution TEM (HRTEM) mode.

6.4 Results and Discussion

6.4.1 Characterization of $(\text{NH}_4)_4\text{U}_{1-x}\text{Th}_x\text{F}_8$

The product phase composition of the mixed oxide starting systems is shown in Table 6.1. For samples containing up to 60 wt% ThO_2 , powder XRD patterns of the product ammonium actinide fluoride showed that they contain $(\text{NH}_4)_4\text{U}_{1-x}\text{Th}_x\text{F}_8$ solid solution with some impurity peaks at 12.6° , 16.2° , and 17.2° 2theta values (Figure 6.1c). Drying at 80°C for one week seems to remove most of these impurity peaks (Figure 6.1b), suggesting that they were due to ammonium fluoride and/or unreacted ammonium bifluoride residue in the samples. For samples containing 70 wt% to 90 wt% ThO_2 , the product is observed to contain two separated ammonium actinide fluoride chemical phases.

For the single phase systems, the impact of initial ThO_2 wt% on the lattice parameter of the product ammonium actinide fluoride is shown in Figure 6.2. All of a , b , and c lattice parameters increase linearly with respect to the increase in thorium level. Therefore, according to Vegard's law these six samples contain ammonium actinide fluoride solid solutions of chemical composition $(\text{NH}_4)_4\text{U}_{1-x}\text{Th}_x\text{F}_8$.

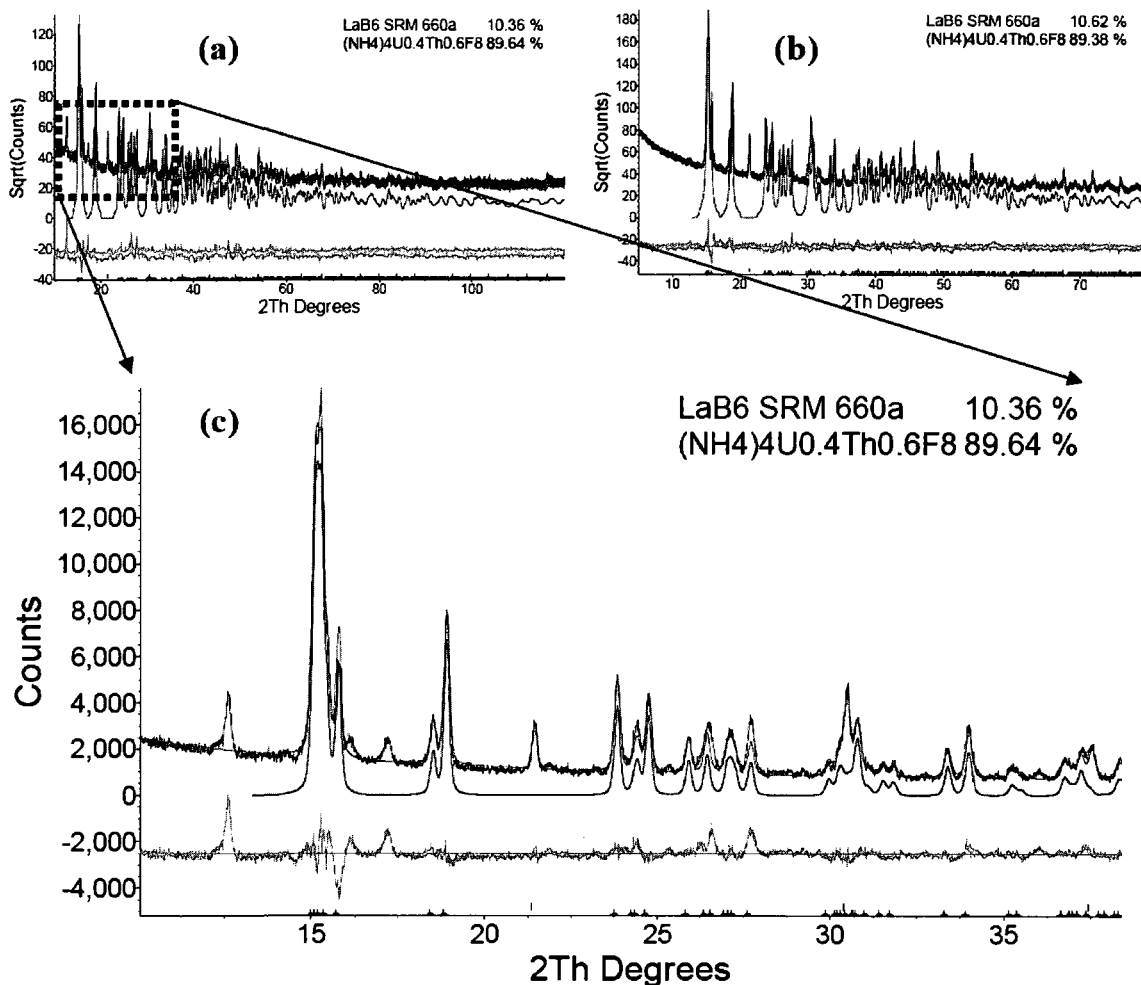


Figure 6.1 Drying effect on the sample phase purity: (a) XRD powder refinement of UT6 as-synthesized, (b) UT6 sample after dried at 80 °C for 7 days, and (c) enlarged powder pattern of as-synthesized UT6.

The SEM micrographs of samples UT1, UT6, and UT8 are shown in Figure 6.3. These images show that the product appears to consist of incompletely crystallized particle surfaces with similar grain morphology in all samples (including those not shown here). Elemental distribution (inset of Figure 6.4) confirms the presence of U/Th, F, and N elements in these samples. The Th-N edge starts to show a prominent peak as the Th wt% of the sample increases. In UT1, a well oriented single peak for U can be seen

(Figure 6.4). In UT6 and UT8, the Th peak separates out from U peak suggesting a phase separation especially for the UT8 sample as seen in XRD.

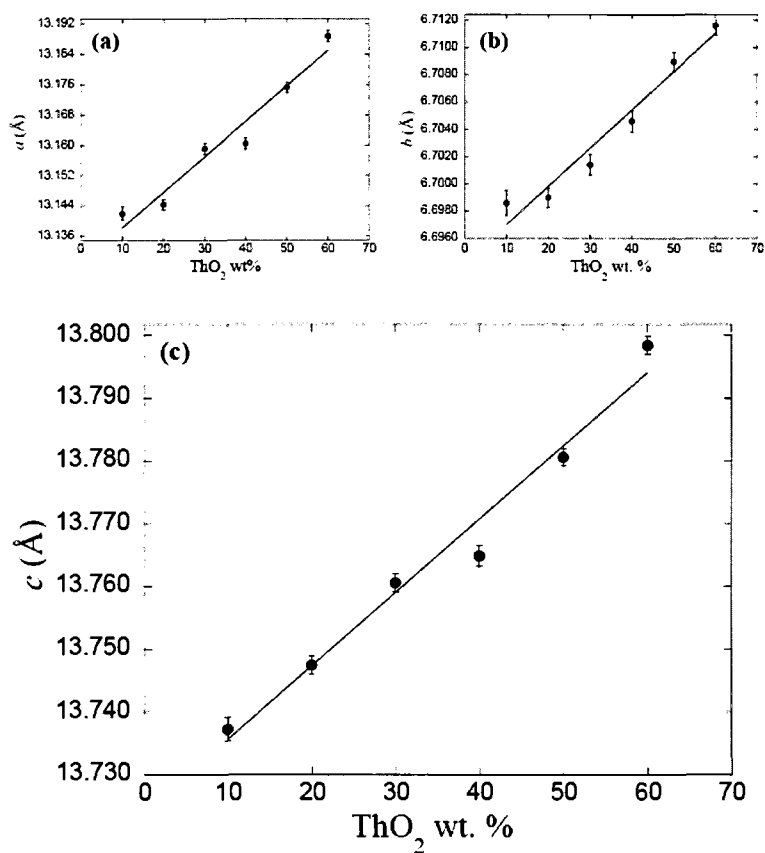


Figure 6.2 Lattice parameter variation of the monoclinic (space group of $C2/c$) $(\text{NH}_4)_4\text{UF}_8$ as a function of ThO_2 wt.% in the first six samples: (a) variation in a ; (b) variation in b ; (c) variation in c .

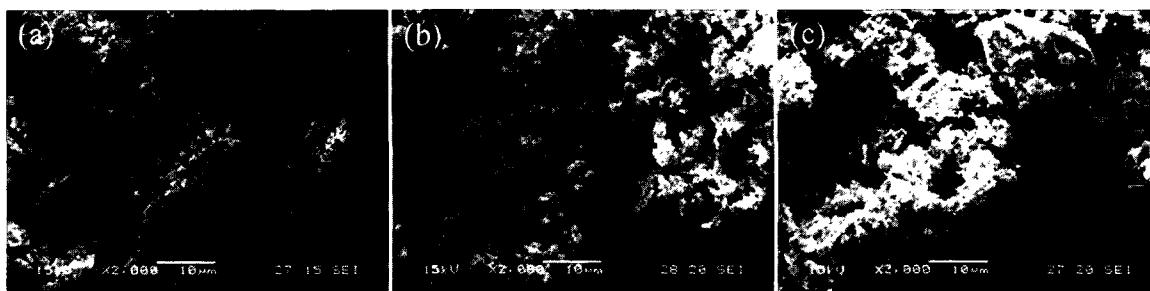


Figure 6.3 Secondary electron SEM micrographs of three as-synthesized samples: (a) UT1; (b) UT6; (c) UT8.

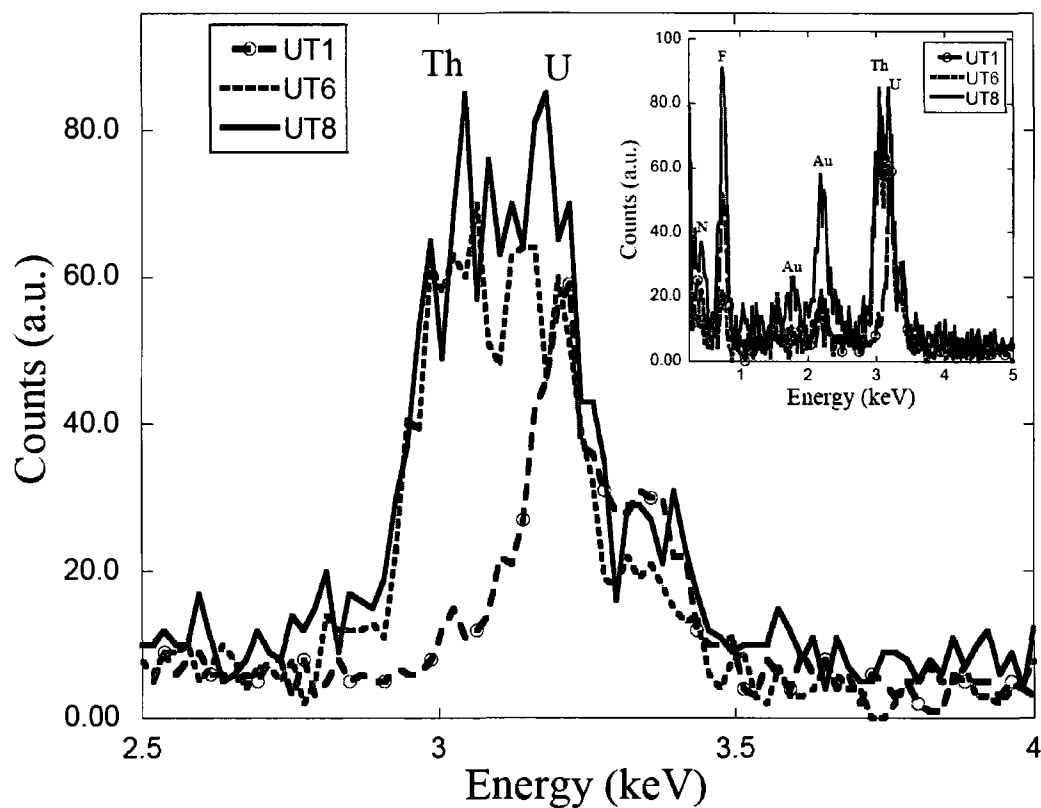


Figure 6.4 A comparison of the Th and U N-edge areas in EDS spectra of UT1, UT6, and UT8. Inset is the full spectra.

6.4.2 Ammonolysis of $(NH_4)_4U_{1-x}Th_xF_8$

In order to further investigate the feasibility of making U-Th mixed nitrides, one of the $(NH_4)_4(U, Th)F_8$ samples containing 10 wt% thorium was selected. This particular sample was tested because it was the first sample and has the lowest thorium level. Heat treatment of this sample was performed at different temperatures as shown in Table 6.2. At 150 °C, the original sample did not decompose into other compounds. Starting from 450 °C, formation of other compounds was seen. This temperature was also identified to at which the fluorides start to form. Complete decomposition of the ammonium fluoride into the nitride happened at 725 °C (Figure 6.5). The sample made by heating the ammonium fluoride at 725 °C for 5 min consisted of UN_2 and 3.08 wt % UO_2 , but with

some impurity peaks in the XRD pattern of the sample. To examine the reaction kinetics, additional experiments were performed in which the reaction time at temperature was varied. Longer heating showed a decrease of these unknown minor peaks in the XRD patterns together with a ThO₂ phase separation from UN₂ phase. At 800 °C, a similar behavior was seen in the samples synthesized. Sometimes, the ThO₂ level in these samples was more than 10 wt % probably due to some UO₂ phase solubility in the ThO₂ phase.

Table 6.2 Products observed for the heat treatment of (NH₄)₄U_{0.9}Th_{0.1}F₈ under NH₃ gas.

Temperature	Time/min	Products and wt. %				Unknown peaks in XRD
		UF ₄	UO ₂	UN ₂	ThO ₂	
*150	10	-	-	-	-	-
450	5	92.88	7.12	-	-	-
550	5	83.46	6.35	10.19	-	-
650	5	45.265	8.298	46.44	-	-
725	5	-	3.08	96.92	-	Yes
725	10	-	1.26	83.83	10.3	Yes
725	14	-	1.23	88.94	9.83	Yes
725	15	-	16.5	73.5	10	-
750	5	-	4.188	84.75	11.06	-
800	5	-	-	88.17	11.83	-
800	60	-	-	88.27	11.73	-

* 100 % (NH₄)₄(U, Th)F₈.

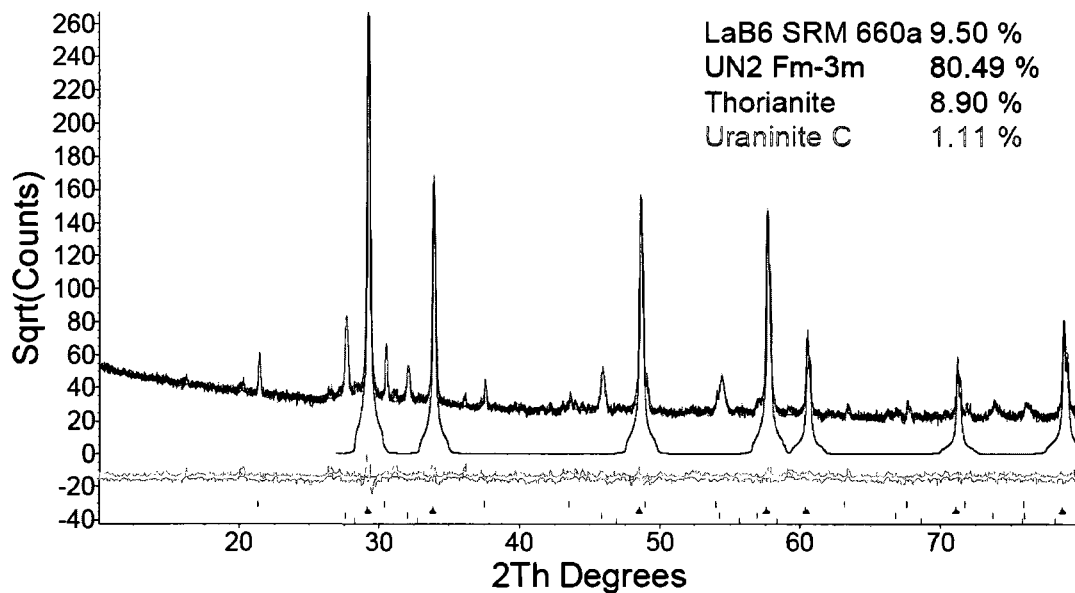


Figure 6.5 XRD powder pattern refinement of sample synthesized by heating UT1 at 725°C for 14min in NH₃(g).

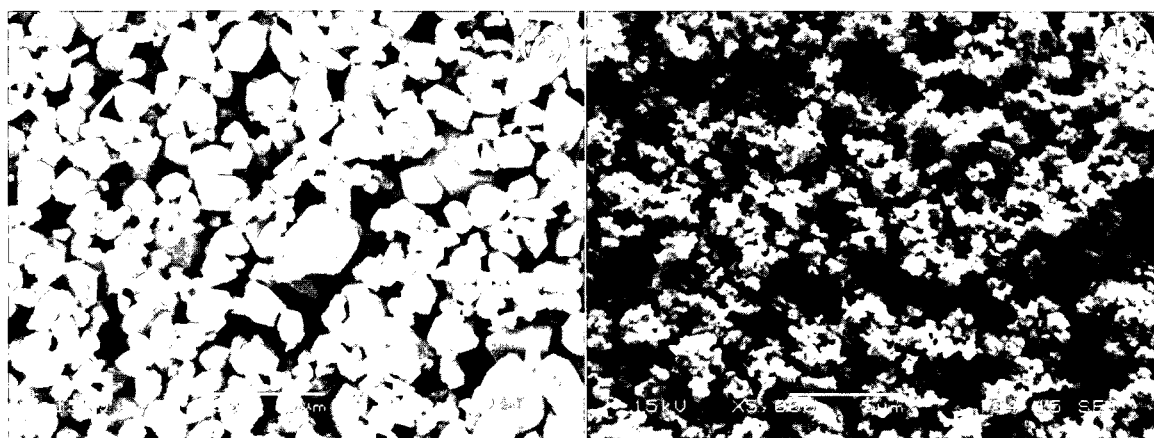


Figure 6.6 SEM micrographs of (a) UN₂ and (b) (U, Th)N₂/ThO₂ samples.

These two SEM micrographs in Figure 6.6 show that morphologies of UN₂ and U-Th-Nitride samples are different. Figure 6.6b displays smaller particles than of Figure 6.6a. U-Th-Nitride also shows more amorphous characteristics than the UN₂ suggesting an amorphization effect from Th incorporation.

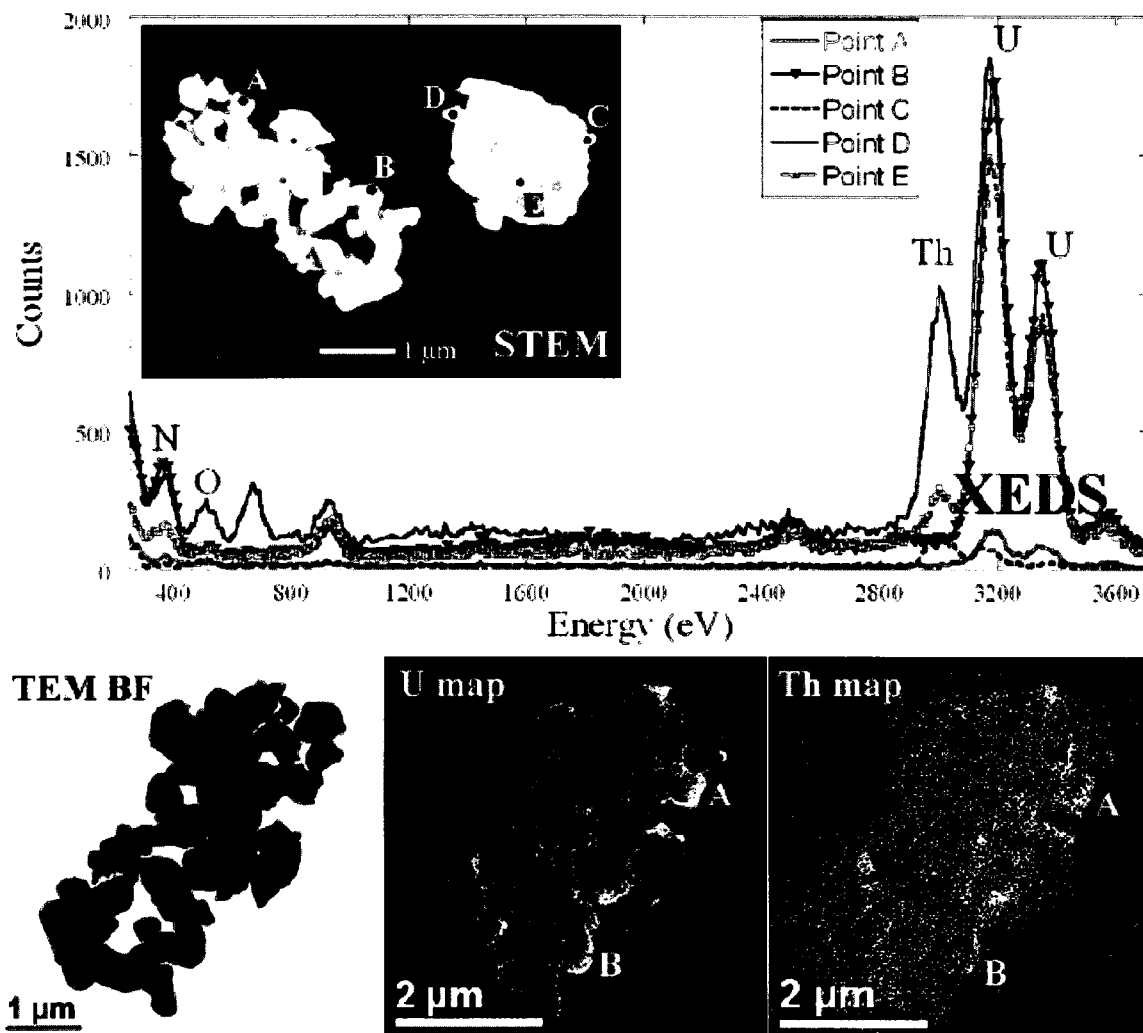


Figure 6.7 XEDS of the as-synthesized sample by heating $(\text{NH}_4)_4\text{U}_{0.9}\text{Th}_{0.1}\text{F}_8$ under NH_3 gas at 725°C for 10 min. Inset is the STEM image. TEM BF and the EELS maps of U and Th are also displayed.

The XEDS spectra of the particles of nitride/oxide mixed sample synthesized by heating $(\text{NH}_4)_4\text{U}_{0.9}\text{Th}_{0.1}\text{F}_8$ under NH_3 gas at 725°C for 10 min are shown in Figure 6.7. The N and O distribution in $(\text{U}, \text{Th})\text{N}_2/\text{ThO}_2$ sample is random depending on the particle being analyzed (top left inset of Figure 6.7). Particle areas denoted by points A and B mainly contain nitrogen and uranium. The EELS maps also revealed these two areas to contain mostly U and some Th. These observations suggest incorporation of Th into the

UN₂ matrix. Also, presence of oxygen without any nitrogen at point C demonstrates a oxide formation at the surface of the particles.

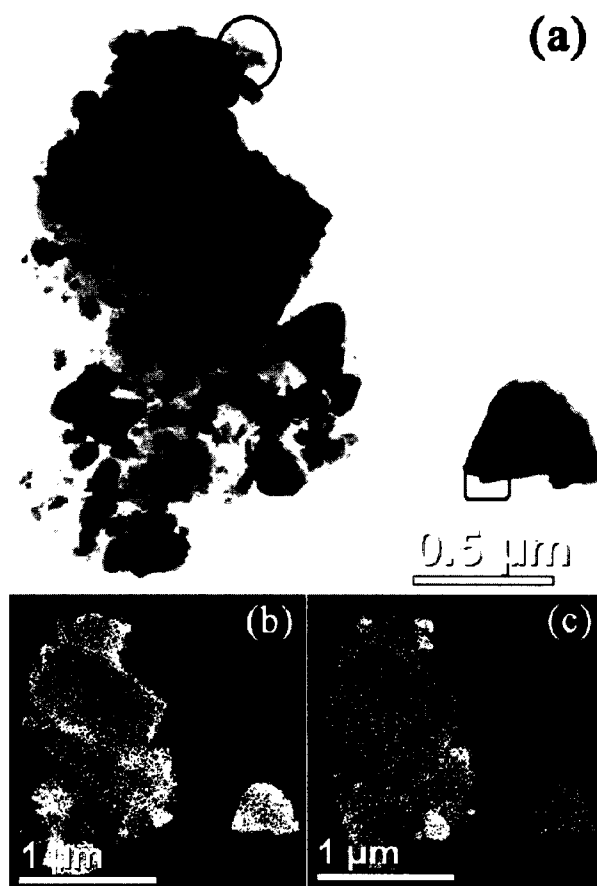


Figure 6.8 (a) TEM BF image, (b) U map, and (c) Th map of (U, Th)N₂/U-ThO₂.

Figure 6.8 displays a TEM BF image and U and Th maps of another set of particles. The HRTEM image of the particle denoted by a circle is shown in Figure 6.9. This area was chosen because of the high concentrations of U and Th that have been observed in Figures 6.8b and 6.8c. Figure 6.10 represents HRTEM images of two nanoparticle areas of the single particle in Figure 6.8a (rounded rectangle).

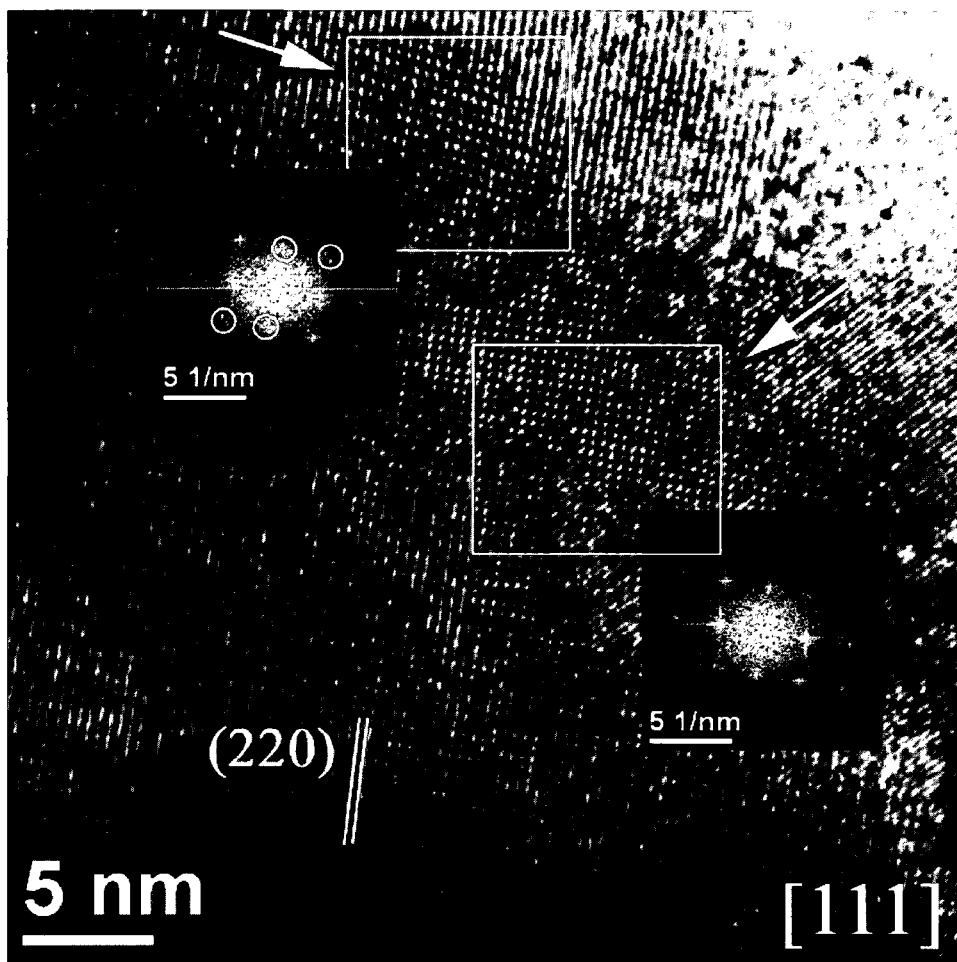


Figure 6.9 A HRTEM image of the circled particle area in Figure 6.8.

The HRTEM image in Figure 6.9 displays a large area containing lattice fringes of UN_2 due to (220) planes. At first, it looks like a single crystal area. However, detailed analysis showed the presence of another lattice fringe orientation as indicated by top left arrow. This second set of lattice fringes oriented slightly different to that of bulk of this area causing extra diffraction spots in FFT inserted at top left. This disorientation and the formation of extra spots in the corresponding FFT indicate a possible incorporation of Th in UN_2 matrix in its nanostructure.

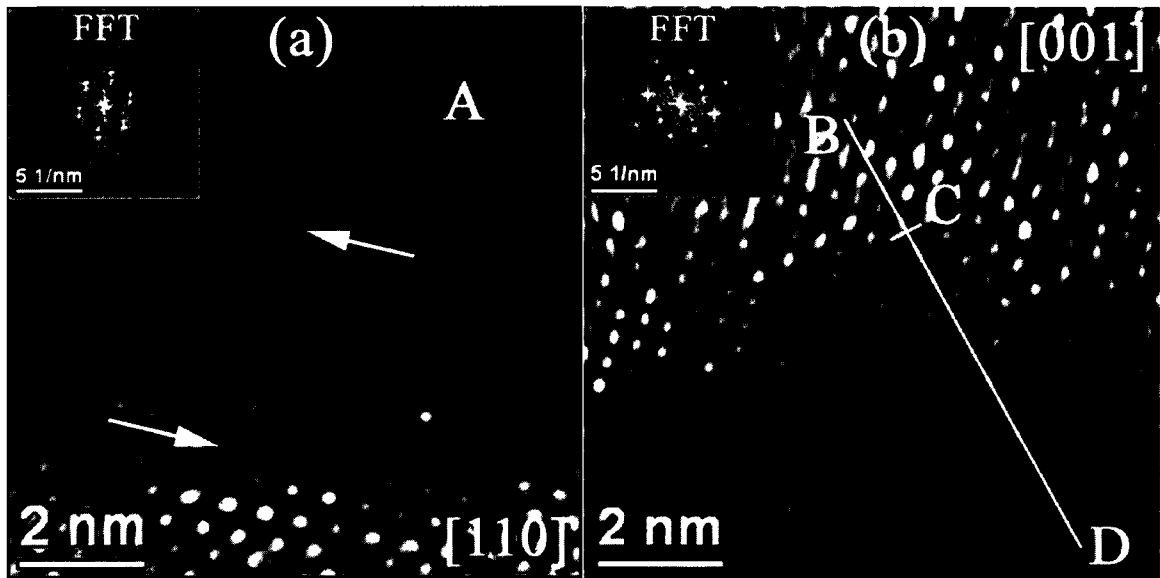


Figure 6.10 HRTEM images of two areas of the single particle shown in Figure 6.9.

HRTEM of two areas of the single particle (Figure 6.8a) shown in Figure 6.10. Both these particle areas contain lattice fringe details due to UN_2 . In Figure 6.10a, lattice fringes of (111) plane are present. This area consists of disoriented lattice fringes at number of locations as indicated by arrows. Small areas within the particle containing fewer details can also be detected (area A). Figure 6.10b shows the reflections of (200) planes of UN_2 mostly. These reflections start changing when going from B through D forming different type of lattice fringes with closer spacing from C to D than from the original (C to B and beyond). The corresponding FFT micrograph (inset of Figure 6.10b) also consists of extra diffraction spots confirming this observation. Incorporation of a second phase is probably the reason for both these observations. Given the secondary oxide phases form mostly at the surface of the uranium nitride particles, it can be concluded that Th is incorporated into UN_2 matrix.

Table 6.3 Observed reaction products for the heating of $(\text{NH}_4)_4(\text{U, Th})\text{F}_8$ for 1 through 4 wt% of thorium under NH_3 . There is up to a 1% error in the wt% values.

ThO ₂ wt%	Temp. /°C	Time/ min	Product wt% and lattice parameters (Å)					
			UN ₂	L.P.	ThO ₂	L.P.	UO ₂	L.P.
1	725	15	89.2	5.3059 (3)	7.84	5.586 (5)	2.97	5.4686 (4)
2	725	12	84.2	5.3072 (1)	5.26	5.584 (2)	10.5	5.4702 (3)
3	725	10	87.4	5.3063 (2)	9.36	5.589 (1)	3.2	5.465 (2)
4	725	10	91.5	5.3077(2)	3.8	5.5927(5)	4.7	5.462 (2)

* Lattice parameters of the UO₂ and ThO₂ source samples are (ref value: 5.4682) and 5.5982(3), respectively.

Since less than 10 wt% of Th solubility in the UN₂ phase was seen from the TEM studies, four more $(\text{NH}_4)_4(\text{U, Th})\text{F}_8$ samples were synthesized with Th contents from 1 to 4 wt%. These four samples were subjected to heat treatment at 725 °C under NH_3 . The 725 °C temperature was selected because it was the lowest temperature at which the $(\text{NH}_4)_4(\text{U, Th})\text{F}_8$ decomposition was completed forming UN₂ (Table 6.2).

The results obtained for these four samples are shown in Table 6.3. The oxide levels are greater than 10 wt% in the first three samples. However, the differences in the lattice parameters of UO₂ and ThO₂ phases of these samples compared to the source compounds indicate a mutual solubility of these two chemical phases. Therefore, it can be concluded that there is a very small amount of Th solubility in UN₂ matrix.

6.4.3 Thermal behavior of $(\text{NH}_4)_4\text{U}_{1-x}\text{Th}_x\text{F}_8$ under flowing air

Table 6.4 shows the impact of reaction temperature on the conversion of the $(\text{NH}_4)_4\text{U}_{0.9}\text{Th}_{0.1}\text{F}_8$ sample under air. At 550 and 800 °C, the conversion of the ammonium fluorides to the oxide is not completed after heating for 30 or 60 minutes. Complete

conversion to the oxide phase was seen starting from 900 °C temperature with minimal impurity peaks in the XRD patterns.

Table 6.4 Results obtained for the heating of the $(\text{NH}_4)_4\text{U}_{0.9}\text{Th}_{0.1}\text{F}_8$ under air.

Temp./°C	Time (min)	Products		Impurity peaks
		Primary	Secondary	
550	30	UF ₄	UO ₂ F ₂ , U ₃ O ₈	-
800	60	ThF ₄	U ₃ O ₈ , *SS, ThO ₂	-
900	30	U ₃ O ₈	SS, ThO ₂	yes
1000	30	U ₃ O ₈	SS, ThO ₂	yes
1100	30	SS	-	-

*SS: oxide solid-solution

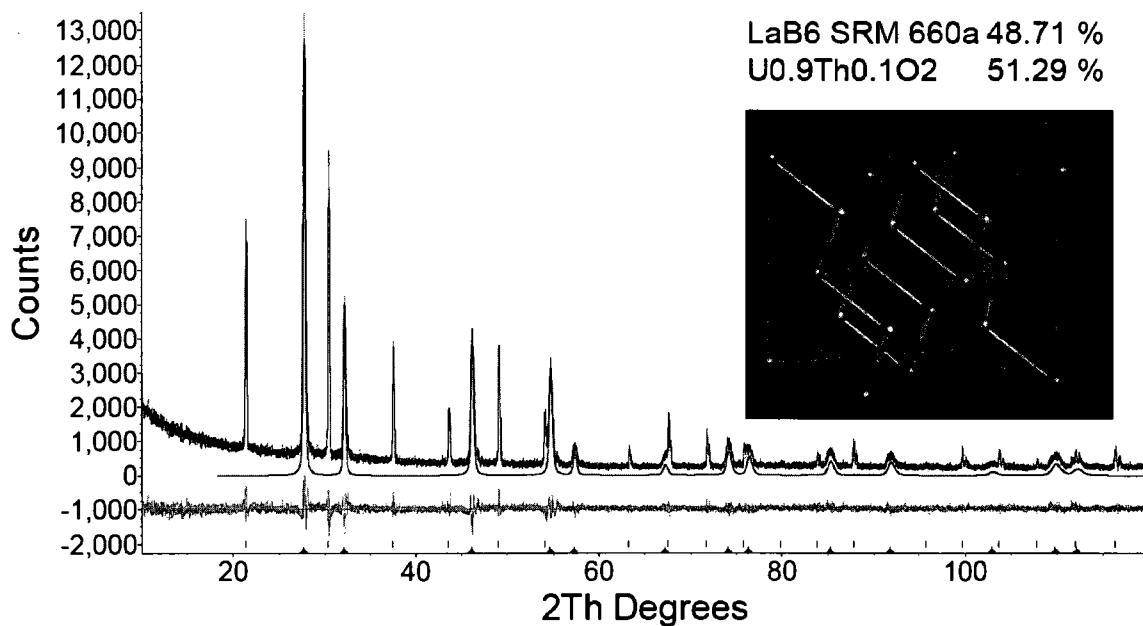


Figure 6.11 XRD powder pattern refinement and the Fourier map (inset) of $\text{U}_{0.9}\text{Th}_{0.1}\text{O}_2$ solid solution synthesized at 1100 °C.

Increasing the reaction temperature to 1100 °C results in a single-phased $U_{0.9}Th_{0.1}O_2$ solid-solution (SS) (Figure 6.11) after 30 minutes. During these experiments, however, significant weight loss (> 70 %) was observed, most likely due to the rapid reaction of fluorides under a continuous flow of air.

6.4.4 Heat treatment of $(NH_4)_4U_{1-x}Th_xF_8$ under static air

Table 6.5 Heat treatment of the samples at 1100 °C for 30 minutes under air.

Sample	Th wt %	Products		U ₃ O ₈ wt %
		Primary	Secondary	
UT 1	10	SS	U ₃ O ₈	83.736
UT 2	20	SS	U ₃ O ₈ , ThO ₂	61.075
UT 3	30	SS	U ₃ O ₈ , ThO ₂	48.839
UT 4	40	SS	U ₃ O ₈ , ThO ₂	34.177
UT 5	50	SS	U ₃ O ₈ , ThO ₂	22.124
UT 6	60	SS	-	-
UT 7	70	SS	U ₃ O ₈	0.900
UT 8	80	SS	U ₃ O ₈ , UO ₂ (25.084)	1.080
UT 9	90	SS	-	-

Since an oxide solid solution was obtained by heating $(NH_4)_4U_{0.9}Th_{0.1}F_8$ at 1100 °C for 30 min under a stream of air, the same temperature and time was used for the other samples. To minimize sample loss by entrainment in the flowing air stream, the reaction was performed in a box furnace that is open to the atmosphere. Table 6.5 summarizes the results obtained for each sample. Under these experimental conditions, the first five samples containing 10-50 wt % thorium formed oxide solid-solutions together with some

secondary phases (ThO_2 and U_3O_8). Samples of 60, 70, and 90 wt % thorium produced the expected oxide solid-solutions without any secondary chemical phases. However, the sample at 80 wt % thorium behaved slightly different. This sample contained a small amount of U_3O_8 as a secondary phase, but there was a ~ 25 wt % UO_2 chemical phase. This result was checked by repeating the experiment two times and the results were approximately the same (Figure 6.12). Thus the 80 wt % thorium can be inferred as an outlier of the $(\text{U}, \text{Th})\text{O}_2$ solid-solutions containing ≥ 60 wt% thorium under these experimental conditions.

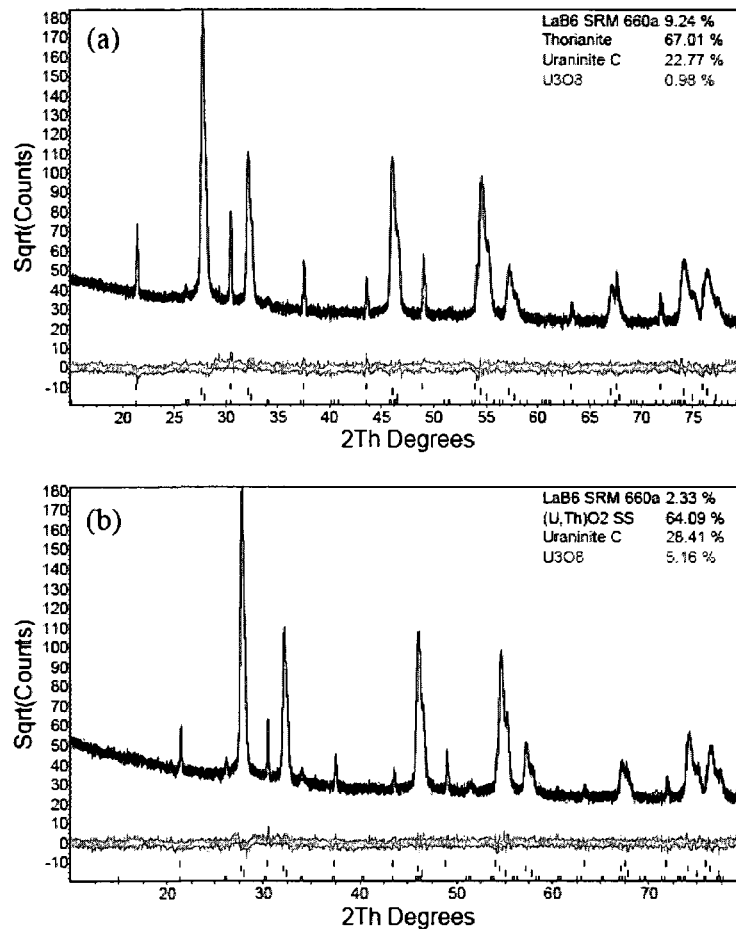


Figure 6.12 Refined XRD powder patterns of $\text{U}_{0.2}\text{Th}_{0.8}\text{F}_8$ synthesized by heating $(\text{NH}_4)_4(\text{U}_{0.2}\text{Th}_{0.8})\text{F}_8$ at 1100°C for 30 min: (a) first time; (b) second time.

Reduction of the U_3O_8 product phase was attempted using sample UT2 by heating under NH_3 at 650 °C for 1 hour [14]. This reaction produced two separated oxide phases (Figure 6.13). Given the difficulties in producing solid-solution samples from the dry mixing of actinide oxide powders [5, 6] this result is not unexpected as no additional homogenization of the intermediate products in this synthesis was performed.

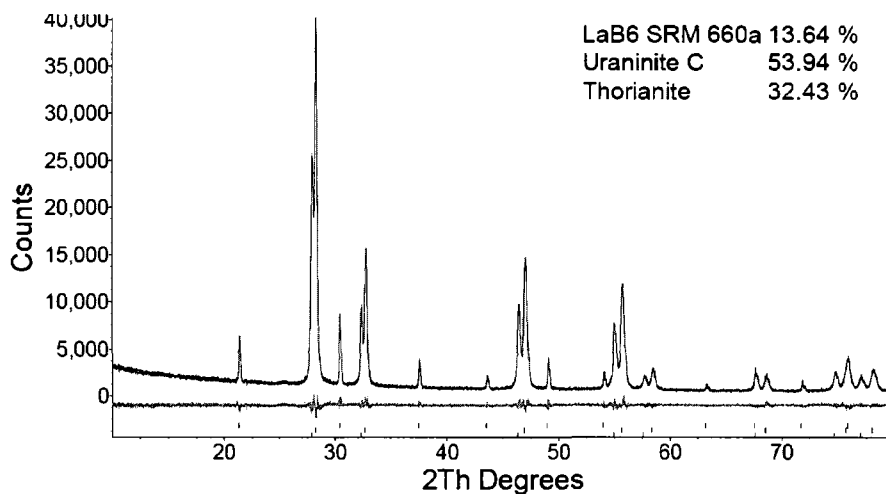


Figure 6.13 XRD refinement of $(U, Th)O_2/U_3O_8$ after reduced in NH_3 at 650 °C for 1 hr.
6.4.5 Heat treatment of $(NH_4)_4U_{1-x}Th_xF_8$ under argon

As the conversion of $(NH_4)_4U_{1-x}Th_xF_8$ under air was not successful in synthesizing oxide solid solutions with a single phase for $0.1 \leq x \leq 0.5$, the reaction was studied under argon at the same temperature for 30 min. Heating of UT1 sample under these experimental conditions resulted in $U_{0.9}Th_{0.1}O_2$ solid solution single phase. Initial experiments under flowing argon showed the same weight loss as for the flowing air system. Measurements of the residues in the quartz tube downstream of the sample confirmed the initial hypothesis that the rapid reaction of the fluoride at temperature results in significant entrainment in the gas stream. To reduce this entrainment problem, a

two-step reaction path was developed (Table 6.6). In phase 1, samples are heated in the air-filled quartz tube under static flow conditions to a target temperature. Once the target temperature is reached, argon flow over the sample is initiated and maintained throughout the remainder of the conversion.

Table 6.6 Two-Stage Conversion of 40 wt% Th sample under static air / flowing argon.

Ar flow initiation temperature (°C)	Chemical phases in the product		Weight loss %
	Primary	Secondary	
870	UO ₂	ThO ₂	47.9
820	ThO ₂	UO ₂ and U ₃ O ₈	48.1
710	SS	-	63.4
610	SS	-	57.9

To further reduce the weight loss from the samples due to rapid reaction and entrainment in the cover gas, the heating rate of the furnace was reduced from 50 °C/min to 9 °C/min. Using this two-step heating process, the mass loss was reduced to near theoretical values. For example, for the UT3 sample the mass loss from the two-step heating process was 45.7%, just above the theoretical weight loss (42 wt% for (NH₄)UF₆ to UO₂ reaction) for this reaction, when the argon cover gas flow was initiated at 610 °C. The one-stage method, heating to 1100 °C under a continual argon cover gas flow from the beginning of the heating, resulted in a mass loss of 84.8 wt%. These mass losses may have some variations even after using the optimum experimental conditions due to the extra weights of the excess NH₄HF₂ as well as residual NH₄F impurities in the ammonium actinide fluorides. Argon flow was started at 610 °C because U₃O₈ formation

starts at 400-610 °C [13, 15] temperature range and the fluorides decomposition occurs at a high temperature as shown in Table 6.4. These experimental conditions resulted in the formation of a single-phased oxide solid-solution of the uranium and thorium for the complete series of the samples varying thorium from 10 to 90 wt %. The lattice parameters of these samples vary linearly with respect to the increase in Th wt % (Figure 6.14) obeying the Vegard's law [16]. This further confirms the formation of a series of (U, Th)O₂ solid solutions [5].

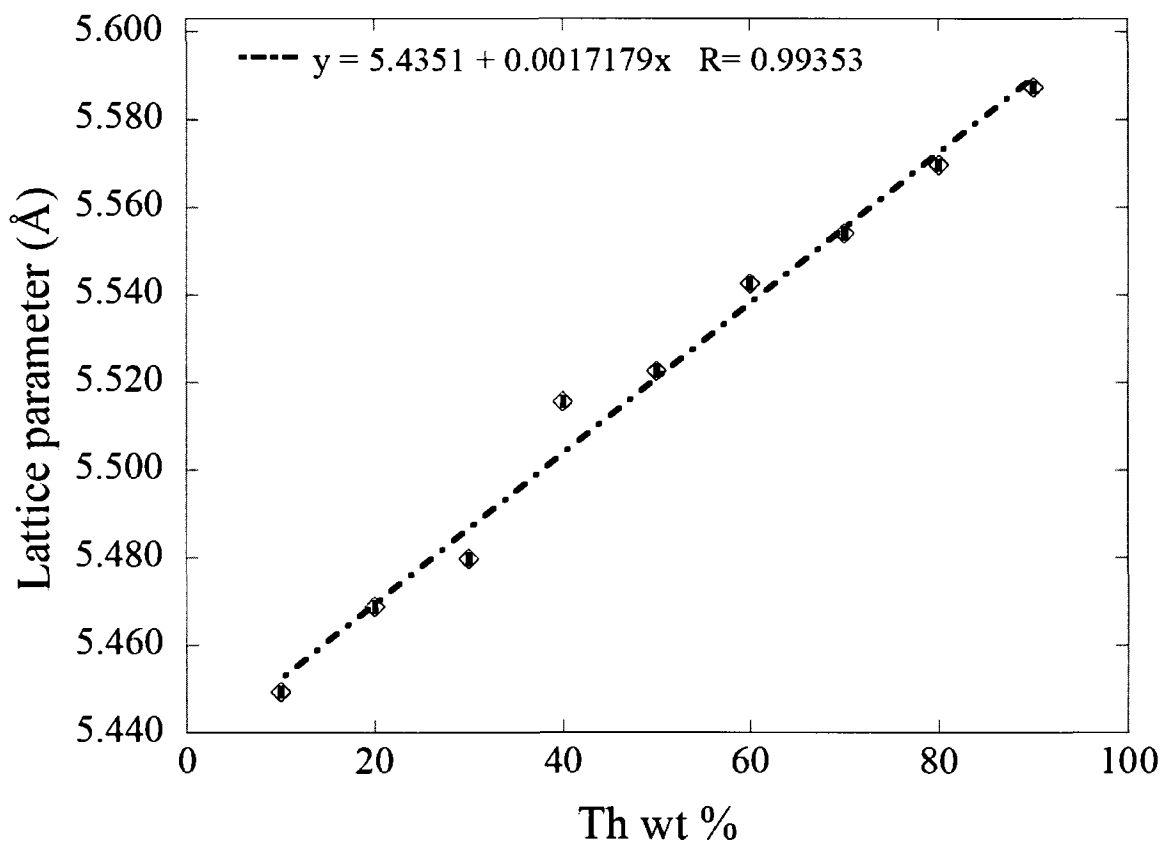


Figure 6.14 Lattice parameter variation of the (U, Th)O₂ solid-solutions as a function of the Th wt % used.

6.4.6 Microscopic characterization of (U, Th)O₂ solid-solutions

Figure 6.15 shows SEM micrographs of four different oxide solid solution samples synthesized under argon. These images show that the product appears to consist of incompletely crystallized particle surfaces with somewhat similar grain morphology. All these samples also consist of particles of randomly distributed morphology. Some areas of the samples contain partially crystallized particles where as some other areas consist of particles without any crystallite facets.

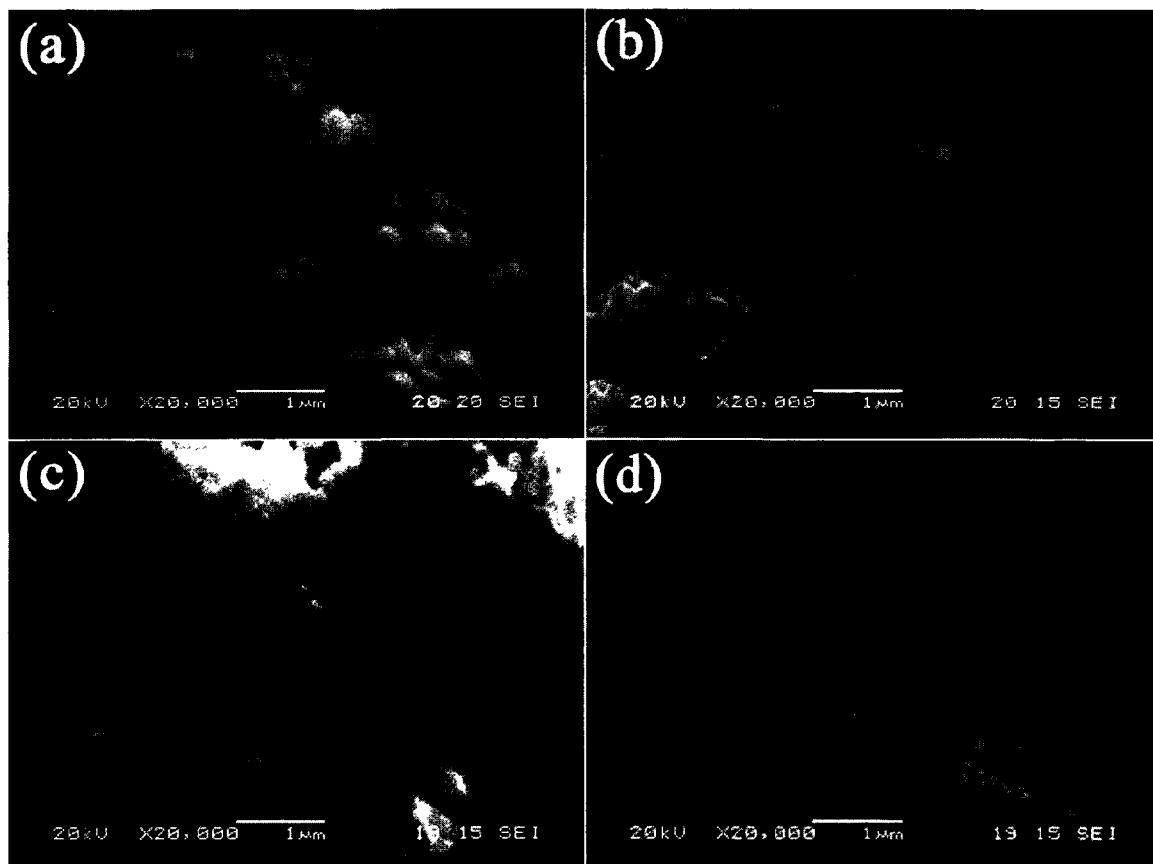


Figure 6.15 Secondary electron SEM micrographs of (U, Th)O₂ solid solutions as a function of Th amounts: (a) 10 wt %; (b) 30 wt %; (c) 50 wt %; (d) 70 wt %.

These random distributions of the particle morphology suggest the samples are not homogeneously distributed. Sintering would probably diminish these characteristics making the samples more crystalline and more organized. Bulk particles of 10 and 30 wt% Th samples are larger than that of 70 and 90 wt% because the agglomerated UO_2 particles are larger than the ThO_2 particles. The 30 wt% Th sample also displays some pore spaces within its particles. Particles in Figure 6.15c and 15d indicate a more round shape compared to that in Figure 6.15a and 15b. This observation indicates a more crystalline character in 50 and 70 wt% Th samples than in the other two. Table 6.7 shows elemental distribution of two samples (60 and 90 wt% Th) with accurate expected element percentages.

Table 6.7 Elemental analysis of oxide solid solutions of 60 and 90 wt% Th.

Sample	Average element %			U/Th ratio	
	U	Th	O	Experimental	Theoretical
60 wt%	30.10	47.05	22.85	0.64	0.67
90 wt%	7.35	66.65	26.00	0.11	0.11

HRTEM of $\text{U}_{0.9}\text{Th}_{0.1}\text{O}_2$ sample particle is shown in Figure 6.16a. The whole area displayed in the figure contains well-crystallized character with lattice fringes correspond to (220) planes. The Bloch simulation in Figure 6.16 b also confirms the crystal structure of the sample. Experimental lattice fringes match well with the simulated images of 0 to -12 mm defocus and 5 to 145 nm thickness values.

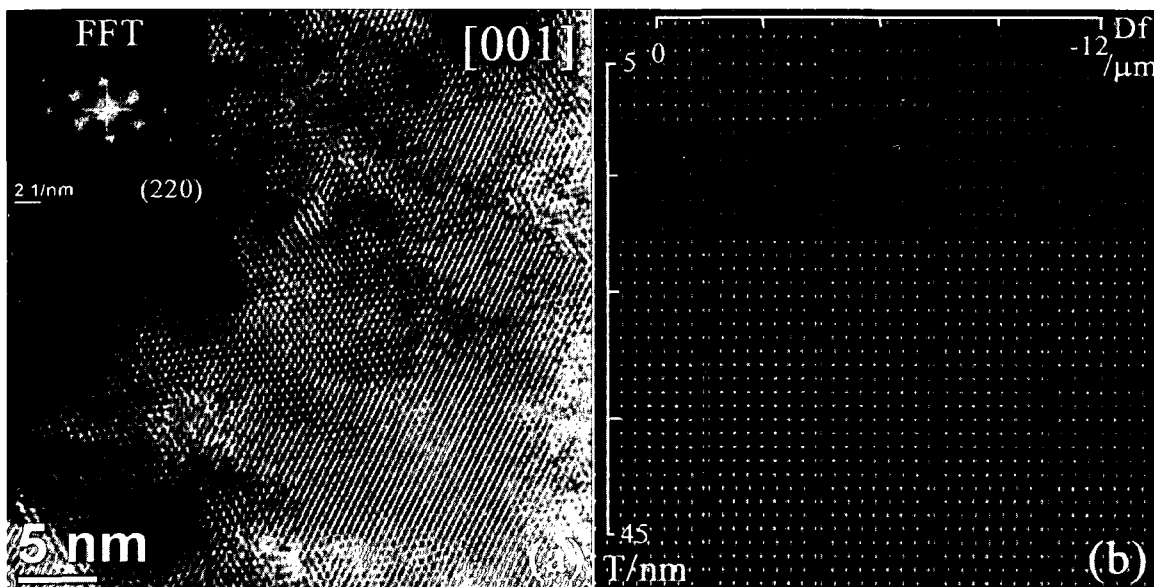


Figure 6.16 (a) HRTEM image of a well-crystallized particle area of $U_{0.9}Th_{0.1}O_2$ solid solution and (b) Bloch simulation of the oxide correspond to (220) reflection along [001].

Some areas of the same sample were identified to consist with grains of different sizes as displayed in Figure 6.17. The magnified image in Figure 6.17b demonstrates that some of these grains contain two directional lattice fringes without any defects. Figure 6.17c shows mainly two directional lattice fringes but with some specific patterns in some of the nanosclae areas within the grain. The arrow pointed along c-o direction represents the lattice fringes directional to that orientation while the three arrows (1, 2, and 3) along o-a direction point the “Z” shape orientations. These nanoscale changes in the oxide lattice fringe orientations suggest an incorporation of thorium into the UO_2 matrix.

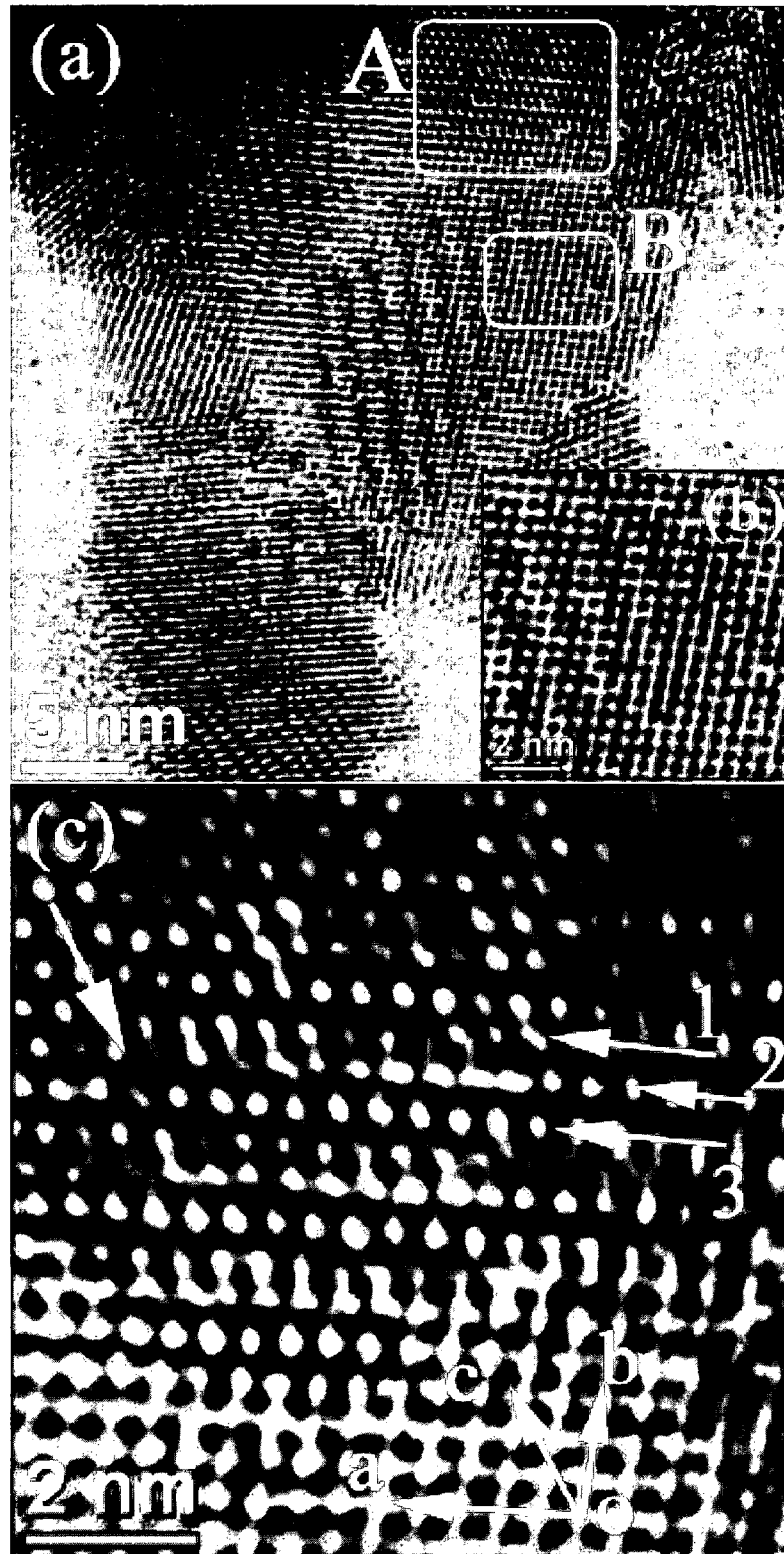


Figure 6.17 HRTEM of another $U_{0.9}Th_{0.1}O_2$ particle area. (a) Grain boundaries, (b) magnified image of area B, and (c) magnified image of area A.

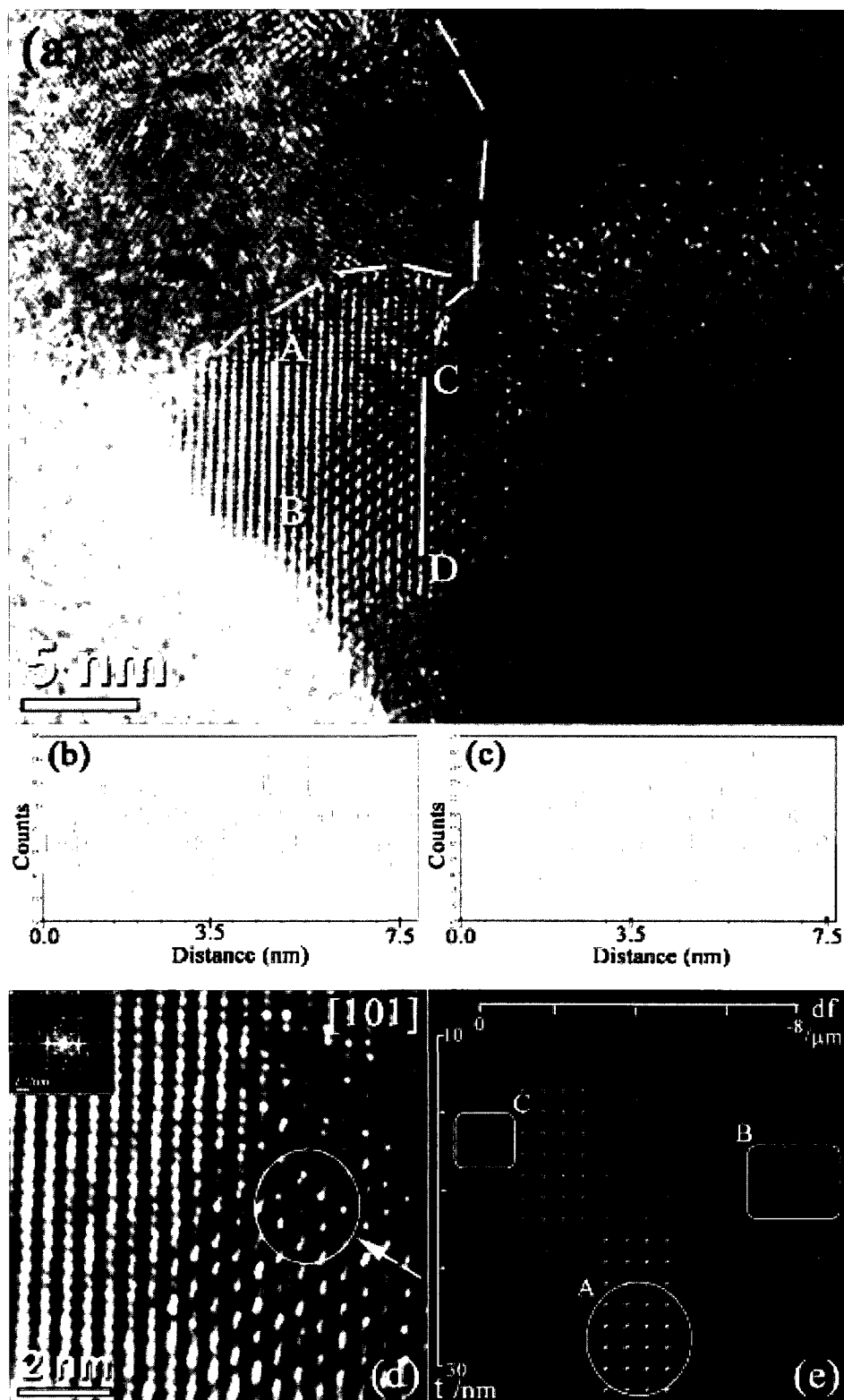


Figure 6.18 (a) HRTEM image and experimental intensity profiles along (b) AB and (c) CD. Magnified image of the area in between AB and CD lines (d) and the Bloch simulation of UO_2 due to (111) planes along [101] zone axis.

$U_{0.9}Th_{0.1}O_2$ sample also contain particle areas where lattice fringes show more compact space filling than expected. Figure 6.18 shows a detailed HRTEM analysis of such as a particle area. A grain boundary displaying a separation of two grains with one elongated grain towards the other is shown in Figure 6.18a. The experimental intensity profiles along AB (Figures 6.18b) and CD (Figure 6.18c) reveal that the atomic layers in these two areas have 2-fold and 1-fold order in space filling. The second grain (top left side of the image) however does not have lattice fringe orientation that can cause such space filling. Figure 6.18d shows a magnified image of the area in between AB and CD lines. Bloch simulations (Figure 6.18e) obtained for (111) planes of the compound along [101] zone axis also confirm that defocus or thickness variance of the compound cannot be the reason for such nanostructural behavior. Lattice fringes circled in Figures 6.18d and 6.18e matches up to a certain level, and the change in defocus or the thickness could cause their formation like the ones highlighted by rectangles in Figure 6.18e. Therefore, the 2-fold order found here can be considered as due to thorium incorporation into the UO_2 matrix.

The HRTEM/intensity profiles shown in Figure 6.19 are from a sample of as-synthesized $U_{0.4}Th_{0.6}O_2$ oxide solid solution. This figure shows three different layers of grains. The first and last layers have high intensity as shown in experimental intensity profiles. The middle layer consisted of less intensity and it spreads throughout the focused area. At the two boundaries (areas B and C) where the middle layer interacts with others, lattice fringe orientations of the two layers can be observed interchangeably. This indicates that the middle layer acts as bridge to mix the other two together.

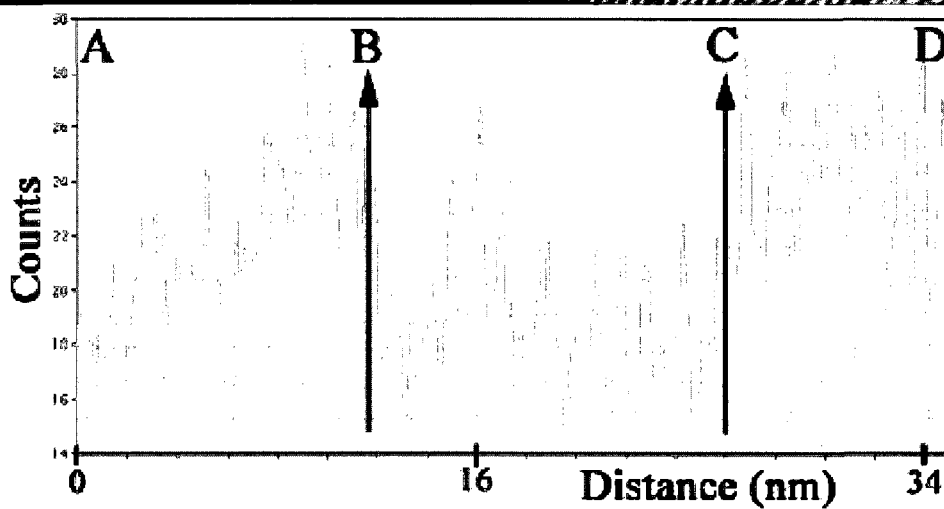
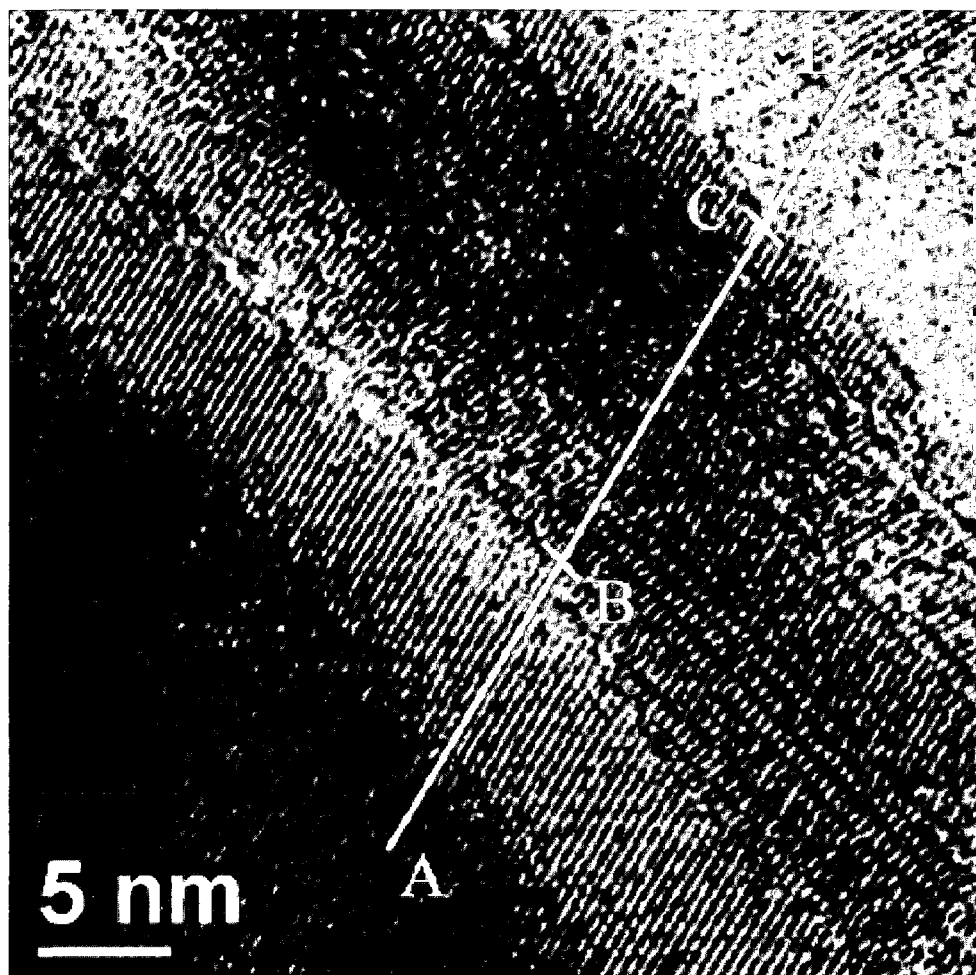


Figure 6.19 HRTEM of $U_{0.4}Th_{0.6}O_2$ oxide solid solution. Intensity profiles along A through D are also presented.

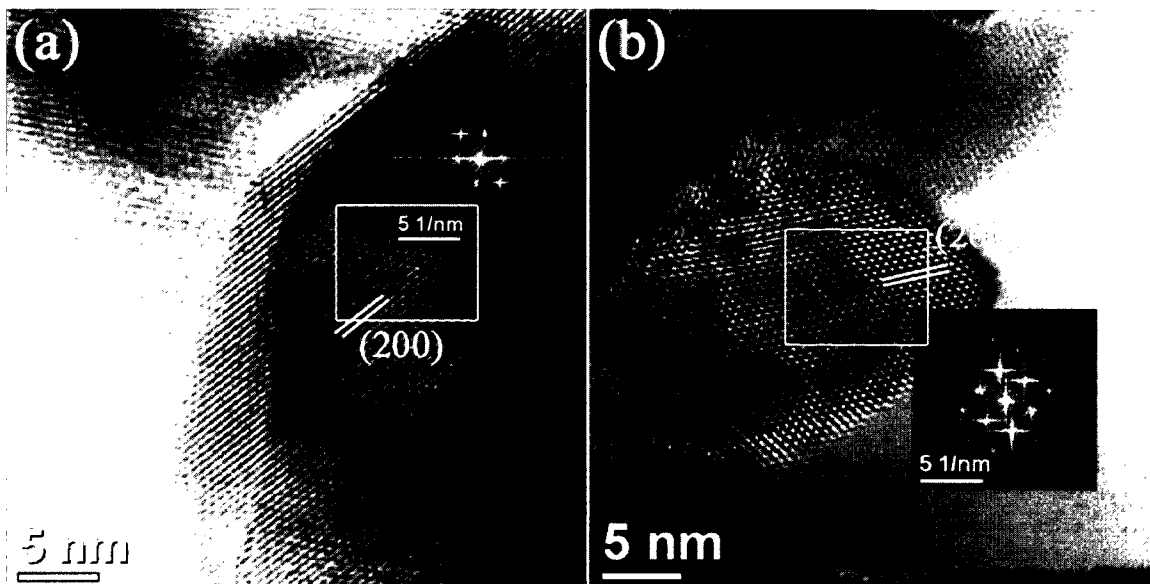


Figure 6.20 HRTEM of two particle areas of $U_{0.2}Th_{0.8}O_2$ solid solution sample.

$U_{0.2}Th_{0.8}O_2$ also demonstrated to contain high crystalline characteristics in its nanostructure. Figure 6.20a shows few particles without any defects in their lattice fringes. Within these particles some localized grains of high lattice fringe order can also be observed as in Figure 6.20b.

Even in this sample, particle areas of some defects could be identified. Figure 6.21 represents an example. This figure shows a considerably large area containing single crystal characteristics, but the direction of the lattice fringes along AB changes at B/C positions as indicated by an arrow. The fringe formation is then progressed up to the edge of the particle (position D). These lattice fringes also start to show some missing information (circles) within approximately 2nm range. These observations suggest possible crystallization inhibitions due to incorporation of the minor oxide (UO_2) in the ThO_2 , which is dominant at 80 wt% Th, of the solid solution.

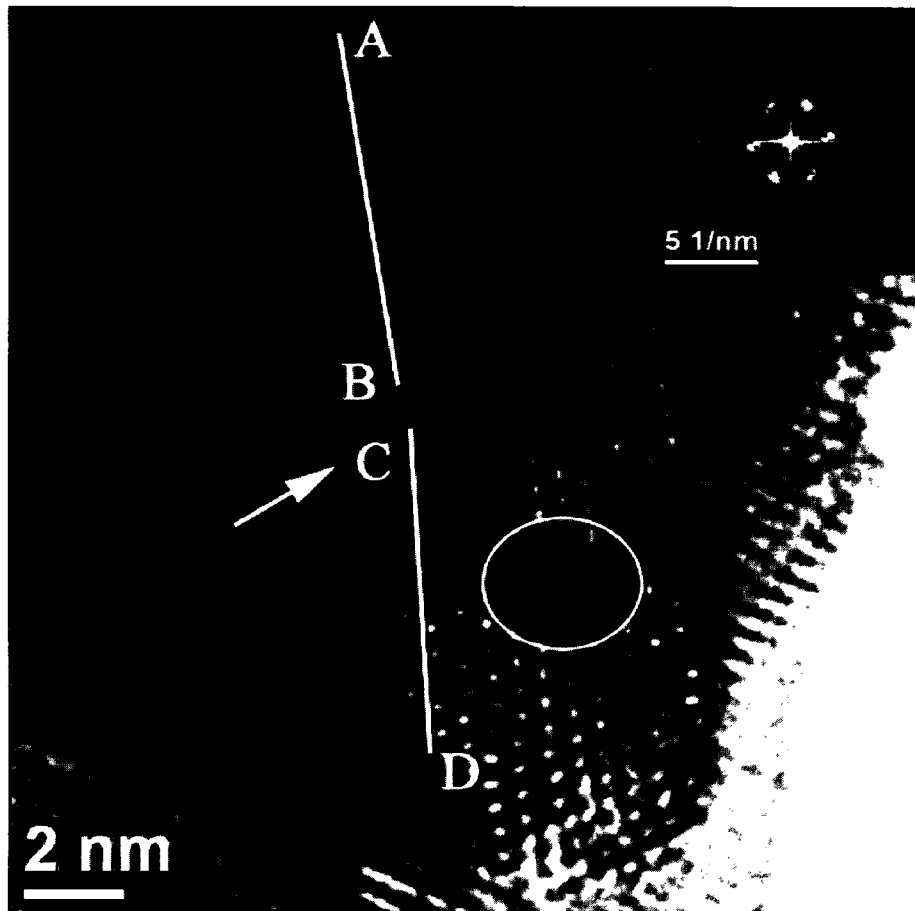


Figure 6.21 Single crystal area of $U_{0.2}Th_{0.8}O_2$ solid solution with minor defects.

Again crystalline domains oriented along different directions are present in $U_{0.1}Th_{0.9}O_2$ as well (Figure 6.22a). HRTEM in Figure 6.22b was obtained by focusing the particle about 20 nm from the bottom of area in Figure 6.22a. This figure indicates some deformed lattice fringes possibly oxide solid solution formation. Twin boundary of the same sample was also seen as depicted in Figure 6.23. This figure further shows a high crystalline order of the lattice fringes correspond to (111) planes of the oxide. Bloch simulation further verifies the six-member atomic rings formed along the direction.

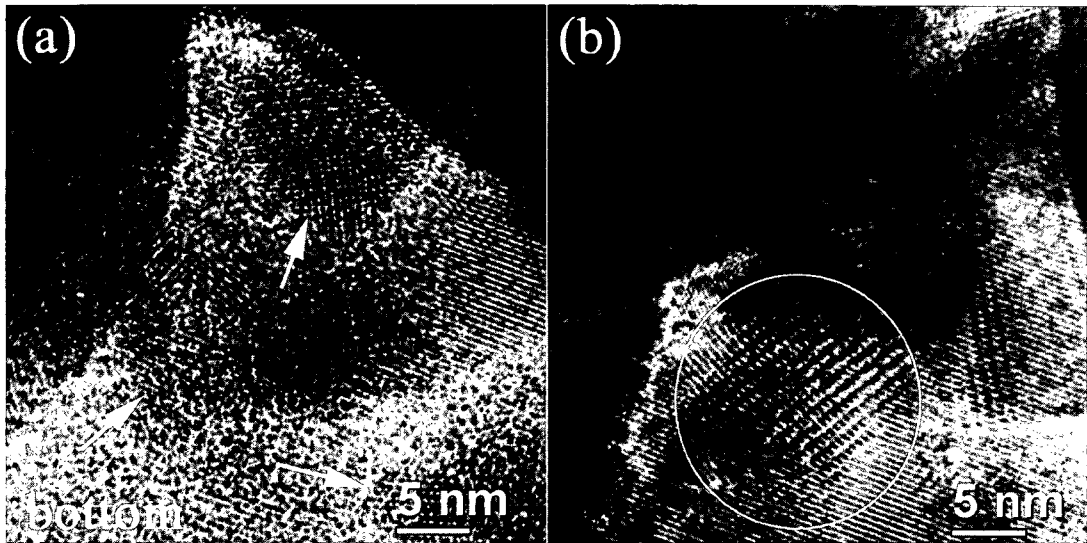


Figure 6.22 HRTEM images of the as-synthesized $U_{0.2}Th_{0.8}O_2$ sample.

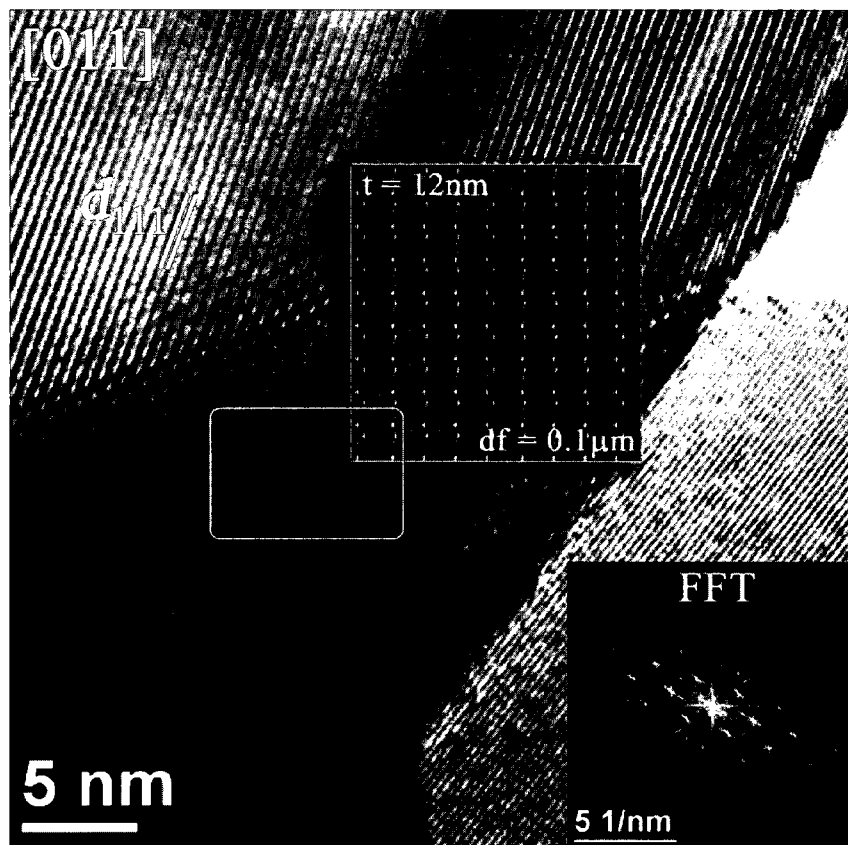


Figure 6.23 HRTEM image showing a twin boundary of the as-synthesized $U_{0.2}Th_{0.8}O_2$ sample. Insets are the calculated Bloch images and the FFT.

6.5 Conclusions

Experiments conducted on the $(\text{NH}_4)_4(\text{U}, \text{Th})\text{F}_8$ samples containing 10 wt% Th displayed an oxide chemical phase separation from the UN_2 matrix. Further characterizations of these samples by TEM techniques, however, revealed an incorporation of Th into the UN_2 nanostructure. Further experiments performed on four $(\text{NH}_4)_4(\text{U}, \text{Th})\text{F}_8$ samples of different Th levels up to 4 wt% showed a very small amount (<1 wt%) of Th incorporation into UN_2 according to the mutual solubility of UO_2 and ThO_2 in each other.

Synthesis of $(\text{U}, \text{Th})\text{O}_2$ solid solutions from the actinide oxides by a low-temperature fluoride route was investigated. In this process, an $(\text{NH}_4)_4\text{U}_{1-x}\text{Th}_x\text{F}_8$ intermediate phase was synthesized by mixing UO_2 and ThO_2 with NH_4HF_2 . $(\text{NH}_4)_4\text{U}_{1-x}\text{Th}_x\text{F}_8$ solid-solutions were formed up to $x = 0.6$. At higher thorium content ($x \geq 0.7$), two separate phases, $(\text{NH}_4)_4\text{UF}_8$ and $(\text{NH}_4)_4\text{ThF}_8$, were formed. The intermediate ammonium actinide fluoride phase was then subsequently heated under different atmospheres to check the feasibility of making $(\text{U}, \text{Th})\text{O}_2$ solid solutions.

First sets of experiments performed under a stream of air and static air showed a complete conversion of the ammonium fluorides of some compositions into the corresponding oxide solid solutions after heating them up to a maximum temperature of 1100 °C for 30 min. Heat treatment of the ammonium fluorides under an air flow produced $(\text{U}, \text{Th})\text{O}_2$ solid solutions with some minor impurity phases. Also, unexpected high weight losses were identified in these experiments mostly due to entrainment of the sample with the cover gas. Therefore, heating the fluorides under a static environment was performed. These conditions however produced single-phased $(\text{U}, \text{Th})\text{O}_2$ solid solutions only when the thorium content is greater than 50 wt %. Samples of other compositions showed to contain considerable amounts of a secondary U_3O_8 chemical

phase explaining why samples of Th > 50 wt% resulted the oxide solid solutions. Heating the ammonium fluorides under argon flow also produced (U, Th)O₂ solid solutions but with high weight losses. Theoretically expected weight losses with the single-phased characteristics were obtained by a two-phased heating. At first, samples were heated in an air-filled quartz tube under static flow conditions to a target temperature of 610 °C and then the argon flow over the sample was initiated and maintained throughout the remainder of the heat treatment. Argon flow at the second stage was necessary to hinder further oxidation of the tetravalent actinide oxide solid solutions into U₃O₈. With these optimized experimental conditions, a complete series of U_{1-x}Th_xO₂ solid-solutions for 0.1 ≤ x ≤ 0.9 was synthesized.

Microscopic studies showed the oxide solid-solutions to have much similar morphology at bulk level. A high degree of crystallinity was observed in some areas of the oxide solid solutions at nanoscale. Particle containing different orientations and grain boundaries were observed in these oxides. Bridging effects of particle layers and some deformations in the lattice fringe formations were also found due possibly due to the incorporation of second oxide phase into the major oxide matrix. Compact space filling in nanostructures was also found to be observant in these oxide solid solutions.

References

- (1) Akie, H.T.; Muromura, T.; Takano, H.; Matsuura, S. *Nucl. Technol.* **1994**, *107*, 182.
- (2) Fourest, B.; Vincent, T.; Lagarde, G.; Hubert, S.; Baudoin, P. *J. Nucl. Mater.* **2000**, *282*, 180-185.

- (3) Hubert, S.; Barthelet, K.; Fourest, B.; Lagarde, G.; Dacheux, N.; Baglan, N. *J. Nucl. Mater.* **2001**, *297*, 206-213.
- (4) Heisbourg, G.; Hubert, S.; Dacheux, N.; Purans, J. *J. Nucl. Mater.* **2004**, *335*, 5-13.
- (5) Cohen, I.; Berman, R. M. *J. Nucl. Mater.* **1966**, *18*, 77-107.
- (6) Eichler, R.; Hanus, D.; Krellmann, J.; Lob, R.; Roepenack, H. *J. Nucl. Mater.* **1984**, *124*, 9-13.
- (7) Sari, C.; Benedict, U.; Blank, H. *J. Nucl. Mater.* **1970**, *35*, 267-277.
- (8) Tel, H.; Eral, M.; Altas, Y. *J. Nucl. Mater.* **1998**, *256*, 18-24.
- (9) Yamagishi, Y.T. S. *J. Nucl. Mater.* **1992**, *189*, 134-140.
- (10) Yeamans, C. B.; Silva, G. W. C.; Cerefice, G.S.; Czerwinski, K.R.; Hartmann, T.; Burrell, A.K.; Sattelberger, A.P. *J. Nucl. Mater.* **2008**, *374*, 75-78.
- (11) Wani, B. N.; Patwe, S. J.; Rao, U. R. K.; Venkateswarlu, K. S. *J. Fluorine Chem.* **1989**, *44*, 177-185.
- (12) Schlechter, M.; Kooi, L.; Billiau, R.; Charlier, R. A.; Dumont, G. L. *J. Nucl. Mater.* **1965**, *15*, 189-200.
- (13) Le Page, A. H.; Fane, A.G. *J. Inorg. Nucl. Chem.* **1974**, *36*, 87-92.
- (14) Valdivieso, F.; Pijolat, M.; Soustelle, M. Jourde, J. *Solid State Ionics* **2001**, *141-142*, 117-122.
- (15) Yang, J. H.; Rhee, Y. W.; Kang, K. W.; Kim, K. S.; Song, K. W.; Lee, S. J. *J. Nucl. Mater.* **2007**, *360*, 208-213.
- (16) Bamberger, C. E.; Base Jr, C. F. *J. Nucl. Mater.* **1970**, *35*, 177-182.

CHAPTER 7

CONCLUSIONS AND RECOMMENDATIONS

7.1 Uranium System

Use of the fluorite route was successful in synthesizing UN. Optimum experimental conditions for the synthesis of UN with 97 wt% phase purity were determined. Further experimentation of the uranium system was performed to study reaction mechanism and kinetics. Decomposition of UN₂ in an inert atmosphere resulted in forming UN_x where $1 \leq x \leq 2$. U₂N₃ and UNF were found to be the intermediate stoichiometric compositions between UN₂ and UN and UF₄ and UN₂, respectively. Lattice parameters of both UN₂ and U₂N₃ displayed a linear increase with respect to the temperature used to synthesize the samples. The lattice parameter of UN did not show any special relationship to the temperature been used to synthesize it although it showed to have range of values even at one particular temperature. Kinetics involved in the UN₂ decomposition was also studied at three different temperatures. Rate constants of the UN₂ to UN reaction at 1000, 1050, and 1100 °C were determined to be 0.07 ± 0.01 , 0.21 ± 0.02 , and $1.3 \pm 0.3 \text{ s}^{-1} \times 10^3$, respectively. Activation energy of the reaction was calculated to be $423.8 \pm 0.3 \text{ kJ/mol}$ based on the Pseudo-first-order kinetics.

Microscopy was used extensively to study the morphology and nanostructures. Bulk particles of UN₂, U₂N₃, and UN demonstrated a similar morphology. Only a slight morphology difference was observed in the UN particles with respect the extent of

crystallization at their discrete faces. A high crystallinity in these UN_x nanostructures was also observed with HRTEM. A high-ordered lattice fringes with multiple channels of UN was detected in some nano particle areas. Also, UN_2 and U_2N_3 had well-packed high order in their lattice fringe orientations. These microscopic evaluations further explained the UO_2 phase formation in UN particles. UN was more susceptible to oxygen in air than UN_2 or U_2N_3 . However, the oxygen reaction with UN was comparatively slow (about 5 wt% increase of the UO_2 content in three months). Discovery of UO_2 formation mainly on the particle surfaces or edges explained the slow rates of UN reactivity with oxygen.

7.2 Thorium System

The fluoride route used to synthesize UN_x was not successful in synthesizing ThN_x using similar experimental conditions. However, new findings related to the Th system were reported. Solid state reaction of ThO_2 and NH_4HF_2 at room temperature proved to consist of one known and two unknown intermediate chemical phases with a terminal product of $(NH_4)_4ThF_8$ composition. The known intermediate was found to be $(NH_4)_3ThF_7$ with stability up to few months in the reaction mixture containing unreacted ThO_2 and excess NH_4HF_2 . The terminal product of the ammonolysis of ammonium thorium fluoride up to $1100^\circ C$ was found to be $ThNF$. Thermal decomposition of this compound to make ThN_x was not successful under Ar, Ar/ H_2 (5%), N_2 , or N_2/H_2 (5%) atmospheres up to the same temperature. It is recommended to try temperatures greater than $1100^\circ C$ in decomposing $ThNF$ further to check the feasibility of making ThN_x . These decompositions will have to be done in a furnace of very high pure inert atmosphere to avoid formation of ThO_2 . Finding a series of low stoichiometric ThN_xF_y

compositions however helped proposing a possible mechanism to this reaction as discussed in the corresponding chapter. Microscopic evaluation showed that particles of $(\text{NH}_4)_4\text{ThF}_8$ had well-crystallized acicular shape while ThNF exhibited plate-like character with some pore spaces. Nanostructures of the $(\text{NH}_4)_4\text{ThF}_8$ and ThNF illustrated polycrystalline and single crystal characteristics, respectively. Single crystal areas were found in $(\text{NH}_4)_4\text{ThF}_8$ compound mainly of small domains. High crystalline order of the ThNF nanostructure was also observed.

Introduction of LiNH_2 into the reaction media at the ammonolysis step of the fluoride route induced formation of ThN_x resulting Th_2N_3 . However, the oxidation state of Th in Th_2N_3 has not been previously investigated earlier. Thorium cannot have mixed tetravalent and pentavalent state as necessitated by the stoichiometry of Th_2N_3 assuming an N^{3-} oxidation state. Elemental distribution of the as-synthesized Th_2N_3 samples also showed that $\text{Th}_2\text{N}_2\text{O}$ is not the chemical phase in these samples even though the XRD pattern of it matches with the sesquinitride. Tetravalent zirconium is a suitable Th homolog for the nitrides system. Similar electronic configuration of Zr in the valence shells to that of Th leads one to believe the difficulty in forming the necessary mixed oxidation state given nitrogen has 3- oxidation state in a ZrN_x chemical composition. Nevertheless, zirconium based research works in early nineties report the observation of Zr_2N_3 [1]. The same study showed that Zr_2N_3 also oxidizes very easily in air. Presence of colloidal Zr_2N_3 has also found [2]. Another study reported the identification of Zr_3N_4 and not the Zr_2N_3 chemical composition [3]. This work also described the formation of a series of amides as a result of decomposition of $\text{Zr}(\text{NH}_3)\text{Cl}_4$. These compounds contained chemical compositions of $\text{Zr}(\text{NH}_2)_4$ and $\text{Zr}(\text{NH})_2$. The nitride, Zr_3N_4 , was obtained

heating $Zr(NH)_2$ at 350 °C. The final compound produced by decomposing $Zr(NH)_2$ was Zr_3N . These observations suggest a possibility of NH group involvement in the Zr_2N_3 if it is to be present. Therefore, $Th_2N_2(NH)$ chemical phase, which preserves the 4+ oxidation state for thorium, can be suggested to be contained in the prepared Th samples in this work. Since the $LiNH_2$ used in the synthesis is a logical source of NH ligand, this idea can further be supported. Further experimentations on identifying the presence of NH by FTIR studies are suggested. Another observation of these samples were the presence of ThO_2 as the impurity phase even though the cover gases used had the same purity levels as for uranium system. Microscopic characterization of these samples showed that ThO_2 probably have been formed interchangeably with Th_2N_3 due to high susceptibility of thorium nitrides as a general observation towards oxygen.

7.3 Neptunium System

Synthesis of neptunium nitrides was the most difficult of all compounds that have been used in this research work. Only small amounts were used and the handling of these materials was difficult due to high radioactivity of the samples. Synthesis of the reactants (the ammonium neptunium fluorides) was performed at 80 – 100 °C temperatures because of the slow kinetics of the $NpO_2(s)$ with $NH_4HF_2(s)$. The fluoride route was however usable to synthesize NpN . Two ammonium neptunium fluorides were identified from the reaction of $NpO_2(s)$ with solid $NH_4HF_2(s)$. The reaction at 100 °C took less than 7 days to produce $(NH_4)_4NpF_8$ which could be transformed into $(NH_4)_2NpF_6$ after heating it for less than 2 months at 80 °C. $(NH_4)_4NpF_8$ has never been reported before, and it has a crystal structure similar to that of monoclinic $(NH_4)UF_8$ with a $C2/c$ space group. The

second compound, $(\text{NH}_4)_2\text{NpF}_6$, found to have an orthorhombic unit cell and a *Pbcn* space group. This $(\text{NH}_4)_2\text{NpF}_6$ can also be made by heating $(\text{NH}_4)\text{NpF}_8$ at a temperature of 250 °C under $\text{NH}_3(\text{g})$. Five more new compounds of neptunium were identified in the ammonolysis step of the ammonium neptunium fluorides. Compound names and their structural details are summarized in Table 7.1.

Table 7.1 New compounds identified in the ammonolysis of $(\text{NH}_4)_x\text{NpF}_y$.

Compound	Structure details	
	Crystal system	Unit cell
NH_4NpF_5	Monoclinic	<i>P 1 21/c1</i>
$\text{NH}_4\text{Np}_3\text{F}_{13}$	Orthorhombic	<i>Pm21b</i>
NpN_xF_y	Tetragonal	<i>P4/nmmS</i>
NpN_2	Cubic	<i>Fm$\bar{3}m$</i>
Np_2N_3	Cubic	<i>Ia$\bar{3}$</i>

Ammonolysis followed by heating the resulting products (NpN_2 or Np_2N_3) in an inert atmosphere such as high purity argon could be used to make NpN as in the case of UN. NpO_2 secondary phase contaminations were greater at 1100 °C than at 900 °C. Using Zr sponge as an oxygen getter, a reasonable high purity NpN could be synthesized for the chemical characterizations. Kinetics study on the reactivity of NpN with oxygen at ambient conditions showed that the reaction is fast at the beginning and comes to a steady-state condition after about 60 days. SEM images of NpN_2 and Np_2N_3 showed some morphological similarities with respect to their particle shape and sizes. NpN

however displayed to have different morphology. Nanostructures of both higher nitrides (NpN_2 and Np_2N_3) were of high ordered and crystalline. Similar characteristics were identified in NpN nanostructure at particle areas without secondary phases. TEM analysis performed on NpN samples containing large amounts of NpO_2 showed that separate particles of each phase were present in them. Nanoscale single crystals of NpO_2 were observed in some areas of high oxygen contents. Particles containing only nitrogen or both nitrogen and some oxygen showed that mostly the particle surfaces of NpN were affected by NpO_2 crystallizations. NpN oxidations when it was synthesized and after the synthesis were thus confirmed. Use of lower temperatures than $900\text{ }^\circ\text{C}$ and the use of a glove box containing inert atmospheric conditions are recommended for the synthesis of NpN for high phase purity.

7.4 Uranium and Thorium Mixed System

Use of the fluoride route on mixed actinide systems up to $1100\text{ }^\circ\text{C}$ was also tested in this research project. Uranium and thorium system was tested varying the thorium content from 10 to 90 wt%. General chemical composition of the ammonium fluorides of uranium and thorium mixed systems can be given as $(\text{NH}_4)_4\text{U}_{1-x}\text{Th}_x\text{F}_8$. A single phase was identified up to 60 wt% thorium. Change in the lattice parameters of these as-synthesized compounds with respect to the change in thorium weight percentages confirmed a solid solution behavior. From 70 to 90 wt%, the samples produced consisted of separate $(\text{NH}_4)_4\text{UF}_8$ and $(\text{NH}_4)_4\text{ThF}_8$ chemical phases. EDS studies showed a separation of the thorium energy peak in the spectra starting from 60 wt% thorium

sample confirming the XRD results. These compounds appear to consist of incompletely crystallized particle surfaces of similar morphology.

Ammonolysis of these samples containing a single solid solution or two separated compounds produced UN_2 as expected. A UO_2/ThO_2 chemical phase always separated out from the main nitride. The fluoride route was not thus successful in synthesizing (U, Th) N_2 solid solutions at large thorium concentrations. However, microscopic studies such as SEM, EDS, and XEDS showed a small amount of thorium to be incorporated into the UN_2 matrix. Further evaluation of nanostructures of these as-synthesized $\text{UN}_2/\text{Th-U-O}_2$ samples with HRTEM also confirmed this observation. Experiments performed on samples containing from 1 to 4 wt% thorium also displayed separation of Th/ UO_2 chemical phases. These observations demonstrated an unsuccessful use of the low-temperature fluoride route to synthesize (U, Th) N_2 and hence the (U, Th)N compounds. Probable reason for this finding would be the preference of thorium element's oxidation state (4^+).

After failing to synthesize (U, Th) N_x with these compositions, further experimentations on the system were done to check making (U, Th) O_2 solid solutions at a temperature of 1100 °C. Initial experiments on heating the $(\text{NH}_4)_4\text{U}_{1-x}\text{Th}_x\text{F}_8$ samples in air or argon produced (U, Th) O_2 solid solutions with some limitations. After optimizing the experimental conditions however produced the expected oxide solid solutions for the complete series of thorium. This novel route used to synthesize (U, Th) O_2 solid solution is proposed for mixed actinide oxide synthesis.

References

- (1) Wedekind, E. *Zeitschrift fuer Anorganische Chemie* **1905**, 45, 385-95.
- (2) Wedekind, E. *Zeitschrift fuer Chemie und Industrie der Kolloide*, **1909**, 2, 289-93.
- (3) Bruere, P.; Chauvenet, E. *Compt. rend.* **1918**, 167, 201-3.

VITA

Graduate College
University of Nevada, Las Vegas

Gunanda Waduge Chinthaka Silva

Local Address:

3663 S. Valley View, Apt. # 611
Las Vegas, NV 89103

Home Address:

A-3, 695, Soysapura, Moratuwa
Sri Lanka

Degrees:

Bachelor of Science, Chemistry, 2000
University of Colombo, Sri Lanka

Master of Science, Chemistry, 2005
University of Nevada, Las Vegas, USA

Awards:

Best Presentation in Material Science, American Nuclear Society Student Conference
2004 Wisconsin, Madison April, 2004

Dissertation Title: Evaluation of Low-Temperature Fluoride Routes to Synthesize
Actinide Nitrides and Oxide Solid Solutions

Dissertation Examination Committee:

Chairperson, Kenneth R. Czerwinski, Ph. D.
Committee Member, Alfred P. Sattelberger, Ph. D.
Committee Member, Gary S. Cerefice, Ph. D.
Graduate Faculty Representative, Ralf Sudowe, Ph. D.